Modelling and control of hybrid propulsion systems for multirotor unmanned aerial vehicles

Krznar, Matija

University of Zagreb

Faculty of Mechanical Engineering and Naval Architecture

Matija Krznar

MODELLING AND CONTROL OF HYBRID PROPULSION SYSTEMS FOR MULTIROTOR UNMANNED AERIAL VEHICLES

doctoral thesis

Zagreb, 2020

University of Zagreb

Faculty of Mechanical Engineering and Naval Architecture

Matija Krznar

MODELLING AND CONTROL OF HYBRID PROPULSION SYSTEMS FOR MULTIROTOR UNMANNED AERIAL VEHICLES

doctoral thesis

Supervisor: Danijel Pavković, PhD, Associate Professor

Zagreb, 2020

Sveučilište u Zagrebu

Fakultet strojarstva i brodogradnje

Matija Krznar

MODELIRANJE I REGULACIJA HIBRIDNIH POGONSKIH SUSTAVA VIŠEROTORSKIH BESPILOTNIH LETJELICA

doktorski rad

Mentor: Dr. sc. Danijel Pavković, izvanredni profesor

Zagreb, 2020

Bibliography data

UDC:	623.746
Keywords:	Multirotor Unmanned Aerial Vehicle; Hybrid Multirotor Propulsion; Hybrid–electric power unit; Identification and Modelling of multirotor propulsion; Internal combustion engine - electrical generator set, DC–DC converter; Lithium–Polymer battery;
Scientific area:	Mechanical engineering
Scientific field:	Product engineering
Institution:	Faculty of Mechanical Engineering and Naval Architecture
Supervisor:	Danijel Pavković, PhD, Associate Professor
Number of pages:	183
Number of figures:	140
Number of tables:	13
Number of references:	193
Date of examination:	30. October 2020.
Committee:	Josip Kasać, PhD, Full Professor, Department of Robotics and Production System Automation, Faculty of Mechanical Engineering and Naval Architecture, University of Zagreb – Chairman of the Committee Stjepan Bogdan, PhD, Full Professor, Faculty of Electrical Engineering and Computing, Department of Control and Computer Engineering, Faculty of Electrical Engineering and Computing, University of Zagreb – External member Mihael Cipek, PhD, Assistant Professor, Department of Robotics and Production System Automation, Faculty of Mechanical Engineering and Naval Architecture, University of Zagreb – Member
Institution in which this work is archived:	Faculty of Mechanical Engineering and Naval Architecture, University of Zagreb

Supervisor Information

Danijel Pavković, PhD, Associate Professor
Department of Robotics and Production System Automation
Faculty of Mechanical Engineering and Naval Architecture, University of Zagreb
Croatian scientist ID: 232586
https://scholar.google.hr/citations?user=EYo5QcMAAAAJ&hl=en

Danijel Pavković (b. 1975) received his B.Sc. and M.Sc. degrees in Electrical Engineering in 1998 and 2003, respectively, and his Ph.D. degree in Mechanical Engineering in 2007, all from the University of Zagreb, Croatia. Since 2016, he has been an Associate Professor at the Faculty of Mechanical Engineering and Naval Architecture of the University of Zagreb, where he participates in teaching activities in the field of electrical and electronics engineering, sensor and instrumentation systems, microprocessor control systems and power electronics systems. Up to date, he has participated on 30 research, development and technology projects supported by the Ministry of Science, Education and Sport of the Republic of Croatia, the Ford Motor Company, Jaguar Cars Ltd., the CROSCO Integrated Drilling and Well Services Company, European Commission (within FP7 and H2020 framework programs), Croatian Science Foundation, and Croatian Agency for SMEs, Innovations and Investments (HAMAG-BICRO). His current research interests include modeling, estimation and control of battery and ultracapacitor energy storage systems and power converters in hybrid power systems, electrical servosystems applications with emphasis on oil-drilling systems automation and retrofitting, and hybrid propulsion systems for unmanned aerial vehicles. He authored or co-authored 28 journal papers indexed in CC/SCI/SCI-Ex databases, eight papers in other journals, 71 papers presented at international conferences, one scientific book, one book chapter, one patent, and a number of technical reports and studies. His research efforts have been acknowledged by the National Science Award for young researchers in 2005. He has been an active member of KoREMA and IEEE societies for over fifteen years. He is also a member of the Scientific Council for Oil and Gas Economy and Energy of the Croatian Academy of Sciences and Arts (HAZU) since 2018, and the constituting member of the Center for Research Excellence for Data Science and Cooperative Systems (ACROSS-DATASCIENCE) since its inception in 2015.

Acknowledgement

I would like to give extensive thanks to my esteemed supervisor professor Danijel Pavković, for guidance and support during this research.

Special thanks go to my life-long friends Denis Kotarski and Petar Piljek for their valuable advices, and assistance at every stage of this research project.

I would also like to thank professor Davor Zorc, for useful advices and discussions during the development and manufacturing of the electrical part of thesis and continuous support and guidance in my academics career. Your work and legacy will live on, may you rest in peace.

Extensive and special thanks goes to Davor Juric, Karlo Barto and Matej Šavora for help with development of experimental setup.

Substantial credit goes to Mario Schröter, for consultations about hybrid power unit and results validation.

Big thanks to Juraj Benić for Latex discussion and advices. Additional thanks to Filip Maletić and Mario Hrgetić for suggestions.

To all of my colleagues and friends at the Faculty of Mechanical Engineering and Naval Architecture, thank you for creating an enjoyable and productive working environment.

My sincere thanks go to the Committee members for the helpful suggestions and for their time to read the thesis.

Finally, I would like to greatly acknowledge with gratitude, the support and love from my wife Ivona Profeta Krznar. Without her tremendous understanding and encouragement in the past few years, it would be impossible for me to complete this research.

Contents

List of Figures

List of Tables

List of Symbols

φ	Equivalence ratio
ϕ, θ, ψ	Roll, pitch, yaw angles, rad
ρ_{atm}	Atmospheric density, kg/m^3
b	Motor viscous friction constant, Nms
K_e	Motor back-emf constant
η_{bth}	Brake thermal efficinecy
h_{cal}	Fuel calorific value, kJ/kg
$\mathbf{\Gamma}$	Control allocation matrix
$G_{o,i}$	Conductiviy, S
λ	Connection rod ratio
A	Cross-section area m^2
i	Current, A
ζ	Damping ratio
$D_2, D_3 \dots D_n$	Damping optimum characteristic ratios
T_d	Dead time (delay)
e	Back electromotive force
E_i	Energy densitiy, kWh/kgm
$\boldsymbol{F}$	Force vector, N
f^{E1}	Frame, Auxiliary frame 1
f^{E2}	Frame, Auxiliary frame 2
f^B	Frame, Body
f^E	Frame, Earth (fixed)
$\dot{E}_{fuel}$	Fuel energy per second, kJ/s
K_i	Gain, in general
R	Ideal gas constant, J/molK
$\boldsymbol{J}$	Generalised rotation and transformation matrix
g	Gravity acceleration constant, 9.81 ms^{-2}
$\boldsymbol{u}$	Control vector, input of multirotor dynamics model
Qi	Heat energy, J
η_{ith}	Indicated thermal efficinecy
L_i	Inductance, H
$\boldsymbol{I}$	Inertia vector, kgm^2
J_{TP}	Inertia, total motor+propeller, kgm^2
B_i	Linearisation coefficient
m	Mass, kg

W_i	Inlet mass airflow, kg/s
W_o	Outlet mass airflow, kg/s
η_{mech}	Mechanical efficinecy
$\boldsymbol{\omega}$	Angular velocity vector, rad
P_{el}	Power, electrical, W
P_{mech}	Power, mechanical, W
r_p	Pressure ratio
$\boldsymbol{\Omega}$	Propeller squared angular velocity vector
PWM	PWM on-time, µs
R_i	Resistance, Ω
$\boldsymbol{R}$	Rotational matrix
ξ	State of Charge
γ	Specific heat ratio, C_p/C_v
v_i	Velocity of i, m/s
ϑ	Temperature, K
$G_i(s))$	Transfer function
T_e	Closed–loop equivalent time constant
K_t	Motor torque constant
$\boldsymbol{\tau}$	Torque vector, Nm
$\boldsymbol{T}$	Transformation matrix
$\boldsymbol{\eta}$	Vehicle orientation, rad
$\boldsymbol{\xi}$	Vehicle position, m
η_v	Volumetric efficinecy
v	Voltage, V
KV	Voltage constant, rpm/V

Acronyms

6-DOF	six degrees of freedom
AC	Alterating Current
ADC	Analog to Digital Conversion
AFR	Air–Fuel ratio
BDC	Bottom Dead Centre
BEMF	Back Electromotive Force
BESS	battery energy storage system
BLDC	Brushless Direct Current
BPMS	Brushless Permanent Magnet Syncronous
CAD	Computer Aided Design
CCW	Counter-clockwise
COG	Center of Gravity
COM	Center of Mass
CPU	Central Processing Unit
CW	Clockwise
DC	Direct Current
DC–DC	Direct Current to Direct Current
DoD	Depth of Discharge
ECU	Engine Control Unit
ESC	Electronic Speed Controller
FC	Flight Controller/Computer

FEM	Finite Element Method
GPS	Global Positioning Satelites
H_2	Hydrogen gas molecule
HEPS	Hybrid–Electric Propulsion Systems
ICE	Internal Combustion Engine
IMU	Inertial Measurement Unit
LIDAR	Light Detection and Ranging
LiPo	Lithium Polimer
MAF	Mass Air Flow
MPC	Model Predictive Control
MSCS	Master Supervision Controller Software
MVEM	Mean–Value Engine Model
NED	North–Earth–Down
NiMh	Nickel Metal Hybrid
OCV	Open circuit voltage
PD	proportional–derivative
PI	proportional–integral
PID	proportional-integral-derivative
PLC	Programmable Logic Controller
PMDC	Pemanent Magned Direct Current
PMSM	Permanent Magnet Synchronous Motor
PV	Photo Voltage
PWM	Pulse Widith Modulation
RAM	Random Access Memory
RC	Radio Control
ROM	Read Only Memory

RPM	Revolutions per minute
SI	Spark Ignited
SoC	State of Charge
SoH	State of Health
TDC	Top Dead Centre
TWR	Thrust to Weight ratio
UAV	Unmanned Aerial Vehicles
VTOL	Vertical Takeoff and Landing

Summary

Unmanned Aerial Vehicles (UAV) are categorized as autonomous or remotely controlled aircraft that hold a many favourable features allowing them a wide range of useful applications. In order to successfully complete a flight mission, the aircraft must comply with the required flight performance indices. Aircraft performance depends strongly on the propulsion system and therefore different flight characteristics require different propulsion implementations. In contrast to well–known benefits of UAVs utilisation, in particular multirotor type of UAV, there is one major drawback regarding the on–board available energy. Most common electrically powered aircraft can last in the air for 15 to 30 minutes, while the best ones may last up to 60 minutes.

Therefore, to overcome the aforementioned drawbacks of purely–electric energy source in multirotor aircraft, alternative propulsion systems combining two different energy sources (hybrid power systems) are considered. In this work, a methodological approach to the design of a hybrid propulsion unit for multirotor aircraft consisting of an internal combustion engine, electricity generator and electrochemical battery is described.

For this purpose, analysis and modelling of individual components of the propulsion system have been carried out. Physical parameters of dynamic models are identified by means of experimental measurements. Based on the obtained data, a detailed model of a hybrid electrical propulsion configuration was proposed and suitable control strategies for the hybrid power system have been designed. The proposed control system design methodology has been verified by exhaustive computer simulations and experimentally by using different experimental setups.

Keywords: Multirotor Unmanned Aerial Vehicle; Hybrid Multirotor Propulsion;
Hybrid–electric power unit; Identification and Modelling of multirotor propulsion;
Internal combustion engine - electrical generator set, DC–DC converter;
Lithium–Polymer battery;

Prošireni sažetak

Bespilotne letjelice s više rotora pripadaju u kategoriju autonomnih ili daljinski upravljanih zrakoplova karakteriziranih nizom svojstava koje im omogućuju širok raspon korisnih primjena. U svrhu uspješnog ispunjenja letačke misije, letjelica mora zadovoljiti tražene performanse. Uporabljivost takvih letjelica uvelike ovisi o pogonskom sustavu, te zbog toga letački zadaci različitih profila zahtijevaju različite vrste i konfiguracije pogona, sposobnosti vertikalnog polijetanja i slijetanja, *engl.* Vertical Takeoff and Landing (VTOL), kao i održavanja stacionarnih i sporih letova. Letjelice ovog tipa imaju širok raspon korisnih primjena, kao što je podrška iz zraka prilikom nadgledanja, pomoć kod katastrofa ili misija traženja i spašavanja, granične patrole i detekcije neovlaštene prisutnost uz otkrivanje upada i slično. Moderne višerotorske letjelice se sve više koriste u rekreativne i natjecateljske uloge kao što su utrke, snimanje iz zraka uključujući trodimenzijsko skeniranje objekata ili terena, te u poljoprivredne svrhe poput kontrole rasta vegetacije i kontrole utjecaja štetočina.

Zahvaljujući ubrzanom razvoju sastavnih komponenti poput senzorskog sustava, mikrokontrolera, te pogona i baterija, danas su dostupne različite višerotorske letjelice bazirane na „software“–u i „hardwareu“–u otvorenog koda. Takve letjelice prikladne su za istraživanje i ispitivanje različitih regulacijskih sustava stabilizacije leta. Međutim, dinamika takvih sustava je inherentno nestabilna, što znači da letjelica ne zadržava zadanu putanju, osim ako se ne primjenjuju stabilizacijske akcije. Letjelicu karakterizira šest stupnjeva slobode gibanja (tj. tri translacije i tri rotacije), dok je njena dinamika nelinearna. Također, sustav može biti pod–upravljan ukoliko konfiguracija pogonskog sustava ne omogućava neovisno gibanje za svaki stupanj slobode, odnosno drugim riječima, ako se rotacijsko i translacijsko gibanje vozila ne može razdvojiti na nezavisne komponente.

Veliki nedostatak je ograničeno vrijeme leta od obično 15–60 minuta (autonomija) i ograničenja nosivosti korisnog tereta, pri čemu je povećanje veličine tereta u korelaciji sa kraćim vremenom trajanja leta. Određena poboljšanja autonomije više–rotorskih bespilotnih letjelica dobivena su korištenjem motora s unutarnjim izgaranjem kao glavnim pogonom propelera. Za takve sustave, glavni problem je kada letjelica zahtijeva brzu i preciznu kontrolu brzine vrtnje propelera kako bi se postigao željeni profil leta, gdje dinamika motora s unutrašnim izgaranjem potencijalno nije dovoljno brza.

Pogonski sustav letjelice ključan je i neophodan modul koji ima zadatak osigurati stalni potisak propelera kako bi se održao stabilan let. Performanse, učinkovitost i korisnost letjelice značajno ovise o pogonskim karakteristikama i mogućnostima. Tipičan pogon sastoji se od većeg broja propelera spojenih na odgovarajuće pogonske motore koji rotacijom generiraju okretni moment a posljedično i potisak propelera. Pritom izvedbe mogu biti s fiksnim ili varijabilnim kutom propelera, koaksijalno montirani i montirani pod kutem. U literaturama je pokazano da svaki izbor konfiguracije pogonskog sustava ima značajan utjecaj na ponašanje letjelice. Za potrebe održavanja stabilnog lebdećeg položaja, minimalni zahtjev je ostvarenje neto sile potiska koja je približno jednaka težini letjelice. U praksi se pokazalo da bi omjer ukupne potisne sile propelera i težine letjelice, *engl.* Thrust to Weight ratio (TWR) trebao bi biti okvirno dva ili više kako bi se osiguralo dovoljno snage za zadovoljavajuće performanse letjelice.

Propeleri su učestalo pogonjeni električnim motorima s elektroničkom komutacijom, trapeznih oblika elektormotorne sile, *engl.* Brushless Direct Current (BLDC) ili sinusoidalnih oblika elektromotorne sile, *engl.* Permanent Magnet Synchronous Motor (PMSM) koji su opremljeni odgovarajućim regulatorima brzine vrtnje. U većini slučajeva vratilo motora izravno je spojeno s propelerom bez prijenosnog mehanizma (tj. zupčanog ili lančanog pogona). Premda je BLDC odnosno PMSM motor složeniji za analizu prilikom sinteze sustava upravljanja, posjeduje povoljnija svojstva od istosmjernog motora s četkicama i mehaničkim komutatorom, *engl.* Direct Current (DC) Machine zbog veće učinkovitosti u pretvorbi električne u mehaničku energiju i niskih zahtjeva za održavanjem. BLDC i PMSM motori obično su pogonjeni pravokutno oblikovanim faznim naponom kroz šest koraka komutacije. U naprednijim strukturama koristi se i vektorsko upravljanje, posebice za PMSM.

Trofazna armatura može biti spojena u zvijezdu (wye) ili trokut (delta) konfiguraciju namota. Pojednostavljeni ekvivalentni model Unmanned Aerial Vehicles (UAV) motora može se izvesti u svrhu analize i modeliranja dinamike pogonskog sustava.

Elektrokemijske baterije raširenо se koriste kao izvor napajanja više–rotorskih letjelica. Litij–polimerne, *engl.* Lithium Polimer (LiPo) baterije u upotrebi su zbog velike gustoće energije, mogućnosti isporuke značajne snage u kratkim vremenskim intervalima i relativno male mase te predstavljaju najčešću vrstu izvora energije za pogon UAV letjelica, imajući pritom značajne prednosti nad Nikal–Metalnim Hibridnim, *engl.* Nickel Metal Hybrid (NiMh) baterijama u smislu gustoće energije. Međutim, čak i moderne baterije ne mogu osigurati dovoljno energije za dulje letačke misije. Stoga treba istražiti alternativne izvore energije kako bi se povećala autonomija, primjerice primjenu motora s unutarnjim izgaranjem i električnim generatorom i moguće kombinacije s baterijom kao pomoćnim izvorom energije. Kako bi se procijenila preostala zaliha energije baterije, potrebno je pratiti njeno stanje napunjenosti, *engl.* State of Charge (SoC).

Važna komponenta koji omogućuje stabilan let je regulacijski sustav, budući da se letjelica ne može sama stabilizirati bez održavanja upravljačkih komandi za električne motore. Glavni zadatak regulatora je tumačenje ulaznih signala te generiranje izlaznih signala kako bi svaki motor mogao postići traženu brzinu vrtnje. Uobičajeno se sinteza upravljačkih algoritama temelji na pojednostavljenom modelu dinamike tijela zanemarujući složenu dinamiku motora i propelera. Vanjske sile i momenti koje generira pogon su ulazi u sustav dok je orijentacija letjelice definirana tzv. Eulerovim kutovima.

Ovo doktorsko istraživanje opisuje metodološki pristup dizajniranju upravljačkih sustava više–rotorske letjelice sa hibridno–električnom pogonskom jedinicom, temeljenim na kombinaciji motora sa unutrašnjim izgaranjem, električnog generatora i elektrokemijske baterije. Nadalje, izvršena je analiza i modeliranje pojedinih komponenata hibridnog pogonskog sustava. Fizički parametri dinamičkih modela komponenata pogona identificirani su mjerenjima na izgrađenim odgovarajućim eksperimentalnim postavima. Na temelju dobivenih podataka predložen je detaljan model dinamike hibridnog pogonskog sustava za dvije odabrane konfiguracije izvora energije. Predložena metodologija verificirana je računalnim simulacijama i na izgrađenim eksperimentalnim postavima.

U sklopu Laboratorija za elektrotehniku izgrađeni su sljedeći eksperimentalni postavi:

- Laboratorijski postav za ispitivanje agregata u sklopu hibridnog sustava propulzije bespilotne letjelice zasnovanog na motoru s unutarnjim izgaranjem i generatorom temeljenom na beskolektorskom istosmjernom stroju, sa paralelno dodatnom elektrokemijskom baterijom.

- Laboratorijski postav za ispitivanje sustava upravljanja tokovima električne energije temeljenog na DC-DC energetskim pretvaračima i litij–polimernim baterijama.

- Laboratorijski postav za ispitivanje propelerskih potisnika (propulzora) u sklopu sustava hibridne propulzije.

Nakon izgradnje navedenih eksperimentalnih postava proveden je niz mjerenja kojima su identificirani matematički modeli namijenjeni sintezi sustava upravljanja hibridnom propulzijom bespilotne letjelice, odnosno provedena je eksperimentalna provjera odgovarajućuh sustava upravljanja hibridnim pogonom letjelice. Time su postignuti glavni ciljevi istraživanja, odnosno:

- Razrađen je sustavni pristup modeliranju dinamike hibridnog pogonskog sustava više–rotorskih bespilotnih letjelica.
- Temeljem dobivenog dinamičkog modela hibridnog pogonskog sustava i odgovarajućeg postupka sinteze upravljačkog sustava dobivena su poboljšanja u performansama sustava propulzije letjelice.

Provedena istraživanja rezultirala su znanstvenim doprinosima koji se mogu sažeti kako slijedi:

- Identificirani su matematički modeli pojedinih komponenti pogonskog sustava hibridne višerotorske bespilotne letjelice u svrhu dobivanja sveobuhvatnog dinamičkog modela pogonskog sustava, s ciljem poboljšanja procesa sinteze upravljačkog sustava pogona i letjelice.
- Razrađen je postupak projektiranja upravljačkog sustava pogona hibridne letjelice koji uključuje dinamičke karakteristike i eksperimentalno je potvrđen razvijeni sustavni pristup projektiranju regulacijskog sustava hibridne propulzije i letjelice, temeljen na matematičkom modelu koji uključuje dinamičke karakteristike hibridnog pogonskog sustava, čime se u konačnici postižu poboljšane performanse cjelokupnog sustava upravljanja dinamikom letjelice.

Istraživanje prikazano u ovome radu podijeljeno je u šest faza, koje ga opisuju kako slijedi:

1. *Analiza dinamike i modeliranje pojedinih komponenata hibridnog pogonskog sustava*
   U prvoj fazi provodi se matematičko modeliranje sastavnih komponenti pogona hibridne letjelice, koje su međusobno povezane i na različite načine pridonose dinamici letjelice. Kako bi se istražio cijeli raspon dinamike pogonskog sustava, istu je potrebno podijeliti na elementarne komponente i provesti temeljitu analizu, koristeći pritom odgovarajuće fizikalne zakonitosti za opisivanje značajki pogona, na temelju čega se razvijaju dinamički modeli koji su pogodni za računalne simulacije

2. *Eksperimentalna mjerenja i identifikacija fizikalnih konstanti*
   Za potrebe razvoja odgovarajućih dinamičkih modela komponenata pogonskog sustava letjelice, na izgrađenim postavima provode se eksperimentalana mjerenja za identifikaciju fizikalnih konstanti. Snimanje rezultata ostvareno je povezivanjem senzorskog sustava s računalom pomoću odgovarajućeg sučelja za prikupljanje signala u realnom vremenu i spremanje prodataka za naknadnu analizu na računalu.

3. *Razvoj modela hibridnog pogonskog sustava letjelice*
   Koristeći prethodno dobivene modele pogonskih podsustava postavlja se model pogona na kojem se temelji sinteza regulacijskog sustava hibridnog pogona letjelice. Također, predlaže se sveobuhvatni model hibridne propulzije za dvije konfiguracije razmatrane u ovom radu.

4. *Implementacija sustava upravljanja hibridnom propulzijom*
   Eksperimentalna implementacija razvijenih upravljačkih algoritama izvodi se na mikrokontrolerskom sustavu čije je programiranje podržano unutar Matlab/Simulink™ programskog okruženja koje omogućuje generiranje i učitavanje odgovarajućeg programskog koda.

5. *Eksperimentalna validacija predložene metode*
   Za razvijenu metodologiju sustavi upravljanja hibridnim pogonom letjelice ispituju se u realnim uvjetima rada, koristeći pritom izgrađene eksperimentalne postave.

6. *Završetak*
   Izvedba zaključaka iz provedenih istraživanja. Prikupljanje rezultata i analiza znanstvenog doprinosa, objavljivanje znanstvenih radova.

1 Introduction

This chapter provides a brief introduction to the topic as well the main motivation for this thesis. Furthermore, the overview of current state–of–the–research is presented, followed by the goals and scientific contribution of this work. The final sub–chapter outlines the thesis structure.

Unmanned Aerial Vehicles (UAV) represent a distinct class of aircraft that can be guided autonomously (without being subjected to outside control) or by remote control from ground without a human pilot aboard [1–3].

Multirotors or multicopters are rotorcrafts with more than two lift–generating rotors. Usually, they are designed and arranged in a such way to enable Vertical Takeoff and Landing (VTOL), stationary hovering, and satisfactory forward flight characteristics. The orientation and stability of aircraft are maintained by adjusting the speed of each propeller independently, thus causing the differential thrust and resulting torque to set the aircraft in motion [1–3]. Aforementioned properties give these aircraft a wide range of useful applications (see Figure 1.1), such as: support of disaster relief or search and rescue [4, 5], security applications i.e. border patrol and unauthorized ingress detection [6, 7], aerial photography including 3D and thermal mapping of objects and terrain [8], inspection of high–tension power lines [9], agricultural purposes such as vegetation growth and pest control [10].

Multirotors possess certain advantages when compared to the traditional unmanned aerial platforms, such as aeroplanes and helicopters. Even though aeroplanes outperform multirotors in terms of flight autonomy and speed, as well as with respect to air drag and related fuel economy indices, they typically do not have VTOL flight and hovering capability, with only few military aircraft as exceptions to this rule, such as Hawker Harrier Jump Jet [11] and Lockheed–Martin F–35 Lightning II [12], both possessing jet engine thrust vectoring capabilities, and Bell–Boeing V–22 Osprey, whose VTOL ability is due to utilisation of tilt–rotors [13].

Helicopters, on the other hand, even though inherently capable of VTOL hovering operation, are still inferior due to the need for complex mechanical transmission of torque from the prime mover (ussualy internal combustion engine) to propellers. In contrast to

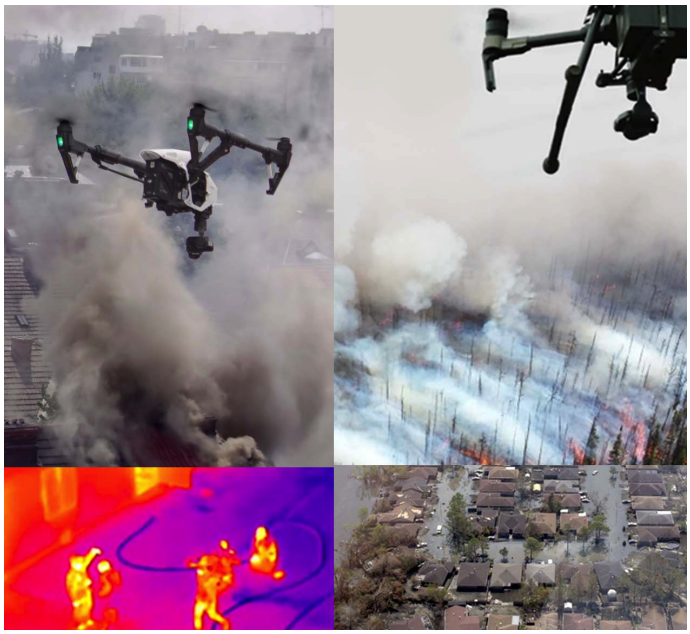

(a)

(b)

(c)

(d)

(e)

(f)

Figure 1.1: UAV applications (a) Firefighting and rescue, adopted from [14], (b) Security [15, 16], (c) Aerial photography [17], (d) Inspection [18], (e) Agriculture [19], (f) Delivery [20]

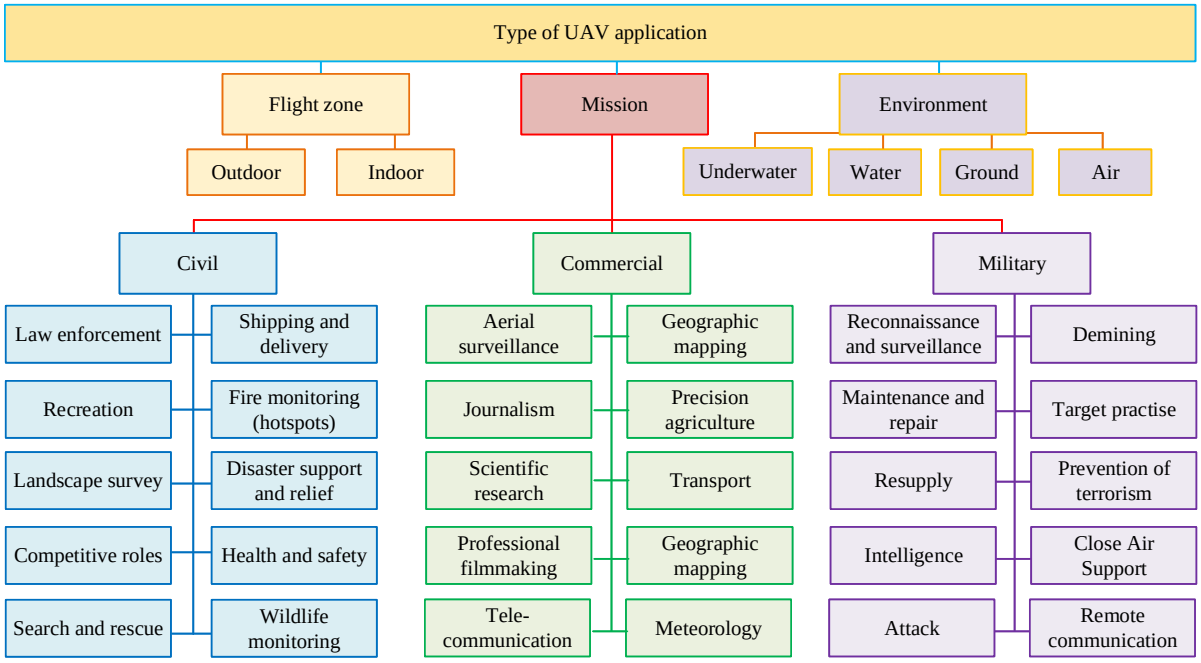

Figure 1.2: UAV categorisation

helicopters, most multirotor UAVs have purely electrical transmission of power from the energy source (i.e. on–board battery energy storage system) to the propeller electrical drives, which implies simplicity of power transmission and related straightforward control of individual multirotor propulsion units. However, this mechanical simplicity is paid for by the complexity of the underlying electronics systems, as multirotors require a dedicated electronic flight control system and power electronics interface towards individual propeller electrical drives in order to effectively stabilize the aircraft by commanding appropriate propeller motor speeds according to control inputs generated by the flight controller.

In order to categorise and classify various types of UAVs there are multiple classification schemes that have been proposed and/or are currently in use [1]. Figure 1.2 shows the one possible classification scheme based on application of aircraft. On the graph, mission–based classification is elaborated in a more detail. Based on aerodynamic configuration the UAVs can be classified as:

- Fixed Wing UAV, similar to aeroplanes requires a runway in order to take–off and land. They have significant flight autonomy and high cruising velocities. They are extensively used in a various monitoring applications as meteorological and environmental monitoring and reconnaissance (scouting),

- Rotary wing UAV (multirotor) that use so–called aerofoil shaped wings usually arranged in circular pattern. They are characterised by a vertical take–off and landing capability, as well as stationary flight (hovering), and are very useful for short

range tasks. Also, multirotors consume significantly more energy because thrust is generated only by propellers, unlike the fixed wings where thrust is generated by propulsors and shape of aircraft.

1.1. Motivation

Over the last couple of decades, advances in electronics and materials science allowed production of the cheap lightweight flight controllers, high–power–density electric motors, high–discharge–rate batteries, integrated inertial sensors and global positioning system receivers, digital cameras and many other useful systems that are suitable for UAV applications. However, a major drawback of multirotor UAVs is their inherently limited endurance and flight range, which are directly correlated with the aircraft mass and battery energy storage capacity. For the most common multirotor design, i.e. fully electric quadrotor powered by batteries, flight autonomy typically ranges between 15 and 30 minutes, with 60 minutes flight time currently being the effective upper limit of endurance of battery–powered multirotor UAVs. Hence, in order to overcome the aforementioned drawbacks of purely–electric energy source, alternative propulsion systems combining two or more different energy sources (hybrid power systems) may be considered, such as those based on Internal Combustion Engine (ICE) coupled with the electricity generator, or power sources based on hydrogen fuel cells and photovoltaic power [21–23]. This represented the initial motivation for the research presented in this work.

In that respect, ICE–based hybrid propulsion system would offer distinct advantages because the specific energy density of gasoline fuel of about 12 kWh/kg is about two orders of magnitude greater than the specific energy density of Lithium Polimer (LiPo) battery of about 0.2 – 0.5 kWh/kg [24], so it may offer notable improvements in terms of flight endurance and range (see Figure 1.3). Hybrid–electric propulsion is nowadays typically found in road vehicles and rail transport, as illustrated in [26, 27] and references therein. In contrast to aerial vehicles, land–based vehicles move in two dimensions and their gravity–related constraints are much less emphasised. So, naturally, hybrid propulsion system implementation in UAV would also be a greater challenge compared to land–based vehicles, which was an additional motivation for the proposed research topic.

Moreover, technical specifications of widely available and relatively inexpensive "off the shelf" components are typically incomplete or unreliable, which poses a problem during the aircraft propulsion system design process, because the propulsion component performance needs to be additionally evaluated. Hence, it is also necessary to model the behaviour of individual UAV propulsion system components and identify the key parameters by means of experiments, so that a sufficiently accurate mathematical model of the hybrid

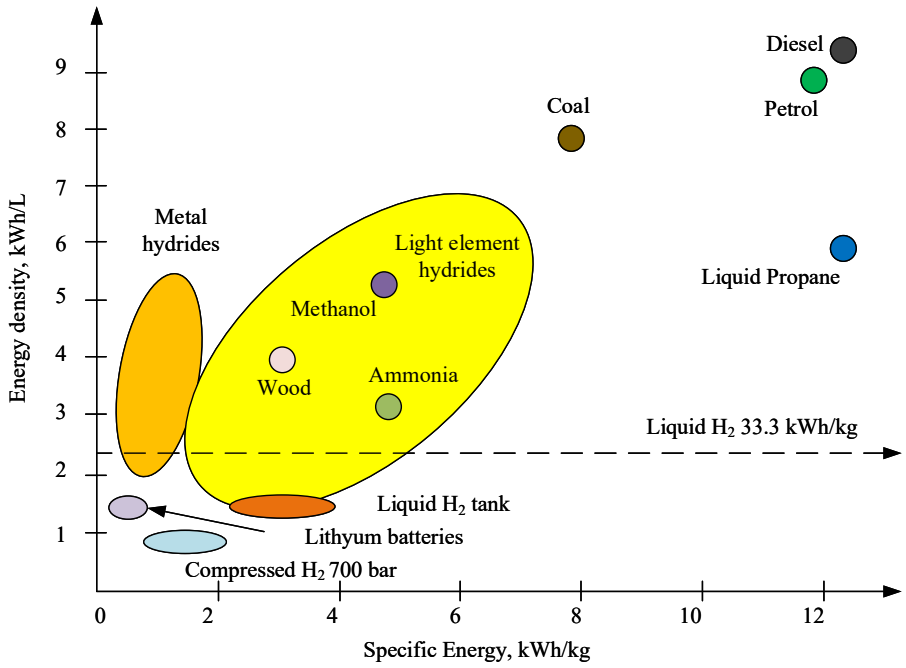

Figure 1.3: Energy densities of various energy storage materials and technologies [25]

propulsion system can be derived to be useful for control system design. Finally, most UAV control platforms offer only a limited ability to modify the control software. This mandates utilisation of fast prototyping hardware with open firmware for the purpose of control system implementation on a realistic UAV platform.

Having this in mind, the research presented herein focuses on the multirotor UAV propulsion based on internal combustion engine coupled with electricity generator, and augmented with the battery energy storage system, and its modelling, identification and control system design. A custom–built hybrid power unit prototype with dedicated control unit has been used for hybrid propulsion control system design experimental verification.

1.2. Overview of current state–of–research

Multirotors, as typical representatives of motion platforms with complex dynamics, are covered by a wide area of research with the highly active research community. Consequently, notable progress has been achieved in this area over the last decade, which stems from the fact that multirotor UAVs have many practical applications, as well from the advances in the field of mechatronics in general. Therefore, in order to perform a systematic review of this broad research field, it can be divided into the following distinct areas:

- Advanced mobile robotics, such as those related to aircraft swarm coordination

and control, computer (machine) vision, pattern recognition and related decision making, aimed at utilising these aircraft more effectively.

- Aircraft system mechanical design, flight mechanics and computation aerodynamics modelling, which are focused on reducing air–drag effects and developing stiff and lightweight airframes, along with identification of key parameters of the aircraft dynamic models.

- Control system design, where various control design approaches are intended to improve the overall flight stability or reference tracking performance are researched and appropriate control strategies are developed.

- Propulsion system research, where propulsion design, efficiency, power management, and means to increase aircraft autonomy, speed and other favourable properties are investigated.

Advanced robotics has most recently dealt with various swarm robotics approaches where multiple units perform useful tasks more effectively [28–32]. On the other hand, very popular are hybrid configurations such as rotor/fixed–wing [33, 34] that combine beneficial properties of both type of aircraft. In order to furthermore increase the utilisation value of UAVs, additional systems are developed, such as robotic manipulators [35–37], autonomous flight by utilising sensor system for environment perception and state estimation [38, 39], model predictive control approaches [40], distributed and multi–agent control approaches [41, 42] and many others. Mechanical system design deals with overall design of aircraft, as well as the frame structure and propulsion configuration [43–46]. For further development purposes it is required to identify physical constants of aircraft (i.e. moments of inertia) online, by using the method presented in reference [47].

Control system design research for multirotors includes different approaches to UAV flight controller design and implementation, wherein several control methods predominate in practical applications, and those are quite extensively researched. A good introduction to multirotor control systems is given in reference [48]. Most commonly used in multirotor aircraft dynamics control are traditional linear proportional–integral (PI) and proportional–derivative (PD) controllers and their combinations [49–51, 51], with a good overview of linear control methods given in reference [52]. However, more complex nonlinear control schemes, such as back-stepping control or sliding–mode control and their derivates are becoming more widely researched [53], with Model Predictive Control (MPC) approaches and those based on deep learning methodologies representing the current cutting–edge in flight control systems being thoroughly researched in the literature [54, 55]. These advanced flight control approaches typically offer notable improvements in terms

of tracking accuracy for reference trajectory tracking problems when compared to more traditional control methods, but this is paid for by significantly more complex control law implementation in real flight controller hardware. The research [56] presents several control methodologies for multirotor UAVs. Significant research of control systems also includes the following literature [48, 56, 57].

The aforementioned research in advanced mobile robotics, aircraft system mechanics and aerodynamics, and flight control system frequently assumes that the aircraft propulsion system is near–ideal, meaning that flight controller commands are directly translated into accurate propeller thrust (rotational speed) with minimum delay for all operating conditions. Also, the propulsion system represents the most crucial subsystem of a multirotor aircraft, and its research and development of appropriate hardware and low–level control systems is inextricably related to any subsequent research in the above–mentioned fields.

In general, UAV propulsion system consists of a power source (such as LiPo battery, internal combustion engine, hydrogen fuel cells, photovoltaic panels and different hybrid power supply configurations) supplying the propulsors, comprising of propellers connected to electric motors driven by respective motor drivers and controlled by embedded speed controllers. An excellent introductory overview of propulsion systems and experimental identification is given in reference [58], whereas reference [59] presents the methodology for propulsion component selection based on the simplified modelling and describes the popular online drive system validation software tool suitable for preliminary calculations during initial aircraft design. In [60] authors discuss the effects of propeller configuration on the propulsion system efficiency of a multi–rotor UAV, including detailed tests of different propeller types, along with the analysis of different overlapping propellers configurations. The latter configuration may be particularly well–suited when optimising aircraft configuration because it allows utilisation of larger propellers or shorter length of the multi–rotor arms while being able to maintain the same level of propulsion system efficiency.

Brushless Permanent Magnet Syncronous (BPMS) motors [61] are most commonly used for the multirotor UAV applications due to their ability to be designed as lightweight machines, typically by using the so-called outrunner configuration [61, 62]. Thorough analysis of brushless motor operation is given in references [63–65], with working principles and detailed dynamics models presented therein. Furthermore, analysis of brushless motor feasibility for hybrid propulsion of UAV is given in [66], wherein the machine designed therein can be operated as the internal combustion engine starter and generator, as well as the main motor.

According to reference [67], electrochemical batteries are the most common power

source in multi rotor UAV's. The research presented therein concerns the power consumption of fully electric rotorcraft and derives an endurance estimation model for such aircraft powered by LiPo batteries commonly used in UAV applications. Theoretical analysis in [67] is also supported by experimental flight tests using a commercial quadrotor unit. In reference [68] a battery State of Charge (SoC) based altitude controller was developed and experimentally verified. The aforementioned work provides a valuable insight into the dynamics modelling of both LiPo batteries and propeller drives comprising brushless motors and power electronics hardware including embedded brushless machine speed controllers. Especially when battery SoC and State of Health (SoH) estimation are concerned, highly accurate and sufficiently detailed models are required, because battery model parameters may notably vary with operating point (SoC) and ageing effects (see [69, 70] and references therein). Kalman filtering methodology is typically used for battery SoC / SoH estimation [69]. Utilisation of internal combustion engines for aircraft propulsion is very common in air-planes and helicopters, wherein these engines should be reliable, lightweight and characterised by high power output and high power density. Research presented in [71] is focused on the design and implementation of an Engine Control Unit (ECU) to control a two–stroke ICE for an UAV, in particular on controlling the Air–Fuel ratio (AFR) of the combustion process by measuring the exhaust gas composition and manipulating the quantity of injected fuel by using the electronic fuel injector. In reference [72] authors propose an implementation of hybrid–electric power system, which has been thoroughly tested in simulations. Results from [72] indicate that improved flight endurance can be achieved for the fixed wing aircraft, but also point out to several issues with small–scale/low–power internal combustion engines, such as emphasised and complex vibration signatures and requirement of forced–convection cooling or other type of thermal management. Experimental identification and modelling of internal combustion engine–based propulsion is described in detail in reference [73], including both static and dynamic characteristics of the propulsion system. In particular, authors present a method to determine the static throttle–speed and speed–thrust dependencies which form the basis for main rotor speed PI controller design. Thus, obtained results suggest that this approach may be suitable for attitude control of a large quadrotor.

Due to the highly non-linear nature of the internal combustion engine static characteristic and torque dynamics, a more precise approach based on the so–called Mean–Value Engine Model (MVEM) may offer additional benefits in terms of PI or proportional-integral-derivative (PID) controller performance (response speed) optimisation for different engine operating regimes [74]. To this end, reference [75] considers a PI controller with feed–forward load compensator for improved hybrid propulsion system engine speed control subject to abrupt power-train load changes. Since UAV applications are typically

characterised by strict weight constraints, reference [76] proposes a sensor–less approach to speed control of ICE–generator set, whereas speed information is either obtained from the readily available generator voltage and current measurements or using the relatively unsophisticated rotor position measurements from embedded Hall sensors used to detect electrical machine phase switching sequence. In both cases a Kalman filter is used to obtain a rather low noise estimate of the internal combustion engine speed. On the other hand, the design, implementation and analysis of internal combustion engine plus electricity generator hybrid propulsion system for a triple tilt–rotor UAV are presented in reference [77], wherein the hybrid power–plant architecture is designed while honouring the constraints on the characteristics of the power–plant components for three fundamental hybrid–electric configurations. The dynamic model and attitude control principle is also given for the hybrid–propulsion UAV, and flight dynamics performance testing was conducted by means of flight experiments on the developed UAV prototype.

A review of existing and current developments in the field of Hybrid–Electric Propulsion Systems (HEPS) for small fixed–wing UAV is presented in [78]. Authors provide a detailed description and simulation of a parallel HEPS for a small fixed–wing UAV. A modelling approach for the electrical power system architecture suitable for UAV is given in [79] wherein generic power system architecture is presented and the proposed and the hybrid power supply model is validated experimentally on a DC–AC inverter plus Permanent Magnet Synchronous Motor (PMSM) laboratory setup. A Brushless Direct Current (BLDC) generator plus active front end rectifier as power source for an ICE–based hybrid–propulsion UAV has been researched in [80], wherein such a configuration can offer distinct advantages in terms of minimising the number of components, while using PI and PID controllers for engine speed and internal DC bus voltage control.

A comprehensive power distribution approach presented in [81] utilises a parallelised array of low–cost DC-DC power converters and battery energy storage, wherein the proposed centralised power management control system effectively coordinates different power sources while maintaining the UAV's internal DC bus voltage close to the prescribed value. For the purpose of finding optimal hybrid power–train configuration and components, reference [82] proposes a parameter matching method between coaxial rotor–based UAV and the hybrid power system requirements that satisfy the predefined rotor power supply and UAV flight performance. Test results presented in [83] corroborate the feasibility of the parameter matching method and its accuracy. The behaviour of different power sources within a hybrid electric propulsion system of an UAV was investigated in [84] by means of simulations, which were subsequently used to predict the hybrid electric power system behaviour before the costly flight test. Thus, the proposed approach can be a useful tool in determining the feasibility and efficiency of the on–board

power system.

Similar to research presented in [72], reference [21] analyses several realistic challenges related to internal combustion engine–based hybrid–electric propulsion systems, such as mechanical vibrations, engine cooling issues and acoustic noise and their implications to operation of a compact power unit comprising a small–scale internal combustion engine plus suitable electricity generator. It has been shown in [21] that such small internal combustion engines produce complex and powerful vibrations which cannot be merely reduced to the rotation of the engine crankshaft or motion of the piston.

As an alternative to utilisation of internal combustion engines as prime movers in hybrid propulsion UAV, reference [84] investigates the potential of hydrogen fuel cell stacks as power supplies for small UAV's. In particular, reference [84] compares five different power-train options by means of simulations, namely those based on lithium–ion batteries ($LiNiCoAlO_2$ and lithium–air), ICE with integrated rotary generator, parallel hybrid power-train configuration with ICE, free piston engine with integrated linear generator, and the proton exchange membrane fuel cell.

The use of a fuel cell stack as the main source of power for a small unmanned aerial vehicle is shown in [85], where investigation was based on the commercial "Aeropack" hybrid power supply consisting of a fuel cell stack and a battery pack. Authors present the following characteristics of the hybrid system: voltage–current dependences, stability of performance for various loading and Hydrogen gas molecule (H_2) sourcing (pressurized H_2 cylinders or chemical sources of H_2), interaction between the fuel cell stack and the battery pack within the power supply and consumption of hydrogen fuel as a function of loading. The functionality of the fuel cell–battery hybrid system has been demonstrated by a successful flight test of the UAV prototype. In contrast to the aforementioned hybrid power sources, photovoltaic power is mostly utilised on fixed wing UAVs, and shows promising potentials only as an auxiliary power source, as indicated in [86–88].

Based on the review of research activities in this field, the following conclusions are drawn. The above overview shows that the problem of aircraft autonomy is being actively investigated and various advanced propulsion systems are currently being researched in order to satisfy the requirements for low power consumption, low mass and high output power within small dimensions. In most cases, hybrid propulsion research is conducted for fixed wing aircraft, whereas multirotor aircraft are almost exclusively fully electric, with some applications of fuel cells and similar energy sources. Taking into account the above issues related to specific energy density, mass, ease of operation and performance, and price and availability, hybrid propulsion of multirotor UAV's based on an internal combustion engine coupled to an electricity generator and utilising a battery energy storage system as auxiliary power supply should provide many attractive research challenges

in the field, while simultaneously opening new research frontiers which might ultimately improve knowledge levels in multiple research sub–areas.

1.3. Aim, hypothesis and contribution

The aim of research presented herein is to develop a systematic approach to modelling the dynamics of the hybrid propulsion systems for multirotor UAVs and improved control system design process for the propulsion system and aerial vehicle itself. In particular, the proposed research focuses on the hybrid propulsion and drive system of a multirotor unmanned aerial vehicle.

The propulsion unit is based on the internal combustion engine coupled to an electricity generator connected alongside the battery energy storage system to the common DC bus supplying the individual propeller electrical drives. Research activities presented herein included: hybrid propulsion system topology analysis, mathematical modelling and process model identification, development of the control system and experimental validation. Appropriate physical modelling principles are used to identify the governing physical equations and to obtain suitable dynamic models of individual propulsion system components, ultimately used as a basis for subsequent control system design. A custom–built hybrid power unit prototype with dedicated control unit is eventually used for the experimental verification of thus designed hybrid propulsion control system.

Having this in mind, the hypothesis of this work is that the utilisation of hybrid power system with improved control system design approach based on a hybrid propulsion system model can result in improved flight endurance of an unmanned aerial vehicle. The research conducted in this work has ultimately resulted in the following original scientific contributions in the area of UAVs:

- Identification and mathematical modelling of individual components of a propulsion system for the purpose of a comprehensive dynamic model of the hybrid propulsion system with aim of improving control system design.
- Development of a systematic approach to control system design of multirotor aircraft with hybrid propulsion, based on a mathematical model.

1.4. Thesis structure

This thesis is organized as follows:
Chapter 1 is introduction with motivation, aim, contribution and hypothesis of this research. It also presents an in–depth literature review of the current state–of–the–research

in the field of UAVs and related hybrid propulsion systems and provides the overview of the thesis structure.

Chapter 2 presents a brief overview of UAV technology and individual components utilised in multirotor UAVs for the purpose of better understanding of the content presented in subsequent chapters of this thesis. A basic overview of multirotor topologies is also given herein.

Chapter 3 presents the overview of hybrid propulsion system of a multirotor aircraft, and detailed descriptions of operation principle for all underlying components.

Chapter 4 presents the detailed analysis, modelling, identification and simulations of a hybrid propulsion system and its underlying components.

Chapter 5 deals with control system design for the hybrid power unit and the aircraft. It also presents detailed models of control systems and the subsequently developed simulation models.

Chapter 6 is the chapter that deals with experimental validation of proposed hybrid power unit concept.

Chapter 7 presents the main conclusions of this thesis.

2 Preliminaries

This chapter is focused on the preliminaries required for comprehensive understanding of concepts presented in this thesis. Initially, the operation principle of multirotor Unmanned Aerial Vehicles (UAV)'s and overview of multirotor configurations are presented, followed by a short overview of propulsion systems and their components. Finally, different coordinate systems and their respective mutual transformations are given, along with the Euler–Newton based kinematics and dynamics for a rigid body with six degrees of freedom (6-DOF) used to describe the motion of the aircraft.

2.1. Principle of operation

A multirotor, also called a multirotor helicopter or multicopter, is an aircraft that is lifted and propelled by n rotors, where propellers are attached to their respective motors (see Figure 2.1) Rotors are typically aligned in a so–called "square" or "cross" configuration, where two propellers on opposite diagonal corners of the square rotate in Clockwise (CW) direction, while the other two propellers rotate in Counter-clockwise (CCW) direction. Such aircraft have 6-DOF of motion, and four input control variables: *thrust*, *roll*, *pitch* and *yaw*.

(a) (b)

Figure 2.1: Multirotor types: quadrotor [89] (a), hexarotor [90] (b)

The continuous flight stability is provided by adequate control–based actuation of individual rotors (propeller drives) and suitable power systems which facilitate ample power supply to individual rotors. In order to ensure favourable performance and successful mission completion, a control system implemented within the flight computer must be able to gather and process different signals in real time from appropriate sensors (so–called sensor fusion), estimate/predict all unknown variables (disturbances), calculate appropriate control signals and commit control commands to actuators (i.e. to take certain control actions).

Multirotor propulsion system is a crucial and indispensable module whose task is to provide the necessary thrust in order to maintain stable flight of the aircraft. The UAV performance, effectiveness, and utility depend strongly on the propulsion capabilities. A typical propulsion unit comprises multiple propellers attached to respective motors, wherein four, six or eight propellers are typically used, and are arranged in different configurations. Individual propellers are usually driven by electrical motors, equipped with corresponding electronic speed controllers and supplied by the battery power source [58]

In order to put the aircraft into a stably held position (so–called hovering, see (see Figure 2.2), the net thrust of all propellers must be compensate gravitational force, thus cancelling out the weight of the aircraft. In order to increase the altitude (to ascend the aircraft), the rotational speed (in revolutions per minute, or RPM) of motors must be equally increased for all motors. As a consequence, a non–zero upward resultant force appears (i.e. generated lift is greater than the aircraft weight), and the aircraft ascends with constant acceleration. Descending is opposite to ascending, so a mutual decrease of all propellers' velocities causes the thrust to decrease below the thrust needed to support the weight of the aircraft, so it descends (Figure 2.2).

Rotation around z–axis or so–called *yaw* is induced by unbalanced torques of motors

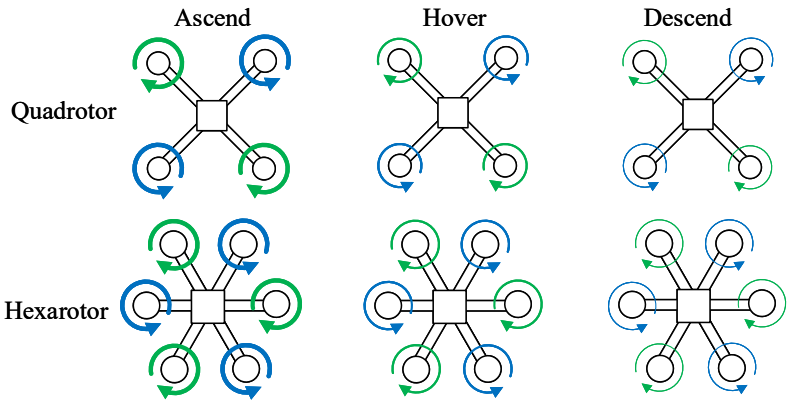

Figure 2.2: Ascend, hover and descend operation of multirotor

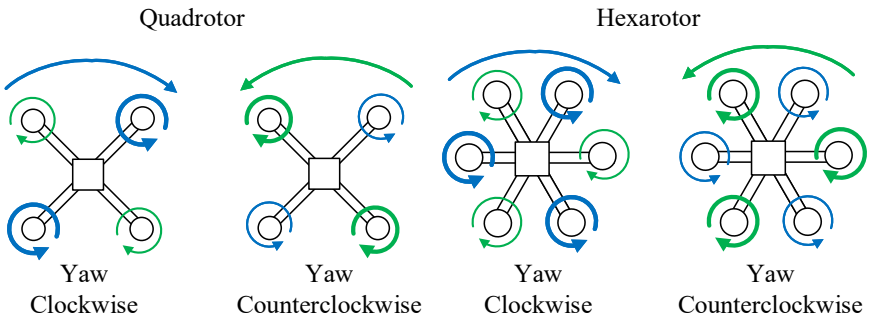

Figure 2.3: Yaw motion of multirotor

connected to individual propellers. Because of this imbalance, the clockwise and counter clockwise torques cannot cancel out completely, and the aircraft has a positive or negative resultant torque about yaw axis. If a clockwise motor pair decreases its RPM by a certain percentage and at the same time the counter–clockwise pair increases its RPM by the same percentage, the aircraft will retain the overall upwards thrust and maintain altitude, but the net torque acting upon the aircraft is unbalanced, with the resulting (reaction) torque oriented in CW direction (opposite to torque of faster–spinning motors), so the multirotor will yaw to the right (see Figure 2.3).

Forward or backward movement is caused by the rotation around y–axis, which is usually referred as *pitch* motion (Figure 2.4). By increasing the speed of the propellers at the rear and decreasing the speed of the propellers in the front, imbalance of thrust produces the torque that rotates the aircraft around the respective axis. Since the thrust is decreased at one side by the same amount as is increased at the other, the net thrust remains the same.

Left and right motion of aircraft is caused by rotation around the x–axis or *roll* motion, similar to *pitch* motion, i.e. by increasing the speed of propellers on one side, and decreasing the speed of the propellers on the other side, the thrust imbalance occurs, creating a torque that rotates the aircraft about the x–axis (see Figure 2.4).

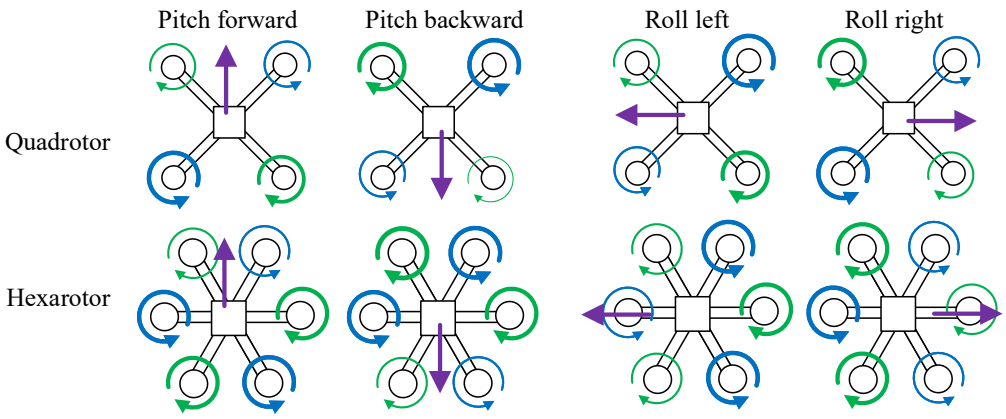

Figure 2.4: Roll and pitch motion of multirotor

2.2. Multirotor configuration

Multirotor configuration is predominantly determined by the propeller arrangement, which is defined by the geometric positions (locations) and characteristics of the propulsion units. Having this in mind, multirotor aircraft can be categorised into the following configurations (see Figure 2.5) [91]:

- flat (quadrotor, hexarotor, octarotor),
- coaxial flat (Y6, X8 multirotor),
- overlapping flat,
- non–flat (passively or actively tilted) multirotor UAV's,
- different combinations of above configurations.

The most common, and by far the most used multirotor configuration is the one with four rotors, the so–called quadrotor or quadcopter [44]. There are usually three frame shapes: "X", "+" and "H". Compared to quadrotor with similar propeller electrical drives, hexarotor provide greater lifting capacity by employing extra motors, mounted typically at equal angular distances on a symmetric frame, and implemented as two sets of propellers, with three CW and three CCW propellers in each [92].

Hexarotors can provide redundancy if a single motor failure occurs, providing enough remaining thrust so that the aircraft can remain flight–worthy with stable dynamics in order to perform safe landing. Octocopters are like quadcopters and hexacopters, where flight performance is similar to the hexarotor with higher power demand, more payload capability and improved redundancy and robustness to propeller faults. Furthermore, hexacopter and octocopter can be made with coaxial motor–arrangement, where counter

rotating propellers are placed one on top of another. Note that coaxial configurations can result in smaller aerial vehicles for the same number of propellers and are also used for certain difficult tasks such as lifting of heavy load. However, coaxial configurations can be less energy–efficient and, thus, may provide less flight time than non–coaxial configurations.

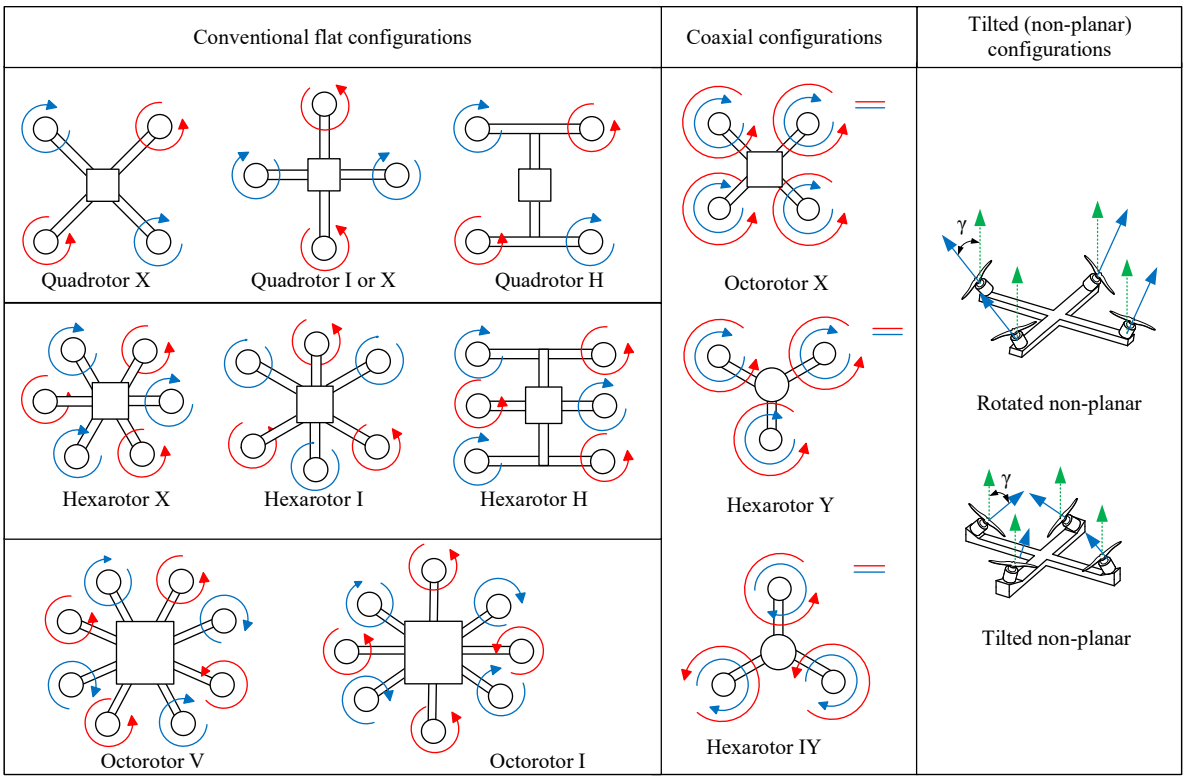

Figure 2.5: Multirotor configurations

2.3. On-board hardware

The most fundamental components of a multirotor aircraft are:

- Body (frame),
- Electrical motors with Electronics Speed Controllers (ESC),
- Propellers,
- Power source (battery),
- Flight Controller,
- Radio Control (RC) receiver and remote controller.

Also, there are optional components and peripherals such as: camera and video transmitter, telemetry radio transmitter, Global Positioning Satelites (GPS) receiver, 4G modem and many other auxiliary components and accessories.

2.4. Frame

Aircraft frame is the main structure of a multirotor with its purpose for mounting and holding all of the components together (see Figure 2.6a, 2.6b). From the design point of view, frames can vary by shapes, dimensions, and materials. Aircraft frame needs to be lightweight, but still rigid enough with sufficient damping properties in order to minimize the vibrations generated by the propulsion system. Purpose and size of multirotor is determined by the frame wheelbase (Figure 2.6c), which is defined as a circle with the diameter that is the shortest distance between opposite propeller motors.

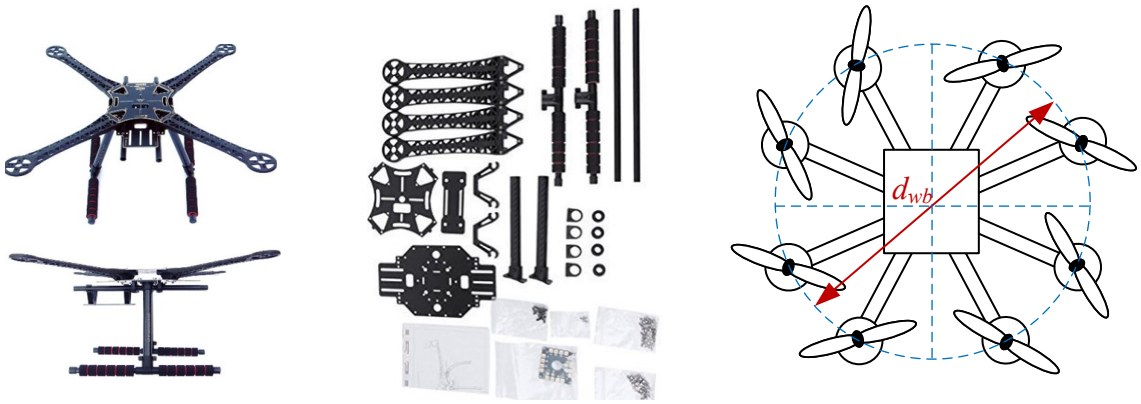

(a) (b) (c)

Figure 2.6: Assembled quadrotor frame with landing gear and gimbal mount [93] (a), parts of frame assembly [94] (b), wheelbase diameter definition (c)

2.5. Electrical motors

Brushed Direct Current (DC) and Brushless Permanent Magnet Syncronous (BPMS) motors are the two most common types of motors used in multirotors (shown on Figure 2.7), with brushless motors mostly used on larger multirotors such as those for racing, aerial photography and other larger UAV's, while brushed DC motors typically used on micro drones and toy drones.

Brushless motors are electronically commutated and usually have three connecting wires (corresponding to three phases of stator windings) where order of connection to Electronic Speed Controller (ESC) is important. Namely, swapping any of the three

(a) (b) (c)

Figure 2.7: DC motor for toy multirotor [95] (a), small BPMS motor [96] (b), large BPMS motor [97] (c)

phases will change the direction of the motor rotation, but some ESC's make it possible to change rotation direction in firmware.

The dimensions of brushless motors are coded by a 4–digit number of form *aabb*. Where *aa* is the stator width (or stator diameter), while *bb* is the stator height. For commercially available motors, manufacturers usually indicate the so called KV value which is defined as a guideline value of how many revolutions per minute will unloaded motor achieve per unit input voltage (per single volt). To be noted, KV value is different from motor voltage constant K_v used in dynamics modelling of motor.

BPMS machine (see Figure 2.8) consists of the rotor shaft (1) with attached rotor magnet (4), Hall sensors (logic level Hall probes) for rotor angle detection (6), stator case with stator windings (marked 3 and 2, respectively in Figure 2.8) and stator winding phase connections (marked 5 in Figure 2.8).

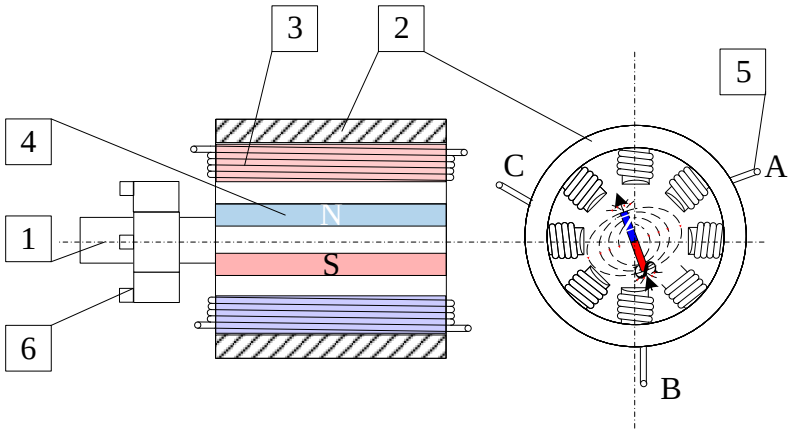

Figure 2.8: BLDC machine exterior and interior parts

(a) (b) (c)

Figure 2.9: Small ECS 10 Amps for racing multirotors [101] (a), ECS 30 Amps, for 10–11 inch propellers [102] (b), ESC 180 Amps, for large aircraft [103] (c)

ESC are integrated inverter/switching power supply which provide three phase bidirectional square voltage to drive the motor. BPMS machine phase commutation depends on the rotor position which can be determined by sensor–based or position sensorless methods [98–100]. Motor speed is affected by the voltage duty–cycle variation (i.e. Pulse Widith Modulation (PWM) switching action with respect to DC power supply voltage). With higher PWM duty cycle, phase voltage increases, and consequently angular velocity of the motor also increases. ESC is characterised by a current rating that is measured in amperes. Current rating can be referred to as continuous current and burst (peak) current, where continuous current rating indicates the maximum amount of current that ESC can handle at normal (permanent) operation. Burst current limit is higher than the continuous current rating, and it represents the maximum current that ESC can withstand for a short period of time. ESC's currently available on the market are based on ATMEL (8–bit) and ARM Cortex (32–bit) processor architectures. As for input signal types, ESC can operate on various protocols, such as standard PWM, OneShot, DShot and others. Photographs of several types of ESC's are shown in Figure 2.9, starting a low–power ESC in Figure 2.9a, through medium power demand units, as the one shown in Figure 2.9b, to high–power units, such as the one shown in Figure 2.9c.

2.6. Propellers

Multirotor propellers (shown on Figure 2.10) generate aerodynamical forces and torques that induce aircraft movement. For stable flight it is necessary to achieve sufficient vertical lift force in order to counter the weight of the vehicle, along with other necessary forces and torques to control the attitude and altitude of the aircraft during its flight.

The propeller acts like a rotating wing. It is known from aerodynamics of wings that the pressure over the top of a lifting wing is lower than the pressure below the wing. A spinning propeller sets up a pressure lower from that of the free airstream in front of the

(a) (b) (c)

Figure 2.10: a) 5045 – 3 blade propeller [104] (a), 8045 – 2 blade propeller [105] (b), 2266 – 2 blade propeller [106](c)

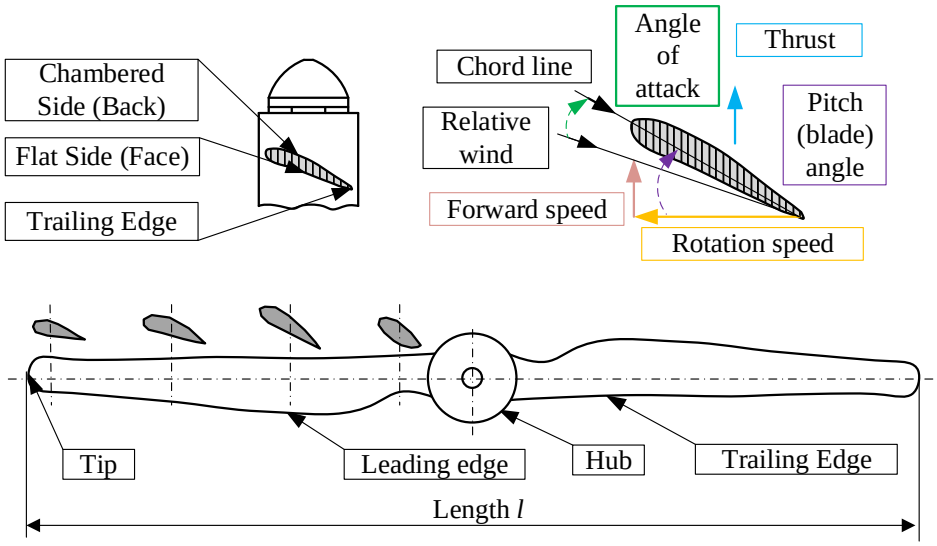

Figure 2.11: Propeller geometry and cross section

propeller and higher than that of the free airstream behind the propeller. Propellers are differentiated apart by length, pitch, number of blades and rotation direction (see Figure 2.11). Manufacturers most commonly use two coding formats: $l{\times}p{\times}b$ and $llpp{\times}l$, where l is length, p is pitch and b is number of blades.

The length of a propeller is the diameter of an imaginary circle the propeller tip traces while spinning. Pitch is defined as the travel distance of one single propeller rotation. The angle of attack is the angle between the so–called "chord line" and the vector representing the relative motion between the propeller and the air (Figure 2.11). Propellers can have any number of blades, but most common are those with two, three and four blades. The blades are relatively long and thin, and the cross section through the blade perpendicular to the length of propeller represents so–called air foil shape. Propellers are made from various materials, such as polymers (plastics), composites, carbon fibres, wood and other materials.

(a) (b) (c)

Figure 2.12: Various commercial flight computers: F4 STM32 Flight Controller [108] (a), DJI Naza M– Lite [109] (b), Pixhawk 4 autopilot [110] (c)

2.7. Flight controller

Flight Controller/Computer (FC) is the main hardware board for processing and operation of the UAV system [107]. FC runs various tasks, such as interpretation of pilot commands given by stick inputs on the TX (Radio Transmitter), interfaces with sensors and processes signals, communicates with ground control or anther aircraft, runs flight stabilisation algorithms (control laws) and controls speed of rotors.

The FC compromises of Central Processing Unit (CPU), Random Access Memory (RAM) and Read Only Memory (ROM), signal inputs, signal outputs and sensors. FC are designed utilising embedded system structure. In present time, 32–bit processor architectures with higher computing power and memory have suppressed usage 8–bit ones. Usual CPU frequencies range from 72 MHz to 480 MHz and more, where memory capacity ranges from 128 KB to 1 MB.

Besides the processor and memory units, FCs usually include integrated Inertial Measurement Unit (IMU) that combines multiple accelerometers, gyroscopes and magnetometers. The measurements from these sensors are used to determine the angular position of the UAV about the horizontal axes (x and y-axis). Also, a magnetometer sensor is used as a digital compass in order to detect the earth's magnetic field. These measurements combined with the data from the gyroscopes determine angular position about the z-axis. For outdoor applications, a barometric pressure sensor is embedded in order to estimate the altitude of the aircraft.

The FC is also a master controller for other devices, i.e. GPS modules, Light Detection and Ranging (LIDAR) sensors, Optical Flow cameras and other. Vibrations and high frequency mechanical noise emitted from motors and propellers can cause problems with onboard sensors, so FC chassis is mounted on dampers (i.e. rubber bobbins, foam or gel) in order to reduce vibrations influence. Popular commercial FC are shown on Figure 2.12.

2.8. Power plant configurations

The selection of power units for UAVs is one of the most crucial and complicated process. Power plant must enable the best use of the characteristics of the airframe and produce appropriate thrust to meet all the requirements for the aircraft.

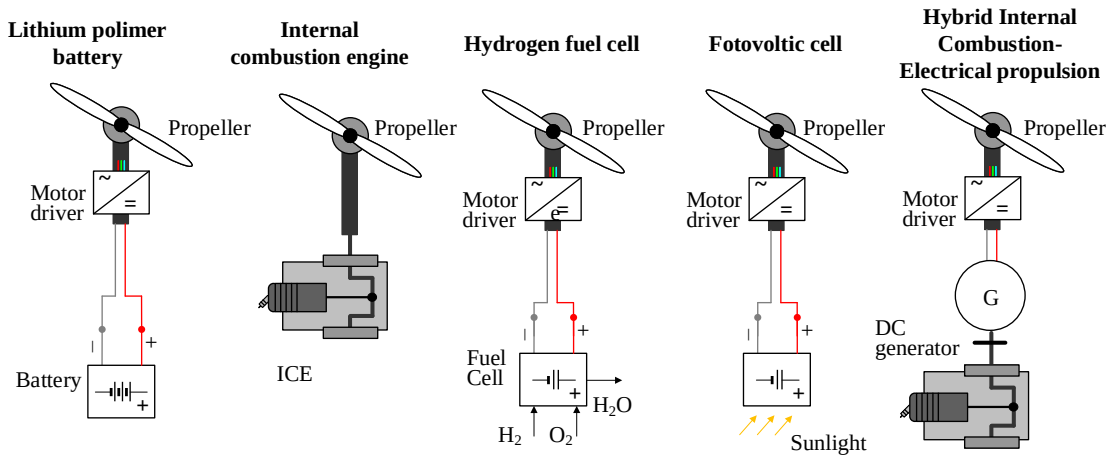

Figure 2.13: Various power plant configurations

Some of usual configurations are based on (see Figure 2.13):

- High power Lithium polymer or similar battery,
- Internal combustion engine,
- Hydrogen fuel cell,
- Photovoltaic solar powered cell,
- Hybrid IC–electrical propulsion and
- Other power source combinations.

Lithium Polimer (LiPo) batteries are the most common power source found in multirotors because of their favourable characteristics, such as the high energy density and high discharge rate. Batteries are assembled from multiple LiPo cells, wherein each cell has a nominal voltage of 3.7 V. LiPo battery is designed to operate within the bounds of permitted cell voltages, i.e. from 3 V to 4.2 V. Namely, discharging below 3 V almost certainly causes irreversible damage and performance loss, while cell over–charging above 4.2 V is potentially dangerous and can cause the battery unit to catch fire. LiPo batteries are rated by their nominal voltage, cell count (usually number of cells connected in series and shown as a number followed by “S” on the battery nameplate data), capacity in mAh

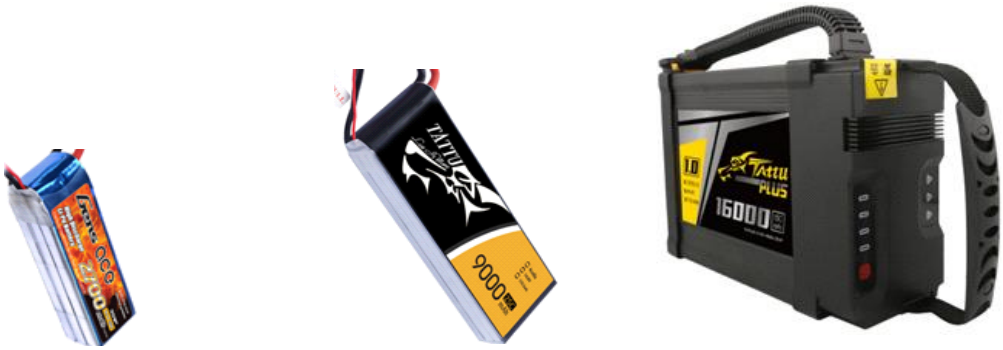

(a) (b) (c)

Figure 2.14: Typical LiPo batteries for multirotors [111]: small battery 2700 mAh (a), medium-large battery 9000 mAh (b), large battery 16000 mAh (c)

and discharge rate or C rating. The latter is an indicator of the continuous discharge rate of a battery and is used in order to determine the maximum constant current you can draw from the battery pack safely without damaging the battery. Maximum current draw is calculated as a multiple of battery capacity and C rating. Another important factor is the relationship between the battery mass and capacity. Figure 2.14 shows photographs of the available batteries on the market and indicates relationships between the battery capacity and geometrical size.

The Internal Combustion Engine (ICE) is a critical component of the hybrid–electric unit, which converts the chemical energy of gasoline (or other liquid fuel) into mechanical and thermal energy. Typical overall efficiency of internal combustion engines is about 20–30%. In this study, a smaller single piston, two–stroke engine and a two–piston, four–strike boxer engine were compared (see Figure 2.15). For internal combustion engine, the power source of propulsion system is liquid fuel, which stores a significant amount of chemical energy. In most cases, petrol (gasoline) or diesel is used as fuel. The main disadvantage of a combustion engine is its low thermal efficiency, and very commonly the ICE has to operate outside of its optimal operating range. The response time for the throttle input of combustion engines is poor compared to electric motors. Moreover, ICE is difficult to set up due to its mechanical complexity and connection with propeller. Therefore, managing of this type of propulsion system may get complicated.

A fuel cell is an electrochemical cell that converts the chemical energy of a certain fuel (typically hydrogen) and an oxidizing agent (typically oxygen) into electricity through a pair of reduction–oxidation (redox) reactions [22, 85, 116]. Electricity is produced continuously for as long as fuel and oxygen are supplied. Fuel cells are different from most electrochemical batteries (except for the so–called redox flow batteries [117]) in that they require a continuous flow of fuel and oxygen (usually from air) to sustain the chemical

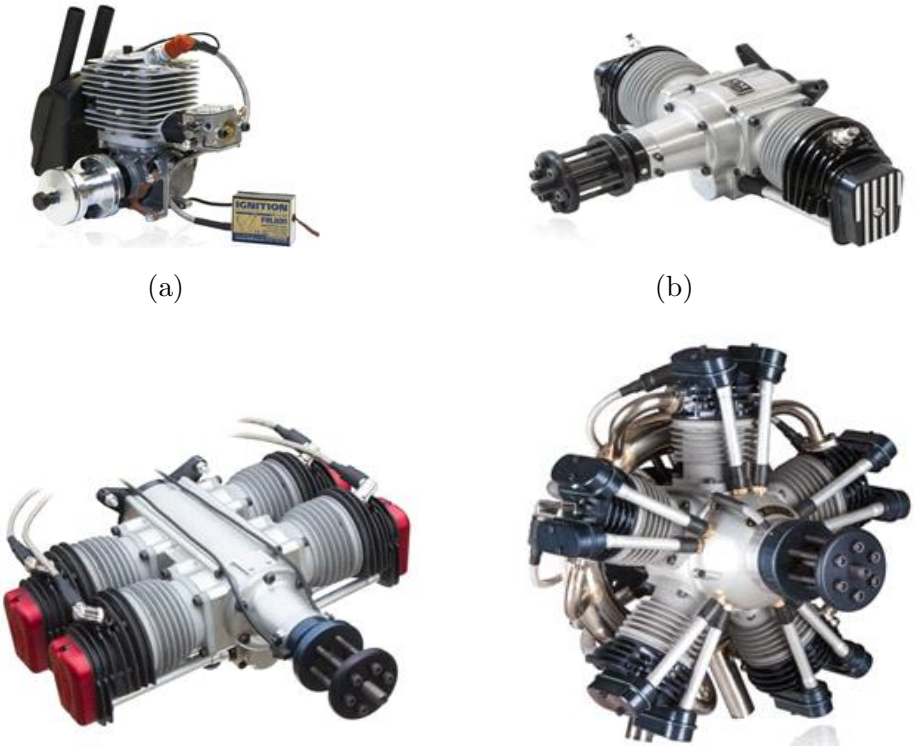

(a) (b)

(c) (d)

Figure 2.15: 62 ccm 2T single cylinder gasoline engine [112] (a), 85 ccm 4T boxer twin gasoline engine [113] (b) 280 ccm 4T, boxer, four cylinder gasoline engine [114] (c), 250 ccm 4T, five cylinder radial gasoline engine [115] (d)

reaction, whereas in most electrochemical batteries the chemical energy usually comes from metals and their ions or oxides that are already present within the battery. Typical commercial fuel cell and multirotor are shown on Figure 2.16.

A solar cell based propulsion converts sunlight directly into electricity, either for direct power or for storage. The power output of solar cells is relatively small, thus multiple cell units is required. Aircraft of this type are built for high–altitude, long–endurance applications. It is possible to keep the craft in the air all night by a backup storage system, which supplies power during the hours of darkness and recharges during the day. Small and large solar powered UAV's are shown on Figure 2.17.

Hybrid power system is a combination of at least two distinct power sources used in a way to outperform individual capabilities of particular power source. The hybrid–electric system proposed in this research suppresses the drawbacks of pure electric power source by using fuel as the main energy source powering the internal combustion engine and the electricity generator set. The basic idea of such hybrid–electric propulsion is to generate electric power by means of an electricity generator and appropriate DC rectifier to the system operating voltage level. The battery that is connected to the generator in parallel

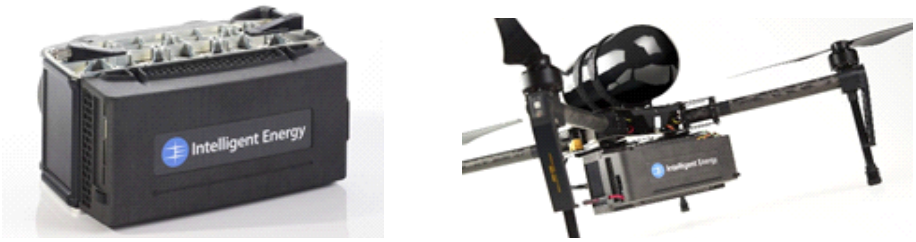

(a) (b)

Figure 2.16: Fuel cell module 800 W [118] (a), Fuel cell mounted to multirotor [118] (b)

(a) (b)

Figure 2.17: Small hand–launched solar–powered UAV [119] (a), Helios by NASA Prototype, ultra–lightweight flying wing [120] (b)

is used for load levelling within the hybrid drive, because it can provide a fast discharge response, so it is able to cover power peaks that cannot be handled by the power generated from the generator. Since the power density of liquid fuel (gasoline) is much higher than that of batteries, while a suitable control strategy can be used to maintain the ICE within an optimal fuel efficiency operating region, this type of propulsion offers distinct advantages over the conventional ones. Several commercial solutions are available (see Figures 2.18 and 2.19). Such propulsion is very expensive, yet not fully optimised and researched.

(a) (b)

Figure 2.18: Walkera QL1200 [121] (a), H2 hybrid power unit for multirotors [122] (b)

Figure 2.19: GAIA 160 hybrid multirotor [123]

2.9. Kinematics and dynamics

The considered multirotor topology in this research is conventional flat type with four or six rotors mounted on a cross shaped frame. It is required that frame structure has a good robustness, strength and small mass in comparing to the motor/propeller set and power source (i.e. batteries) overall mass. Each propeller is connected rigidly to the motor and rotation axes of all propellers are fixed and parallel. Also, air flow is in downward direction to get upward lift and propellers have fixed-pitch blades.

Kinematics and dynamics of multirotor can be described using Newton–Euler formalism with following assumptions:

- Origin of the body-fixed frame is coincident with the Center of Mass (COM) and Center of Gravity (COG) of the body frame,
- Axes of the body-frame coincide with the aircraft body principal axes of inertia and inertia matrix is time-invariant and diagonal,s
- Measurements from sensors on-board are usually given in body-fixed frame,
- Control forces are given in body-fixed frame (on aircraft),
- Propellers are rigid, there is no blade flapping,
- Propeller thrust and drag are proportional to the square of the propeller angular speed.

2.9.1. Coordinate systems and transformations

In order to describe vehicle motion in three–dimensional space it is necessary to obtain a proper mathematical model of multirotor dynamics and kinematics [91, 92]. To begin with, a suitable set of coordinate frames are defined for the purpose of describing the

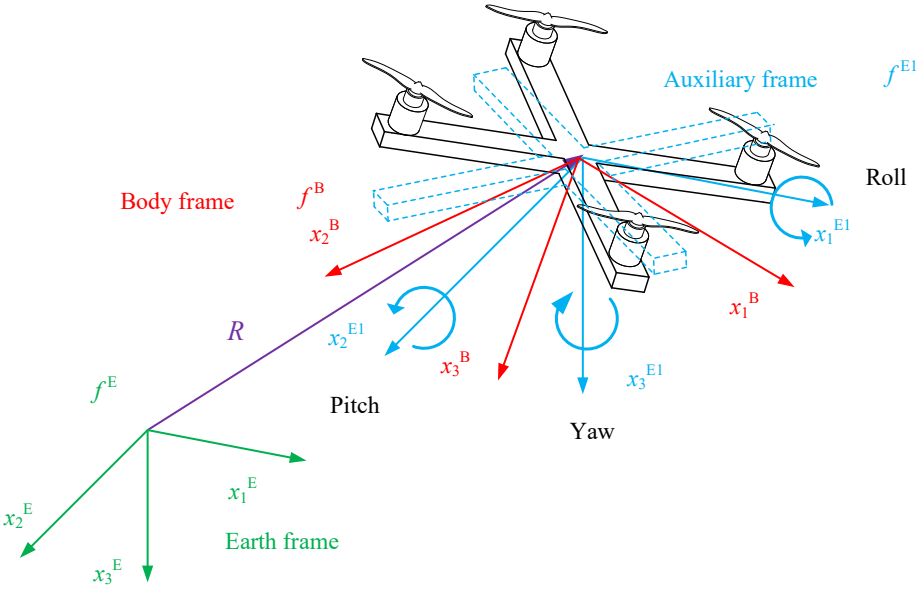

Figure 2.20: Earth and body frame

multirotor translational and rotational motion. Most commonly used coordinate system convention in aviation is right–oriented North–Earth–Down (NED) convention.

In the aforementioned NED definition, the inertial coordinate frame, f^E remains fixed and serves as a reference, where x–axis of the inertial frame points towards geographical north, y–axis points towards geographical east and z–axis is oriented downwards with respect to Earth ground level.

Auxiliary coordinate frame (vehicle carried) f^{E1} with origin in multirotor COG describes the translational motion with respect to the inertial coordinate frame f^{E1} .

The body coordinate frame f^B has origin that coincides with the origin of the auxiliary coordinate frame f^{E1}. Because body frame is fixed to the UAV it rotates with the aircraft and therefore describes the rotational motion with respect to f^{E1} as shown in Figure 2.20.

Vehicle position $\boldsymbol{\xi}$ and orientation $\boldsymbol{\eta}$ are defined in earth frame f^E. Transformation from inertial (Earth) to body frame is described by three consecutive rotations. Since the onboard sensors and propulsion subsystem are defined with respect to the body frame, it is more suitable to formulate the motion equations, force vector $\mathbf{F}$ and torque vector $\boldsymbol{\tau}$ in the body frame.

First rotation is defined as positive rotation about z-axis of auxiliary frame by *yaw* angle ψ:

$$\mathbf{R}_1(\psi) = \begin{bmatrix} \cos\psi & \sin\psi & 0 \\ -\sin\psi & \cos\psi & 0 \\ 0 & 0 & 1 \end{bmatrix} \tag{2.1}$$

Yaw rotation defines a new coordinate frame where the z–axis is aligned with the inertial frame and x and y-axes are rotated by the yaw angle. New coordinate frame obtained by rotation is named *vehicle–1 frame*. The orientation of the *vehicle–1 frame* after yaw rotation is show in Figure 2.21.

Second rotation is obtained by rotating *the vehicle–1* in a right–handed rotation about y–axis of *vehicle–1 frame* by *pitch* angle θ (see Figure 2.21):

$$\mathbf{R}_2(\theta) = \begin{bmatrix} \cos\theta & 0 & -\sin\theta \\ 0 & 1 & 0 \\ \sin\theta & 0 & \cos\theta \end{bmatrix} \tag{2.2}$$

This rotation defines a new coordinate frame where the y–axis is aligned with the *vehicle–1* frame, x and y axes are rotated.

Third rotation is obtained by rotating the *vehicle–2 frame* in a right–handed rotation about x–axis of *vehicle–2 frame*, by *roll* angle ϕ (see Figure 2.21):

$$\mathbf{R}_3(\phi) = \begin{bmatrix} 1 & 0 & 0 \\ 0 & \cos\phi & \sin\phi \\ 0 & -\sin\phi & \cos\phi \end{bmatrix} \tag{2.3}$$

On an aircraft, the *body frame* x–axis typically points out the nose (front), the y–axis points out the right side, and the z–axis points out the bottom of the aircraft.

By transforming unit vectors of from one to another frame using trigonometry, it is possible to express complete rotational matrix as product of sequential rotations as:

$$\mathbf{R}_{BE} = \begin{bmatrix} \cos\psi\cos\theta & \cos\theta\sin\psi & -\sin\theta \\ \cos\psi\sin\phi\sin\theta - \cos\phi\sin\psi & \cos\phi\sin\psi + \sin\phi\sin\psi\sin\theta & \cos\theta\sin\phi \\ \sin\phi\sin\psi + \cos\phi\cos\psi\sin\theta & \cos\theta\sin\psi\sin\theta - \cos\psi\sin\phi & \cos\phi\cos\theta \end{bmatrix} \tag{2.4}$$

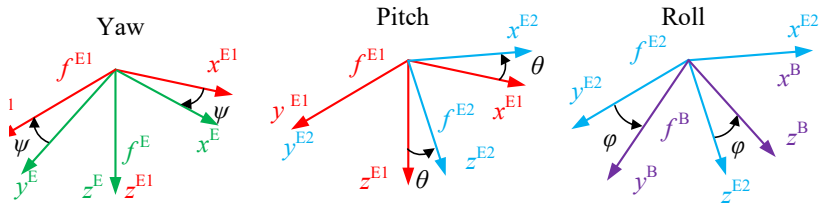

Figure 2.21: Yaw–pitch–roll rotation order

The rotation matrix is orthogonal thus ${\mathbf{R}_{BE}}^{-1} = {\mathbf{R}_{BE}}^{T} = \mathbf{R}_{EB}$.

2.9.2. Kinematics

Aircraft position and orientation in the *inertial reference frame* is defined by the vector $\boldsymbol{\varepsilon}$ that consists of the linear $\boldsymbol{\xi} = \begin{bmatrix} x & y & z \end{bmatrix}^T$ and angular $\boldsymbol{\eta} = \begin{bmatrix} \phi & \theta & \psi \end{bmatrix}^T$ position vectors [43, 91, 92]:

$$\boldsymbol{\varepsilon} = \begin{bmatrix} \boldsymbol{\xi} & \boldsymbol{\eta} \end{bmatrix}^T = \begin{bmatrix} x & y & z & \phi & \theta & \psi \end{bmatrix}^T \tag{2.5}$$

Attitude $\boldsymbol{\nu}$ is defined as body orientation of f^B with the respect to the auxiliary frame, referred as f^{E1}. Multirotor orientation is defined by three consecutive rotations around the f^{E1} coordinate axes, where *roll–pitch–yaw* order is applied using Tait-Bryan angles formalism [124, 125]. Vehicle velocity in body frame is defined by linear $\mathbf{v}^B = \begin{bmatrix} u & v & w \end{bmatrix}^T$ and angular $\boldsymbol{\omega}^B = \begin{bmatrix} p & q & r \end{bmatrix}^T$ velocities:

$$\boldsymbol{\nu} = \begin{bmatrix} \mathbf{v}^B & \boldsymbol{\omega}^B \end{bmatrix}^T = \begin{bmatrix} u & v & w & p & q & r \end{bmatrix}^T \tag{2.6}$$

Relationship between linear velocity in the body frame $\mathbf{v}^B = \begin{bmatrix} u & v & w \end{bmatrix}^T$ and linear velocity in inertial frame $\mathbf{v}^E = \dot{\boldsymbol{\xi}} = \begin{bmatrix} \dot{x} & \dot{y} & \dot{z} \end{bmatrix}^T$ is defined by the so–called rotation matrix $\mathbf{R}_{BE}$.

Relationship between the angular velocity in *body frame* $\boldsymbol{\omega}^B = \begin{bmatrix} p & q & r \end{bmatrix}^T$ and the angular velocity in the *inertial frame* $\boldsymbol{\omega}^E = \dot{\boldsymbol{\eta}} = \begin{bmatrix} \dot{\phi} & \dot{\theta} & \dot{\psi} \end{bmatrix}^T$ is defined by the so–called transformation matrix $\mathbf{T}$.

$$\boldsymbol{\omega}^B = \mathbf{R}_3(\phi)\mathbf{R}_2(\theta)\mathbf{R}_1(\psi)\begin{bmatrix} 0 \\ 0 \\ \dot{\psi} \end{bmatrix} + \mathbf{R}_3(\phi)\mathbf{R}_2(\theta)\begin{bmatrix} 0 \\ \dot{\theta} \\ 0 \end{bmatrix} + \mathbf{R}_3(\phi)\begin{bmatrix} \dot{\phi} \\ 0 \\ 0 \end{bmatrix} \tag{2.7}$$

Transformation matrix can be obtained by resolving Euler angle rates from the *inertial frame* to the *body frame*, from above equation as basis. Finally is obtained:

$$\begin{bmatrix} p \\ q \\ r \end{bmatrix} = \mathbf{T}_{BE}\begin{bmatrix} \dot{\phi} \\ \dot{\theta} \\ \dot{\psi} \end{bmatrix} = \begin{bmatrix} 1 & 0 & -\sin\theta \\ 0 & \cos\phi & \sin\phi\cos\theta \\ 0 & -\sin\phi & \cos\phi\ \cos\theta \end{bmatrix}\begin{bmatrix} \dot{\phi} \\ \dot{\theta} \\ \dot{\psi} \end{bmatrix} \tag{2.8}$$

By inverting the transformation matrix as ${\mathbf{T}_{BE}}^{-1} = \mathbf{T}_{EB}$, the following result is obtained:

$$\begin{bmatrix} \dot{\phi} \\ \dot{\theta} \\ \dot{\psi} \end{bmatrix} = \mathbf{T}_{EB}\begin{bmatrix} p \\ q \\ r \end{bmatrix} = \begin{bmatrix} 1 & \sin\theta\tan\theta & \cos\phi\tan\theta \\ 0 & \cos\phi & -\sin\phi \\ 0 & \frac{\sin\phi}{\cos\theta} & \frac{\cos\phi}{\cos\theta} \end{bmatrix}\begin{bmatrix} p \\ q \\ r \end{bmatrix} \tag{2.9}$$

Kinematics of a rigid body with 6-DOF is given by the following equation:

$$\dot{\boldsymbol{\varepsilon}} = \mathbf{J}\boldsymbol{\nu} \tag{2.10}$$

where $\boldsymbol{\varepsilon}$ is the generalized velocity vector in f^E, $\boldsymbol{\nu}$ is the generalized velocity vector in f^B, and $\mathbf{J}$ is the generalized rotation and transformation matrix.

Generalized velocity vector in f^B, is defined as a combination of translational and rotational velocities.

Generalized rotation and transformation matrix transfers velocities from f^B to f^E, which represents a more natural way of multirotors motion observation:

$$\mathbf{J} = \begin{bmatrix} \mathbf{R}_{BE} & 0_{3x3} \\ 0_{3x3} & \mathbf{T}_{BE} \end{bmatrix} \tag{2.11}$$

2.9.3. Translational and rotational dynamics

The translational (linear) motion of a rigid body based on the second Newton's law can be defined for the inertial and body frame respectively [92, 126]:

$$m\ddot{\boldsymbol{\xi}} = \mathbf{F}_E \tag{2.12}$$

$$m\dot{\mathbf{v}}_B + \boldsymbol{\omega}_B \times (m\mathbf{v}_B) = \mathbf{F}_B \tag{2.13}$$

where m is aircraft mass, $\ddot{\boldsymbol{\xi}}$ is acceleration with respect to f_E, $\mathbf{F}_E$ is the force vector with the respect to the f_E, $\mathbf{F}_B$ is the force vector with the respect to the f_B. The rotational (angular) motion of a rigid body based on the second Euler law with respect to the body frame is described by following [43, 91, 92]:

$$\mathbf{I}\dot{\boldsymbol{\omega}}_B + \boldsymbol{\omega}_B \times (\mathbf{I}\boldsymbol{\omega}_B) = \boldsymbol{\tau}_B \tag{2.14}$$

where $\boldsymbol{\omega}_B$ are angular velocities with the respect to the body frame, f_B, $\boldsymbol{\tau}_B$ is the torque (moment) vector with the respect to the f_B and $\mathbf{I}$ is the inertia matrix.

By applying the assumption that the multirotor frame has a symmetrical structure, inertia matrix becomes a diagonal matrix. Mass is represented by a diagonal matrix with same elements.

$$\mathbf{I} = \begin{bmatrix} I_x & 0 & 0 \\ 0 & I_y & 0 \\ 0 & 0 & I_z \end{bmatrix} \tag{2.15}$$

$$\mathbf{m} = \begin{bmatrix} m & 0 & 0 \\ 0 & m & 0 \\ 0 & 0 & m \end{bmatrix} \tag{2.16}$$

The forces $\mathbf{F}_B$ and torques $\boldsymbol{\tau}_B$ acting on the multirotor include: gravity effects, aerodynamic drag forces and torques, propeller thrust forces and drag torques, and the gyroscopic effects.

The gravitational force acting on the multirotor COG in the body frame can be obtained by multiplying the rotation matrix with the gravitational force vector in the inertia coordinate frame:

$$\mathbf{F}_{\mathbf{g}_E} = \begin{bmatrix} 0 \\ 0 \\ mg \end{bmatrix} \tag{2.17}$$

$$\mathbf{F}_{\mathbf{g}_B} = \mathbf{R}_{EB} \begin{bmatrix} 0 \\ 0 \\ mg \end{bmatrix} = \begin{bmatrix} \sin\theta \\ \sin\phi\cos\theta \\ \cos\phi\cos\theta \end{bmatrix} \tag{2.18}$$

Because the motor/propeller set is rigidly connected to the frame, it follows frame translational and rotational movements. For the case airframe precession the gyroscopic effect $\mathbf{o}_B$ occurs:

$$\mathbf{o}_B = \boldsymbol{\omega}_B \times J_{TP} \begin{bmatrix} 0 \\ 0 \\ (-1)^i \omega_i \end{bmatrix} \tag{2.19}$$

where speed of propeller i is denoted as ω_i, the total motor inertia moment (around the rotor axis) is J_{TP} and it depends on the dimensions and geometry of the rotor, $(-1)^i$ is the sign of the i–th rotor rotation where CW rotations have a positive sign while CCW rotations have a negative sign. The total gyroscopic for quadrotor and hexarotor is given as:

$$\mathbf{o}_{B,4} = \begin{bmatrix} qJ_{TP}(-\omega_1 + \omega_2 - \omega_3 + \omega_4) \\ -pJ_{TP}(-\omega_1 + \omega_2 - \omega_3 + \omega_4) \\ 0 \end{bmatrix} \tag{2.20}$$

$$\mathbf{o}_{B,6} = \begin{bmatrix} qJ_{TP}(-\omega_1 + \omega_2 - \omega_3 + \omega_4 - \omega_5 + \omega_6) \\ -pJ_{TP}(-\omega_1 + \omega_2 - \omega_3 + \omega_4 - \omega_5 + \omega_6) \\ 0 \end{bmatrix} \tag{2.21}$$

Air friction effects occurs due body movement trough medium (air) and usually neglected for control system design purposes. However, for completeness, they can be described by a simplified model of first or second order (in f_E):

$$\mathbf{F}_{dr} = -\mathbf{K}_{dr0,trans}\dot{\boldsymbol{\xi}} \tag{2.22}$$

$$\mathbf{F}_{dr} = -\mathbf{K}_{dr1,trans}\dot{\boldsymbol{\xi}}^2 \tag{2.23}$$

where $\mathbf{K}_{dri}$ are proportionality coefficients in form of diagonal matrices. These coefficients contain complex dependencies and usually are determined experientially (i.e. in wind tunnels).

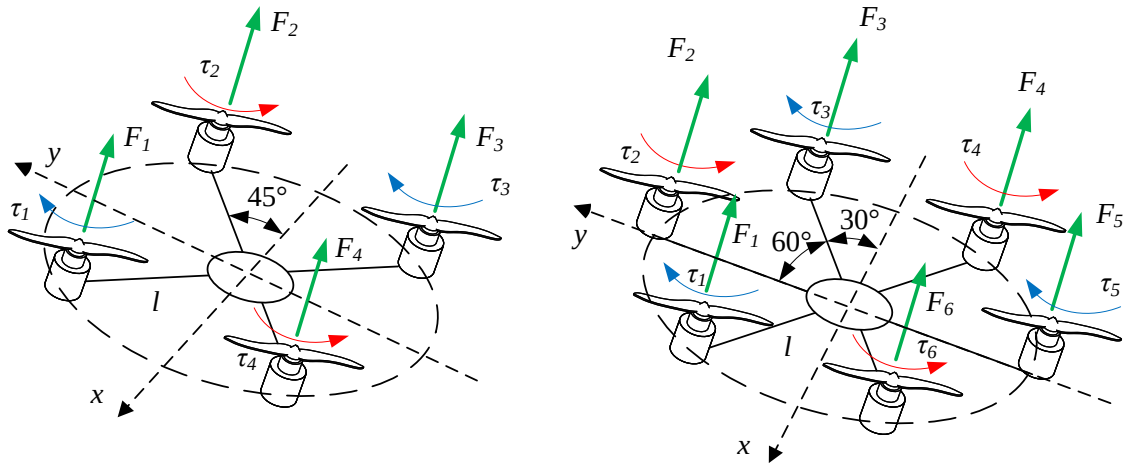

Figure 2.22: Quadrotor and Hexarotor geometry for control allocation

Control vector is defined as the input of a multirotor dynamic model [43, 91, 92], and it consists of the combined propulsion force vector and torque vector in general:

$$\mathbf{u} = \mathbf{\Gamma\Omega} \tag{2.24}$$

where $\mathbf{\Gamma}$ is defined as control allocation matrix that relates angular rotor velocities with control vector and $\mathbf{\Omega}$ is rotors squared angular velocity vector $\mathbf{\Omega} = \begin{bmatrix} \omega_1^2 & \omega_2^2 & \cdots & \omega_n^2 \end{bmatrix}^T$.

Total lift force is defined as the sum of thrust from propellers directed along z-axis of body frame:

$$\mathbf{F}_T = \Sigma \mathbf{F}_{Ti} \tag{2.25}$$

Propellers/motors that generate thrust are positioned at the ends of multirotor arms and they induce torques around the different axes of rotation. As shown in Figure 2.22, by using geometry the produced torque is determined for each axis. For the x-axis torque $\boldsymbol{\tau}_\phi$ is defined for quadrotor and hexarotor respectively as:

$$\boldsymbol{\tau}_{\phi,4} = -F_1\frac{l\sqrt{2}}{2} - F_2\frac{l\sqrt{2}}{2} + F_3\frac{l\sqrt{2}}{2} + F_4\frac{l\sqrt{2}}{2} \tag{2.26}$$

$$\boldsymbol{\tau}_{\phi,6} = -F_1\frac{l}{2} - F_2 l - F_3\frac{l}{2} + F_4\frac{l}{2} + F_5 l + F_6\frac{l}{2} \tag{2.27}$$

For the y-axis torque $\boldsymbol{\tau}_\theta$ is defined for quadrotor and hexarotor respectively as:

$$\boldsymbol{\tau}_{\phi,4} = F_1\frac{l\sqrt{2}}{2} - F_2\frac{l\sqrt{2}}{2} - F_3\frac{l\sqrt{2}}{2} + F_4\frac{l\sqrt{2}}{2} \tag{2.28}$$

$$\boldsymbol{\tau}_{\theta,6} = F_1\frac{l\sqrt{3}}{2} - F_3\frac{l\sqrt{3}}{2} - F_4\frac{l\sqrt{3}}{2} + F_6\frac{l\sqrt{3}}{2} \tag{2.29}$$

The torque around the z-axis $\boldsymbol{\tau}_\psi$ occurs with respect to the Newton's third law. Due to the motor torque input to the propeller, a reaction is exerted to motor in form of equal

magnitude, but opposite direction to the propeller rotation, for quadrotor and hexarotor configuration respectively:

$$\boldsymbol{\tau}_{\psi,4} = -\tau_1 + \tau_2 - \tau_3 + \tau_4 \tag{2.30}$$

$$\boldsymbol{\tau}_{\psi,6} = -\tau_1 + \tau_2 - \tau_3 + \tau_4 - \tau_5 + \tau_6 \tag{2.31}$$

Control allocation matrix for flat quadrotor and flat hexarotor are respectively given according to the Figure 2.22 by the following expressions (where K_T and K_D are thrust and drag coefficients defined in propeller modelling section of Chapter 3):

$$\Gamma^4 = \begin{bmatrix} -K_T & -K_T & -K_T & -K_T \\ -\frac{\sqrt{2}}{2}K_T l & -\frac{\sqrt{2}}{2}K_T l & \frac{\sqrt{2}}{2}K_T l & \frac{\sqrt{2}}{2}K_T l \\ \frac{\sqrt{2}}{2}K_T l & -\frac{\sqrt{2}}{2}K_T l & -\frac{\sqrt{2}}{2}K_T l & \frac{\sqrt{2}}{2}K_T l \\ -K_D & K_D & -K_D & K_D \end{bmatrix} \tag{2.32}$$

$$\Gamma^6 = \begin{bmatrix} -K_T & -K_T & -K_T & -K_T & -K_T & -K_T \\ -\frac{1}{2}K_T l & -K_T l & -\frac{1}{2}K_T l & \frac{1}{2}K_T l & K_T l & \frac{1}{2}K_T l \\ \frac{\sqrt{3}}{2}K_T l & 0 & -\frac{\sqrt{3}}{2}K_T l & -\frac{\sqrt{3}}{2}K_T l & 0 & \frac{\sqrt{3}}{2}K_T l \\ -K_D & K_D & -K_D & K_D & -K_D & K_D \end{bmatrix} \tag{2.33}$$

In conclusion, multirotor dynamics is described by differential equations that were derived by using the Newton–Euler method which are the same as those describing a rotating 6-DOF rigid body.

3 Hybrid propulsion system modelling

This chapter describes the basic configurations (topologies) of hybrid propulsion systems commonly used in UAVs. Furthermore, constituent components (subsystems) of the hybrid–propulsion multirotors have been analysed and modelled. Propulsion subsystems outlined herein include the internal combustion engine, the electricity generator and electrical motors, the electro–chemical battery, Direct Current to Direct Current (DC–DC) converters, rectifier and propellers. For each component, the operating principle is explained and a dynamic model suitable for designing the control system is developed.

3.1. Hybrid propulsion overview

The aircraft power supply system must provide ample electrical power in order to achieve satisfactory in–flight dynamic performance (manoeuvring capability), as well as the sustained power output (energy production) in order to maintain the flight for a prescribed amount of time. The most commonly used purely electrical propulsion system uses batteries for energy storage and power supply for electric motors driving the propellers. It has advantages of fast response (small response time), and very precise thrust control, with the main drawbacks being limited flight time and long recharging time. As elaborated in Chapter 2, it is possible to utilise a hybrid propulsion system to alleviate the aforementioned disadvantages of the battery–based propulsion system. Such a hybrid system possesses at least two energy sources that work in synergy, and together contribute to the total generated power within the power-train (shown on Figure 3.1).

Power generated by the primary power source is fed to the *power converter no. 1*, where it is either converted to mechanical or electrical power which is then forwarded to the so–called common power bus. Power generated by the secondary power source also enters the common bus via the *power converter no. 2*. There are two more power flows (shown by dashed lines). One of them replenishes the secondary source from the primary source during the period when the aircraft is either grounded, or has a excess of energy within the system, while the other power flow replenishes the secondary power source during the energy recuperation regime, such as during regenerative braking events in

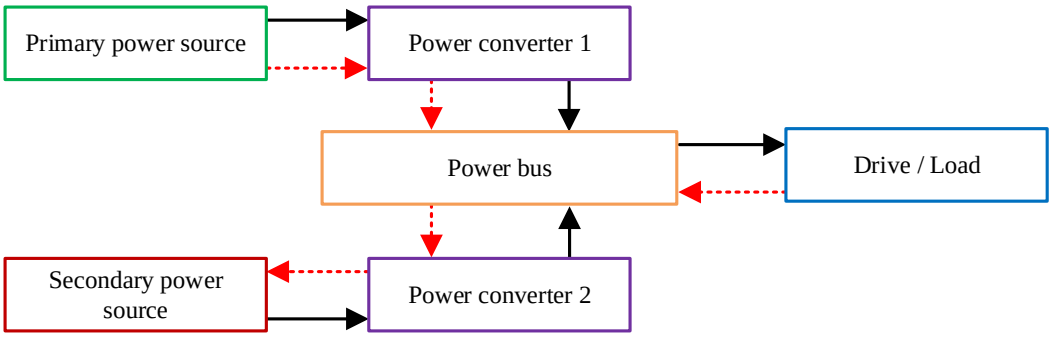

Figure 3.1: Hybrid system concept

hybrid vehicles [127–129]. From the proposed concept it is possible to define many variants of the hybrid propulsion system, with the most commonly used topologies corresponding to the series, parallel, series–parallel, complex and alternative power source–based hybrid power-train.

Typical elements of a hybrid–electric propulsion system for multirotor aircraft are shown in Figure 3.2. Propellers are used as thrust generators, and they are connected to electric motors via a fixed or variable gear ratio mechanical transmission. Electric motors are driven by their respective power converters which can be supplied by electric power from a variety of sources, such as the electrochemical battery, and the electricity generator driven by an Internal Combustion Engine (ICE), with Photo Voltage (PV) panels and fuel cells being a relatively rarely used power source alternatives. In the former case of power supply based on ICE plus electricity generator and the battery energy storage, the two sources of energy are the chemical energy of the fuel (gasoline or methanol) and the electrochemical energy of redox reactions within battery electrochemical cells. In particular, battery energy storage can be easily integrated into the hybrid power system because of its rather compact nature and the possibility to control the output voltage and current via suitable DC-DC power converters. Auxiliary components include couplings and the fuel tank for the ICE–based generator set, and propeller drive electric motor controllers. The main advantage of a hybrid system combining the electric propulsion (electric motors + propellers) with the ICE–based generator set augmented by a battery

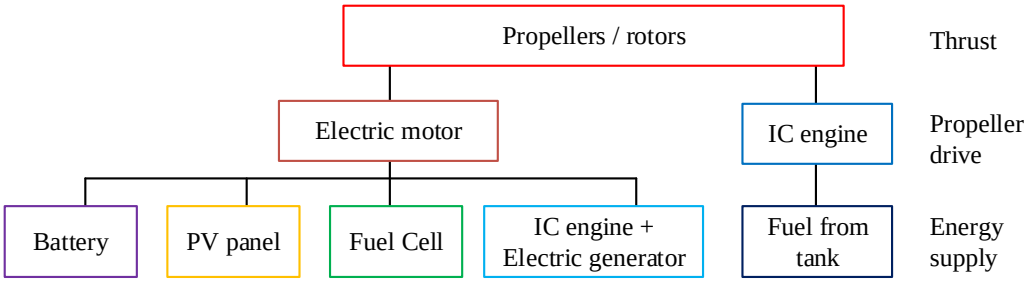

Figure 3.2: Hybrid system components

energy storage (and possibly electrolytic capacitors or super-capacitors), is the possibility of obtaining fast response of the propulsion electric motor drives, and, thus, also achieving very good overall control system performance. Simultaneously, such a power system can exploit the rather large energy capacity of the ICE (in terms of chemical energy of the fuel), thus achieving enhanced flight endurance [127–129].

For the preliminary estimate of the hybrid power–train suitable for hybrid multirotors, the following assumptions regarding energy efficiency can be made:

- IC engine theoretical efficiency is bounded by compression ratio and adiabatic ratio coefficient, and can have value around 0.5, but realistic process has efficiency typically being between 0.2 and 0.3 due various factors,
- Electric motor (Direct Current (DC), Permanent Magnet Synchronous Motor (PMSM), Brushless Direct Current (BLDC)) efficiency can theoretically reach 0.99, but realistic average efficiency of electric motors (Power < 3 kW) typically lies between 0.7 and 0.9 (with higher values typically associated with PMSM/BLDC machines and larger power ratings),
- Energy density of gasoline is 12.88 kWh/kg, while the energy density of the most commonly used Lithium Polimer (LiPo) battery lies between 0.2 kWh/kg and 0.5 kWh/kg depending on the battery design (round cell, prismatic cell or pouch–type).

Table 3.1: Energy densities of various power sources and energy storage system

Storage material	Energy type	Specific energy, MJ/kg	Specific energy, kWh/kg
Diesel	Chemical	48	13.33
Gasoline (Petrol)	Chemical	46.4	12.88
Methanol	Chemical	19.7	5.47
Lithium metal battery	Electrochemical	1.8	0.5
Lithium Ion battery	Electrochemical	0.36 – 0.875	0.1 – 0.24
Alkaline battery	Electrochemical	0.5	0.138
Nickel–metal hydride battery	Electrochemical	0.288	0.08
Lead acid battery	Electrochemical	0.17	0.047
Super-capacitor	Electrical electrostatic	0.01–0.036	0.0027 – 0.01
Electrolytic capacitor	Electrical electrostatic	0.00001–0.0002	0.0000027 – 0.000055

Based on the above characteristics of the petrol–based internal combustion engine DC electrical machine, the following estimate of the output energy density of such en-

gine–generator set can be made:

$$E_{total} = E_{gasoline}\eta_{ICeng}\eta_{DCmot} = 12.88 \cdot 0.2 \cdot 0.7 \approx 1.8 \text{ kWh/kg} \tag{3.1}$$

Even after scaling down the energy density of gasoline by the engine thermal efficiency and its mechanical losses, as well as taking the lower estimate of the electrical machine (generator) efficiency, thus obtained energy density of the ICE–electricity generator set still overcomes the energy density of the battery approximately five times, in particular:

$$\frac{E_{total}}{E_{LiPo}} = \frac{1.8}{0.35} \approx 5.1 \tag{3.2}$$

3.1.1. Series power-train configuration

In a series hybrid power-train configuration (shown on Figure 3.3), propellers are only driven by electric motors. The internal combustion engine mechanical power is converted into electrical power by an electricity generator (equipped with a rectifier if Alterating Current (AC) machine or DC machine is used), which is utilised to directly provide power to electrical motors and to charge the battery.

The advantage of such configuration is that the internal combustion engine is completely decoupled from rotors thrust generation and can be independently operated in the vicinity of the optimum operating point, i.e. maximum torque/power, corresponding to the optimal fuel efficiency. Furthermore, the simplicity of the concept allows for the implementation of a simple power control system.

The main disadvantage is that electrical motors need to provide for the total mechanical power of the propulsion system, and, thus, they need to be dimensioned for the maximum propulsion system power rating. Moreover, using a generator rated for full propulsion system power requirement further adds to the overall mass of such a propulsion system configuration.

Regarding efficiency, the propulsion system fuel efficiency is smaller compared to other configurations which can facilitate direct connection of the IC engine to the propellers, as mechanical power is first converted to electrical power, followed by a second conversion from electrical to mechanical power for driving the propellers [127].

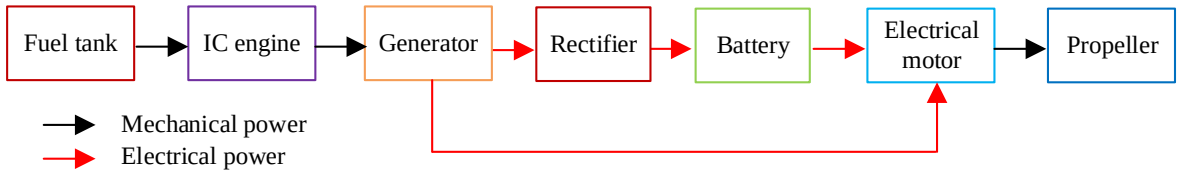

Figure 3.3: Schematic of series hybrid power–train configuration

3.1.2. Parallel power-train configuration

The parallel hybrid power-train configuration (Figure 3.4) is characterized by two parallel propulsion power paths which are coupled mechanically. These power conversion paths are related to the chemical energy conversion to mechanical work within the IC engine and the conversion of the electrical power from the battery to mechanical power at propulsion system electric motors. In this arrangement, both the electric motor and the IC engine can drive the propeller, either independently or in combination. Torque of both power units is added using mechanical torque coupling. Parallel configuration also allows for charging of batteries, while the internal combustion engine simultaneously drives the propeller and the electrical motor, which is in that case being used as a generator.

In order to facilitate independent operation of both power conversion paths, a mechanical disconnection device should be added in both propulsion paths, which can be facilitated by an electromagnetic clutch or a freewheel system [127]. Otherwise, when running isolated, the additional torque of driving the inactive power unit must be provided by the active machine. In addition to the possibility of parallel operation when both drive units power the propellers, parallel configuration can also provide a smaller overall mass of components due to reduction in drive size.

The disadvantages of this configuration are the additional mass and volume of the mechanical coupling and the requirement for a more sophisticated control system. Furthermore, the operation of the internal combustion engine may be sub–optimal with respect to the series configuration since the ICE directly contributes to the overall thrust, thus being used in a more dynamical manner, i.e. in order to provide for the possibly highly dynamic propeller loads, it may be operated over a wide range of operating regimes.

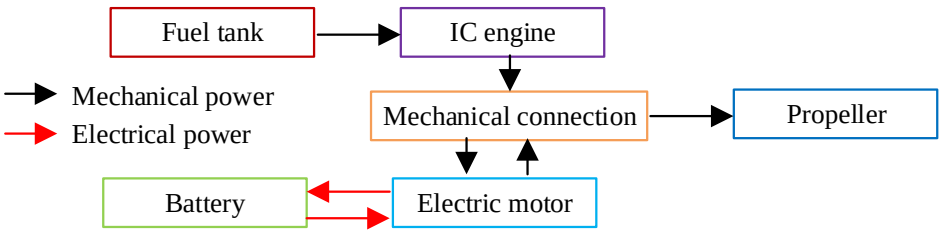

Figure 3.4: Schematic of parallel hybrid power–train configuration

3.1.3. Series-parallel power-train configuration

The series–parallel hybrid power-train configuration (Figure 3.5), also known as the power–split configuration, is a combination of the two configurations described above, i.e. the series and parallel hybrid power–train arrangement. Such configuration consists of

a propeller, internal combustion engine, electric motor and electricity generator that are connected by a mechanical coupling in the form of a planetary gear set.

In this design, load distribution is more flexible than for the series and parallel power-train, thus allowing the engine to operate in its most efficient rotational speed and torque range, regardless of the actual thrust requirements. A further advantage is the ability to switch off the IC motor without mechanically shutting down the whole system. In terms of mass, the planetary gear and auxiliary generator make this system heavier than the parallel hybrid power–train configuration [127].

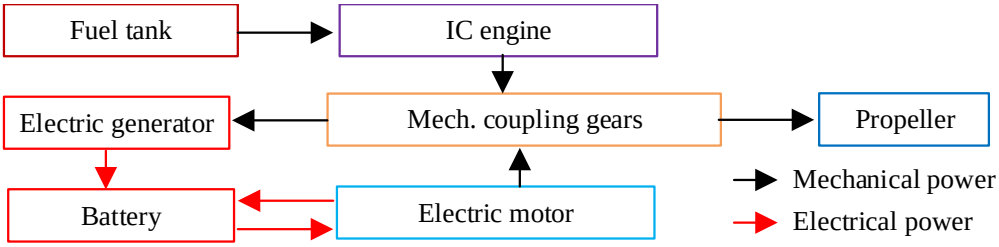

Figure 3.5: Schematic of series–parallel hybrid power–train configuration

3.2. Hybrid propulsion system considered in this work

The analysed configurations of hybrid propulsion system (shown in Figures 3.6 and 3.7) are suitable for a hypothetical multirotor, comprising four or six propeller drives in a flat configuration. Two cases of series ICE–electric hybrid power unit configuration was considered in this study. For all cases the following holds:

- ICE drives the electricity generator (PMSM/BLDC machine is used for that purpose) which provides for quasi steady–state load power supply (i.e. to cover power demands needed for hovering), while the battery unit is used for peak load shaving,
- the study does not consider the existence of an energy recovery system, i.e. the battery energy storage is only charged prior to the flying mission and cannot be charged in–flight,
- the Master Supervision Controller Software (MSCS) is implemented on–board a microcontroller unit and manages the propulsion performance, i.e. power output,
- the ICE rotational speed is controlled by a throttle servo actuator based on a DC servomotor which positions the throttle valve accordingly to the output of throttle controller with DC bus voltage reference target and the DC bus voltage measurement–based feedback.

In the first case (Figure 3.6), the internal combustion engine is directly connected to the generator, and generator phases are connected directly to a full–wave three–phase rectifier. The battery is added in parallel to serve as an additional power source in operating conditions corresponding to high loads, for example when a high–magnitude sudden change of electrical load occurs within a relatively short time interval, i.e. until the engine–generator power output transient is finished.

In particular, it has been observed from experiments that the ICE is unable to build up required torque response to a sudden (stepwise) load change within a short time frame, because the dynamics of the ICE is rather slow compared to the dynamics of the battery which can deliver high amounts of current almost instantly (over 50 Amperes within milliseconds). For such a system, a DC bus voltage controller based on modified proportional-integral-derivative (PID) structure has been developed (see Chapter 5), which takes as its input (i.e. feedback signal) the measurement of DC bus voltage and commands the ICE throttle valve angle, in order to deliver the required power imposed by the electrical torque demand (load) from the generator.

In the second case (Figure 3.7), a network of parallel DC–DC converters is added to the topology used in the first scenario, and analysed. Such approach is not able to provide better efficiency of power system compared to the first case, but enables independent control of the DC–bus voltage (e.g. 24 V or 48 V) regardless of the generator input when the input voltage is within operating range of the individual DC power converters ($V_{in,min} = 30$ V, $V_{in,max} = 70$ V). For such system, a load sharing control scheme has been developed (see Chapter 5) for the case of the step down (buck) converter parallel system. The same principles can be applied to raise the DC–bus voltage to a higher level, using the so–called step–up (boost) topology of the DC–DC power converters.

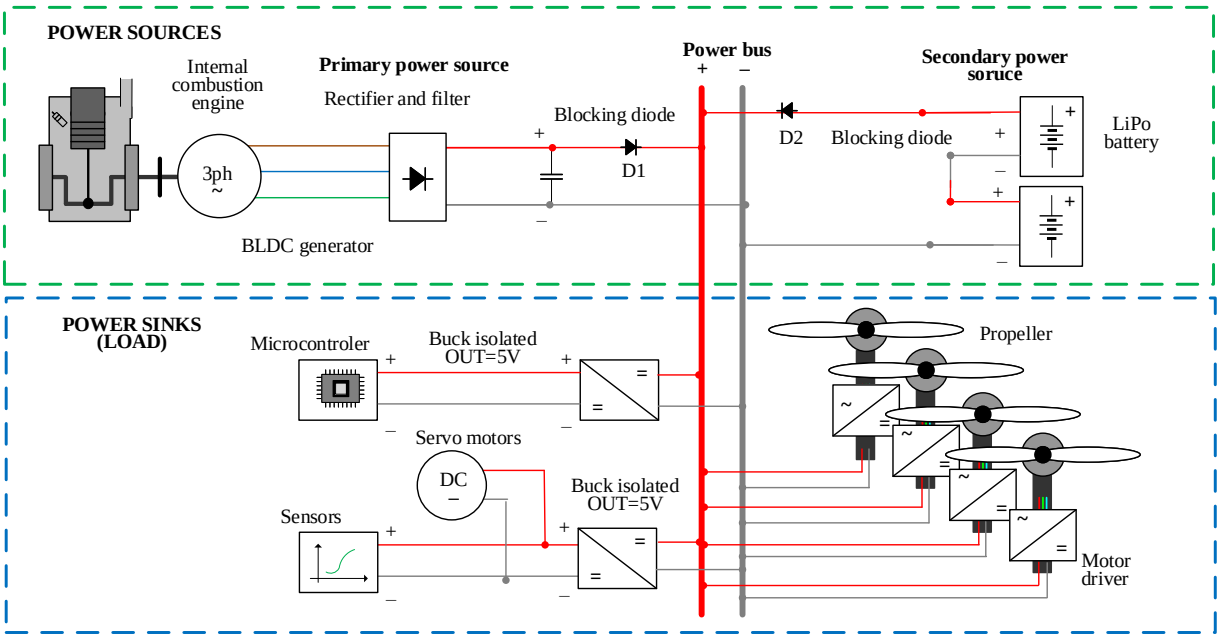

Figure 3.6: Schematic of first case considered hybrid propulsion system configuration

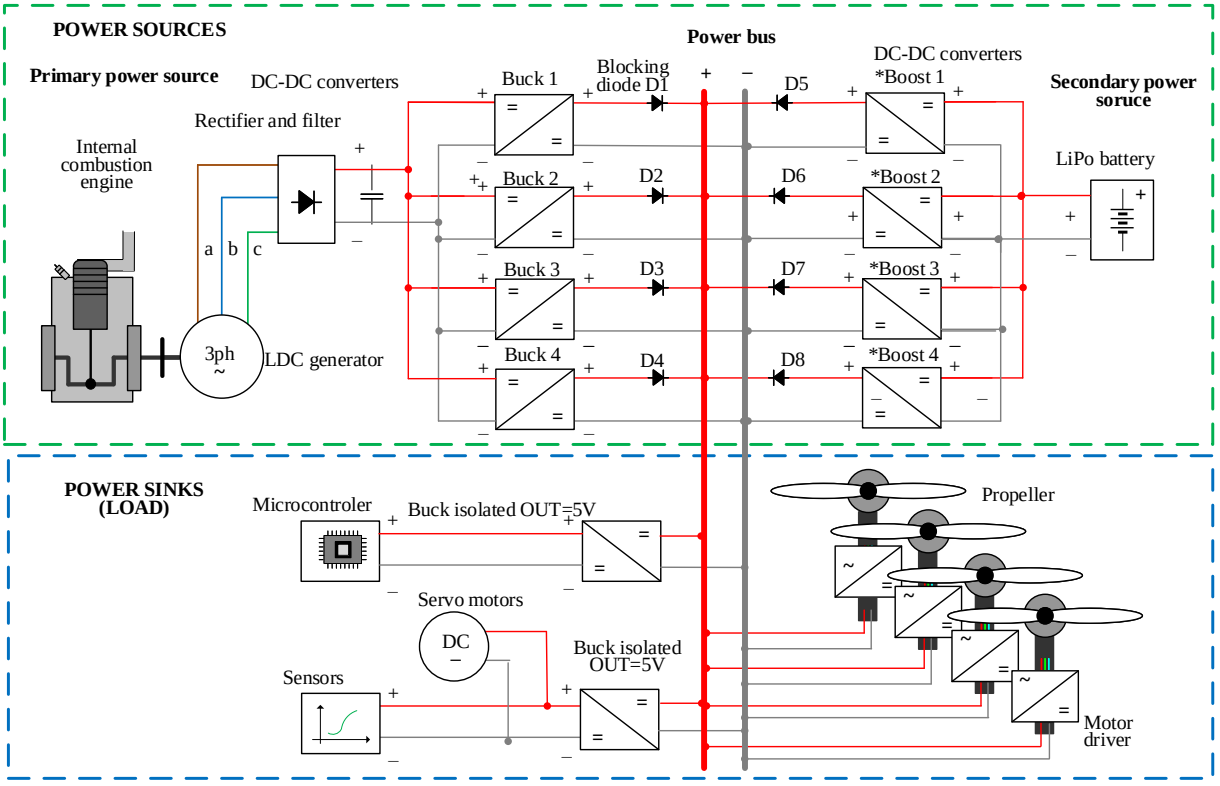

Figure 3.7: Schematic of second case considered hybrid propulsion system configuration

3.3. Hybrid multirotor sizing

In order to determine the required power to propel the aircraft, it is necessary to define its size and the required payload capability. Due to structural similarity, classic approach to helicopter propulsion system design can also be applied to multirotors. The sizing methodology presented herein is based on the relevant data about commercially available off–the-shelf components. Based on the collected and processed data, relationships between the sizes of the motors and propellers have been identified. According to the classical methodology for aircraft sizing, the design take–off mass is given by the total mass of the aircraft at the beginning of the mission [59, 130]. For an electrically powered flying platform, the take–off mass remains constant along the mission while for fuel–powered (internal combustion engine–based) configuration the mass reduces. Aircraft mass equation can be expressed as:

$$m_{TO} = m_{FR} + m_{PR} + m_{AV} + m_{PS} + m_{PL} \tag{3.3}$$

where m_{FR} is the aircraft frame mass, m_{PR} is the total mass of motors and propellers, m_{AV} is the avionics mass, m_{PS} is power source mass and m_{PL} is the payload mass.

Hovering conditions for a multirotor are achieved when the total aircraft weight is balanced by the sum of all thrusts generated by propellers:

$$F_{TO} = m_{TO}g = \sum_{n=0}^{i} F_{Ti} \tag{3.4}$$

The above expression is valid only for ideal static (steady–state) conditions, without including the aerodynamic effects such as drag or wind conditions. In order to include the aforementioned effects while retaining the simplicity of calculation, the total thrust F_{TO} can be multiplied by a non–dimensional constant called thrust–to–weight ratio TW, in order to obtain the static thrust that guarantees specific performance in the air depending on the application. Total required thrust F_{RTO} and required thrust per motor F_{TR} can be calculated as:

$$F_{RTO} = TW F_{TO} = TW m_{TO} g \tag{3.5}$$

$$F_{TR} = \frac{F_{RTO}}{n} \tag{3.6}$$

where n is number of propellers. This approach has been validated in practice by many test flights for various multirotor sizes and designs. In most cases, thrust to weight ratio of 2 allows multirotor to hover at approx. 50% rated propulsion system power. The next step in the calculation of the required propulsion system performance is to determine the required propeller size. In order to fully identify constants of a motor–propeller system, it is required to measure the following parameters:

- voltage v and current i,
- throttle input PWM,
- motor load from propeller or torque T_l and motor speed ω_m.

If multiple measurements are conducted for different inputs (i.e. varying throttle), it is possible to obtain the following relationships:

- mechanical power as a function of torque and speed P_{mech},
- electrical power as a function of voltage and current P_{elec},
- motor efficiency as a function of a mechanical and electrical power ratio.

The output speed depends on the throttle command (expressed in percentage of the rated value), and of the load (torque in Nm). If order to completely characterize a particular motor, it is required to test it with multiple input voltages and different loads. However, for sizing purposes, testing at standard (rated) input voltage is sufficiently precise. For identifying propeller constants, it is required to measure the following parameters:

- propeller thrust (in N) and angular velocity (in rpm),
- propeller load (drag torque) expressed in Nm.

The procedure and obtained parameters are presented in Chapter 4.

In order to justify the installation of a hybrid power unit, it is necessary to analyse which aircraft configurations show potential for installation of the ICE–generator set. The input data used in this analysis is obtained from a renowned component manufacturer, which includes the current draw, voltage, thrust, torque, rpm and other, for a defined group of propellers ranging from 18 – 30 inches. For each size of the propeller, several different propulsor sets (motor + generator + ESC) have been considered. In order to investigate the power consumption of a typical propulsion unit considering its propeller size, the three power states were considered:

- medium–low power consumption at 50% of propeller throttle command,
- medium–high power consumption at 75% of propeller throttle command,
- peak power consumption at 100% propeller throttle command.

Visualisation of data is shown on Figure 3.8 where graphs show the average values of input power and thrust per motor for each member of propeller group (18 – 30 inch). The total thrust of the aircraft at 50%, 75% and 100% of the throttle command has been calculated and the total power consumption of such aircraft is shown in Table 3.2 and Figure 3.9.

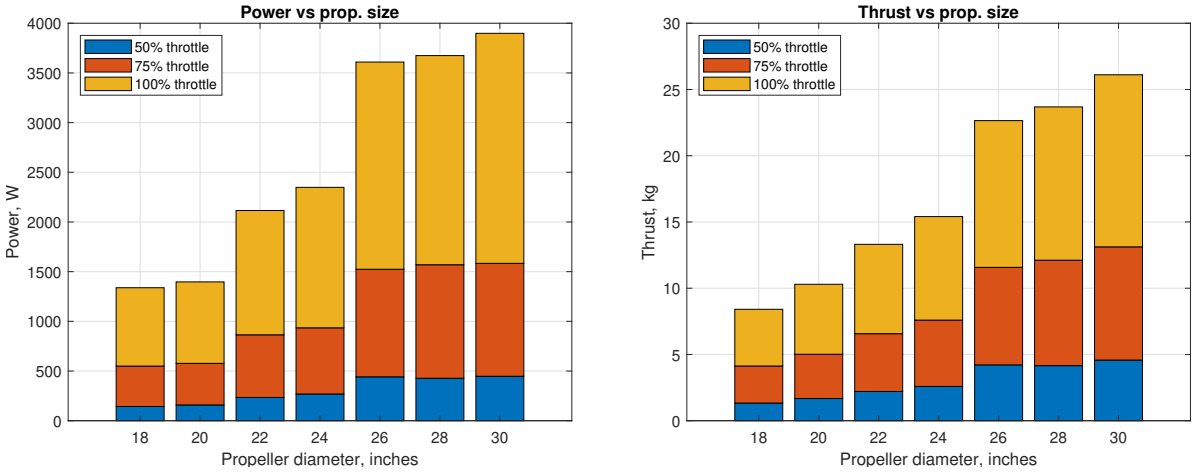

(a) (b)

Figure 3.8: Power (a) and thrust (b) per propeller size

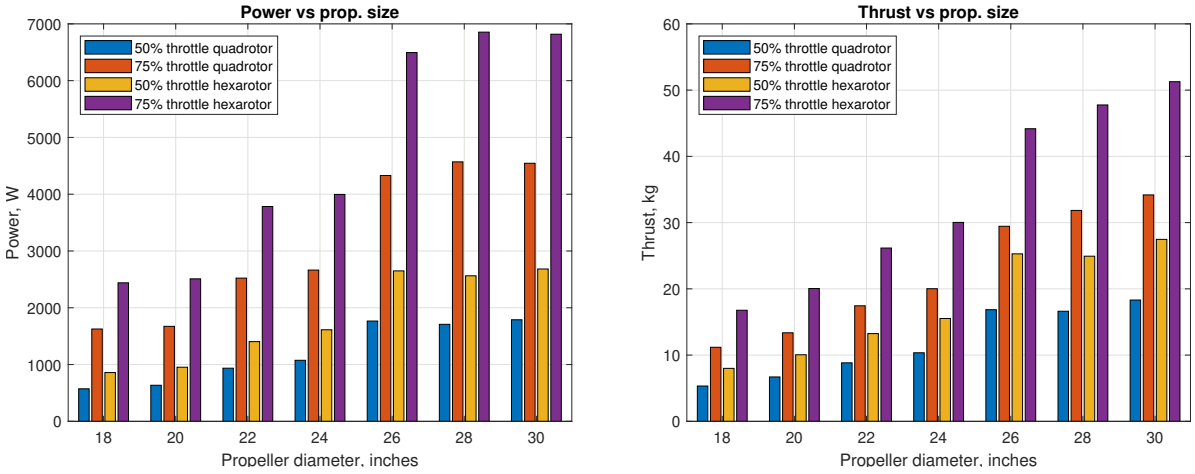

(a) (b)

Figure 3.9: Power (a) and thrust (b) per multirotor configuration and propeller size

Table 3.2: Power and thrust characteristics of preliminary propulsion dimensioning

Propeller, inch	Quadr. thrust 50% throttle, kg	Quadr. input power 50% throttle, W	Quadr. thrust 75% of throttle, kg	Quadr. input power 75% of throttle, W	Hexr. thrust 50% of throttle, kg	Hexr. input power 50% of throttle, W	Hexr. thrust 75% of throttle, kg	Hexr. input power 75% throttle, W
18	5.3	572.8	11.18	1626	7.99	859.2	16.77	2439
20	6.7	635.5	13.37	1673	10.05	953.3	20.05	2510
22	8.8	936	17.44	2522	13.25	1404	26.16	3784
24	10.35	1075	20.02	2664	15.53	1613	30.03	3996
26	16.85	1766	29.45	4330	25.28	2650	44.17	6494
28	16.62	1709	31.84	4570	24.93	2563	47.76	6854
30	18.31	1789	34.18	4545	27.47	2683	51.27	6818

In order to select an appropriate ICE for power unit building purposes, it is required to consider several factors such as:

- continuous and peak power,
- fuel consumption,
- overall mass.

Based on the aforementioned requirements, a case study using commercially obtainable ICEs and generators is carried out. Since there are many different engines available on the market, this study will be limited to engines used for scale model building purposes and model aviation, such as model helicopters and aeroplanes and remotely controlled cars. Also, ICEs are limited to the following gasoline–fuelled Otto–type engines: single cylinder two and four stroke engines, boxer twin and quad cylinder engines and multi–cylinder radial engines with engine power output of up to 20 HP. The input data is obtained from renowned manufacturers comprising engine mass, power, torque, rpm range, fuel consumption draw, and other. Most important parameters as power, mass and cost are analysed and shown in Figure 3.10

In order to transform the mechanical power from the ICE to its electrical counterpart, suitable lightweight Brushless Permanent Magnet Syncronous (BPMS) machines should be considered as generators. BPMS machines with power ranging up to (or even exceeding) 15 kW have been considered for this purpose, and the overall results of their analysis are shown in Figure 3.11.

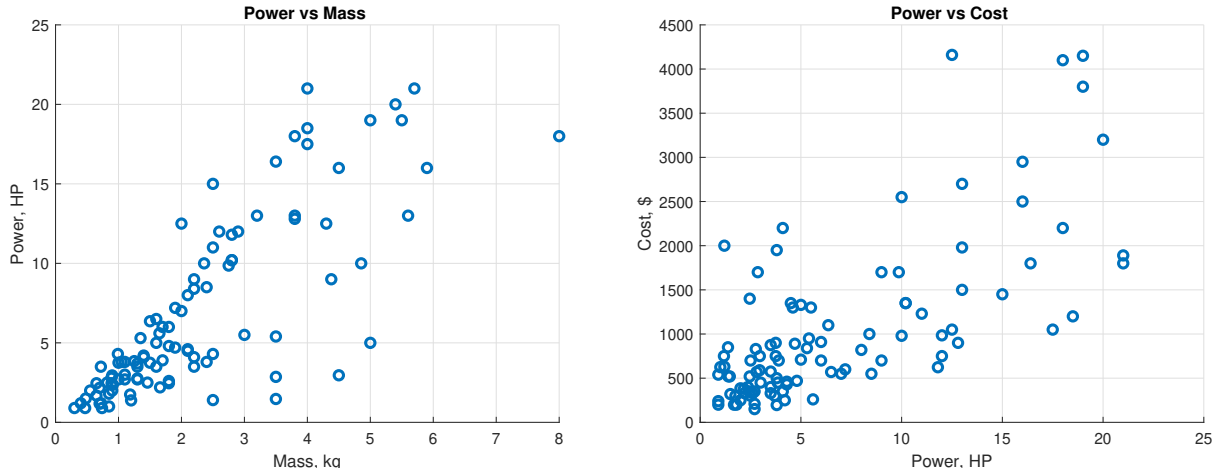

(a) (b)

Figure 3.10: Results of preliminary ICE sizing study: scatter plot of power in relation to mass (a), scatter plot of power in relation to cost (b)

From results shown in Figures 3.10 and 3.11 the following conclusions can be made:

- There is a large selection of ICEs in range up to 10 HP (horse–power) with engine mass up to 4 kg,
- Engines within the aforementioned HP range cost between 100 and 1500 USD,
- Most BPMS machines suitable for generator unit purposes are within 5 kW power range, not many higher–power generators are available (in particular, only four lightweight BPMS machines have been found with their power rated 10 kW or

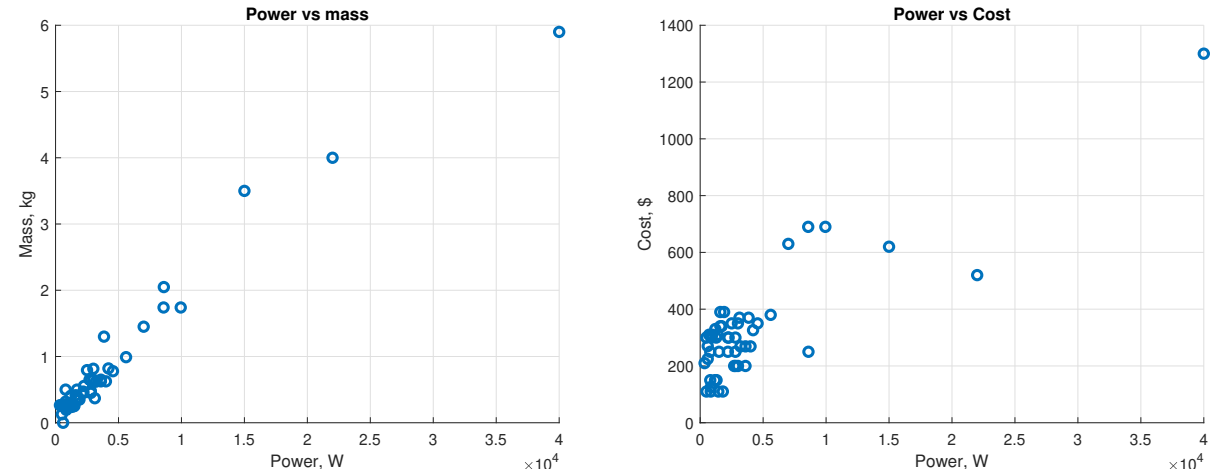

(a) (b)

Figure 3.11: Results of preliminary BPMS machine sizing: scatter plot of power in relation to mass (a), scatter plot of power in relation to cost (b)

more),

- Electrical scooter or electrical bicycle motors are promising due to high power rating (>3000 W),
- Voltage constant KV (rpm/V) is usually low (<200 KV), generators can give high current output (>50 A), this is very important as current magnitude is proportional to the generator load torque (engine input torque),
- Mass of available generators is typically between 0,5 – 3 kg (for lower power range, up to 10 kW), while higher–power machines mass (over 10 kW) is typically between 3.5 and 6 kg.

Several conclusions have been drawn during initial testing of a model aircraft two stroke ICE (see Chapter 4), and considering its power output, torque, fuel consumption and engine vibrations. First, in the case when two stroke engines intended for model aircraft (i.e. fixed wing) are considered, a significant problem with low inertial mass and cooling are present. Secondly, when a four–stroke engine is considered, a higher overall fuel efficiency is available, but such an engine produces mechanical power every two revolutions of the crankcase and requires sufficient inertial mass in order to suppress its inherent torque pulsations.

In order to avoid mechanical interventions within the engine (installation of additional inertial mass and solution for effective cooling), the RC car engine designated G320RC produced by Zenoah is selected (see Chapter 4). It has a favourable built–in flywheel mass at the crankshaft (due to built–in impeller and pull starter). Its maximum power output is 2400 W and its maximum torque output is 2 Nm. The total mass of the engine–generator set is approximately 4 kg (without considering the fuel mass).

Finally, according to aforementioned sizing criteria and manufacturer data analysis, it was concluded that for a hybrid drive of 2–3 kW of power that has mass around 3–5 kg, it would be favourable to use propellers with diameters between 20 and 24 inches (see Table 3.2).

However, it would also be possible to use a smaller–size system based on 17–inch to 20–inch propellers that can operate on a 24 V DC-bus.

3.4. Internal combustion engine

Internal combustion engine is a form of a thermal engine, a mechanical device that utilizes thermal energy and converts it into mechanical energy in order to perform useful work. A heat source is required to generate thermal energy that brings the working

substance (medium) to a high temperature state and induces mechanical work through a specific thermodynamic process where the higher energy state temperature of a working medium or substance transitions into a lower energy state characterised by a lower temperature according to the thermodynamic process characteristic curve [131]. In general, thermal or heat engines can be classified into Internal Combustion Engines (ICE) and External Combustion Engines (ECE). Furthermore, they can be classified by the type of mechanical motion as rotary engines and reciprocating engines. Detailed classification of heat engines can be found in [131–135].

ICE burn (combust) the fuel mixed with air inside the engine cylinder. After compression and combustion of the mixture, the combustion products (working medium) are highly pressurised and thus produce force that acts on the reciprocating piston (or rotor) in the cylinder which initiates piston motion. Gasoline engines are used by in cars, ship's and aircraft, while gas engines and gas turbines (both ICE and ECE) are used for high–power industry demands and aircraft. Diesel engines, apart from cars and trucks are also used in railway trains (locomotives), boats and ships, as well as in the industry for remote site power supply purposes [136].

Output power production of an ICE follows a rigid predefined cycle of operations in a sequential manner [131]. Most common type of engine is the four–stroke cycle engine, where the cycle of operation is completed in four strokes of the piston or two revolutions of the crankshaft. Each stroke rotates the crankshaft by 180 degrees and hence the cycle of four strokes corresponds to 720 degrees of crankshaft rotation. The two stroke engines, having one power stroke per every rotation, could theoretically produce twice the power output of four stroke engines. In realistic operating conditions the actual power output increase is only 30%, because of the increased heating and thermal losses [131–133].

3.4.1. IC engines cycles and engine performance

The four–stroke cycle (see e.g. [131–135]) is defined as (shown on Figure 3.12a):

- *Intake (Suction, Induction) stroke*, wherein the inlet valve is open, and the piston moves downward through the cylinder, inducing a fuel mixture,
- *Compression stroke*, wherein both valves are closed, and the piston moves upwards trough the cylinder and compresses the fuel–air mixture. The ignition occurs when the piston arrives near the Top Dead Centre (TDC),
- *Expansion (Power, Working) stroke*, during which the combustion propagates throughout the air–fuel mix (charge), increasing the pressure and temperature, and forcing the piston downwards, wherein the exhaust valve opens at the end of the power stroke near the Bottom Dead Centre (BDC),

- *Exhaust stroke* where the remaining gases are expelled trough the exhaust valves by the piston motion upwards within the cylinder.

In the case of two–stroke engines, the cycle is completed in two strokes of the piston, or one revolution of the crankshaft, thus eliminating separate induction and exhaust strokes. In particular, the two–stroke cycle according to [131–135] is defined as (shown on Figure 3.12b):

- *Compression stroke*, wherein the piston travels upwards through the cylinder, and thus compresses the medium. Ignition occurs before TDC is reached, while the bottom side of the piston is simultaneously drawing in the fresh mixture through the inlet valve,

- *Power stroke*, wherein the combustion of fuel increases the temperature and pressure within the cylinder and moves the piston downwards. At the same time, the piston compresses the fuel mixture within the crankcase. As the piston approaches the end of a stroke, the exhaust port is opened, and blow–down occurs. At the BDC the transfer port is also open, and the mixture contained within the crankcase expands into the cylinder. Once the upward motion is initiated again, the piston first closes the transfer port, followed by the closure of the exhaust port.

The performance of an ICE can be evaluated as a quantity of a heat energy originating from the fuel combustion and thus turned into useful work attainable at the engine shaft [131–134]. Thermal efficiency at full load of internal combustion engines ranges from about 20% small gasoline engines up to more than 50% for large slow–running diesel engines, which are the most efficient means currently available of turning the heat of combustion of fuel into mechanical power [131].

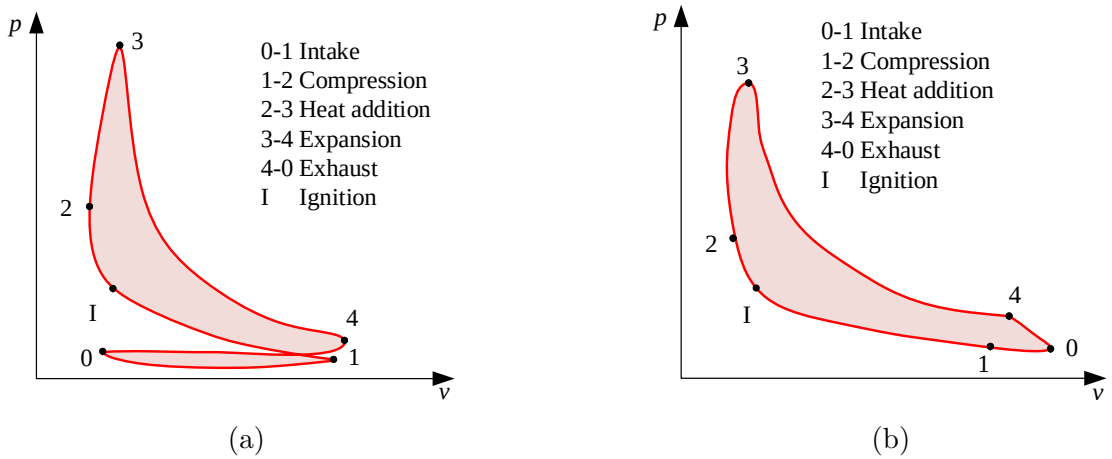

(a) (b)

Figure 3.12: Indicator diagrams for spark ignited IC engines [131]: four stroke engine (a), two stroke engine (b)

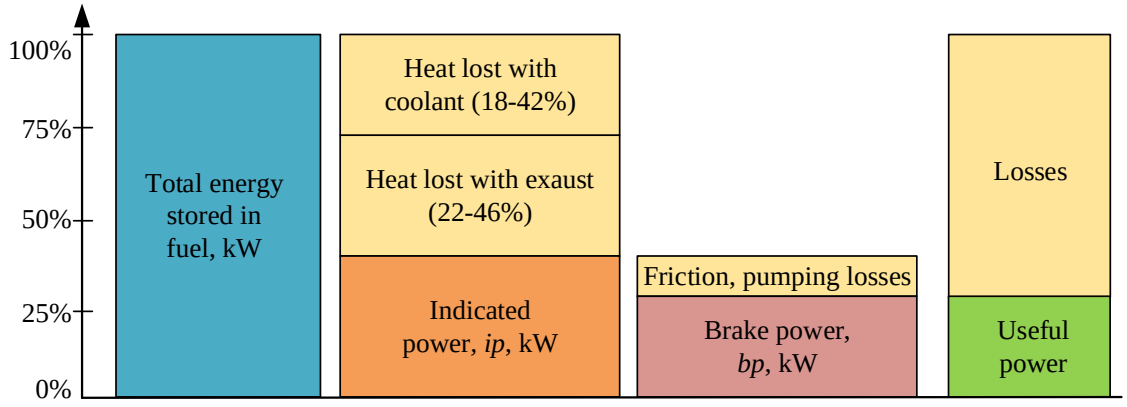

Figure 3.13: Energy distribution of typical IC engine components [127, 128, 131]

The combustion heat that is not converted into useful work appears as energy loss, such as in the exhaust gases, in the cooling medium and as convection and radiation from the hot surfaces of the engine (see Figure 3.13).

The most important engine performance parameters are [131]:

- Indicated thermal efficiency,
- Brake thermal efficiency,
- Mechanical efficiency,
- Volumetric efficiency,
- Relative efficiency or efficiency ratio,
- Mean effective pressure,
- Mean speed of piston,
- Specific fuel consumption,
- Air–fuel ratio and
- Calorific value of fuel.

During chemical energy conversion into heat by means of fuel combustion, thus released heat energy cannot be fully converted into mechanical work. The so–called *indicated power* is the heat energy that is utilised to drive the piston. During force transmission trough the connecting rod and the crankshaft, friction and pumping loses are introduced. Sum of all loses expressed as lost power is referred as *frictional power* FP.

Indicated thermal efficiency (η_{ith}) represents the ratio of indicated power and fuel energy per second (kJ/s):

$$\eta_{ith} = \frac{IP}{\dot{E}_{fuel}} = \frac{IP}{\dot{m}_{fuel} h_{cal}} \tag{3.7}$$

Brake thermal efficiency (η_{bth}) is defined as ratio of brake power BP and fuel energy:

$$\eta_{bth} = \frac{BP}{\dot{m}_{fuel} h_{cal}} \tag{3.8}$$

Mechanical efficiency (η_m) is the ratio of brake power (or delivered power) and indicated power (provided to the piston). It is alternatively referred to as the brake thermal efficiency in order to emphasize the thermal character of this efficiency parameter:

$$\eta_m = \frac{BP}{IP} = \frac{BP}{BP + FP} \tag{3.9}$$

By a large degree, the performance of an engine is dependent on the so–called *volumetric efficiency* (η_v), which is defined as the ratio of the actual volumetric flow rate of air into the intake and the rate at which the volume is displaced by the system:

$$\eta_v = \frac{\dot{m}_a}{\rho_{atm} V_s} \tag{3.10}$$

Typical volumetric efficiencies for spark–ignited (SI or gasoline) engines at full throttle range between 80 and 85%, while for compression ignited (CI) engines it is between 85 – 90%.

Mean effective pressure (p_m) is defined as the average pressure inside cylinder and it is based on the calculated or measured power output. For every speed there is specific *indicated mean effective pressure* $IMEP$ and corresponding *brake mean effective pressure* $BMEP$. They can be obtained from the indicated and brake power:

$$p_{im} = \frac{60000 IP}{LAnK} \tag{3.11}$$

$$p_{bm} = \frac{60000 BP}{LAnK} \tag{3.12}$$

where IP is the indicated power (in kW), p_{im} is the indicated mean effective pressure (N/mm^2), L is the stroke length, A is the piston cross section area (m^2), N is the rotational speed in rpm, n is the rpm dependent on number of power strokes defined as $N/2$ for four–stroke and N for two–stroke engine [131], and K is the number of cylinders.
Another quantity called *specific power output* (P_s) represents the power output per piston area. It is proportional to the mean effective pressure and mean piston speed according to:

$$P_s = \frac{BP}{A_p} \tag{3.13}$$

Fuel consumption characteristics of engine are expressed in terms of *specific fuel consumption* (SFC) in kilograms of fuel per kilowatt–hour.

$$SFC = \frac{\text{Fuel consumption per time}}{\text{Power}} \tag{3.14}$$

The proportion of fuel and air within the engine is important for combustion and efficiency. It is expressed as a ratio of the fuel vs. air mass flow. A mixture that has more fuel than the chemically optimal stoichiometric mixture (in terms of ideal combustion) is called *rich*, while the mixture that contains less fuel is called *lean*. The actual fuel–air ratio vs. stoichiometric ratio is called *equivalence ratio*, which is defined as follows:

$$\varphi = \frac{\text{Actual fuel-air ratio}}{\text{Stoichiometric fuel-air ratio}} \tag{3.15}$$

Calorific or heating value of a fuel is the thermal energy released per unit quantity of the fuel when that fuel is burned (combusted) completely, and products of combustion are cooled back to the initial temperature of the mixture. Engine performance ratings can indicate peak power over the prescribed time interval, and the normal operational power, where engine gives good long–term performance. Typical design and performance data for most common SI and CI engines are given in Table 3.3.

Table 3.3: Energy densities of various power sources and energy storage system [131]

	Cycle type	Compression ratio	Bore (mm)	Stroke / Bore ratio	RPM	Max. BMEP (bar)	Weight to Power ratio, kg/kW	Aprox. Best BSF, g/kWh
Spark Ignited								
Small, motorcycle	2,4	6–10	50–85	1.2–0.9	4500–7500	4–10	5.5–2.5	350
Standard passenger car	4	8–10	70–100	1.1–0.9	4500–6500	7–10	4–2	270
Truck, Bus	4	7–9	90–130	1.2–0.7	3600– 5000	6.5–7	6.5–2.5	300
Large gas engines	2,4	8–12	220–450	1.1–1.4	300–900	6.8–12	23–35	200
Wankel engines	4	9	0.57 dm per chamber		6000–8000	9.5–1.5	1.6–0.9	300
Compression Ignited								
Standard passenger car	4	16–20	75–100	1.2–0.9	4000–5000	5–7,5	5–2.5	250
Truck, Bus	4	16–20	100–150	1.3–0.8	2100–4000	6–9	7–4	210
Railway locomotive	4,2	16–18	150–400	1.1–1.3	400–1800	7–23	6–18	190
Large diesel engines	2	10–12	400–1000	1.2–3	100–400	9–17	12–50	180

Analysis of the thermodynamic process for an ICE is relatively complicated due to the complex and interrelated phenomena that occur during engine operation. In order to develop a dynamics model of such system, the model derivation starts with an analysis of components, basic geometry and idealized thermodynamic closed cycle. Detailed information on this subject can be found in [131–135, 137, 138].

3.4.2. Two-stroke engine components and geometry parameters

In order to define specific factors that describe the basic performance of an internal combustion engine within its operating range, it is necessary to define the geometric relationships of the cylinder, piston, piston rod and crankshaft. The two–stroke engine is composed of multiple components that are shown in 3.14 (additional information's can be found in [131–135, 137, 138]).

A *crankcase* is a structure that holds the *crankshaft* in order to enable both the *crankshaft* rotation and reciprocating piston movement.

Crankshaft converts the reciprocating piston action into rotary motion of the output shaft.

Connection rod is a component that interconnects the crankshaft and the piston, thus allowing the transmission of force from the cylinder towards the crankshaft.

Cylinder block is connected to *crankcase* and serves as main supporting structure for *cylinder head*, *spark plugs*, *piston* and *carburettor*.

Piston is a cylindrical component that is tightly fitted into the cylinder, thus enabling smooth linear motion with (ideally) no lateral motion components.

Combustion chamber is a volume in the upper part of the cylinder, wherein combustion of fuel and release of thermal energy and gasses occurs.

Inlet port is an opening through which air–fuel mixture is drawn into the cylinder, and it provides a connection channel between the carburettor and the combustion chamber.

Transfer port transports the fresh fuel/air mixture supplied by the intake from the crankcase to the area of the cylinder above the piston. The transfer port also plays a vital role in cooling the cylinder and scavenging exhaust gases.

Exhaust port connects the exhaust system and the cylinder, and it also allows the products of combustion to be released into the atmosphere.

Sparkplug is a component that is used to ignite medium within the combustion chamber (for spark ignited (SI) engines) and it is positioned on the cylinder head.

Carburettor is a device that prepares the air–fuel (A/F) mixture in a proper ratio for combustion. It has a throttle and a choke valve, and three A/F ratio tuning valves, for

high speed, low speed and idle RPM.

Fuel intake is a connection port towards the carburettor whose operation is based on the Bernoulli's principle, thus facilitating the suction of the fuel. Exhaust is cylindrical body used to cool burning gases and reduce overall motor noise.

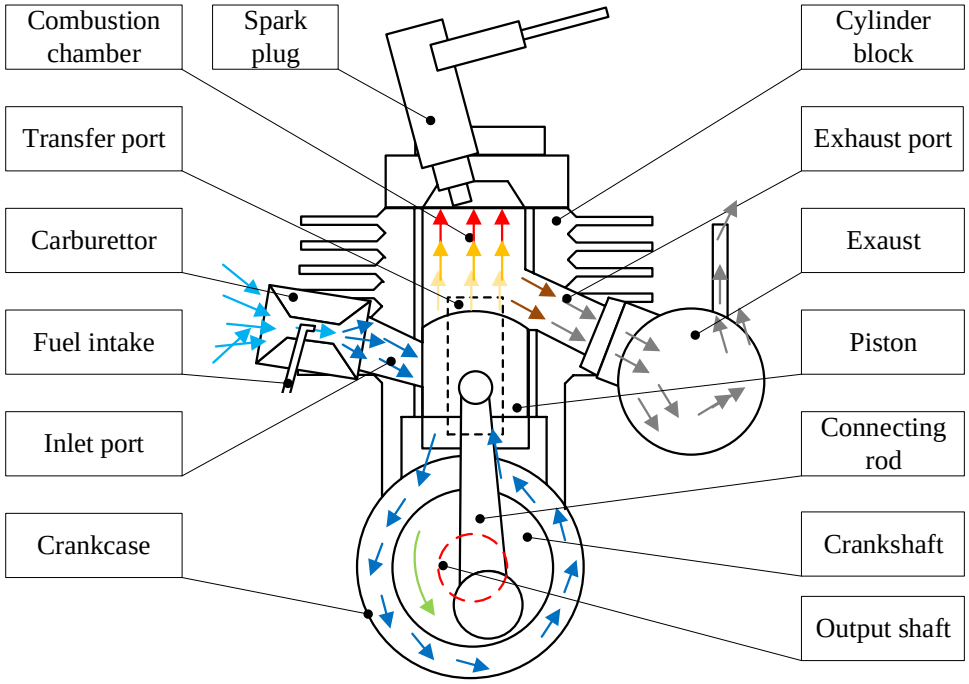

Figure 3.14: Two stroke engine components

There are also some geometrical definitions that need to be listed here. For example, *cylinder bore* (d) defined as inner diameter of the cylinder, while the *piston area* (A) is the area of the circular cross–section with the piston diameter which is equal to the cylinder bore.

Stroke length (H) is the nominal distance that piston travels between two successive reversals of its direction of motion.

Stroke to bore ratio (H/d) is the parameter used for the classification of engine size. For $d < H$ the engine is considered "under–square", whereas for $d = H$ the engine is said to be "square", and for $d > H$ the engine is regarded as "over square".

Dead centre is defined as the position of piston at the moment when the direction of motion is reversed at end of the stroke. Top dead centre is the point at which the piston is furthest from the crankshaft, while the bottom dead centre is the point at which the piston is closest to the crankshaft [131, 138]

The *displacement* of the piston h can be determined by the following equation derived

according to geometrical relationships shown in Figure 3.15:

$$h = r + l - (r\cos\alpha + l\cos\beta) = r\left[(1-\cos\alpha) + \frac{r}{l}\left(1 - \sqrt{1-\sin^2\beta}\right)\right] \tag{3.16}$$

By introducing the so–called *connecting rod ratio* $\lambda = r/l$ and using triangle trigonometry relationships it is possible to obtain the final relationship in the following form:

$$h = r\left[(1-\cos\alpha) + \frac{1}{\lambda}\left(1 - \sqrt{1-\lambda^2\sin^2\alpha}\right)\right] \tag{3.17}$$

Piston speed is defined as:

$$v_p = r\omega\left(\sin\alpha + \lambda\frac{\sin 2\alpha}{2\sqrt{1-\lambda^2\sin^2\alpha}}\right) \tag{3.18}$$

Mean piston speed is defined as:

$$v_{p,m} = 2Hn \tag{3.19}$$

where H represents the *stroke distance* (stroke) and n is the rotational speed of crankshaft in revolutions per minute (rpm). *Displacement* or *swept volume*, V_s is defined as the volume that is "swept" by the piston when moving from one dead centre to the other dead centre. It is expressed as:

$$V_s = AH = \frac{\pi}{4}d^2H \tag{3.20}$$

Clearance volume (V_c) is volume of combustion chamber when piston is at TDC point. Based on these definitions, the *compression ratio* (r) is defined as the ratio of total cylinder volume at BDC (V_t) is and clearance volume V_c:

$$r = \frac{V_t}{V_c} = \frac{V_c + V_s}{V_c} = 1 + \frac{V_s}{V_c} \tag{3.21}$$

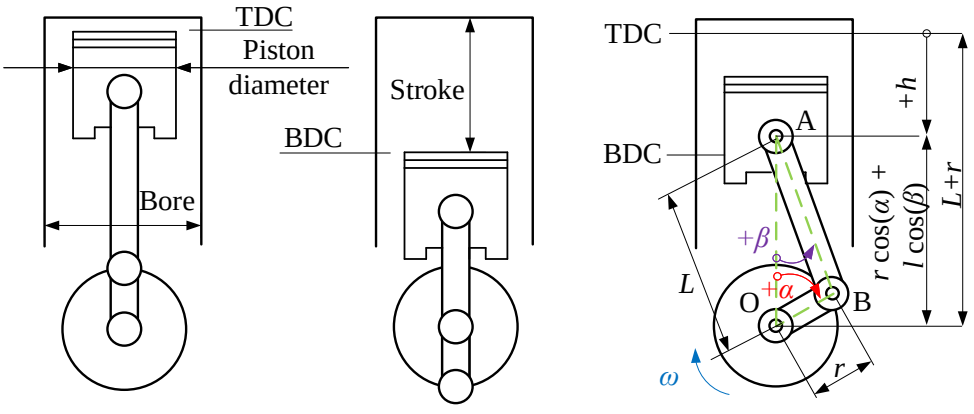

Figure 3.15: Two stroke engine geometry

3.4.3. Theoretical Otto process for air cycle

The Otto cycle consists of four state change processes: *isentropic compression*, *heat addition at constant volume*, *isentropic expansion*, and *release of heat at constant volume*. In the case of a four–stroke Otto cycle, technically there are two additional processes: one for the exhaust of waste heat and combustion products at constant pressure (isobaric), and one for the intake of cool oxygen–rich air also at constant pressure. However, these are omitted herein in order to simplify the analysis. The cycle can be described by the following process steps (see Figure 3.16) [131]:

- 0–1 wherein a mass of air is drawn into the piston/cylinder arrangement at constant pressure,
- 1–2 represents an adiabatic (isentropic) compression of the charge as the piston moves from the BDC towards the TDC,
- 2–3 corresponds to a constant–volume heat transfer to the working gas from an external source while the piston is at the top dead centre. This process corresponds to the ignition of the fuel–air mixture and the subsequent rapid burning in a real engine,
- 3–4 is an adiabatic (isentropic) expansion (power stroke),
- 4–1 completes the cycle by a constant–volume process in which heat is released from the air while the piston is at bottom dead centre,
- The final process (1–0) releases the mass of air from the cylinder into the surrounding atmosphere under constant pressure conditions.

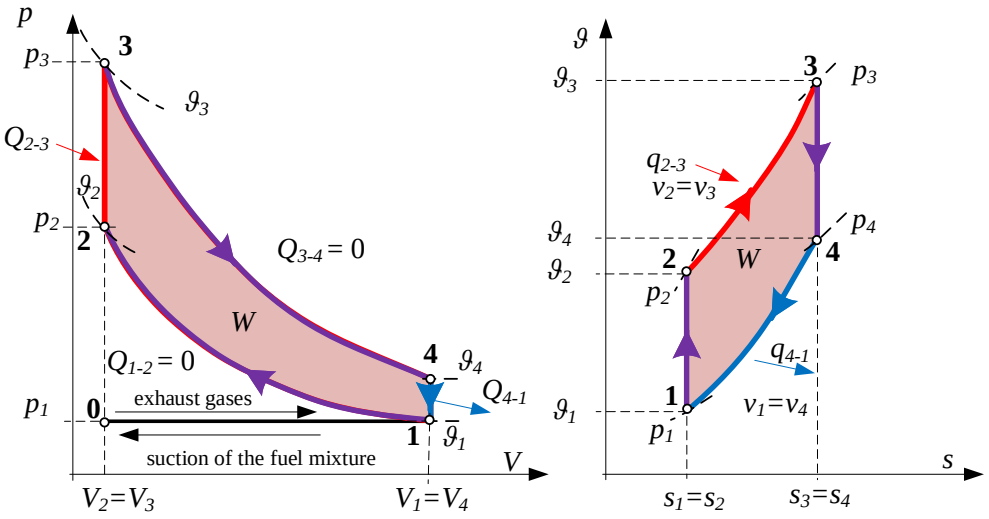

Figure 3.16: Illustration of pressure vs. volume (p–V) and temperature vs. entropy (T–s) diagrams for an ideal Otto process [131]

Constant volume heat addition and release (steps 2 – 3 and 4 – 1) can be described as:

$$Q_{2-3} = mC_V(\vartheta_3 - \vartheta_2) \tag{3.22}$$

$$Q_{4-1} = mC_V(\vartheta_4 - \vartheta_1) \tag{3.23}$$

Constant pressure compression and expansion (steps 1 – 2 and 3 – 4) are defined by:

$$\frac{\vartheta_2}{\vartheta_1} = \left(\frac{V_1}{V_2}\right)^{\gamma-1} \tag{3.24}$$

$$\frac{\vartheta_3}{\vartheta_4} = \left(\frac{V_4}{V_3}\right)^{\gamma-1} \tag{3.25}$$

The volume ratios are defined by means of the *compression ratio* r :

$$r = \frac{V_1}{V_2} = \frac{V_4}{V_3} \tag{3.26}$$

Thermal efficiency of the complete cycle can be defined as:

$$\eta = \frac{Q_{2-3} - Q_{4-1}}{Q_{2-3}} = 1 - \frac{\vartheta_4 - \vartheta_1}{\vartheta_3 - \vartheta_2} = 1 - \frac{1}{r^{\gamma-1}} \tag{3.27}$$

The *net mechanical work* can be expressed as:

$$W_n = \frac{p_3V_3 - p_4V_4}{\gamma - 1} - \frac{p_2V_2 - p_1V_1}{\gamma - 1} \tag{3.28}$$

where the above pressures are related to the compression ratio as follows:

$$r^\gamma = \frac{p_2}{p_1} = \frac{p_4}{p_4} \tag{3.29}$$

Moreover, by introducing the *pressure ratio* r_p:

$$r_p = \frac{p_3}{p_2} = \frac{p_4}{p_1} \tag{3.30}$$

it is possible to express the mechanical work in the following manner:

$$W_n = \frac{p_1V_1}{\gamma - 1}\left(r_p - 1\right)\left(r^{\gamma-1} - 1\right) \tag{3.31}$$

The *mean effective pressure* p_m is given as the ratio of mechanical output work and the swept volume defined as $V_1 - V_2 = V_2(r - 1)$:

$$p_m = \frac{p_1r_1\left(r_p - 1\right)\left(r^{\gamma-1} - 1\right)}{\left(\gamma - 1\right)\left(r - 1\right)} \tag{3.32}$$

3.4.4. Real versus theoretical process

Within a real engine, the thermodynamic process differs from the ideal fuel–air mixture medium process described in the previous section, because in the realistic engine cycle the medium within the cylinder now comprises a mixture of air, fuel vapour and residual flue gases from the previous cycle. Also, the specific heat of the medium is not constant and increases with temperature. Standard air cycles are idealized and based on approximations of complex thermodynamic and chemical phenomena, so the engine power estimated based on the idealised cycle is higher when compared to the output power of an actual (realistic) engine. For example, the actual indicated thermal efficiency of an Otto–cycle heat engine for a compression ratio of 8 is about 28% because of different power losses, while the ideal Otto process is characterised by an indicated thermal efficiency of about 57% [131]. The aforementioned losses are due to:

- Working substance being a mixture of air and fuel vapour combined with the products of combustion left over from the previous cycle, and the related variation of composition, temperature and ratio of fresh mixture due to residual combustion gases,
- Change in chemical composition of working substance due to combustion,
- Variation of specific heat coefficients C_p and C_v with operating temperature,
- Progressive (spatially distributed) and finite time character of the combustion event rather than the "theoretical" instantaneous combustion of the mixture,
- Heat transfer from and to the working medium,
- Exhaust blow–down losses and losses of mechanical work during the expansion stroke due to opening of the exhaust valve,
- Gas leakage and fluid (viscous) friction.

Moreover, it has been shown in [131] that other major contributions to overall losses are:

- Time loss factor, i.e. time required for the mixing of fuel and air and combustion,
- Heat loss due to heat flux between the medium and cylinder walls.

The air–fuel ratio changes during engine operation and affects the composition of gases before and after the combustion takes place. All gases except mono–atomic gases show increase in specific heat with temperature. For temperature ranges encountered within

heat engines (between 300 K and 2000 K) the specific heat dependence is approximately linear with temperature and can be expressed as [131]:

$$\begin{aligned} C_p &= a + k\vartheta \\ C_v &= b + k\vartheta \\ R &= C_p - C_v \end{aligned} \tag{3.33}$$

where R is the ideal gas constant ($R = 8.314$ J/molK). By introducing variable specific heats model (see Figure 3–19), the temperature at the end of compression cycle is defined as:

$$\vartheta_2 = \vartheta_1 \left(\frac{V_1}{V_2} \right)^{k-1}, \quad k = \frac{C_p}{C_v} \tag{3.34}$$

On the other hand, the temperature at the end of expansion cycle is defined as:

$$\vartheta_4 = \vartheta_3 \left(\frac{V_3}{V_4} \right)^{k-1} \tag{3.35}$$

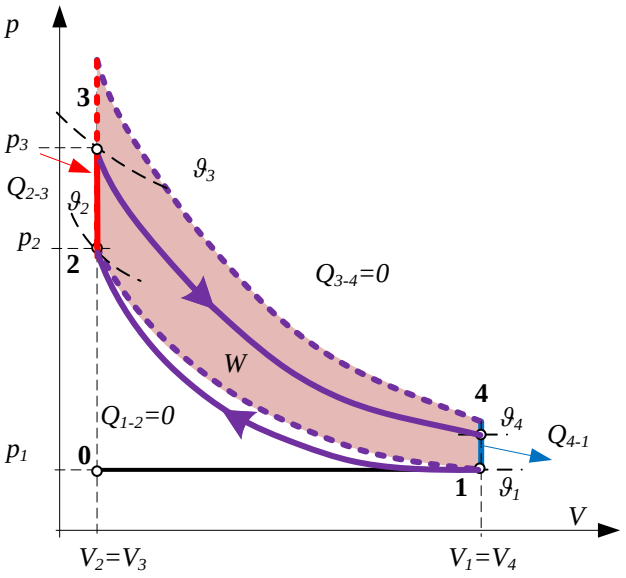

Figure 3.17: Variable specific heat model for Otto process [131]

During the combustion process within the ICE, heat is transferred from the cylinder gases through cylinder walls and cylinder head into the cooling fins or the water jacket. The heat is also lost from the piston head into the piston rings and is carried away by the lubricating oil or medium flow through the cylinder walls. Heat loss magnitude is rather high when compared to other energy losses, because it amounts to about 12% loss of energy. In comparison, the time loss amounts to about 6%, while the exhaust loss is only about 2% of energy losses.

The main effect of the heat loss during the engine combustion and expansion cycle is manifested in the reduction of the maximum temperature, thus resulting in lower specific heats C_p and C_v. Blow–down effect, i.e. the release of the combustion particles from the cylinder when the exhaust valve opens, will also have an effect on the efficiency of the engine, and losses incurred during this phase are called exhaust blown losses, and they depend on the timing of the opening of the exhaust valve. Figure 3–20 shows the p–V diagram of an Otto engine with all three losses (time loss, heat loss and exhaust loss) with the corresponding percentages of each loss during the cycle. It should be noted that the loss of this exhaust blown is 2%, which is comparatively less than the other two losses (time loss amounting to 6% and heat loss amounting to 12%). Hence, exhaust loss will have far less effect on the overall efficiency of the engine.

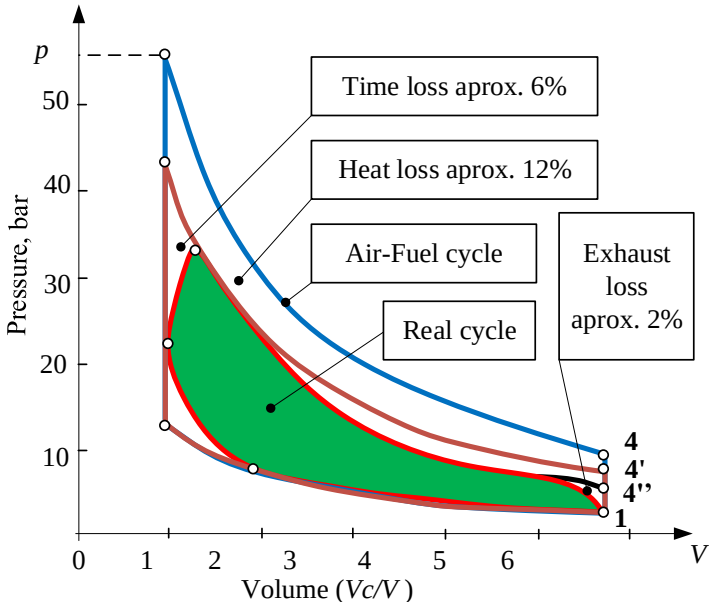

Figure 3.18: Losses occurring in Otto engine cycle [131]

3.4.5. Mean value model of two-stroke engine

For the purpose of implementing a reliable dynamics model of a two–stroke engine for simulation studies and control system design, a nonlinear Mean–Value Engine Model (MVEM) described in [139, 140] is going to be used as a basis for the work conducted herein. This methodology is suitable for the control system design and verification purposes because it covers all important aspects of static and dynamic processes within the engine while being fairly straightforward because it does not include the high frequency dynamics of cyclic/reciprocating piston operation. The latter is accounted for within the MVEM through torque development delay which signifies the fact that the torque produced by the engine does not respond immediately to an increase in the manifold

pressure.

The considered mean value engine model possesses only two state variables: the air pressure in the intake manifold p and the engine rotational speed ω, whereas all other effects are modelled by means of three–dimensional static maps. Figure 3.19 shows the block diagram of a mean value engine model for a Spark Ignited (SI) Otto engine [139–141] . The air pressure dynamics within the intake manifold is by the first–order time derivative of the ideal gas equation assuming constant air temperature ϑ (in K), i.e. the so–called isothermal model:

$$\frac{dp}{dt} = \frac{R\vartheta}{V}\frac{dm}{dt} = \frac{R\vartheta}{V}(W_i - W_o) \tag{3.36}$$

where p is the intake manifold pressure (Pa), m is the mass of air/gas (kg), R is the gas constant (J/kgK), θ is temperature (K), V is the intake manifold volume (m^3), and W_i and W_o are the inlet and outlet mass airflows respectively (kg/s).

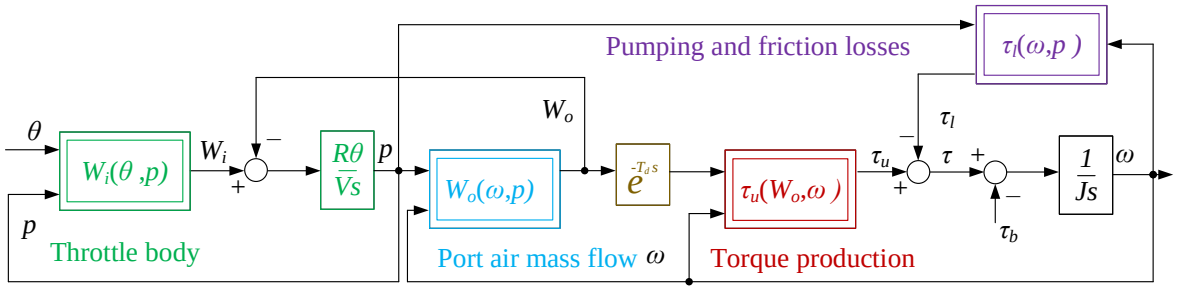

Figure 3.19: Nonlinear MVEM model of SI Otto engine [140]

The model also includes several effects and subsystems that correspond to individual engine parts: the throttle servo–valve, intake manifold, piston pumping effect, rotational dynamics and dead time (delay) T_d due to cyclic operation of the engine. These subsystems can be described by exact physical or semi–empirical mathematical expressions [140, 141], or (as shown herein) by three non-linear static maps defining the inlet and outlet air flow of the intake manifold W_i and W_o, and the active (indicated) torque at the motor shaft [139, 140]. The above model simplifications are based on the following assumptions that have been satisfied for most engine operating modes [142]:

- Variations of the rotational speed ω within a single combustion cycle (related to dead–time T_d) are negligible,
- Indicated torque related to manifold air pressure p is considerably greater than the corresponding load torque due to pumping effect and friction

The parameters of the averaged engine model can be determined based on known physical constants of the model (i.e. manifold volume V and moment of inertia J), while static

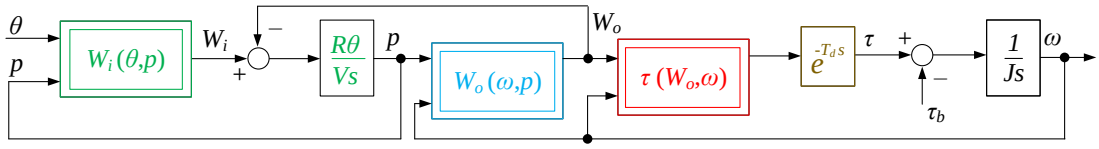

Figure 3.20: Simplified non-linear MVEM model of SI Otto engine [140]

maps can be expressed by analytical expressions [141], or recorded by standard engine dynamometer tests [142, 143]. The model can be further simplified by integrating the indicated motor torque and non-linear load torque τ_L due to pumping and friction in the motor into a single map of the developed motor torque on the shaft $\tau(W_o, \omega)$ as shown on Figure 3.20.

Model linearisation is performed in the vicinity of the engine operating point defined by stationary values of model state variables, i.e. air pressure in the intake manifold p, and the rotational speed ω [140]. The static maps $W_i(\theta, p)$, $\tau_{ind}(W_i, \omega)$ and $\tau_L(p, \omega)$ are given in the form of three–dimensional tables. More information about linearisation and modelling can be found in references [140, 142, 144]. In order to reduce the number of measurements, while still being able to capture relevant transient characteristics of ICE, a previously described MVEM model can be further simplified into a first order engine model. If a small volume of intake manifold is assumed, which is valid for small, low power engines, intake manifold filling dynamics would be rather fast, i.e. negligible. This type of model is still valid for engine control applications, if the bandwidth of a control system is relatively low [145].

When considering such first order model, engine dynamics consists of one state:

$$J\dot{\omega} = \tau_e - \tau_l \tag{3.37}$$

where $\tau_e = f(\theta, \omega)$ is net torque after losses, described by static map. Such map can be obtained from test bench measurements (example map is shown on 3.21). With increasing the throttle angle, net torque τ_e increases monotonically, reaching a maximum and then decreasing. Thus, for each throttle angle there is engine speed with maximum torque output [145]. The active torque on shaft is determined by imposed load (i.e. load from generator) and throttle valve opening angle. By neglecting the intake manifold dynamics, simplified model (with throttle dynamics) is shown in Figure 3.22.

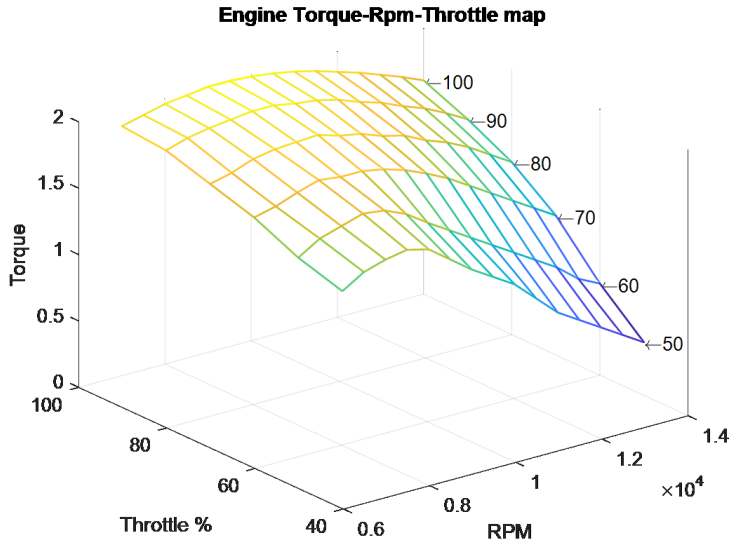

Figure 3.21: Torque–RPM–throttle map of small two–stroke SI Otto engine

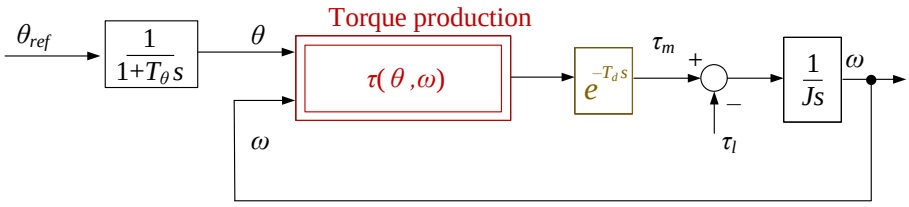

Figure 3.22: Single-map non-linear MVEM model of SI Otto engine

The above model also includes several effects and subsystems that correspond to individual engine parts: the throttle servo–valve, rotational dynamics and dead time (delay) T_d due to cyclic operation of the engine as previously shown. Model linearisation is again performed in the vicinity of the engine operating point defined by stationary values of model state variables for the case of optimum engine torque (approx. 9500 RPM for the selected prime mover, Zenoah G320RC engine), see Figure 3.23.

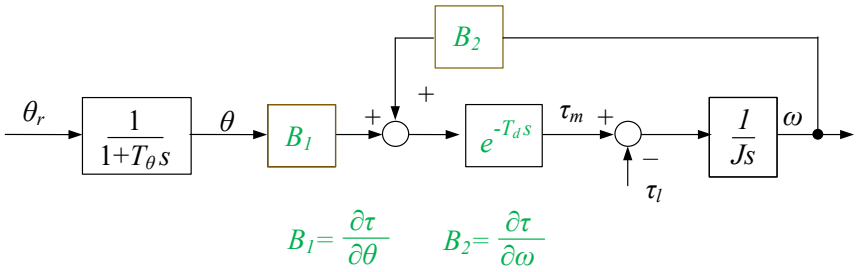

Figure 3.23: Averaged Otto engine model with expressions for model parameters obtained by the linearisation process

In the case when the closed–loop control system dynamics (characterised by the closed–loop equivalent lag T_e) are much slower than the combustion delay ($T_e >> T_d$), the pure delay (dead time) T_d can be approximated by the first two terms of the Taylor series expansion of the exponential term [139]:

$$e^{-T_d s} \approx \frac{1}{T_d s + 1} \tag{3.38}$$

The aforementioned dead time can be interpreted as the mean time between mixture ignitions within cylinders. For a two–stroke engine, combustion occurs at every full rotation of the crankshaft and it can be approximated by following expression:

$$T_d \approx \frac{2\pi}{\frac{n\pi}{30}} = \frac{60}{n} \tag{3.39}$$

Throttle dynamics is considered as a first order lag system and linearised model with throttle dynamics is shown in Figure 3.24

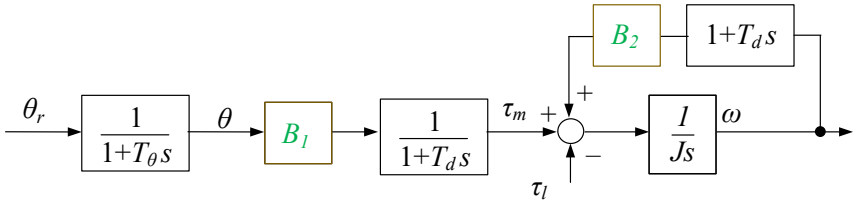

Figure 3.24: Simplified linear model of Otto engine with exact dead time of torque development and rotational dynamics

After linearisation in vicinity of operating point for considered two stroke engine, a feedback characterised by factor B_2 can be neglected due to its very low value ($< -10^{-4}$). Finally, a simplified dynamics model of engine suitable for control system design is shown in Figure 3.25.

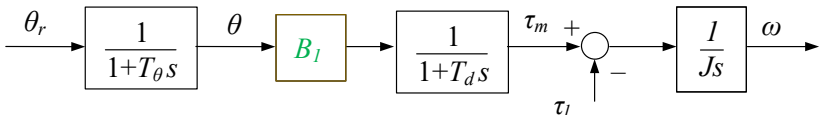

Figure 3.25: Dynamics model of Otto process suitable for control system design

3.5. Electrical motors and generators

Electrical machine is utilised for energy conversion between the electrical system and the mechanical system and vice versa, as shown in Figure 3.26. When electrical machines consume electrical power, they are referred to as motors, and when they produce electricity they are referred to as generators. For an electric motor, its input is the electrical power

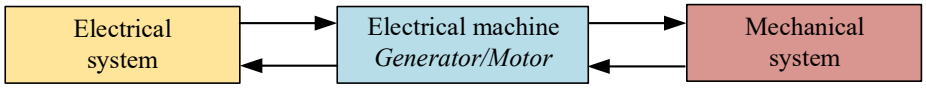

Figure 3.26: Electrical machine energy flow

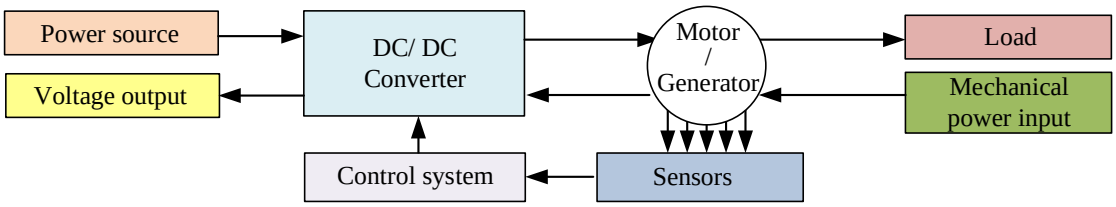

Figure 3.27: Electric drive block diagram

represented by its voltage and current, and the output is mechanical power delivered to the mechanical load, which is characterised by its speed and torque. For a generator, the mechanical power (speed and torque) is converted to electrical power (voltage/current), which is then transmitted towards the electrical system by the electrical machine [146–150]. General categorisation is based on the type of current and voltage, so electrical machines are direct current (DC) machines and alternating current (AC) machines.

A simplified block diagram representation of the electrical drive in Figure 3.27 shows that it consists of a power source, a power converter, electrical motor (electrical machine), load, sensing module, and control module. Power source can either be supplied by an AC line supply (such as in the case of most industrial electrical drives) or from the DC power supply such as the electrochemical battery. In the case of a generator, a mechanical torque represents the input to the system and, thus, its output is the generated voltage which is fed to the power converter, which can then transmit this energy to the grid or the battery if it is built with a regenerative (bidirectional power flow) topology.

Power converters are used to adapt/modify voltage levels and control the power flow. In the case of a motor they generate voltages to drive it, and in case of a generator they are used as controllable rectifiers (assuming that they are built with an internal DC link). In the latter case load represents a current drain from the generator.

Sensors are used to monitor voltages, currents, temperature, rotational (or translational) speed and other key quantities. Information processing is usually performed within a microcomputer system that runs a dedicated control algorithm for switch–mode power conditioning of the power converter.

3.5.1. DC machine model

DC motors and generators (more precisely, DC machines) fall into the category of electrical machines that convert direct current to mechanical power and vice versa. The machine consists of stationary magnets (permanent magnets or electromagnets) arranged in a circular patterns in the case of rotational machine (stator) and a rotor windings (armature) consisting of an insulated wire wrapped around a soft iron core that serves as a magnetic field conductor. Within the rotor several windings are connected in series and connected to the so–called commutator. At least two (or a multiple of two) stator magnets produce a magnetic field that permeates the rotor windings which rotate due to the force (torque) generated by the interaction between the current flowing through the armature and the magnetic field (see Figure 3.28). Due to the design of the rotor and commutator, the motor continues to rotate while being supplied with DC current at its terminal connectors. Basically, there is no mechanical and electrical design difference between a DC motor and a DC generator, i.e. the same machine can be operated as a generator or as a motor [61, 146–150].

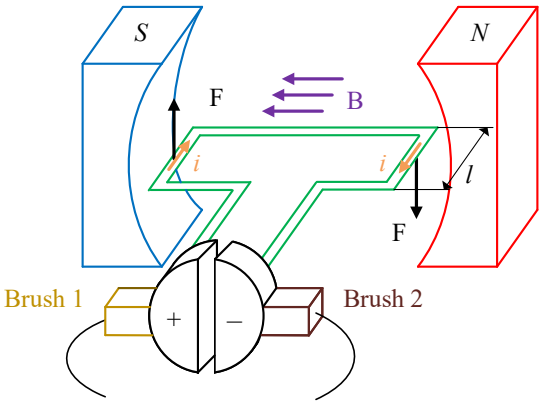

Figure 3.28: Electric DC motor principle schematic

When DC voltage is applied to the connection terminals of the DC machine, and a conductor moves within a homogenous (constant) magnetic field characterised by it magnetic flux density B (see Figure 3.28), thus rotating from brush 1 to brush 2, the current in that conductor reverses direction, and at the same time it is brought under the influence of the next magnetic pole which is of opposite polarity. Consequently, the direction of force acting upon the conductor remains the same. When the armature of a DC machine rotates under the influence of the input or driving torque, the armature conductors move through the magnetic field and hence Back Electromotive Force (BEMF) is induced. In that case the DC machine operates as a generator [61]. The DC machine dynamic model relates electrical and mechanical quantities. This model is composed

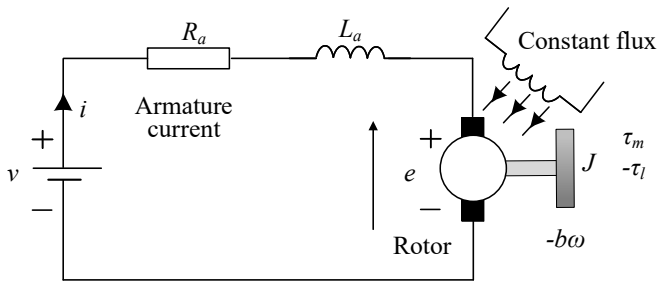

Figure 3.29: DC motor electrical and mechanical schematic

of the series connection of a resistor R_a (armature ohmic resistance in ω), an inductor L_a (armature inductance in H) and generated BEMF e and power supply voltage v (measured in V), as illustrated in Figure 3.29. Armature resistance defines the so–called Joule (heat) losses due to the current flow through a copper conductor and depends on the geometric and material characteristics of the armature windings, such as conductor length and cross–section area. The BEMF e, also known as counter–electromotive force, is characterised by voltage proportional to DC machine speed. In general, the torque generated by the DC machine is proportional to the armature current and the excitation magnetic flux.

For a constant magnetic field–based excitation (e.g. permanent magnet), DC motor torque only depends on the armature current i, that is, the proportionality factor between the developed torque and the current is the so–called torque constant K_t :

$$\tau_m = K_t i_a \tag{3.40}$$

On the other hand, the DC motor back BEMF is proportional to angular velocity:

$$e = K_e \omega_m \tag{3.41}$$

where K_e is the DC machine BEMF constant. If DC machine speed and torque are expressed in SI units rad/s and Nm, for the ideal machine the motor torque and BEMF constants are in fact equal, that is, $K_t = K_e$. Therefore, a single constant $K = K_t = K_e$ can be used to represent both the motor torque constant and BEMF constant. The Kirchhoff's voltage law describes the electrical part of motor, and differential equation of circuit can be expressed as:

$$v_a = e + L_a \frac{di_a}{dt} + i_a R_a \tag{3.42}$$

Using the Newton law of motion for a rotary system it is possible to describes the mechanical part of the machine:

$$\tau_m = \tau_l + b\omega + J\frac{d\omega}{dt} \tag{3.43}$$

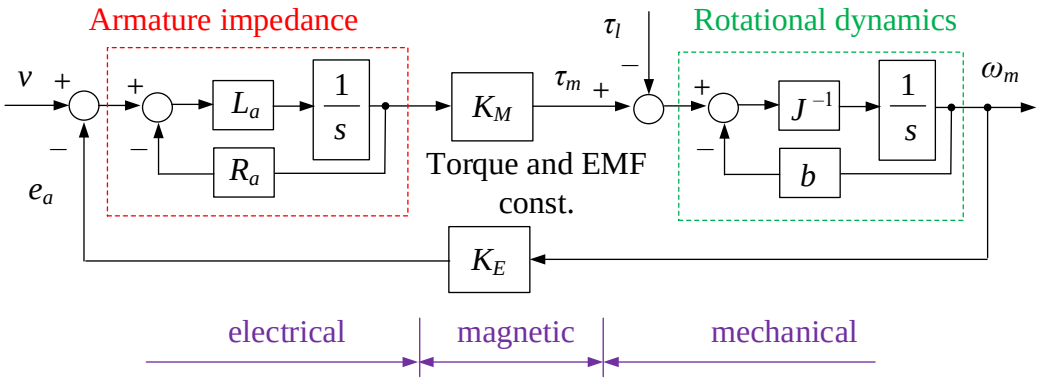

Figure 3.30: Block representation of DC motor dynamics model

where τ_m is developed torque (Nm), τ_l is imposed load torque (Nm), b is motor viscous friction constant (Nms), J is moment of inertia of the rotor (kgm^2) and ω is rotor speed (rad/s).

The governing equations from above can be given in the state–space form by selecting the rotational speed and electric current as the state variables of the particular dynamic system (see Figure 3.30):

$$\frac{di_a}{dt} = \frac{1}{L_a}v - \frac{K_e}{L_a}\omega_m - \frac{R_a}{L_a}i_a \tag{3.44}$$

$$\frac{d\omega}{dt} = \frac{K_t}{J}i_a - \frac{1}{J}\tau_l - \frac{b}{J}\omega \tag{3.45}$$

Finally, state space equations in the matrix–vector form can be obtained by treating the armature voltage (corresponding to external electrical power supply) and load torque as the model inputs, while the rotational speed is chosen as the model output:

$$\begin{bmatrix} \frac{di_a}{dt} \\ \frac{d\omega}{dt} \end{bmatrix} = \begin{bmatrix} \dot{x}_1 \\ \dot{x}_2 \end{bmatrix} = \begin{bmatrix} -\frac{R_a}{L_a} & -\frac{K_e}{L} \\ \frac{K_t}{J} & -\frac{b}{J} \end{bmatrix} \begin{bmatrix} x_1 \\ x_2 \end{bmatrix} + \begin{bmatrix} \frac{1}{L_a} & 0 \\ 0 & -\frac{1}{J} \end{bmatrix} \begin{bmatrix} v \\ \tau_L \end{bmatrix} \tag{3.46}$$

$$y = \begin{bmatrix} 0 & 1 \end{bmatrix} \begin{bmatrix} x_1 \\ x_2 \end{bmatrix} \tag{3.47}$$

In order to obtain a transfer functions from above equations, first it is required to find a state–transition matrix $\Phi(s) = (s\mathbf{I} - \mathbf{A})^{-1}$ where $\mathbf{I}$ is identity matrix with size corresponding to size of state matrix $\mathbf{A}$:

$$\Phi(s) = \begin{bmatrix} \frac{L_a(b+Js)}{a*} & -\frac{K_e J}{a*} \\ \frac{K_t L_a}{a*} & \frac{J(R_a+L_a s)}{a*} \end{bmatrix} \tag{3.48}$$

where $a* = R_a b + K_e K_t + J R_a s + L_a b s + J L_a s^2$.

Transfer functions can be obtained by using $G(s) = \frac{y(s)}{u(s)} = \mathbf{C\Phi B} + \mathbf{D}$ relationship as

follows:

$$G_1(s) = \left.\frac{\omega(s)}{v(s)}\right|_{\tau_L=0} = \frac{K_t}{(R_a b + K_e K_t) + (JR_a + L_a b)s + JL_a s^2} \tag{3.49}$$

$$G_1(s) = \left.\frac{\omega(s)}{\tau_L(s)}\right|_{v=0} = -\frac{R_a \ + \ L_a s}{(R_a b + K_e K_t) + (JR_a + L_a b)s + JL_a s^2} \tag{3.50}$$

The DC–generator dynamics model is similar to the motor model. The generated back EMF voltage is proportional to the rotor speed and can be expressed as:

$$e = K_e \omega \tag{3.51}$$

Armature equation is as follows:

$$v = e - L_a \frac{di_a}{dt} - i_a R_a \tag{3.52}$$

The electromagnetic torque produced by the generator is proportional to the armature current and can be expressed as:

$$\tau_g = K_t i \tag{3.53}$$

The DC generator terminal voltage in the case of resistive load may be defined as:

$$v = R_L i \tag{3.54}$$

However, in the case of common DC link (to which the DC machine armature is connected), this voltage may be determined by other components, such as the terminal voltage of the battery or other bidirectional DC source connected to it. In that case, the analytical calculation of the generator terminal voltage would be far more complex. Generator torque acts as load on the motor that drives DC generator. Mechanical part can be described as:

$$\tau_{mech,in} = \tau_g + J\frac{d\omega}{dt} + b\omega \tag{3.55}$$

The governing equations from above can be given in the state–space form by selecting the rotational speed and electric current as the state variables of the dynamic system:

$$\frac{di_a}{dt} = \frac{K_e}{L_a}\omega - \frac{1}{L_a}v - \frac{R_a}{L_a}i_a \tag{3.56}$$

$$\frac{d\omega}{dt} = \frac{1}{J}\tau_{mech,in} - \frac{K_t}{J}i_a - \frac{b}{J}\omega \tag{3.57}$$

Similarly as in the case of DC generator, state space equations in matrix–vector form can be obtained by treating the armature voltage (corresponding to external electrical power supply) and load torque as the model inputs, while the rotational speed is chosen as the model output:

$$\begin{bmatrix} \frac{di_a}{dt} \\ \frac{d\omega}{dt} \end{bmatrix} = \begin{bmatrix} \dot{x}_1 \\ \dot{x}_2 \end{bmatrix} = \begin{bmatrix} -\frac{R_a}{L_a} & \frac{K_e}{L_a} \\ -\frac{K_t}{J} & -\frac{b}{J} \end{bmatrix} \begin{bmatrix} x_1 \\ x_2 \end{bmatrix} + \begin{bmatrix} -\frac{1}{L_a} & 0 \\ 0 & \frac{1}{J} \end{bmatrix} \begin{bmatrix} v \\ \tau_{mech,in} \end{bmatrix} \tag{3.58}$$

$$y = \begin{bmatrix} R_L & 0 \end{bmatrix} \begin{bmatrix} x_1 \\ x_2 \end{bmatrix} \tag{3.59}$$

State–transition matrix is obtained as:

$$\Phi(s) = \begin{bmatrix} \frac{L_a(b+Js)}{a*} & \frac{K_e J}{a*} \\ -\frac{K_t L_a}{a*} & \frac{J(R_a+L_a s)}{a*} \end{bmatrix} \tag{3.60}$$

where $a* = R_a b + K_e K_t + J R_a s + L_a b s + J L_a s^2$
Finally, the corresponding transfer functions can be obtained by using the well–known relationship $G(s) = \frac{y(s)}{u(s)} = \mathbf{C\Phi B + D}$:

$$G_1(s) = \left.\frac{\omega(s)}{v(s)}\right|_{\tau_{mech,in}=0} = -\frac{b + Js}{(R_a b + K_e K_t) + (J R_a + L_a b)s + J L_a s^2} \tag{3.61}$$

$$G_1(s) = \left.\frac{\omega(s)}{\tau_L(s)}\right|_{v=0} = \frac{K_e}{(R_a b + K_e K_t) + (J R_a + L_a b)s + J L_a s^2} \tag{3.62}$$

3.5.2. Trapezoidal and sinusoidal brushless permanent magnet machine model

The BPMS machine is an alternating current electrical machine, which, unlike brushed DC machine with mechanical commutation, uses electronic commutation to facilitate armature winding current sign (direction) change required for continuous torque production [61, 63, 151, 152]. Such machines are typically driven by a rectangular shaped phase voltage (six step commutation) in case of trapezoidal BEMF shape or sine wave commutation in case of sinusoidal BEMF shape whereas the three–phase armature can be wound in star (wye) or delta configuration.

There exists a great deal of confusion, misconception and inconsistency regarding acronyms and comprehension of these machines in general. Most commonly, trapezoidal machines are referred to as BLDC while sinusoidal machines are referred to as PMSM. A quite detailed explanation for each machine type can be found in [61].

Sinusoidal and trapezoidal permanent magnet brushless machines differ with respect to winding spartial distribution within stator slots, magnetic design regarding airgap and rotor tooth/slot geometry, physical shape of rotor magnets and magnetisation profile [61, 153, 154].

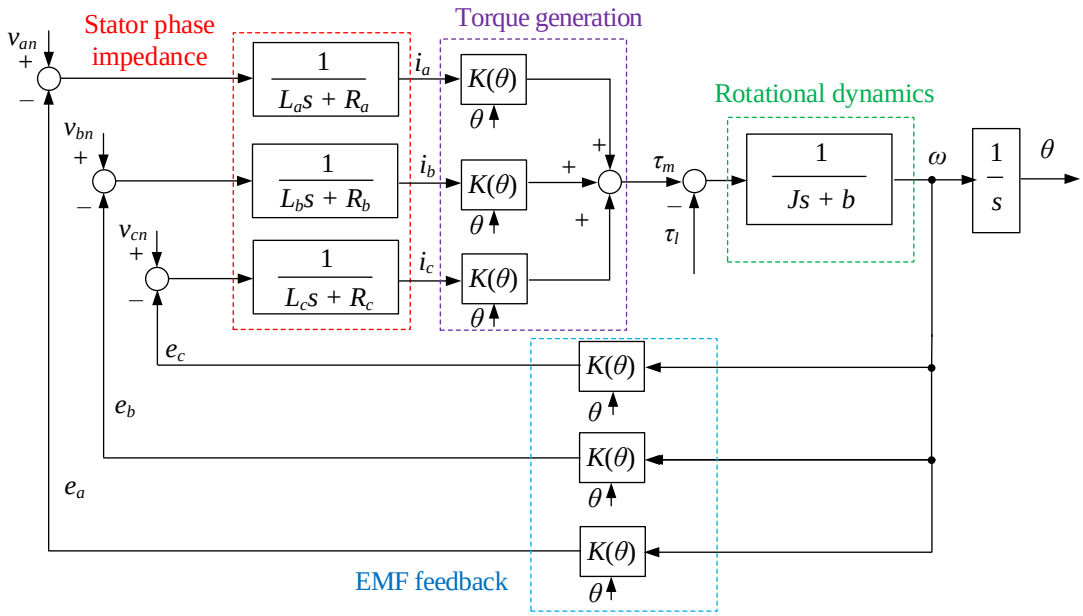

Figure 3.31: Block representation of generalised three phase motor dynamics model (so-called "phase-variable model") [61]

The BEMF and torque functions are depended on rotor-stator flux linkage and rotor position. For the general case, according to Figure 3.31 the contribution of each phase to torque generation can be expressed as [61]:

$$\tau\omega = e_a(\theta_r)\ i_a + e_b(\theta_r)\ i_b + e_c(\theta_r)\ i_c \tag{3.63}$$

From above equation it is possible to conclude that fundamental mechanism of torque production can be generalised regardless of the motor type [61].

Trapezoidal (BLDC)

A star–connected motor with trapezoidal BEMF driven by a three–phase inverter using six step armature commutation is considered herein. For the sake of further analysis, the following assumptions are introduced: resistance and inductance of all the windings are equal, motor ferromagnetic core is not saturated, iron losses are negligible and semiconductor switches are ideal.

Based on the electric circuit representation in Figure 3.32, the motor armature winding equation for i–th $(i = a, b, c)$ phase is:

$$v_i = R_i i_i + L_i \frac{di_i}{dt} + e_i \tag{3.64}$$

where v_i is phase–to–neutral voltage of the i–th phase, i_i is the phase current, R_i and L_i are phase resistance and inductance, and e_i is the phase counter–electromotive force. Note

that individual phase electromotive forces (induced voltages) e_i are dependent on motor position and speed. Each phase winding corresponds to 120° phase (electrical) angle difference and its peak value is defined by the phase induced voltage constant $K_{e,phase}$. The BEMF for i–th phase can be expressed as:

$$e_i = \tfrac{1}{2} K_e f_i(\omega_m) \tag{3.65}$$

$$f_a = f(\phi_e),\ f_b = f\left(\phi_e - \tfrac{2}{3}\pi\right),\ f_c = f\left(\phi_e + \tfrac{2}{3}\pi\right) \tag{3.66}$$

where K_e is line motor voltage constant, which is double the corresponding phase value ($2K_{e,phase} = K_{e,line}$), f_i is the normalized trapezoidal curve dependent on motor electrical angle $\phi_e = \phi_m$ where p is the number of machine poles, ϕ_m is the rotor mechanical angle and ω_m is the mechanical angular speed. The total electromagnetic torque output can be represented as a sum total of each phase contribution as follows:

$$\tau_e = \frac{K_e}{2}\left(f_a i_a + f_b i_b + f_c i_c\right) \tag{3.67}$$

Electrical machine rotational dynamics for both BLDC and PMSM, including the non-linear load (i.e. viscous friction-like drag torque load), is given by the following equation:

$$\tau_e - \tau_d = b\omega + J\frac{d\omega}{dt} \tag{3.68}$$

where τ_e is the rotor generated electrical torque, τ_d is viscous friction-like drag torque load, b is the viscous friction coefficient, and J is the inertia of the machine rotor, which may also include additional inertia of components connected to the machine shaft.

According to the operation principle of the permanent magnet motor with trapezoidal BEMF (usually referred as BLDC), it is known that only two phases conduct simultaneously in the three–phase stator winding at each time point. Thus, the neutral point voltage can be derived as follows:

$$v_n = \frac{1}{3}\left[(v_a + v_b + v_c) - (e_a + e_b + e_c)\right] \tag{3.69}$$

Finally, block representation of BLDC motor dynamics model is shown in Figure 3.33.

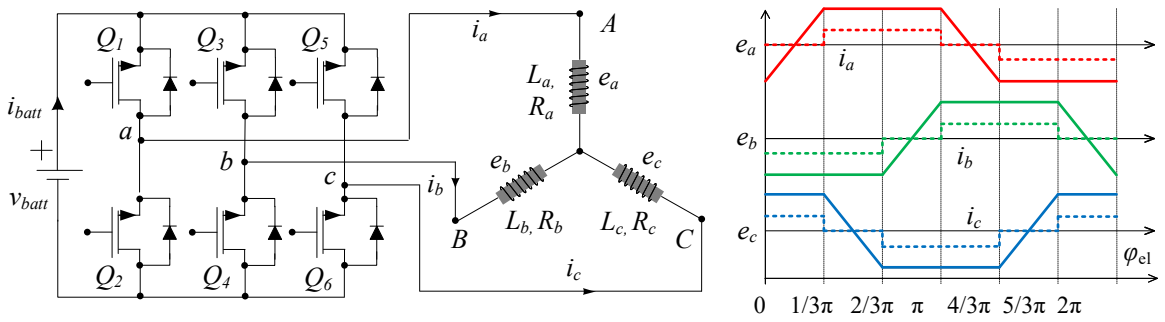

Figure 3.32: BLDC electrical schematic with three–phase inverter, b) trapezoidal back–EMF and current plot

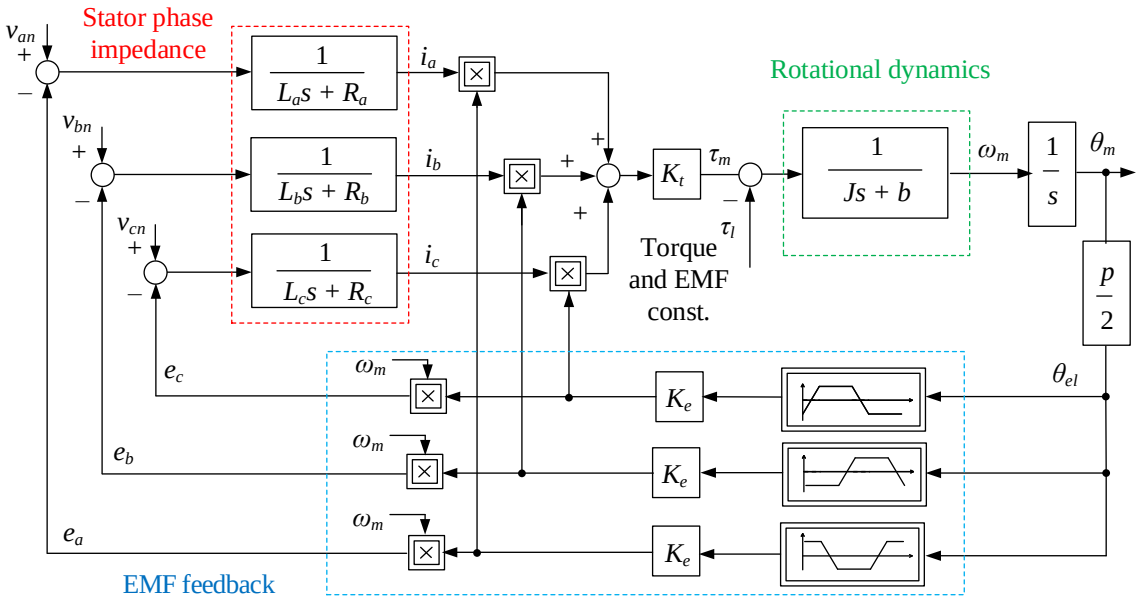

Figure 3.33: Block representation of BLDC motor dynamics model

Sinusoidal (PMSM)

Since the model of the PMSM motor in the stator coordinate system is extremely non-linear, and as such is very complex for control system design purposes, the model is usually realized in the rotating $d-q$ coordinate system (Figure 3.34).

In the $d-q$ reference frame a voltage and flux equations can be expressed as:

$$V_d = R_s i_d + \frac{d\psi_d}{dt} - \omega\psi_q \tag{3.70}$$

$$V_q = R_s i_q + \frac{d\psi_q}{dt} + \omega\psi_d \tag{3.71}$$

$$\psi_d = L_d i_d + \psi_m \tag{3.72}$$

$$\psi_q = L_q i_q \tag{3.73}$$

where V_d, V_q, i_d, i_q are voltages and currents respectively, in $d-q$ axis, R_s is stator winding resistance, ψ_d, ψ_q are flux linkages in $d-q$, ψ_m is main permanent magnet flux linkage, L_d, L_q are inductances in $d-q$ and ω is angular frequency of the rotor.

In order to convert quantities from different reference frames, following transformations can be used:

$$\begin{bmatrix} i_d \\ i_q \\ 0 \end{bmatrix} = T_1 \begin{bmatrix} i_a \\ i_b \\ i_c \end{bmatrix}, \quad \begin{bmatrix} i_x \\ i_y \\ 0 \end{bmatrix} = T_2 \begin{bmatrix} i_a \\ i_b \\ i_c \end{bmatrix}, \quad \begin{bmatrix} i_d \\ i_q \end{bmatrix} = T_3 \begin{bmatrix} i_x \\ i_y \end{bmatrix} \tag{3.74}$$

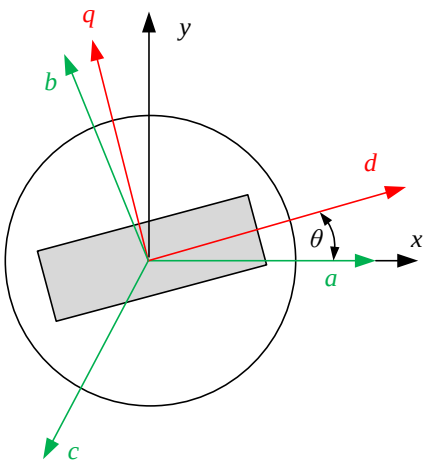

Figure 3.34: PMSM coordinate systems

where transformation matrices T_1, T_2, T_3 are defined as:

$$T_1 = \frac{2}{3}\begin{bmatrix} \cos\theta & \cos(\theta - 2\pi/3) & \cos(\theta + 2\pi/3) \\ \sin\theta & \sin(\theta - 2\pi/3) & \sin(\theta + 2\pi/3) \\ \frac{1}{2} & \frac{1}{2} & \frac{1}{2} \end{bmatrix} \tag{3.75}$$

$$T_2 = \frac{2}{3}\begin{bmatrix} 1 & -\frac{1}{2} & -\frac{1}{2} \\ 0 & -\frac{\sqrt{3}}{2} & \frac{\sqrt{3}}{2} \\ \frac{1}{2} & \frac{1}{2} & \frac{1}{2} \end{bmatrix} \tag{3.76}$$

$$T_3 = \begin{bmatrix} \cos\theta & \sin\theta \\ -\sin\theta & \cos\theta \end{bmatrix} \tag{3.77}$$

Mechanical equation is the same as for BLDC case, and electrical torque can be expressed as:

$$T_e = \frac{3}{2}\frac{p}{2}(\psi_d i_q - \psi_q i_d) \tag{3.78}$$

where p is machine pole count.

3.5.3. DC equvalent model of BLDC machine

When SI units are used, the per–phase BEMF and electromagnetic torque functions are numerically equal and units for each function (volt s/(rad) and Nm/A) are dimensionally equivalent [61]:

$$e\,(t)\,i\,(t) = T\,(t)\,\omega\,(t) \tag{3.79}$$

The above equation holds both for transient and steady state conditions, but it is important to note that the equation only governs the part of energy conversion process that

involves magnetic flux that links both the field excitation and the armature. When instantaneous values of back EMF and torque are replaced with their general descriptions the following result is obtained:

$$K_e(\theta)\,\omega(t)\,i(t) = K_t(\theta)\,i(t)\,\omega(t) \tag{3.80}$$

Regardless of the type of motor or motor controller, the current and velocity on each side of the equation will be the same and may be cancelled, leaving the all–important result previously discussed regarding the DC machine, i.e. $K_t = K_e = K$ assuming that torque and speed are expressed in compatible SI units.

According to Figure 3.32, during each switching sequence one of the three phases is not powered (it is inactive), whereas the two remaining phases are connected to opposite polarities of the DC link voltage (battery voltage v_{batt} in this case). Thus, $i_a = -i_b = i_e$ is valid (based on the notation in Figure 3.32, for $0 \leq \phi_e \leq \pi/3$. During the semiconductor switches conduction stage, the equivalent line voltage v_{eq} across two stator phase windings is a Pulse Widith Modulation (PWM) waveform with magnitude corresponding to source terminal voltage v_t (and its PWM duty cycle $0 < d < 1$ available from controller unit). Therefore, the BLDC stator (armature) winding model may be rewritten for the case of simultaneous conduction of two phases as follows:

$$v_{ab} = dv_t = 2Riv_{eq} + 2L\frac{di_{eq}}{dt} + e_a - e_b \tag{3.81}$$

which can be further simplified to:

$$v_{ab} = R_{eq}i_{eq} + L_{eq}\frac{di_{eq}}{dt} + 2K_e\omega_m \tag{3.82}$$

for the case of trapezoidal (square) distribution of excitation field flux [61,63] The above model is identical to the armature equation of a DC motor [61, 63], with armature phase–to–phase (line) equivalent resistance and inductance $R_{eq} = 2R$ and $L_{eq} = 2L$, and line equivalent BEMF ($e_{eq} = e_a – e_b$) vs. speed ω_m proportionality factor (BEMF constant) $K_{e,dc} = 2\Phi_m$. The same principle can be applied to the calculation of developed BLDC machine torque τ_m , where the case $J\dot{\omega} = \tau_e - \tau_l, i_c = 0, f(\phi_e) = -f(\phi_e - 2\pi/3)$ and $i_a = -i_b = i_{eq}$ is reduced to:

$$\tau_m = \Phi_m[f(\phi_e)i_a + f(\phi_e - 2\pi/3)i_b] = 2\Phi_m i_{eq} \tag{3.83}$$

The above equation is, in turn, identical to the DC motor torque equation [61, 63], with torque τ_m vs. equivalent DC current i_{eq} proportionality factor (torque constant) $K_{m,dc} = 2\Phi_m$.

3.5.4. Losses

The input power of DC machine cannot be fully converted to output power because of unavoidable losses that cause reduction in machine efficiency. Losses can be categorised as: copper losses, iron losses, mechanical losses and stray losses (see Figure 3.35). In a permanent magnet (or BLDC) machine, copper losses occur due to the armature heat losses and can be described as:

$$P_{cu} = {i_a}^2 R_a \tag{3.84}$$

The armature reaction loss is associated with the variation of load acting upon the machine (because armature current is dependent on the load). The iron core losses consist of the hysteresis and eddy current loses. Due to rotation of machine, the core undergoes magnetic reversal. Hysteresis loses for non–sinusoidal flux waveforms (such as in BLDC machine) can be estimated by improved generalized Steinmentz equation expressed as [155, 156]:

$$P_{hy} = \frac{1}{T} \int_0^T k_1 \left| \frac{dB}{dt} \right|^a \left(\Delta B^{b-a} \right) dt \tag{3.85}$$

where a and b, called the Steinmetz coefficients that can be empirically determined from B–H hysteresis curve by means of curve fitting, is peak to peak flux density and is additional parameter dependant on Steinmetz coefficient k from original formulation [156,157]. Because of electromagnetic induction, the electromagnetic force is also induced within the machine iron core and can cause large currents (so–called Eddy currents) due to low ohmic resistance and relatively large cross–section. These losses are usually modelled by Finite Element Method (FEM) tools and appropriate software packages. Mechanical losses are divided into friction loses in bearings and windage loses due to air in machine. Usually are not very large in magnitude. Stray losses are all other type of losses, i.e. flux distortion due to armature reaction, short–circuit current within the coil undergoing commutation and others. Most commonly they are modelled as 1% losses of full load output power. The overall efficiency of BLDC and DC machines is most commonly between 0.7 and 0.9.

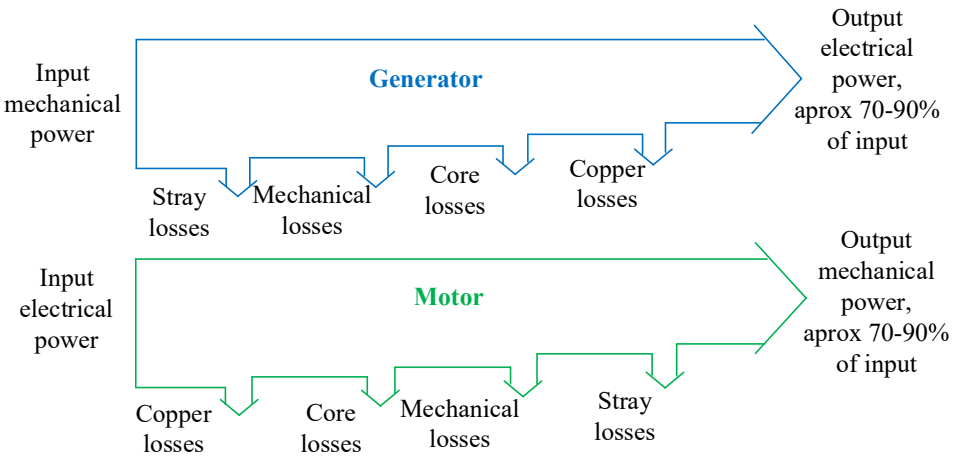

Figure 3.35: Representation of loses in Pemanent Magned Direct Current (PMDC) machines

3.6. Lithium–Polymer Battery

Battery is a device that converts stored chemical energy into electricity using electrochemical oxidation–reduction reactions (battery discharging). During discharging, chemicals within the battery ultimately reach a state of equilibrium wherein the battery is fully discharged, and further reactions are not possible. In the case of a rechargeable system, chemical reactions are reversible, and the battery can be recharged.

Main constituting element of any battery is called a battery cell and battery can consist of one or more cells that are connected in series, parallel, or both, depending on the desired output voltage and capacity. Common classification of batteries is based on the possibility of recharging. Primary batteries (i.e. alkaline batteries used for flashlights, toys, small consumer devices) are not rechargeable and once depleted (discharged) cannot be further used, whereas secondary batteries (i.e. lithium ion batteries used in laptops, cell phones and similar) are designed for multiple use, they have ability to be recharged.

The cell consists of three main components (see Figure 3.36):

- *Anode* or negatively charged electrode that oxidizes or releases electrons through a circuit,
- *Cathode* or positively charged electrode that reduces or accepts electrons,
- *Electrolyte* as a medium for the transfer of charge (ions) between the anode and cathode.

When the battery is charged, oxidation occurs on the positive electrode and reduction on the negative electrode. Upon discharge, the negative electrode oxidizes, while the

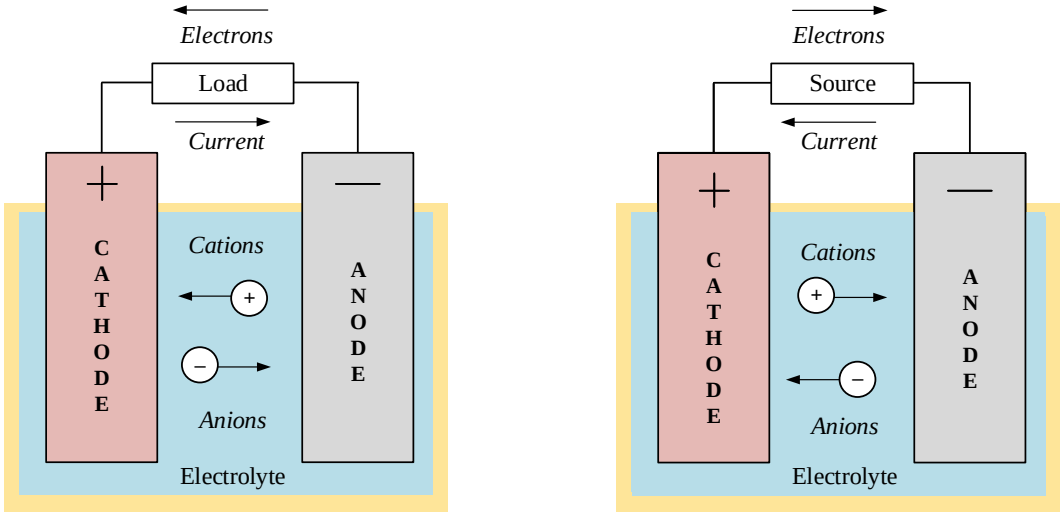

(a) (b)

Figure 3.36: Electrochemical cell functional schematic representation for: Discharge (a) and Charging (b)

positive electrode reduces. Oxidation is a chemical reaction in which electrons are received, where atoms become negatively charged ions (anions). Reduction is the opposite reaction from oxidation in which electrons are released, where atoms become positively charged ions (cations). Oxidation and reduction are also known as redox reactions. Batteries can be described by a large number of parameters that are often interdependent. Battery terminal voltage depends on the cell type, cell connection type, charge status (State of Charge (SoC)), temperature, current, and number of charge and discharge cycles. It is described by the following [158]:

- *Theoretical voltage*, dependent on the cathode and anode material, electrolyte composition and temperature, is usually expressed for normal temperature condition of 25°C,
- *Open circuit voltage*, defined for unloaded case, and this voltage is close to the theoretical voltage,
- *Nominal voltage*, defined as the mean operating voltage,
- *Operating voltage*, defined as the actual amount of voltage when operating a loaded battery (always lower than the open circuit voltage because internal resistance and other effects),
- *Cut–off voltage*, defined as voltage at the end of the battery discharge,

- *Capacity*, usually in ampere–hours is the amount of charge that the battery can effectively deliver to the load for a given discharge current,
- *Operating* and *storage temperature* in °C,
- *C–rating* that defines the charging or discharging current that reflects the charging and discharging time of a fully charged battery over a period of one hour,
- *Internal resistance* or *short circuit resistance* differs for charging and discharging state, and also depends on the state of charge of the battery. Also, as the internal resistance increases, the efficiency of the battery decreases and thermal stability is reduced because more energy is converted into heat,
- *Battery efficiency*, usually defined energy efficiency or Coulomb efficiency (charge eff.),
- *State of charge* (SoC), defined as dimensionless coefficient that describes level of accumulated electric charge in the battery, also Depth of Discharge (DoD) describes battery discharge and is defined as $DoD = 1 - SoC$,
- *Energy Density* defined as nominal battery energy per unit volume (volumetric), or per unit mass (specific),
- *Cycle life*, defined as the number of cycles (charges / discharges) that a battery can withstand before the capacity falls below 80% of the nominal capacity is defined as the battery life cycle,
- *Self–discharge effect*, defined as the amount of charge lost by self–discharge in relation to the nominal charge (at storage temperature), usually in % of SoC per month,
- *Response time* defined for the nominal load change and represents the voltage dynamics when a current step is applied.

There are many different models of electrochemical batteries in the literature, where individual models have been developed for the purpose of describing battery charging and discharging, power losses, thermal effects, battery ageing and other effects. The most commonly used and simplest approach is the one based on so–called Rint model [159] (see Figure 3.37).

In this model the ideal voltage source defines the battery open–circuit voltage. Both internal resistance R_b and open–circuit voltage V_{oc} are dependent on the SoC, State of

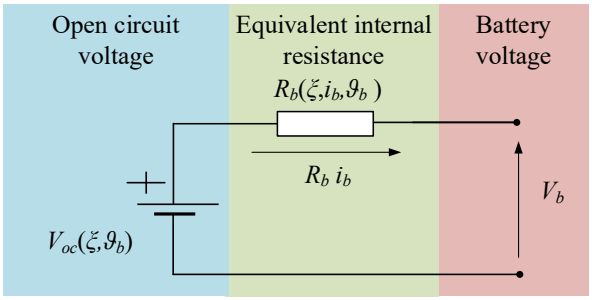

Figure 3.37: Electrochemical battery simplified equivalent electrical circuit model

Health (SoH) and temperature ϑ_b defines the terminal voltage. Load current i_b is positive value at discharging and negative value at charging:

$$v_b = v_{oc} - R_b i_b \tag{3.86}$$

In order to include the dynamic effects of the electrochemical battery terminal voltage V_b, the so–called Thevenin model (which is both reasonably simple and accurate) can be used. The proposed equivalent electrical circuit battery model (see Figure 3.38) consists of a battery series resistance, electrolyte polarization effects, and open–circuit voltage source, thus it is possible to formulate the battery terminal voltage in the following way:

$$\frac{dv_p}{dt} = -\frac{1}{R_p C_p} v_p + \frac{1}{C_p} i_b \tag{3.87}$$

$$v_b = v_{oc} - v_p - i_b R_b \tag{3.88}$$

In the Laplace s–domain model can be defined as [70]:

$$v_b\,(s) = i_b\,(s)\,R_b + \frac{R_p i_b}{T_p s + 1} + V_{oc} \tag{3.89}$$

with time constant defined as $T_p = R_p C_p$. All defined parameters are being dependent on the battery SoC, which is defined as:

$$\xi = SoC = 1 - \frac{Q_{ext}}{C_{tot}} \tag{3.90}$$

where Q_{ext} is the overall discharged battery charge, and C_{tot} is the battery charge capacity. Moreover, the polarization and battery resistive effects are dependent on the battery current and may also exhibit notable dependence on battery operating temperature [160].

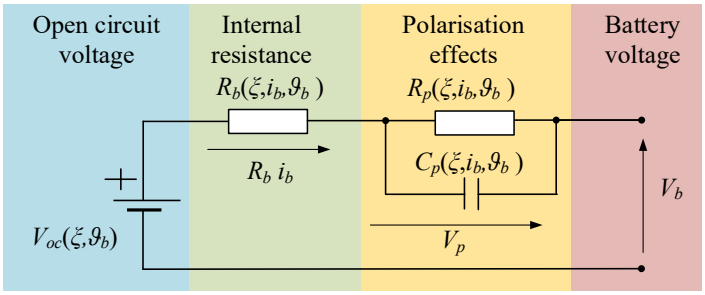

Figure 3.38: Electrochemical battery equivalent electrical circuit model (Thevenin model)

3.7. DC-DC converters

DC–DC converters are power electronics devices that convert DC voltage input from one level to another, while being controlled by a dedicated controller using both feedforward and feedback measurement signals (Figure 3.39). They are also referred as switching converters, because of the semiconductor elements (i.e. diodes and MOS–FET transistors) being exclusively operated as switches.

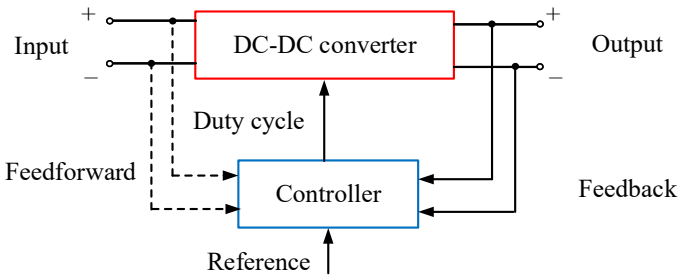

Figure 3.39: Principal representation of DC–DC power converter control system

DC–DC converter alternates (switches) between two sides of the circuit dependant on the control signal [161]. The output voltage can be controlled by varying (modulating) the width of the switch-chopped input pulse, which is basically controlling the duration of the time the electronic switches are open or closed within one cycle at the operating frequency. This principle is also known as PWM [162], and is illustrated by the switching signals in Figure 3.40.

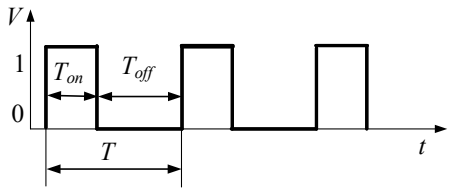

Figure 3.40: Illustration of DC-DC converters switching signal

The three basic configurations of the single–quadrant DC–DC power converters (i.e. buck, boost, and buck–boost) and their transfer characteristics are illustrated in Figure 3.41. The relationship between the input and output voltages is defined by the converter configuration and by the value of duty cycle d according to expressions summarized in Table 3.4. Duty cycle D is defined as a ratio of ON–state time interval T_{on} of the switching element and the converters switching period T (see Figure 3.40):

$$D = \frac{T_{on}}{T} \Rightarrow \begin{cases} T_{on} = TD \\ T_{off} = T(1-D) \end{cases} \tag{3.91}$$

where T is the switching period, T_{on} is time interval of switch ON–state, and the T_{off} is time interval of switch OFF–state. For the above switching phenomena, the switching period and the complementary duty cycle $D^{'}$ are defined as:

$$T = T_{on} + T_{off} \tag{3.92}$$

$$D^{'} = (1-D) \tag{3.93}$$

The power converter output voltage increases with the increase of the duty cycle D for all three configurations, but with different relation between the output and input voltages. Thus, the output voltage is: (i) always lower than the input voltage for the case of buck converter, (ii) always higher than the input voltage for the case of boost converter, and (iii) of the opposite sign with respect to input voltage for the case of buck–boost converter. Note that the output voltage magnitude of buck–boost converter can be lower and higher than the input voltage, depending on the duty cycle (see Figure 3.41).

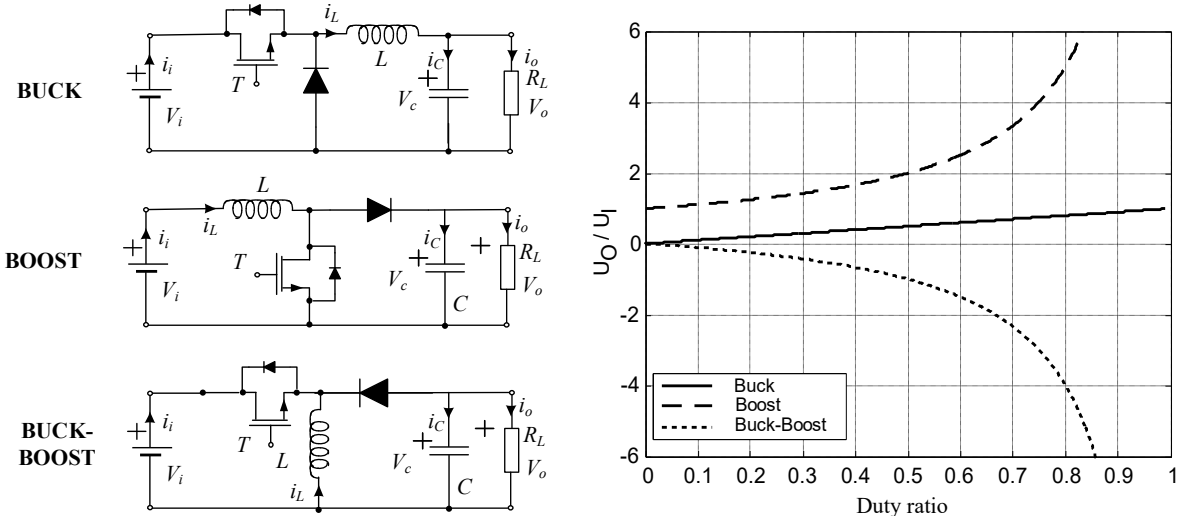

Figure 3.41: Three basic DC–DC power converter topologies and their steady–state transfer characteristics

Table 3.4: DC-DC converters transfer functions equations

Converter topology	V_o/V_i
Buck	D
Boost	$\frac{1}{(1-D)}$
Buck–Boost	$\frac{-D}{(1-D)}$

The method of averaging with small signal approximation is used herein to characterize the transfer functions of DC–DC power converters: line to output and duty ratio to output of converters operated in the continuous conduction modes. During each switching period the converter is described by two circuit topologies defined by the state of switch. One topology is in place when the transistor switch is ON and another is in place when the switch is OFF [162,163] During each of these two intervals, the converter can be described by a set of linear, time–invariant differential equations for ON and OFF time interval, respectively.

$$\mathbf{A}=D\mathrm{A}_1+D'\mathrm{A}_2 \tag{3.94}$$

$$\mathbf{B}=D\mathrm{B}_1+D'\mathrm{B}_2 \tag{3.95}$$

$$\mathbf{C}=D\mathrm{C}_1+D'\mathrm{C}_2 \tag{3.96}$$

The derivation of the state equations for the DC–DC converters under the continuous time domain is explained as follows. The semiconductor switch is turned on and off by a sequence of pulses with a constant switching frequency, . The inductance currents and capacitance voltages are state variables. For the given duty cycle for the k–th period, the systems are given by the following set of state space equations in the continuous–time domain:

$$\dot{\mathbf{x}} = \begin{cases} \mathbf{A}_1\mathbf{x}+\mathbf{B}_1\mathbf{u} & \text{for ON period} \\ \mathbf{A}_2\mathbf{x}+\mathbf{B}_2\mathbf{u} & \text{for OFF period} \end{cases} \tag{3.97}$$

The derivation of individual DC–DC power converter dynamic models is based on the following assumptions:

- converters operate in continuous conduction mode,
- output capacitor has enough capacitance to supply power to the load (a simple resistance) without any significant variation in its voltage,
- voltage drop across the diode when forward biased is zero,

- commutation losses are neither present in the semiconductor switch nor in the diode,
- small signal equivalent circuit is used to derive equations of the s–domain transfer function models,
- capacitor equivalent series resistance (ESR), inductor ohmic resistance and switching losses are neglected in the analysis.

Based on derived state equations for ON and OFF periods, the average system can be defined as:

$$\dot{\mathbf{x}} = [D\mathbf{A}_1 + (1-D)\mathbf{A_2}]\,\mathbf{x} + [D\mathbf{B}_1 + (1-D)\mathbf{B}_2]\,\mathbf{u} \tag{3.98}$$

Next, in order to derive a transfer function of converter, system has to be linearised around equilibrium point. To that end, a small perturbations are introduced:

$$D = \bar{D} + d \tag{3.99}$$

$$\mathbf{x} = \bar{\mathbf{x}} + \mathbf{x}_p \tag{3.100}$$

where d is defined as a small signal perturbation of duty ratio D, $\mathbf{x}_p$ is the small signal perturbation of state variable vector $\mathbf{x}$, $\bar{D}$ is steady state component of D and $\bar{\mathbf{x}}$ is steady state component of $\mathbf{x}$. By using above equation, the average system is transformed by utilising the sum of steady state and perturbation into:

$$\dot{\bar{\mathbf{x}}} + \dot{\mathbf{x}}_p = \left[\left(\bar{D}+d\right)\mathbf{A}_1 + (1-\bar{D}-d)\mathbf{A_2}\right][\bar{\mathbf{x}} + \mathbf{x}_p] + \left[\left(\bar{D}+d\right)\mathbf{B}_1 + (1-\bar{D}-d)\mathbf{B}_2\right]\mathbf{u} \tag{3.101}$$

If a small signal is considered to be zero, then following equation is obtained after rewriting:

$$\dot{\bar{\mathbf{x}}} = \left[\bar{D}\mathbf{A}_1 + (1-\bar{D})\mathbf{A_2}\right]\bar{\mathbf{x}} + \left[\bar{D}\mathbf{B}_1 + (1-\bar{D})\mathbf{B}_2\right]\mathbf{u} \tag{3.102}$$

Furthermore, after inserting above equation into equation with sum of steady state and perturbations, and neglecting the high order products, it is possible to express linearised equation as follows:

$$\dot{\mathbf{x}} = \mathbf{A}^*\mathbf{x} + \mathbf{B}^*\mathbf{u} \tag{3.103}$$

where matrix $\mathbf{A}^*$ (average of matrices $\mathbf{A}_1$ and $\mathbf{A}_2$) is defined as:

$$\mathbf{A}^* = \bar{D}\mathbf{A}_1 + (1-\bar{D})\mathbf{A_2} \tag{3.104}$$

And matrix $\mathbf{B}^*$ (on and off state difference) is defined as:

$$\mathbf{B}^* = [\mathbf{A}_1 - \mathbf{A_2}]\,\bar{\mathbf{x}} + [\mathbf{B}_1 - \mathbf{B}_2]\,\mathbf{u} \tag{3.105}$$

Finally, transfer functions can be obtained by Laplace transform, using the following:

$$G(s) = \frac{\mathbf{x}_p}{d} = [s\mathbf{I} - \mathbf{A}^*]^{-1}\mathbf{B}^* \tag{3.106}$$

3.7.1. Buck converter

Buck converters in a standard form are non–isolated switched–mode step–down DC–DC converters. The DC input voltage at the source is periodically "chopped" (switched ON – OFF) using an electronic switch operating at a set frequency, and the resulting pulsated signal is filtered out and thus the load is operated at an average voltage value that is less than the input voltage. Buck converters use a transistor–diode switching network, as shown in Figure 3–42. This configuration employs the transistor T as the main switch and the diode D as the freewheeling path for the inductor current [163]. The output voltage level at the load is controlled by varying (modulating) the width of the switch chopped input pulse, which is basically controlling the duration of the time the electronic switches, MOS-FETs, are ON or OFF in one cycle of the operating frequency; known as pulse–width modulation.

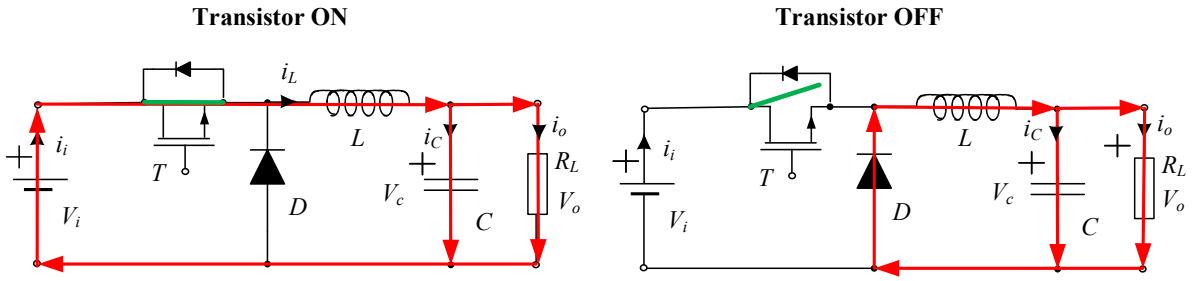

Figure 3.42: Buck converter on and off states

By applying Kirchhoff laws to the Buck converter circuit (see Figure 3.42), the following equations are obtained for the ON and OFF state, respectively:

$$\frac{di_L}{dt} = \frac{V_i - V_o}{L}, \quad \frac{dV_o}{dt} = \frac{i_L}{C} - \frac{V_o}{R_L C} \tag{3.107}$$

$$\frac{di_L}{dt} = -\frac{V_o}{L}, \quad \frac{dV_c}{dt} = \frac{i_L}{C} - \frac{V_c}{R_L C} \tag{3.108}$$

Equations above can be given in the following state space form:

$$\begin{bmatrix} \dot{i}_L \\ \dot{V}_o \end{bmatrix} = \begin{bmatrix} 0 & \frac{-1}{L} \\ \frac{1}{C} & \frac{-1}{R_L C} \end{bmatrix} \begin{bmatrix} i_L \\ V_o \end{bmatrix} + \begin{bmatrix} \frac{1}{L} \\ 0 \end{bmatrix} V_i \tag{3.109}$$

$$\begin{bmatrix} \dot{i}_L \\ \dot{V}_o \end{bmatrix} = \begin{bmatrix} 0 & \frac{-1}{L} \\ \frac{1}{C} & \frac{-1}{R_L C} \end{bmatrix} \begin{bmatrix} i_L \\ V_o \end{bmatrix} + \begin{bmatrix} 0 \\ 0 \end{bmatrix} V_i \tag{3.110}$$

By combining state space ON and OFF models by using equation for averaged system, and substituting $d' = (1–d)$ the linearised averaged model suitable for subsequent analysis

is given as follows:

$$\begin{bmatrix} \dot{i}_{L,p} \\ \dot{V}_{o,p} \end{bmatrix} = \begin{bmatrix} \dot{x}_1 \\ \dot{x}_2 \end{bmatrix} = \begin{bmatrix} 0 & \frac{-1}{L} \\ \frac{1}{C} & \frac{-1}{R_L C} \end{bmatrix} \begin{bmatrix} x_1 \\ x_2 \end{bmatrix} + \begin{bmatrix} \frac{V_i}{L} \\ 0 \end{bmatrix} d \tag{3.111}$$

Finally, the small–signal mode control to output transfer functions are obtained as follows:

$$G_1(s) = \frac{V_{o,p}}{d} = \frac{V_i}{LC} \frac{1}{s^2 + \frac{s}{R_L C} + \frac{1}{LC}} \tag{3.112}$$

$$G_2(s) = \frac{i_{L,p}}{d} = \frac{V_i}{L} \frac{s + \frac{1}{RC}}{s^2 + \frac{s}{RC} + \frac{1}{LC}} \tag{3.113}$$

3.7.2. Boost converter

The DC–DC converter that powers an output load with a voltage level larger than the input source is called the boost (step–up) converter. This boost in the output voltage is achieved by placing the inductor before the switching network as in Figure 3.43.

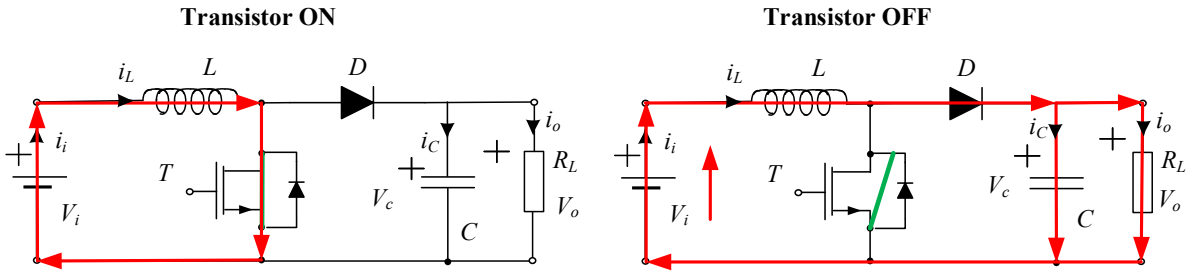

Figure 3.43: Boost converter on and off states

The analysis of the boost converter follows the same procedure as in the case of buck converter. Equations for ON state and OFF state, are given respectively (accordingly to Figure 3.43):

$$\frac{di_L}{dt} = \frac{V_i}{L}, \quad \frac{dV_o}{dt} = -\frac{V_o}{R_L C} \tag{3.114}$$

$$\frac{di_L}{dt} = \frac{V_i}{L} - \frac{V_o}{L}, \quad \frac{dV_o}{dt} = \frac{i_L}{C} - \frac{V_o}{R_L C} \tag{3.115}$$

or, written in state space formulation:

$$\begin{bmatrix} \dot{i}_L \\ \dot{V}_o \end{bmatrix} = \begin{bmatrix} 0 & 0 \\ 0 & \frac{-1}{R_L C} \end{bmatrix} \begin{bmatrix} i_L \\ V_o \end{bmatrix} + \begin{bmatrix} \frac{1}{L} \\ 0 \end{bmatrix} V_i \tag{3.116}$$

$$\begin{bmatrix} \dot{i}_L \\ \dot{V}_o \end{bmatrix} = \begin{bmatrix} 0 & -\frac{1}{L} \\ \frac{1}{C} & \frac{-1}{R_L C} \end{bmatrix} \begin{bmatrix} i_L \\ V_o \end{bmatrix} + \begin{bmatrix} \frac{1}{L} \\ 0 \end{bmatrix} V_i \tag{3.117}$$

By combining state space ON and OFF models by using equation for averaged system, and substituting $d' = (1–d)$ the linearised averaged model suitable for subsequent analysis is given as follows:

$$\begin{bmatrix} \dot{i}_{L,p} \\ \dot{V}_{o,p} \end{bmatrix} = \begin{bmatrix} \dot{x}_1 \\ \dot{x}_2 \end{bmatrix} = \begin{bmatrix} 0 & \frac{-1+D}{L} \\ \frac{1-D}{C} & \frac{-1}{R_L C} \end{bmatrix} \begin{bmatrix} x_1 \\ x_2 \end{bmatrix} + \begin{bmatrix} \frac{V_i}{L} \\ -\frac{i_L}{C} \end{bmatrix} d \tag{3.118}$$

Transfer functions are obtained as:

$$G_1(s) = \frac{V_{o,p}}{d} = \frac{V_i}{R_L C(1-d)^2} \frac{\frac{R_L(1-d)^2}{L} - s}{s^2 + \frac{s}{R_L C} + \frac{(1-d)^2}{LC}} \tag{3.119}$$

$$G_2(s) = \frac{i_{L,p}}{d} = \frac{V_i}{L(1-d)} \frac{s + \frac{2}{R_L C}}{s^2 + \frac{s}{R_L C} + \frac{(1-d)^2}{LC}} \tag{3.120}$$

3.7.3. Analysis of parallel operation of DC–DC converters

The general idea for parallelisation of DC-DC converters is to combine several lightweight and inexpensive off–the–shelf DC–DC power converters within a parallel network, so that their total combined power output equals or exceeds the required power rating of the propulsion system. However, a problem arises due to dispersion of output characteristics between the production power converter units, so that during parallel operation, even the slightest output voltage difference can result in extreme output currents flowing from one power supply unit into the another. Moreover, many power supply data-sheets will specify the device's voltage set–point accuracy. A very common figure for set-point accuracy is somewhere around ±5%, which for a 24 V power supply may result in output voltage being anywhere between 23.52 V and 24.48 V. In example, it is possible to conduct a circuit analysis of four identical 24 V / 800 W power sources, with outputs connected in parallel to feed a certain resistive load. Figure 3.44 shows a generalized model of parallel connection of DC–DC converters outputs, where V_1, V_2, V_3, V_4 are the nominal open–circuit voltages of independent power supplies, $R_{o1}, R_{o2}, R_{o3}, R_{o4}$ are their output impedances (resistances) respectively, and RL is the load resistance.

The analysis of DC electrical circuit by means of superposition principle reveals that load current is the sum of currents that come from each of the independent power sources. In particular, the following relationships are obtained for load voltage V_{RL} and current i_L:

$$V_{RL} = \frac{V_1 G_{o,1} + V_2 G_{o,2} + V_3 G_{o,3} + V_4 G_{o,4}}{G_{o,1} + G_{o,2} + G_{o,3} + G_{o,4} + \frac{1}{R_L}} \tag{3.121}$$

$$i_{RL} = \frac{V_{RL}}{R_L} = \frac{1}{R_L} \frac{V_1 G_{o,1} + V_2 G_{o,2} + V_3 G_{o,3} + V_4 G_{o,4}}{G_{o,1} + G_{o,2} + G_{o,3} + G_{o,4} + \frac{1}{R_L}} \tag{3.122}$$

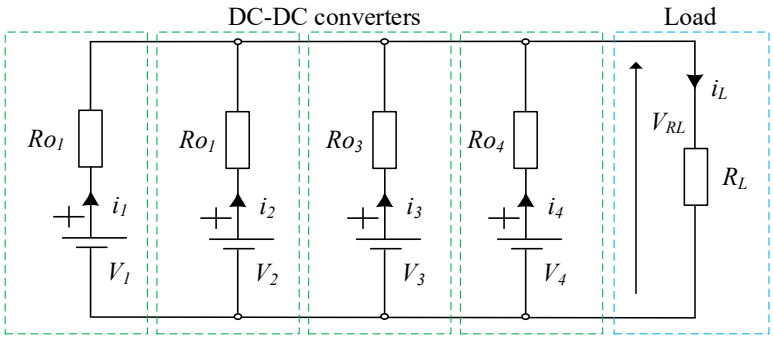

Figure 3.44: Equivalent model of four DC–DC power converter connected in parallel with load.

where $G_{o,i} = 1/R_{o,i}, (i = 1, 2, 3, 4)$ are the voltage source internal conductances, corresponding to reciprocal values of internal resistances. Using this notation, output currents (i_1, i_2, i_3 and i_4) of individual voltage sources may be expressed as:

$$i_m = \left[V_m - \frac{\sum_{i=1}^{4} V_i G_{o,i}}{\sum_{i=1}^{4} G_{o,i} + \frac{1}{R_L}} \right] G_{o,m} \tag{3.123}$$

The above expression can be used to analyse the sensitivity of individual voltage source current to variations of voltage source parameters, i.e. open circuit voltage V_m and internal resistance R_{om} (with $m = 1, 2, 3, 4$ denoting individual voltage source). In particular, the output current variations Δi_m for each voltage source can be expressed in the following form:

$$\Delta i_m = S_{V,m} \Delta V_m + S_{G,m} \Delta G_{o,m} \tag{3.124}$$

with the so–called sensitivity gains (sensitivity functions) $S_{V,m}$ and $S_{G,m}$ defined as:

$$S_{V,m} = V_{RL} = \left[1 - \frac{G_{o,m}}{\sum_{i=1}^{4} G_{o,i} + \frac{1}{R_L}} \right] G_{o,m} \tag{3.125}$$

$$S_{G,m} = V_m - \frac{\left(\sum_{i=1}^{4} V_i G_{o,i} + V_m G_{o,m} \right) \left(\sum_{i=1}^{4} G_{o,i} + \frac{1}{R_L} \right) - G_{o,m} \sum_{i=1}^{4} V_i G_{o,i}}{\left(\sum_{i=1}^{4} G_{o,i} + \frac{1}{R_L} \right)^2} \tag{3.126}$$

Assuming load resistance R_L relatively large compared to the internal resistances of individual voltage sources (R_{o1}, R_{o2}, R_{o3} and R_{o4}), these sensitivity functions can be simplified as follows:

$$S_{V,m} = \left[1 - \frac{G_{o,m}}{\sum_{i=1}^{4} G_{o,i}} \right] G_{o,m} \tag{3.127}$$

$$S_{G,m} = V_m - \frac{\left(\sum_{i=1}^{4} V_i G_{o,i} + V_m G_{o,m}\right) \sum_{i=1}^{4} G_{o,i} - G_{o,m} \sum_{i=1}^{4} V_i G_{o,i}}{\left(\sum_{i=1}^{4} G_{o,i}\right)^2} \tag{3.128}$$

For example, if internal resistances of all voltage sources are the same $R_{o1} = R_{o2} = R_{o3} = R_{o4} = 25\text{m}\Omega$, and if only one voltage source exhibits a 5% variation of the open–circuit voltage with respect to the nominal value 24 V, its output current would be characterised by a variation of $\Delta i_m = 36$ A in that case. That is, this voltage source may be additionally loaded (output current would increase) in the case of open–circuit voltage increase, or it may behave as a current sink if its open–circuit voltage is decreased (current may start flowing into the voltage source). These situations should be avoided by means of additional hardware and control measures.

3.8. Rectifier

A rectifier is an electrical device used for conversion of alternating current that reverses flow direction to direct current that flows in single direction. Rectifier circuits may be realised as single–phase (for the low power applications) or multi–phase (for industrial applications). In a most basic form, rectifier can be classified as:

- Uncontrolled, wherein the output voltage is dependent only on the input voltage and cannot be controlled by external means,
- Controlled, wherein the output voltage is dependent both on input voltage and control signal, thus it can be varied by external means.

For the uncontrolled rectifiers, two topologies are dominant: the half–wave rectification where the positive or negative half of the AC waveform is passed while the other half is blocked (typically used in single–phase applications) and full–wave rectification where the whole input waveform is transferred to the output, as system converts both polarities of the input waveform to a pulsating DC voltage. In the case of half–wave rectifier system, the mean output voltage is lower when compared to the full wave rectification system. Furthermore, rectifiers yield a pulsating direct current waveform, where half–wave rectifiers produce more ripple than full–wave rectifiers, and substantially more filtering is needed to eliminate harmonics of the AC frequency from the output in the former case (Figure 3.45).

Controlled rectifiers are obtained when diodes are replaced by thyristors wherein the output voltage can be varied by changing the firing angle of the thyristor. The thyristor is activated by applying a short–duration pulse to its gate terminal and it is deactivated

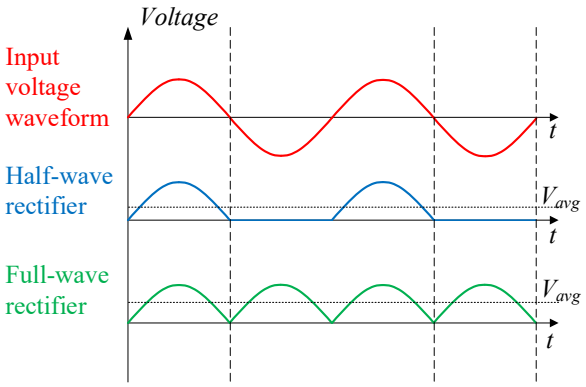

Figure 3.45: Half and full wave rectifier waveforms

due to line communication. By changing gate triggering signal angle, it is possible to control the average voltage output (Figure 3.46).

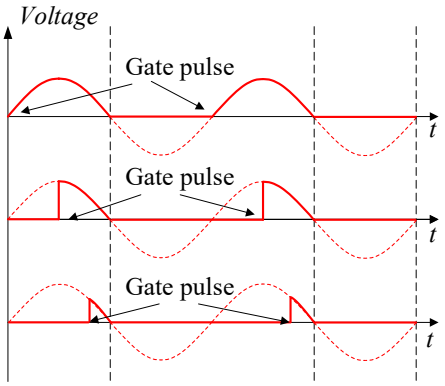

Figure 3.46: Thyristor based rectifier waveforms

3.8.1. Three phase full-bridge diode rectifier

Rectifiers are designed using fundamental rectifying components, i.e. semiconductor diodes. The diode is two terminal nonlinear device whose current–voltage characteristic, besides exhibiting non–linear behaviour, is also polarity dependent. The non–linearity, and polarity characteristics of the diode make it an ideally suited passive rectifier device albeit at the expense of added complexity of circuit design and analysis. The basic circuit symbol of the diode and operating principle are shown in Figure 3.47 Depending on the polarity of the voltage V_d can be:

- Forward Biased, $(V_d > 0)$, Anode voltage is greater than the Cathode voltage, or
- Reverse Biased, $(V_d < 0)$, Cathode voltage is greater than the Anode voltage.

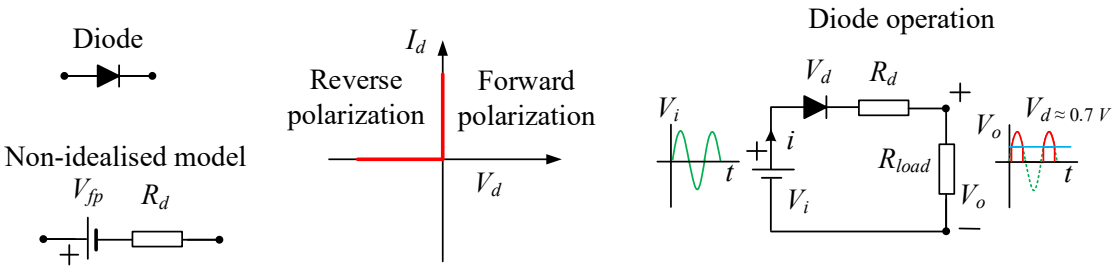

Figure 3.47: Diode circuit model

A three–phase diode rectifier converts a three–phase AC voltage at the input to a DC voltage at the output. Form topology on Figure 3.48, diodes 1,3 and 2,4 represent a full-wave rectifier between phases a and b, while diodes 3, 5 and 4 and 6 represent a full-wave rectifier between phases b and c and finally, diode pairs 5, 1 and 6, 2 represent a full-wave rectifier between phases C and A. Furthermore, diodes 1, 3 and 5 feed the positive rail and diodes 2, 4 and 6 feed the negative rail. The conduction of diodes consists of matching pairs that changes every 60 electrifal degrees in a following pattern: 1 and 2, 1 and 6, 3 and 6, 3 and 4, 5 and 4, 5 and 2 as shown in Figure 3.48.

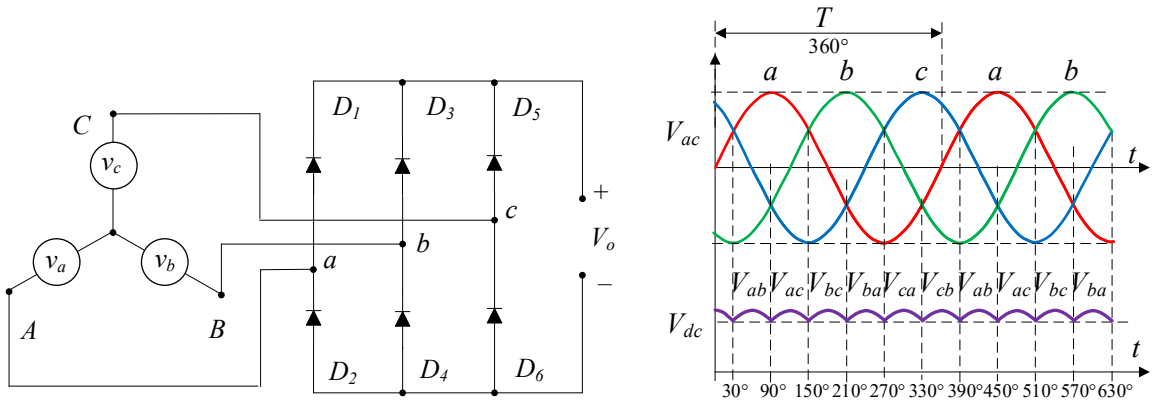

Figure 3.48: Three phase rectifier schematics and waveforms

Input voltages to rectifier are defined as :

$$V_1 = V_s \sin \omega t,\ V_2 = V_s \sin(\omega t - 120°),\ V_3 = V_s(\omega t - 240°) \tag{3.129}$$

Average output voltage for sinusoidal input (without inductance on the AC–side) is given as:

$$V_{o,1} = \frac{3\sqrt{3}}{\pi} V_s \tag{3.130}$$

$V_{o,1}$ consideres no conduction losses. Simplified model of uncontrolled, three–phase rectifier with voltage drop and resistance across conductive pair of diodes can be aproxi-

mated as:

$$V_o = V_{o,1} - 2V_d - 2ir_d \tag{3.131}$$

where $V_{o,1}$ is average output voltage without losses, V_d is forward bias voltage drop, ir_d is voltage drop due diode resistance and is V_o average voltage output of model.

3.9. Propellers

The classic propeller motion theory called actuator disc theory, sometimes also referred to as simplified propeller theory or momentum theory provides basic concepts of propeller performance. More detail about this topic is given thoroughly in references [164–167].

The propeller thrust force is typically expressed as:

$$F_T = k_T \rho \omega^2 D^4 \tag{3.132}$$

where k_T is called the thrust coefficient and in general is a function of propeller design, ρ is medium density, ω is angular velocity and D is propeller diameter. For practical purposes with neglecting medium density change with altitude (low altitude flights), constants can be lumped into single thrust constant and the above expression is simplified:

$$F_T = K_T \omega^2 \tag{3.133}$$

Since torque is a force multiplied by the force moment arm length, it can be written as follows:

$$Q_T = k_Q \rho \omega^2 D^5 \tag{3.134}$$

where $k_Q$is called the torque coefficient and in general is a function of propeller design, ρ is medium density, ω is angular velocity and D is propeller diameter. For practical purposes constants and by neglecting medium density change, constants can be lumped into a single thrust–related constant and the expression is simplified to:

$$Q_T = K_Q \omega^2 \tag{3.135}$$

3.10. Comprehensive propulsion model

A comprehensive hybrid propulsion model is built based on the known interconnections of individual sub–models of constituent components of the hybrid power supply and the aircraft propulsion system, that are connected into a functional ensemble. The purpose of such model is to facilitate the systematic simulation of the dynamic states of the overall propulsion system, as well as to analyse its power losses in order to estimate the overall hybrid propulsion system efficiency. More precisely, based on the particular configuration

of such a model, it is possible to predict the behaviour of the hybridised propulsion system under different operating conditions, compare the advantages and disadvantages of different types of propulsion, predict its energy consumption and more. The fidelity of such a model depends on the detail of each individual propulsion system sub-model and manifests itself as a trade–off between accuracy and reasonable execution speed on the target computer hardware.

Using the previously developed hybrid propulsion component sub–models in Chapter 3, it is possible to assemble the comprehensive propulsion models for the two considered topologies presented in Chapter 3. The first topology (IC engine + Generator with direct engine–based DC bus voltage control) defined in Chapter 5, is illustrated by the principal block diagram representation in Figure 3.49. The model consists of the ICE generator set (with non-linear dynamics of ICE), DC–bus dynamics and non-linear battery dynamics model, controlled by the target bus controller which directly commands the ICE throttle angle reference.

Similarly, it is possible to obtain a comprehensive model for the second considered topology (ICE + Generator + parallel DC–DC converters) as shown in Figure 3.50. This model includes all components from first topology and is extended by the parallel DC–DC converters power sharing topology with the main controller of the engine–generator set being used for ICE throttle control. In this way engine variables (torque and speed) can be effectively decoupled from the DC bus variables (voltage and current), which are controlled by two separate controllers.

By using the previously recorded fuel consumption maps of the ICE and the battery SoC maps (Chapter 4) it is possible to estimate the hybrid power system fuel consumption for different load states. Specifically, for an arbitrary flight task, it would be possible to estimate the flight endurance and energy/fuel consumption by using an appropriate model of the aircraft propulsor system (motors, motor drivers and propeller sets) together with the aircraft flight dynamics model, it is possible to extract individual rotor angular speeds and torques, and thus calculate the electrical load to the hybrid power supply system. It would then be possible to estimate the overall energy required and instantaneous power consumption of the aircraft by using the comprehensive propulsion models outlined above.

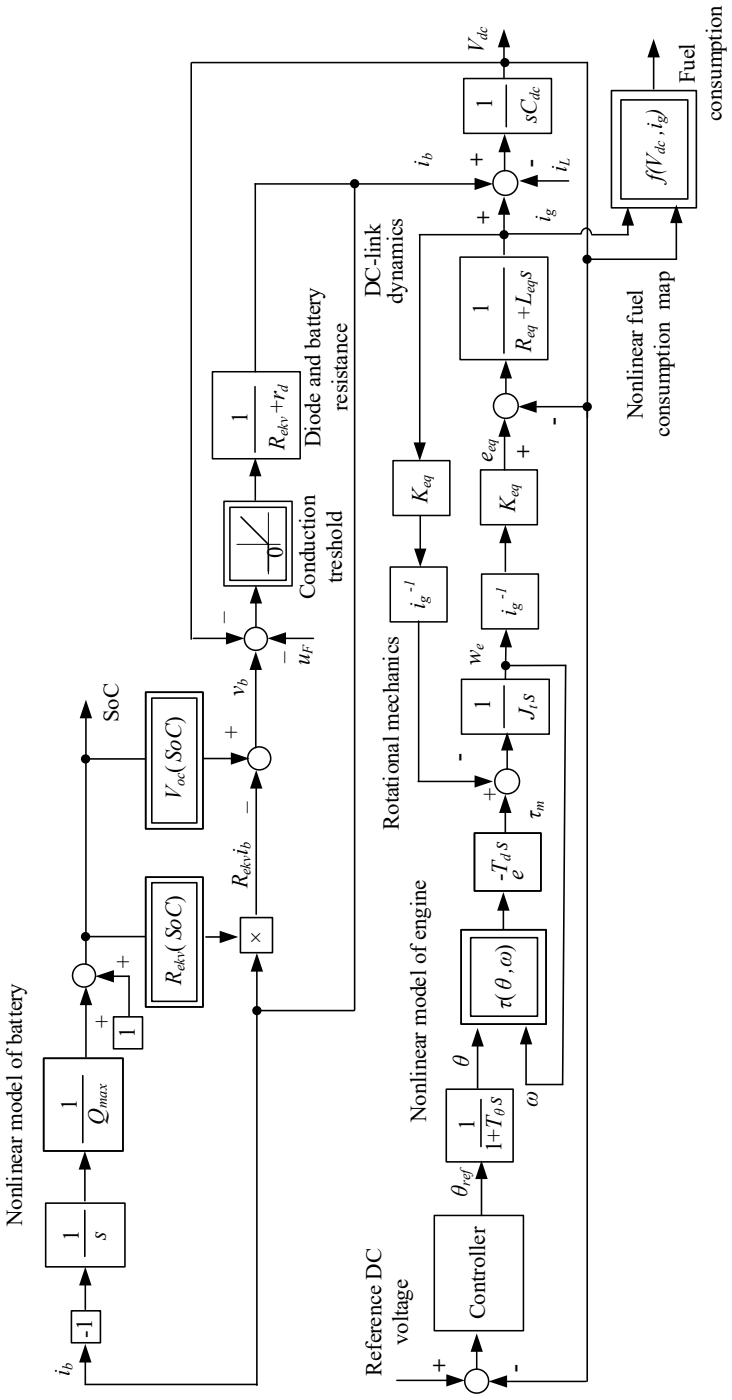

Figure 3.49: Comprehensive propulsion model for first topology

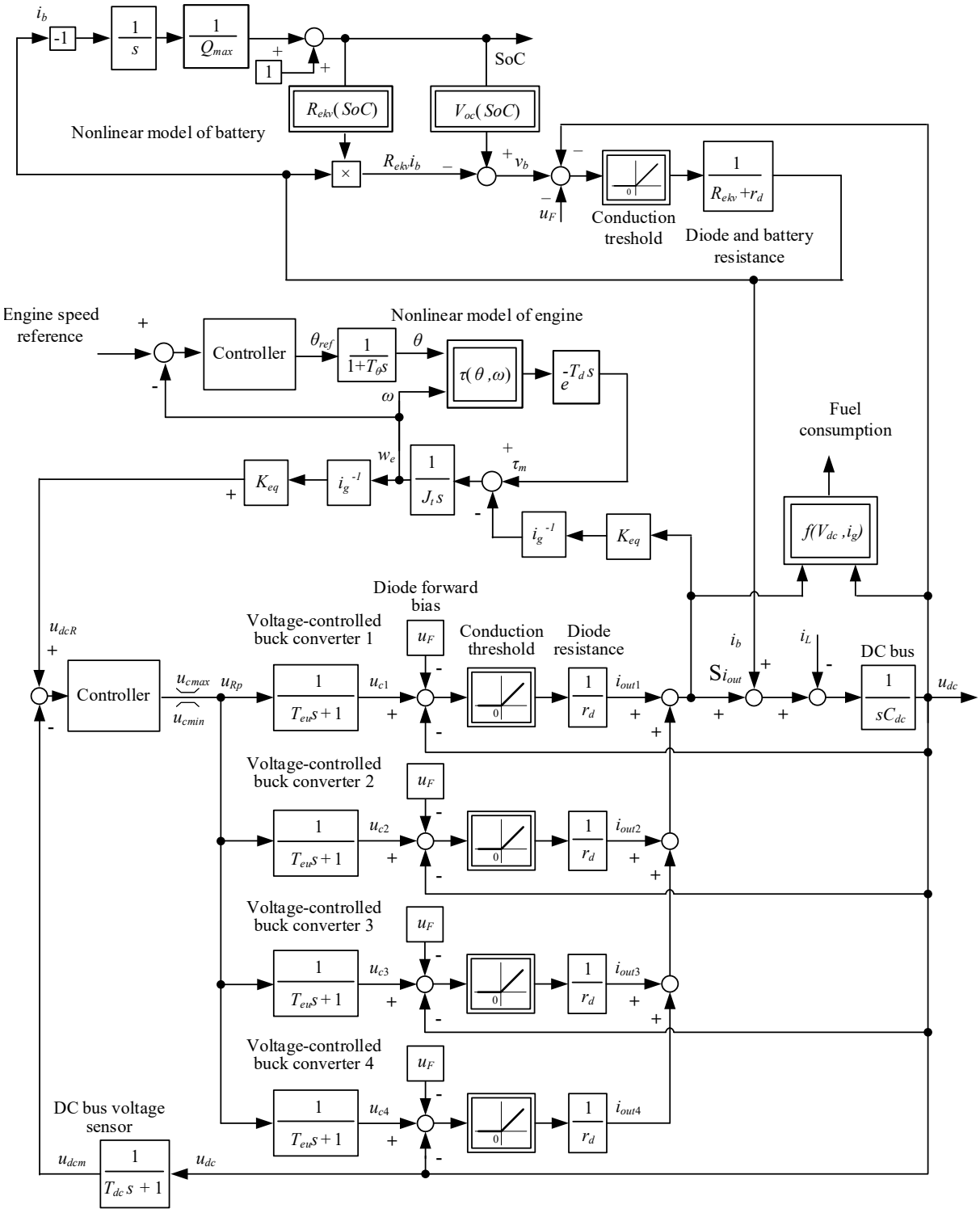

Figure 3.50: Comprehensive propulsion model for second topology

4 Hybrid propulsion identification and simulation

This chapter presents the process model identification and estimation of parameters used in mathematical models of hybrid propulsion system (as defined in Chapter 3), comprising of an internal combustion engine, electricity generator, DC–DC converters and battery that jointly supply the propeller drives through the common DC bus.

4.1. Two-stroke spark ignited Internal Combustion Engine (ICE)

For the purpose of design and construction of the experimental hybrid power unit, the first choice was a Titan ZG 45PCI (see Figure 4.1) engine by Toni Clark [168, 169]. This engine is based on a Zenoah G450PU unit, equipped with an aluminium–crankcase two–stroke engine. The engine is equipped with an embedded microprocessor–controlled spark ignition system. It is usually used within aerobatic airplane models with wingspans of up to 2 m. Technical specifications of the engine are given in Table 4.1.

Upon conducting preliminary tests with Titan ZG 45PCI it was clear that engine possesses a low internal mass, lacks starting rope and impeller assembly for cooling. It was very difficult to keep this engine below 100 °C because when engine is used on a model air-plane the propeller also cools engine down. Furthermore, low inertial mass causes power delivered to the shaft is affected with stroke operation of engine. As a result, shaft torque is not near constant and it led to damaged or broken shaft couplings and damage to the bearings of both IC motor and generator. Because of aforementioned reasons, the Zenoah G320 RC (see Figure 4.2) [170, 171] engine was selected. It is usually used as engine for the remote–controlled car models (scale 1:5). Technical specifications of the engine are given in Table 4.1. Dimensions, power and torque output curves are provided by the supplier and shown in Figure 4.3

As presented in Chapter 3, the dominant steady–state behaviour and dynamics of the ICE operation are typically modelled by using the so–called Mean–Value Engine Model (MVEM) approach [140, 141]. Figures 4.4a and 4.4b compare the possible two

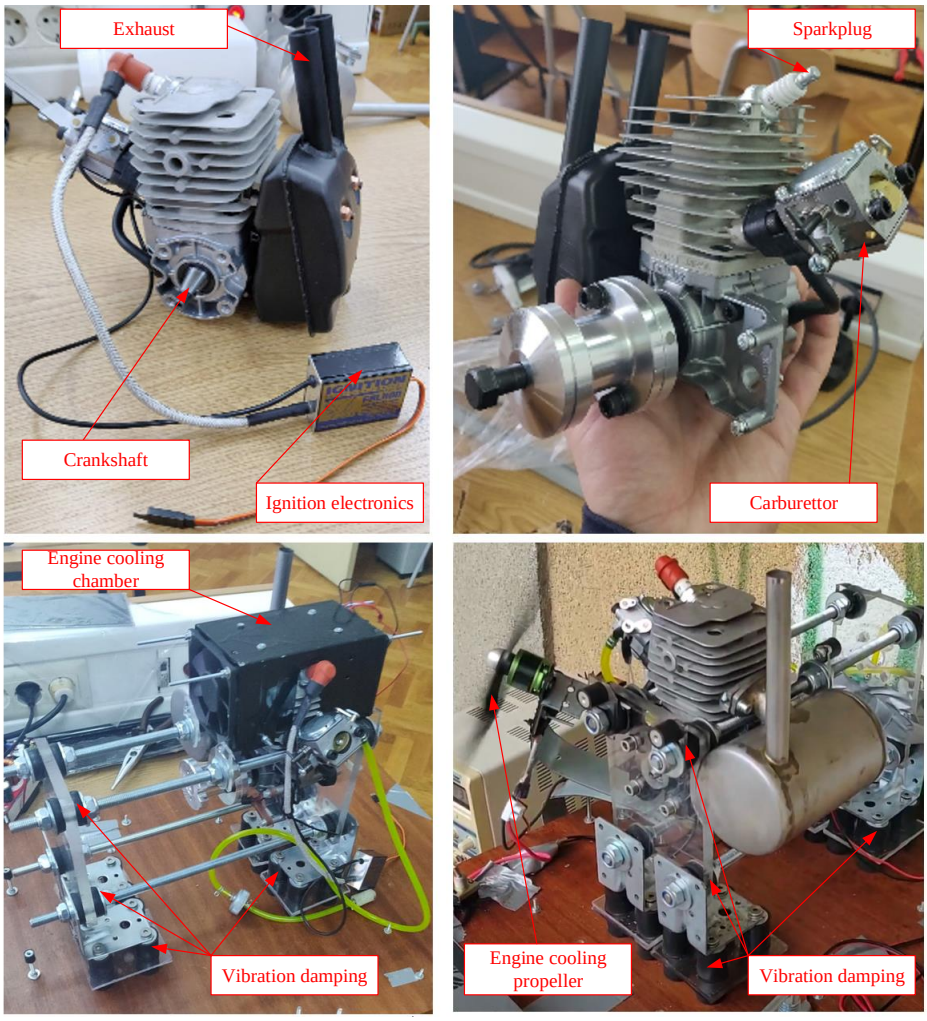

Figure 4.1: Photographs of Titan ZG45 engine and abandoned test bench concepts

realisations of the MVEM model, which have been considered in this work. In particular, the first case (Figure 4.4a) corresponds to a more comprehensive model characterised by two non-linear static maps describing the throttle valve and intake manifold mass flows and torque production non-linear characteristics. In the second case shown in Figure 4.4a, a single non-linear static map describes the steady–state relationship between developed torque at specific angular speed and the throttle angle, which is justified when the intake manifold filling dynamics are very fast (typical for low–displacement/low–power engines). Finally, engine model also includes the overall inertia at the engine shaft (which can be estimated from piston and crankshaft dimensional data using Computer Aided Design (CAD) software) and the combustion–related torque development delay (dead time).

The ICE model, linearised in the vicinity of engine torque vs. speed operating point (τ_m and ω), is characterized by the torque development equivalent gain and time constant, and the simplified first–order lag representation of the combustion–related torque dead time [140, 144], as shown in Figure 4.4c.

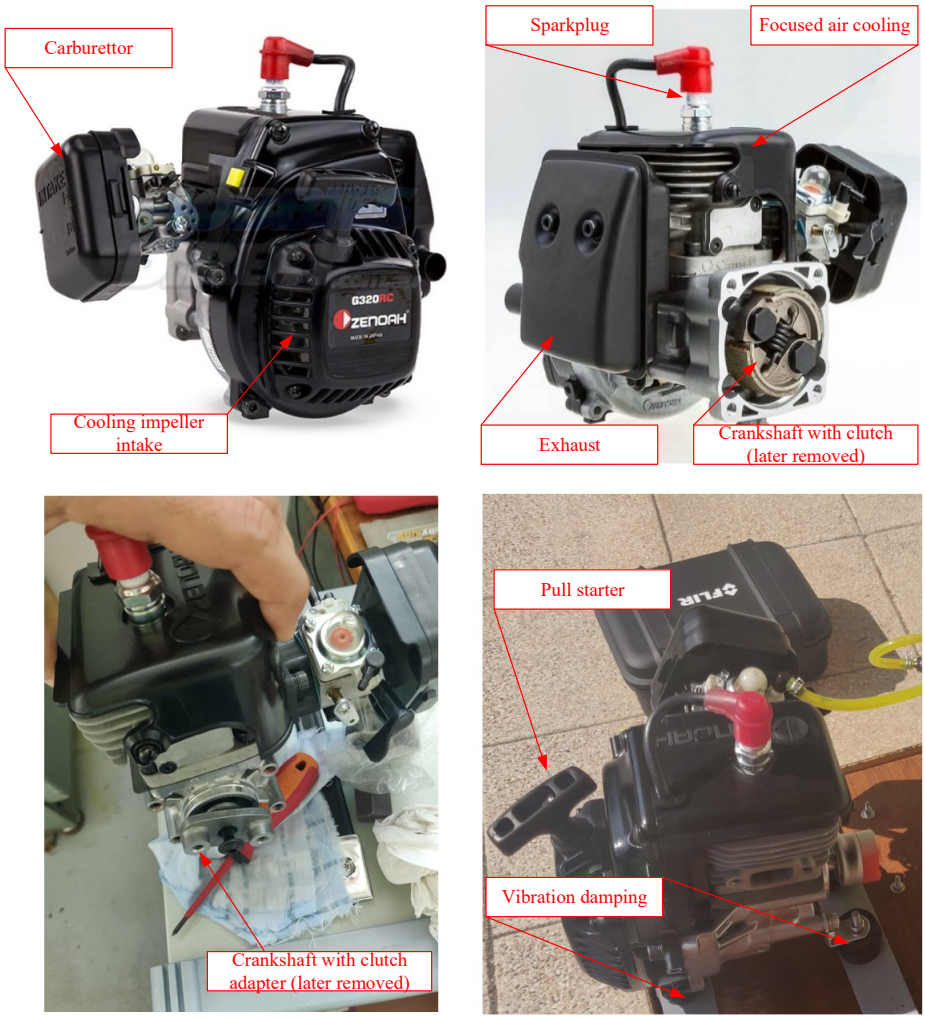

Figure 4.2: Photographs of Zenoah G320RC engines

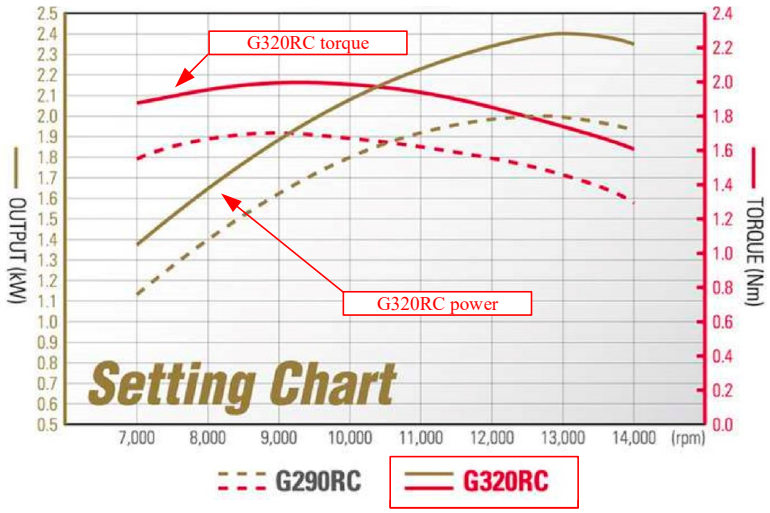

Figure 4.3: Power and torque curves for G320RC provided by supplier [170]

Table 4.1: ICE engine technical parameters [171, 169]

Property	Description	
Model	G320RC	ZG45PCI (G450PU)
Type	Air cooled two stroke cycle gasoline engine	Air cooled two stroke cycle gasoline engine
Fuel	Eurosuper 95 Gasoline and synthetic 2–stroke oil mixture 25:1	Eurosuper 95 Gasoline and synthetic 2–stroke oil mixture 40:1
Displacement	31.8 cm3	45.0 cm3
Bore × Stroke	38 mm × 28 mm	43 mm × 31 mm
Compression ratio	9.1:1	7.9: 1
Maximum power output	Up to 3.22 HP (2.4 kW)	Up to 3.5 HP (2.6 kW)
Operating engine speed range	4000 – 18000 rpm	2000 – 10000 rpm
Carburettor	Walbro WT–1107	Warlbro HDA–48D
Ignition system	Transistor charger ignition	Microprocessor controlled ignition Falkon PCI–HV1.3
Spark plug	NGK CMR7H	Champion RCJ–7Y
Length × width × height	16.7 cm × 21.5 cm × 19.6 cm	16.2 cm × 19.1 cm × 18.2 cm
Mass	2.3 kg	2.1 kg

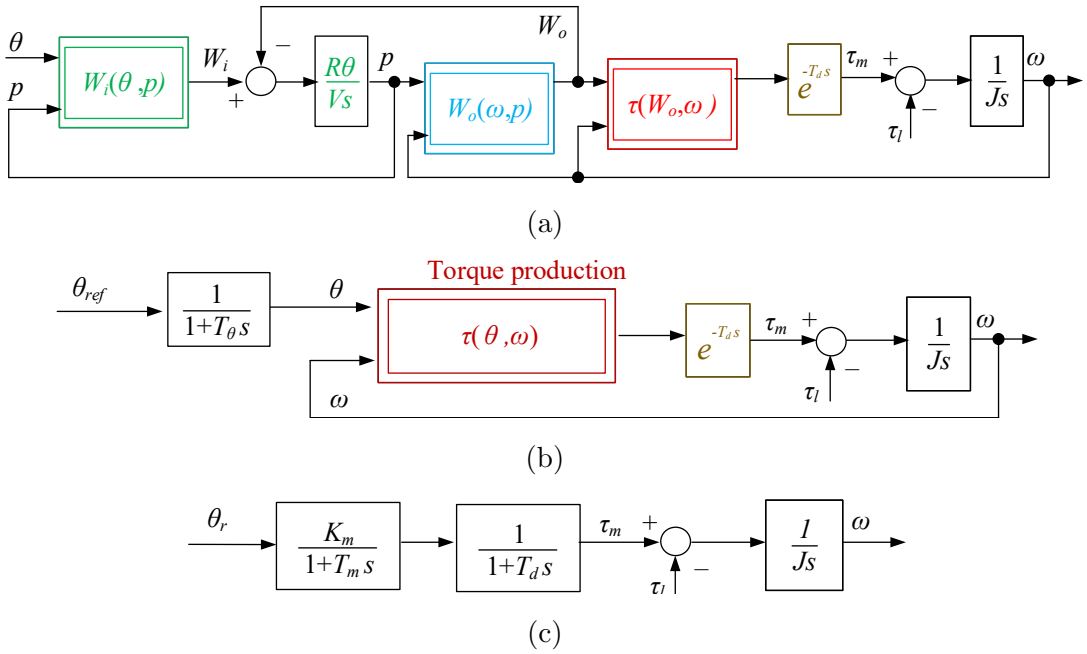

Figure 4.4: Non-linear mean value model of ICE (a), simplified non-linear mean value model of ICE (b), model linearised in the vicinity of ICE operating point (c)

4.1.1. Experimental setup

An experimental setup for ICE is required for the validation of hybrid power unit dynamic models and development of different control strategies and estimation methods considered in this work. A schematic diagram of the experimental setup currently being developed for future research is shown in Figure 4.5, which is based on findings presented in [140, 144]. Namely, internal combustion engine characterisation requires measurement of the following quantities: developed engine torque, engine rotational speed (crankshaft speed/angle), mass airflow, throttle angle, and air pressure and temperature in the intake manifold. The setup should be able to accommodate gasoline engines suitable for integration into multirotor aircraft, with power ratings up to 30 HP, rated torques of up to 30 Nm, and rotational speeds exceeding 8000 min^{-1}. In order to record the power/torque characteristics it is required to impose a controllable load to the ICE.

A good, high–bandwidth solution can be implemented using an electrical servo–machine, as shown in [144]. Furthermore, signal acquisition from different sensors and basic control capabilities can be implemented by using a state–of–the–art control and acquisition platform, such as National Instruments CompactRIO [172], or a Programmable Logic Controller (PLC) that supports real–time data transfer to the host PC for signal logging purposes, such as the Mitsubishi Electric Co. FX5 series [173] (available in our lab), so that measurement acquisition can be fully automated. The setup mechanical system

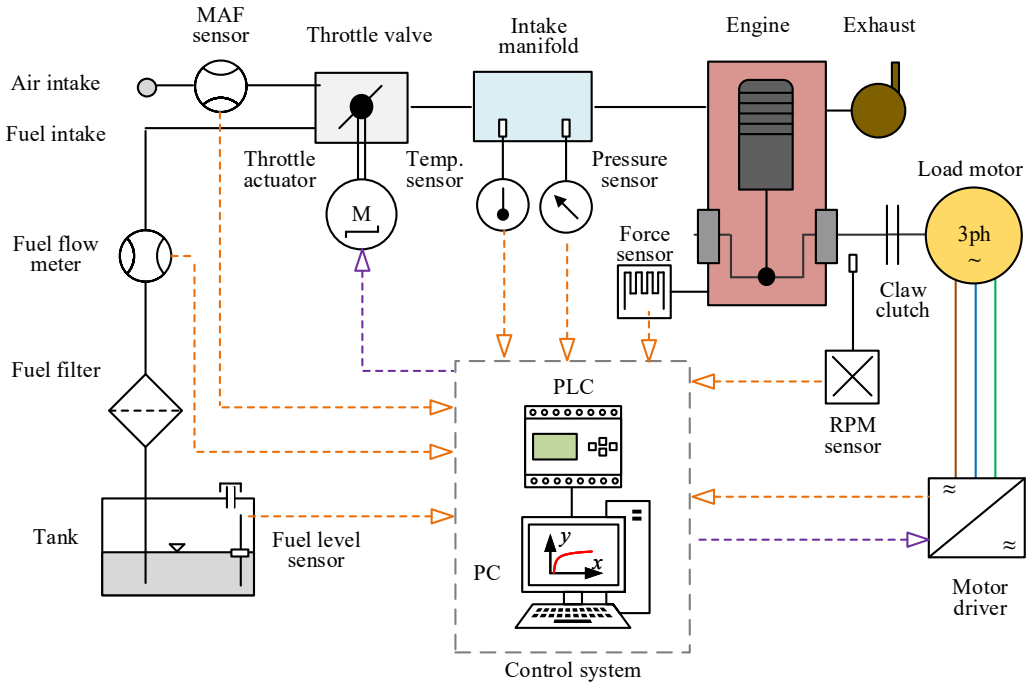

Figure 4.5: Schematic of experimental setup for ICE identification

incorporates mountings for different sensors, such as those for pressure, temperature, angular velocity and torque measurement, as well as fuel lines, internal combustion engine itself and load motor coupling and stand.

For measuring the Mass Air Flow (MAF), standard automotive sensor based on heated grid can be used because it has sufficiently fast dynamics [140, 144] and is relatively low–cost when compared to more specialised sensors. In order to simplify its mounting, the MAF sensor can be positioned in front of the carburettor air intake. The pressure sensor is required to measure the absolute pressure, so a standard sensor based on a tensiometer strips can be used and should be placed inside the intake manifold. The air temperature in the intake manifold can be measured with a T–type thermocouple (copper / constantan). The engine speed (rotation angle) sensor can be realized in the form of a tachometer, which is mounted on the ICE shaft in order to precisely time the fuel–air mix ignition within the cylinder at the correct crankshaft angle. It is possible to utilize the same tachometer signal to measure the engine rotational speed [140,144]. Measurement of the developed torque can be realized by utilizing a pair of load–cells mounted on a stand for measuring $F_{left}$and F_{right} (see Figure 4.6). Measured forces difference is proportional to the developed motor torque τ_m applied over half length of the lever (with length l) connecting the load cells according to the following expression:

$$\tau_m = \frac{l\,(F_{right} - F_{left})}{2} \tag{4.1}$$

The loading machine (electrical servomotor) is used to generate the load torque for the

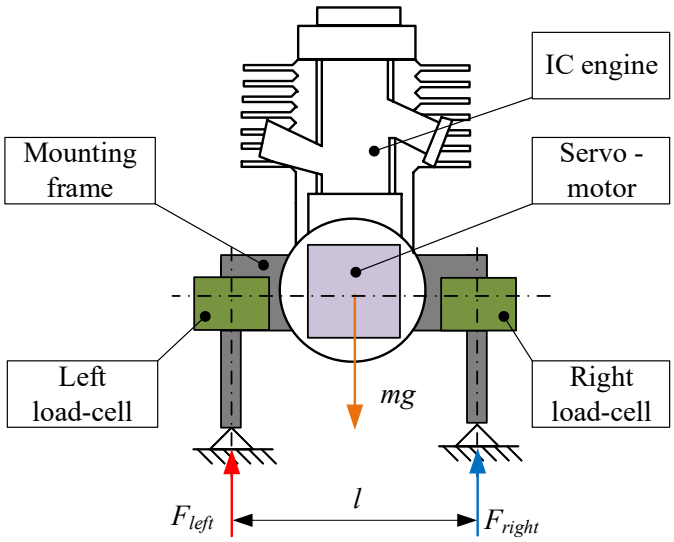

Figure 4.6: Principle of developed torque measurement

ICE. For this purpose, a servomotor supplied by a suitable power converter and controlled by an appropriate microcontroller or PLC unit can be used. Such loading servomotor should be able to operate in two distinct modes (see e.g. [144]):

- Current/torque control mode, where the load torque reference is commanded in order to record the engine load response characteristics),
- Speed control mode, which can be used for starting of the ICE, and for recording of engine static characteristics, such as MVEM model maps, wherein the servomotor maintains the engine speed at the desired value.

The electronic throttle [140, 174, 73] consists of a valve plate, a low power DC drive (typically under 50 W), a double return spring and a potentiometer used as a valve angle sensor θ. Control is usually implemented by the means of servo-system that enables the fine positioning of valve plate. A simplified approach could be utilized instead, replacing a servomotor with a high torque stepper motor to actuate the valve plate. This approach does not require a rotational angle (position) sensor, but it does require relatively straightforward mapping of stepper motor phase sequence signals to angular position. Following this simplification, the throttle valve dynamics can be considered similar to the dynamics of the stepper motor used to control the valve openness. Finally it could be described by a second order linear dynamical model characterised by its natural frequency and damping (second–order or PT2 model) [73].

Figure 4.7 shows the experimental setup used for engine tests in this work. Apart from the engine itself and its fuel supply system, it comprises the microcontroller board used for commanding the engine throttle angle and sensor signal processing, which is connected

to the main PC used for data visualisation and logging purposes. It also comprises the electricity generator and rectifier for the common DC bus power supply of the hybrid power unit (which will be described in the subsequent sub–sections).

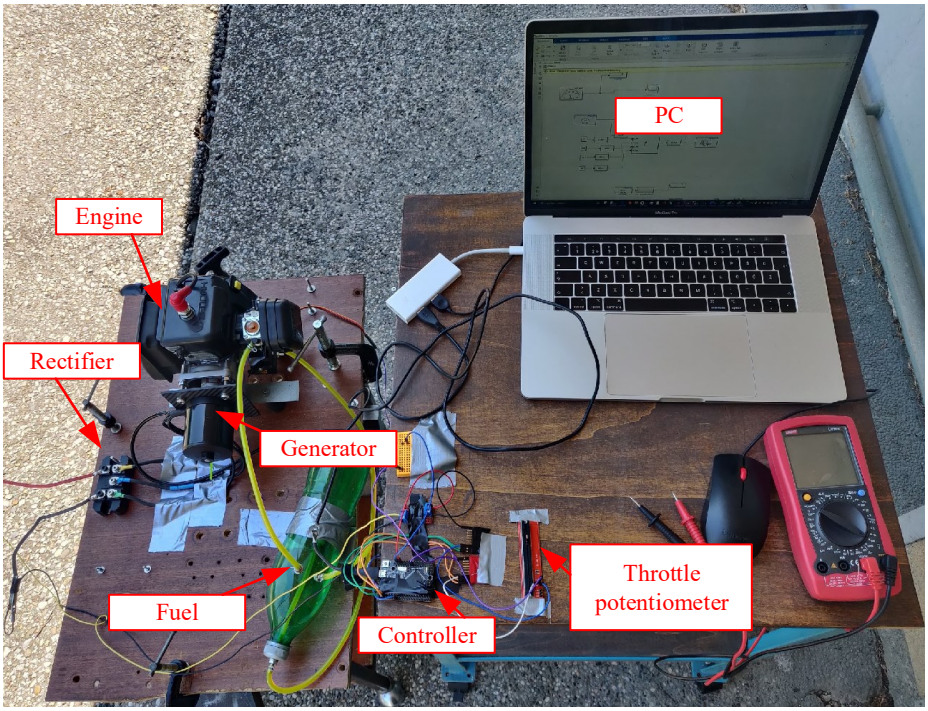

Figure 4.7: ICE test-bench

4.1.2. Engine simulation model

As explained earlier, engine dynamics is described by a simplified model from Chapter 3, comprising the throttle servo-system dynamics, a single torque–throttle–rpm map (Figure 4.4b), and the moment of inertia estimated by using a CAD software and 3D model of the considered Spark Ignited (SI) engine. Thus obtained non-linear torque vs. rpm and throttle map has been linearised (see Figure 4.8) in the vicinity of the operating anticipated engine point (throttle at approx. 75% opening, and engine speed at 9500 rpm) by using numerical linearisation tools within an appropriate software environment (i.e. Matlab/Simulink).

Also, more comprehensive MVEM model maps have been considered and obtained by re–scaling the readily available engine maps of a different (higher–power) engine using a suitable re–sizing methodology (see e.g. [175]), are shown in Figure 4.9. Please note that these maps have been shown to be well–suited for initial engine simulation studies , whereas the simpler for of the internal combustion engine model may be better suited for control system design and final MVEM model experimental identification purposes, using the existing engine experimental setup. This model is also used as a basis for PI

and PID speed controller design in latter sections.

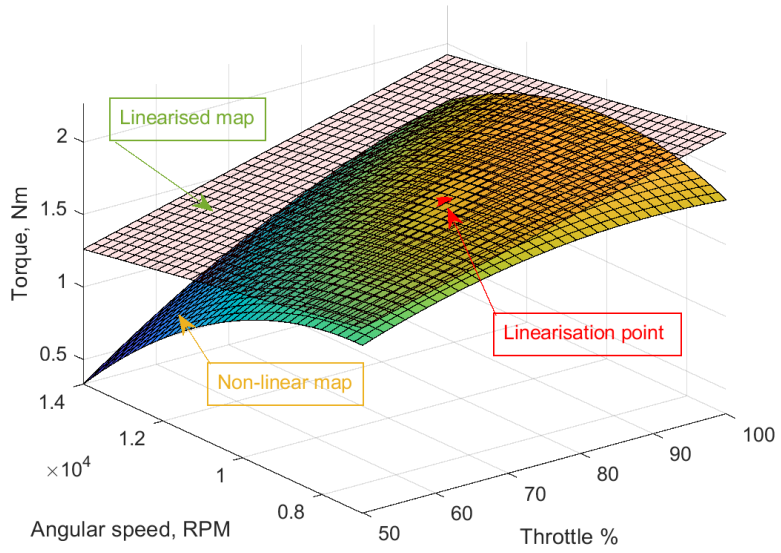

Figure 4.8: Nonlinear form and linearization of torque–rpm–throttle map within simplified MVEM model

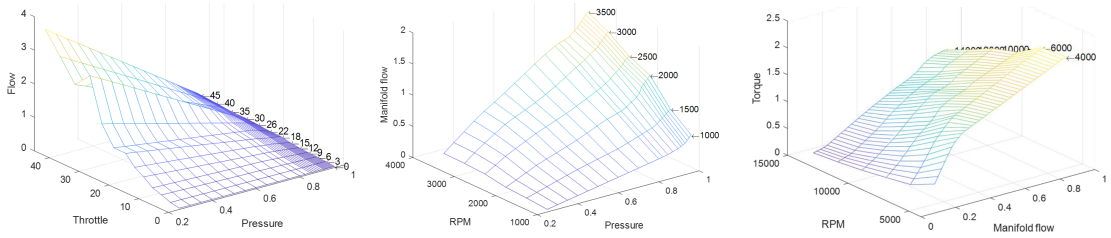

(a) (b) (c)

Figure 4.9: Comprehensive MVEM engine model maps used in simulations: throttle map (a), manifold pressure map (b), torque map (c)

The resulting comprehensive MVEM non-linear simulation model implementation is shown in 4.10a, as described in Chapter 3. It consists of the following sub models: throttle dynamics model, manifold dynamics model, portflow dynamics and torque generation models and the model of rotational inertia.

Figure 4.10b shows the simplified MVEM model with only one static map. It consists of the following sub models: throttle dynamics model and engine dynamics with rotational inertia. The simplified mode receives the throttle position and load (i.e. from generator) as inputs, and outputs the angular (shaft) speed and torque.

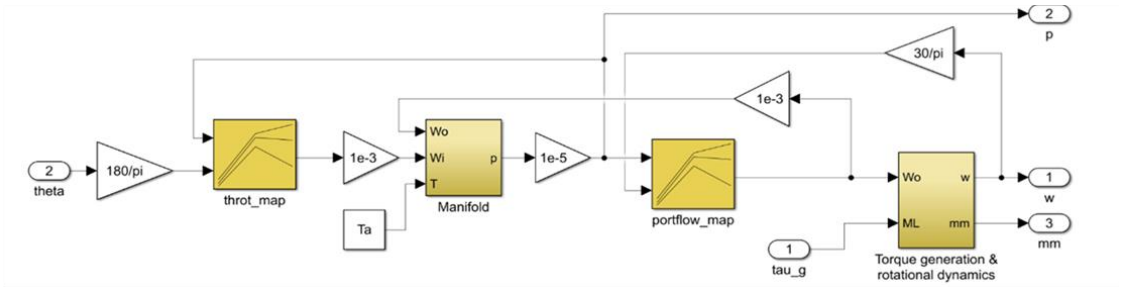

(a)

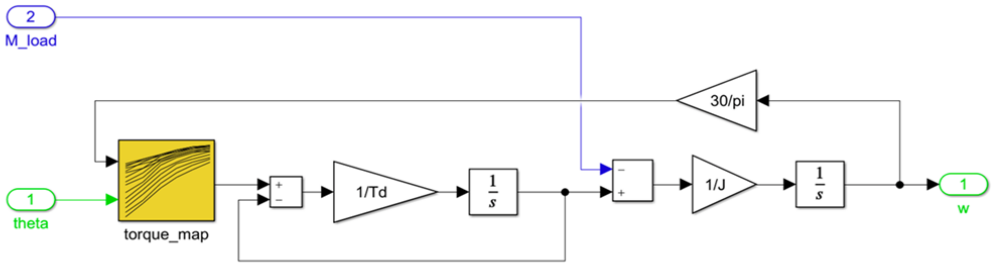

(b)

Figure 4.10: Non-linear simulation models of ICE: traditional MVEM model (a), simplified MVEM model (b)

4.2. Electricity generator

For the construction of experimental hybrid power unit, a lightweight, high power out–runner brushless motor 6374 from Maytech is used as a generator, featuring embedded current/rpm sensors and characterised by EMF constant 170KV (see Figure 4.11a). It is constructed with an enclosed dustproof outer case, and its back electromotive force is characterised by near sinusoidal waveform (see Figure 4.11b). Detailed manufacturer specifications are given in Table 4.2.

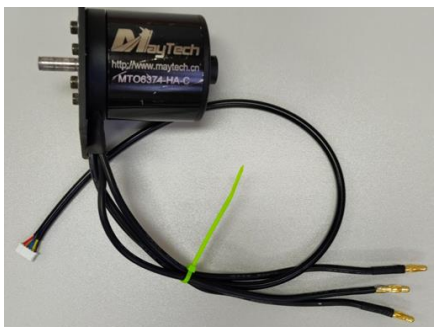

(a)

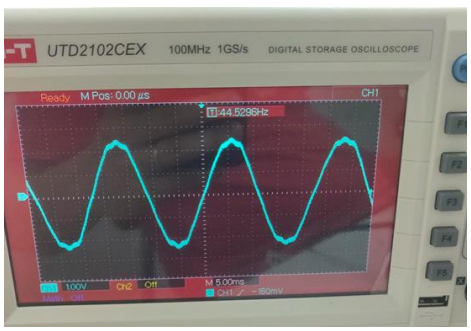

(b)

Figure 4.11: Maytech MTO6374–170–HA–C used as generator (a), line to line back–emf shape (b)

Table 4.2: Electrical motor generator engine specifications and identification [176]

Description	Value
Model No.	MTO6374–170–HA–C
KV	170 rpm/V
Max. Lipo Cell	2-12s Lipo
Max. Current	65 A
Rated Current	60 A
Idle Current	1.5 A
Shaft	8 mm with 3 mm keyway
Sensor cable length	500 mm with 2 mm pitch
Motor Weight	830 g
Max. Power	3550 W
Output Shaft Length	26 mm

4.2.1. Electricity generator/motor experimental setup

In order to fully characterise electrical motor/generator, it is required to have precise measurements of the machine torque and RPM, as well as armature voltage and current. A prototype test bench for that purpose is being developed and built up within this work, and is also going to be used for future studies on this topic. It consists of electrical machine stand, two load cell–type sensors with corresponding signal amplifier circuits, optional loading machine, electronic speed controller, and voltage/current sensors. Load cell sensor is composed of a strain gauge with signal amplifier, and it should be selecet based on the machine size and expected load manufacturer's. In this example a HX711 load cell is used [177]. Signal from HX711 analogue–to–digital converter were processed by the Atmel ATmega microcontroller used for overall setup control and signal processing, and the processed data is subsequently transmitted via USB connection to the virtual serial port in appropriate numerical format, thus enabling data logging on the host personal computer (PC). Figure 4.12 shows the schematic and the realization of the experimental test bench.

A rough estimate of the motor constant K_e value can be obtained as the number of revolutions per minute that the motor will achieve when 1 V (one Volt) is applied at each phase winding with no load attached to the rotor. More precise motor constant measure-

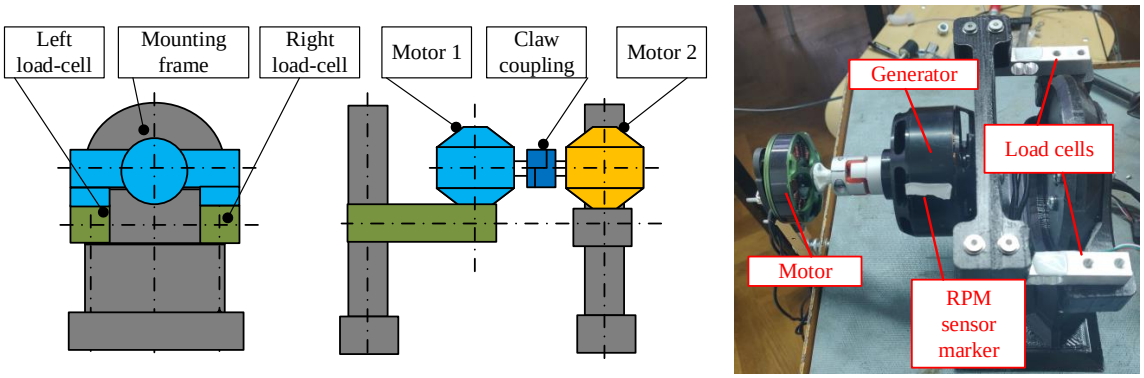

Figure 4.12: Electrical motor/generator test bench realisation example: schematic and photograph of assembled test

ment is based on the ramping of the voltage throttle command from zero to maximum and recording the rotational speed (rpm) and phase voltage profiles (Figure 4.13). By using least squares approximation on thus collected voltage and speed profile data, it is possible to obtain a more accurate approximation of the motor constant. Measurements were conducted on the ICE test bed, with coupled generator and motor. Speed was measured by Hall–effect sensors, while the armature voltage was measured by using a resistor divider network (in order to match it with the analogue–to–digital converter input range). This test can be used to identify voltage constants of both the propulsion motors and electricity generator. Final results of Back Electromotive Force (BEMF) constant identification for the main electricity generator are shown in Table 4.3.

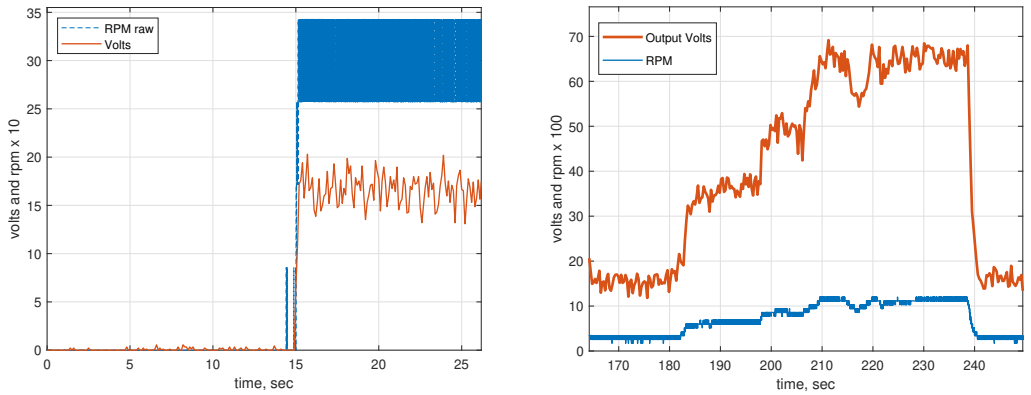

(a) (b)

Figure 4.13: Motor constant identification procedure: constant speed from idle (a), engine ramping and measuring voltage - no load condition (b)

Electrical machine winding resistance and inductance are measured utilising a precise laboratory LCR meter [178]. Phase–to–phase quantities are measured for each possible

phase–to–phase combination, as shown in Figure 4.14 and the phase impedance components (resistance R_{ph} and inductance L_{ph}) are calculated as average values obtained by measurements:

$$R_{ph} = \frac{1}{2} \cdot \frac{R_{AB} + R_{BC} + R_{CA}}{3} = \frac{R_{AB} + R_{BC} + R_{CA}}{6} \tag{4.2}$$

$$L_{ph} = \frac{1}{2} \cdot \frac{L_{AB} + L_{BC} + L_{CA}}{3} = \frac{L_{AB} + L_{BC} + L_{CA}}{6} \tag{4.3}$$

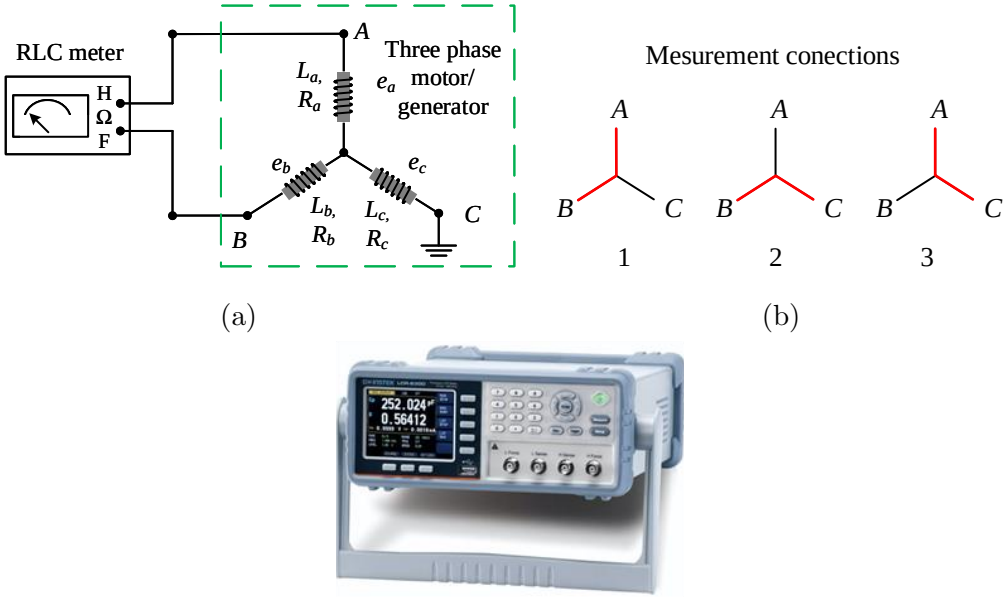

(a) (b)

(c)

Figure 4.14: Electrical motor/generator test bench: measurement principle (a), connection to terminals (b), GW Instek LCR–6002 high Precision LCR Meter (c)

Table 4.3: Generator motor specifications and results of model identification

Description	Value
BEMF shape	Sinusoidal
Line resistance (measured)	0.04068 Ω
Line inductance (measured)	40.43 µH
Voltage constant (measured)	169.8 rpm/V

4.2.2. Simulation model

Identified parameters are used for three–phase motor model. The corresponding simulation model is shown in Figure 4.15 and it consists of following blocks:

- Electric machine armature windings and rotational dynamics shown in Figure 4.16,
- BEMF angular position–dependent profiles, as shown in Figure 4.17a for trapezoid BEMF shape and Figure 4.17b for sinusoidal BEMF shape,
- Switching logic and voltage generation blocks as shown in Figure 4.18.

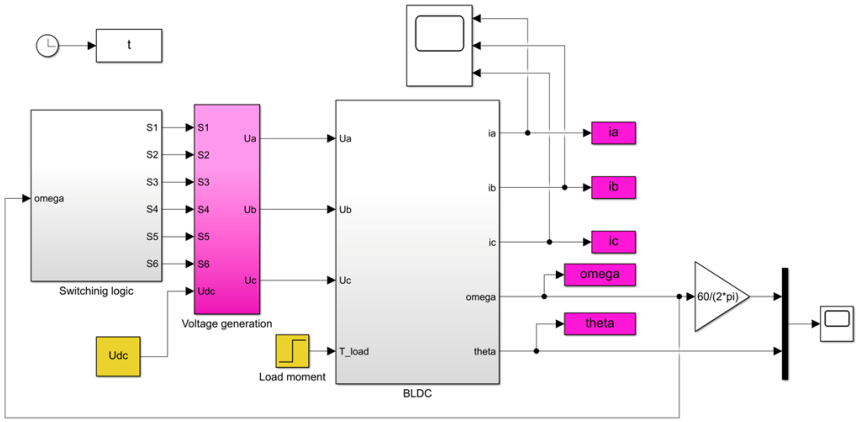

Figure 4.15: Brushless Direct Current (BLDC)/Permanent Magnet Synchronous Motor (PMSM) motor simulation overall model

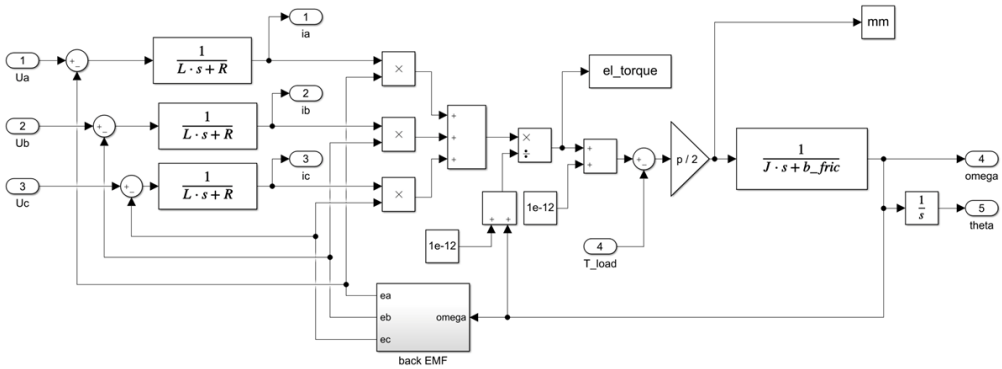

Figure 4.16: BLDC/PMSM motor electrical and mechanical model

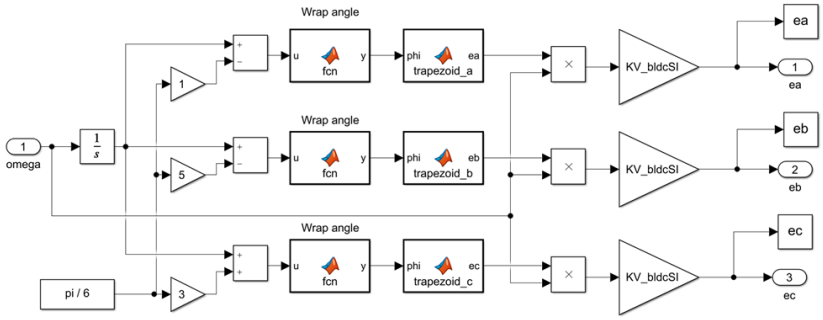

(a)

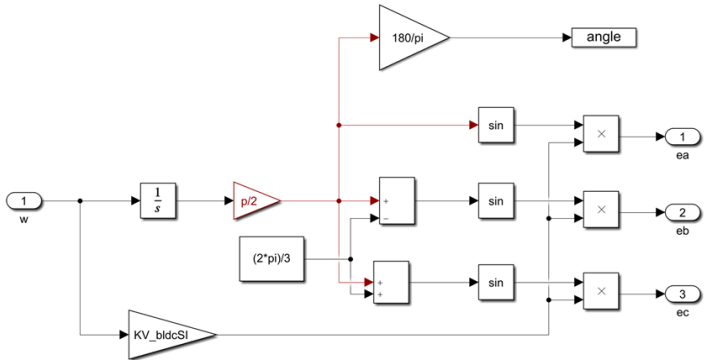

(b)

Figure 4.17: BEMF generator block: trapezoid BEMF shape (a), sinusoidal BEMF shape (b)

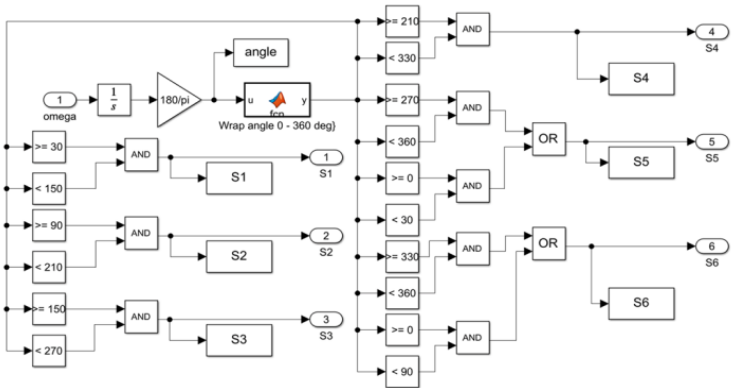

(a)

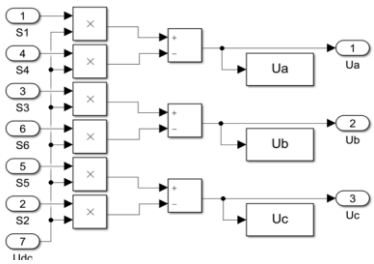

(b)

Figure 4.18: BEMF generator block: switching signals generator (a), voltage generation (b)

4.3. Battery

A Tattu 10000MAH 6S GensAce LiPo battery [179] comprising of six cells connected in series is selected in this research as the electrochemical power source. It is well–suited

Figure 4.19: Tattu 10000 mAh 22.2V 25C 6S1P LiPo Battery Pack with EC5 Plug [179]

for UAV applications due to being packaged with vibration–proof and fire–proof material (see Figure 4.19). In particular, it is rather lightweight and is capable of providing reliable high–discharge–rate power supply while also being able to facilitate relatively long flight times (flight autonomy), as indicated by its technical specifications listed in Table 4.4

Table 4.4: Battery specifications [179]

Description	Value
Manufacturer	Tattu
Number of cells	6s
Nominal voltage	22.2 V
Capacity	10000 mAh
Connector type (main, balancer)	EC5, JST
Discharge Rate	25 C
Dimensions L x W x D mm	174 x 62 x 53
Mass	1.386 kg

4.3.1. Experimental setup

The battery model presented in Chapter 3 is parameterized by recording the model parameter maps for a wide range of battery operating points through an instrumented test bed, whose principal schematic is shown in Figure 4.20. The battery test setup features an Atmel microcontroller for signal acquisition and control tasks and a PC, which performs the collection of battery measurement signals (current i_b, terminal voltage v_b, and operating temperature ϑ_b and the common direct–current (DC) link voltage V_{dc} within the setup. These signals are low–pass filtered to remove the measurement noise and other interfering signals. The setup also comprises a DC load resistor grid, which is used during battery discharging. The photograph of test setup is shown in Figure 4.21.

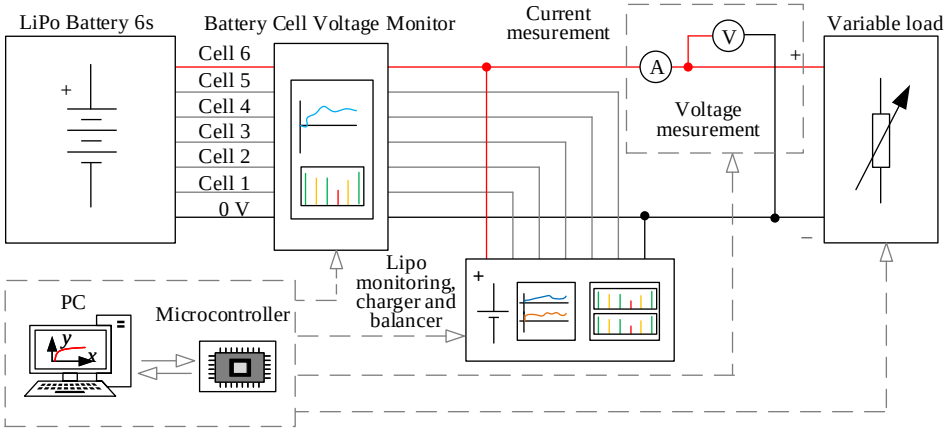

Figure 4.20: Schematic of LiPo battery experimental identification test bench

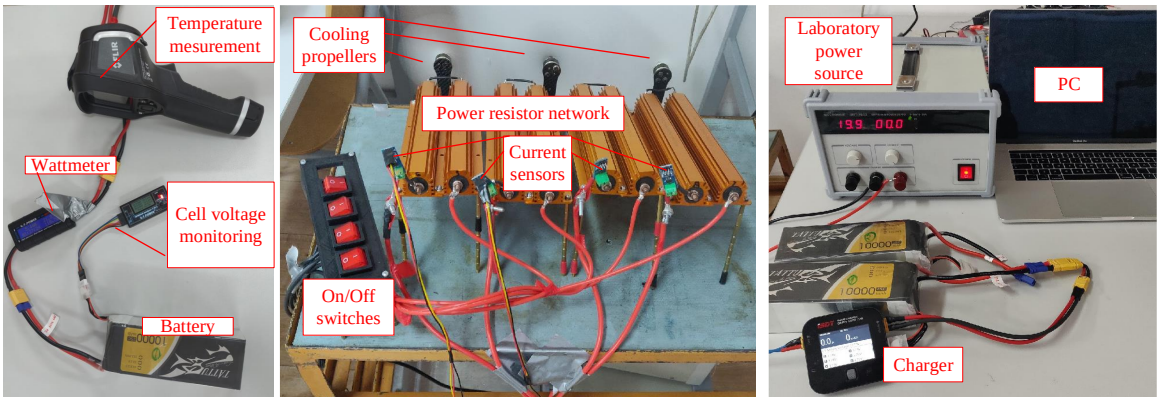

Figure 4.21: LiPo battery experimental test bench implementation

4.3.2. Battery simulation model

The equivalent electrical circuit model (see Chapter 3) comprising the equivalent battery series resistance, and the open–circuit voltage is used as the basis for the battery model identification procedure. The model can be described in the s–domain using battery voltage $v_b(s)$, current $i_b(s)$ and internal resistance R_b:

$$v_b(s) = i_b(s)R_b + V_{oc} \tag{4.4}$$

In the above battery model, all parameters are dependent on the battery state–of–charge, which is defined in the following manner [69]:

$$\xi = 1 - \frac{\Delta Q_b}{Q_{max}(I_b)} \tag{4.5}$$

where $\Delta Q_b = -\int i_b dt$ is the overall discharged battery charge and Q_{max} is the battery charge capacity.

The experimental characterization procedure consists of the initial intermittent discharge test for open–circuit voltage vs. State of Charge (SoC) characteristic identification

and the continuous discharge test used to record the equivalent series resistance characteristic over a wide SoC operating range. The network of parallel resistors (4 Ω per single branch) is employed as a battery load in order to obtain required current profiles (6 – 24 A) within the allowed battery voltage operating range (from 21 V to 25 V).

Open circuit voltage (OCV) is defined as the terminal voltage for the case when no load is connected to the battery, i.e. for the so–called open–circuit condition. Regarding the battery after being charged, the battery terminal voltage will gradually decline to a stable value when it is left in the open–circuit condition sufficiently long; regarding the battery after discharge, the battery terminal voltage will gradually rise to a stable value after the load is removed. Subsequently, after chemical stabilisation of the battery has been acheived (enough time passed since current flow), electromotive force of the battery is basically equal to the open–circuit voltage and it can be used as one of the metrics to determine the amount of energy stored in the battery. Thus, there is a certain relationship between the battery OCV and the battery SoC [69]

In order to relate OCV and SoC an intermittent discharge test was conducted with following steps:

- Initial full charge after stabilisation (achieve electrochemical and heat equilibrium), 4.15 V,
- Discharge battery for a relatively short time interval (i.e. 10 minutes),
- Leave battery in the open–circuit condition to rest for 3 h to settle the terminal voltage,
- Repeat interment discharging steps until OCV per cell is approx. 3.4 – 3.5 V (depleted state).

From aforementioned test it is possible to define OCV vs SoC relation. By charging with different currents (0.25, 0.5, 1C) it has been identified that maximum charge of batteries from 3.5 volts per cell (after stabilisation) to 4.15 V per cell (after stabilisation) is 9800 mAh and it defined 100% SoC. The interment discharging steps were repeated until OCV per cell is approx. 3.4 – 3.5 V (corresponding to depleted state of the cell). From the aforementioned test it is possible to define the OCV vs SoC relationship. The identification results obtained at constant room temperature (30 °C) are shown in Figure 4.22. For internal resistance characterisation, several simplifications to the Thevenin battery model formulation are introduced:

- During continuous discharging (by means of constant load) current does not have sudden changes in magnitude, i.e. it changes (if at all) slowly and continuously,

- From the above requirement, it follows that changes in polarisation voltage are primarily dependent on the polarisation resistance (polarisation capacitance does not affect the polarisation voltage variations),
- Thus, the battery identification results in the much simpler equivalent internal resistance (Rint) model.

From the above simplifications, it is possible to define the terminal voltage under steady–state discharging conditions:

$$v_b(SoC) = V_{oc}(SoC) - i_b\,(R_b + R_c) \tag{4.6}$$

where R_c is polarisation effects resistance, R_b is battery internal resistance, together forming the battery equivalent internal resistance $R_{ekv} = R_b + R_c$. Finally, R_{ekv} can be extracted by using:

$$R_{ekv} = \frac{V_{oc}(SoC) - v_b(SoC)}{i_b} \tag{4.7}$$

Figure 4.24a shows the block diagram representation of the battery simulation model. The equivalent internal resistance is realised as a static map $R_{ekv}(\xi)$, while the open–circuit voltage V_{oc} is represented by static map dependent on state–of–charge $\xi(\Delta Qb)$. Simulation implementation of model is given on Figure 4.24b

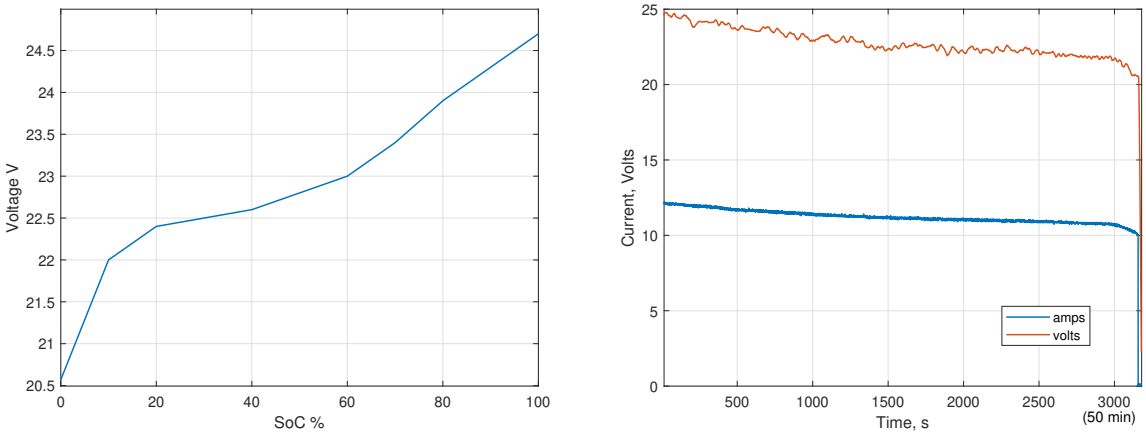

(a) (b)

Figure 4.22: Experimentally–recorded: (a) Open circuit voltage vs SoC for discharging – open–circuit voltage static curve (b) continuous discharge curve (2 ohm load) for internal resistance mapping

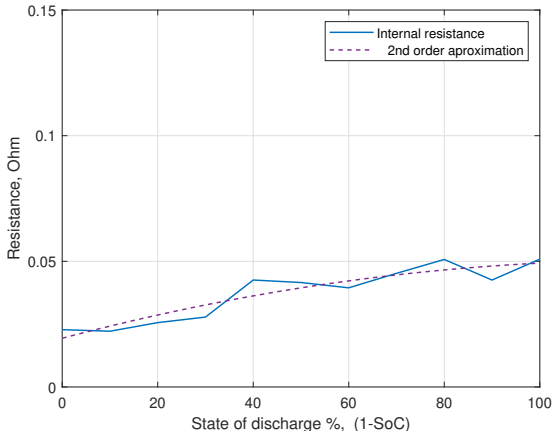

Figure 4.23: Experimentally–recorded and extracted internal resistance vs state of discharge (1−SoC)

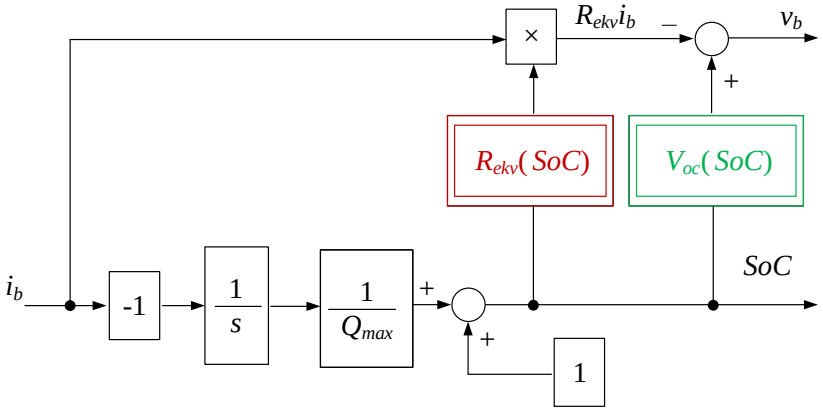

(a)

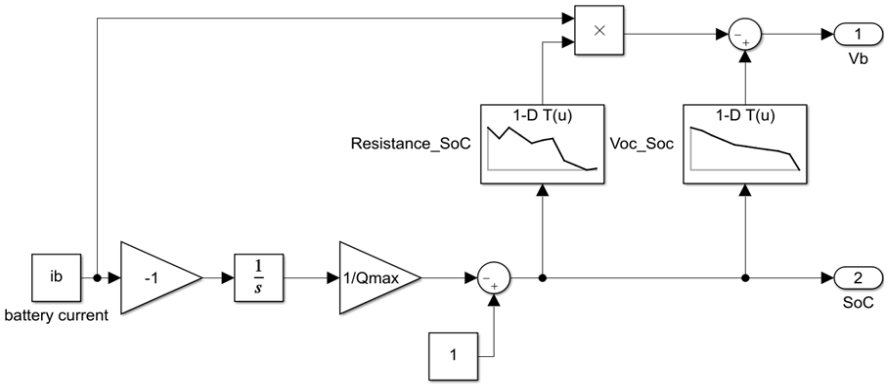

(b)

Figure 4.24: LiPo battery a) model block diagram, b) simulation realisation

4.4. DC-DC converters

In order to convert one level of DC bus voltage to some other required level, a quality switch–mode Direct Current to Direct Current (DC–DC) power converter can be used. Because of rather large power requirements of Unmanned Aerial Vehicles (UAV)s, which is in the order of magnitude of kilowatts, commercially available solutions are very costly and difficult to obtain. Designing a custom power converter poses a great challenge as it involves complex electrical and thermal design, along with the selection of suitable power electronics components. Hence, low–cost off–the–shelf power converter units can be considered as a viable alternative, provided that they can guarantee continuous power supply over the predefined load range.

In order to fully determine the characteristics of an off–the–shelf, inexpensive DC–DC buck converter (Figure 4.25), a reverse engineering method was applied where key components were de–soldered and identified through measurement. Inductance and resistance of the main inductor, and input and output buffer capacitance values can be measured with a high–precision laboratory RLC meter [178]. The frequency of the Pulse Widith Modulation (PWM) generator can be determined by using an oscilloscope and connecting the oscilloscope probe to the PWM circuit output. Specifications and rated quantities for the considered power converter are given in Table 4.5.

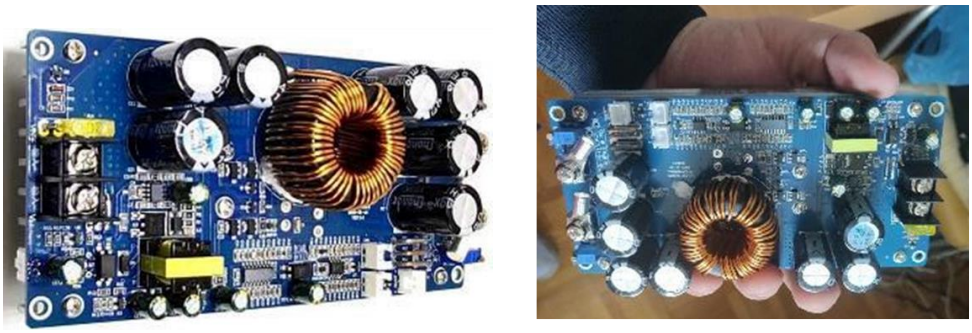

Figure 4.25: DC–DC converter photos

Table 4.5: DC–DC Buck converter supplier specifications [180] and identified quantities

Description	Value
Model and Output power	AP–D5830A , Max. 800 W
Input voltage / current	20 – 70 VDC / Max. 20 A
Output voltage / current	2.5 – 58 V / 0.1 – 30 A
Idle current	<70 mA (24V in / 12 V out)
Output voltage ripple	<120 mV (24V in / 12 V out)
Rated efficiency	0.93 – 0.97
Declared switching frequency	150 KHz
Measured switching frequency	115 kHz (measured by oscilloscope)
Buck Inductance	36.65 μH (measured by laboratory grade LCR meter)
Buck output capacitance	4 mF, 63 V
Dimensions and mass	154 mm x 75 mm x 70 mm, 0.6 kg

4.4.1. Experimental setup

The experimental setup for DC–DC power converter testing (shown in Figures 4.26 and 4.27) consists of the stand, DC power supply, DC–DC buck converters, Lithium Polimer (LiPo) battery, Direct Current (DC) link and capacitors, blocking diodes, current and voltage sensors and a microcomputer control unit that enables PC based data acquisition. The parameters of components are given in Table 4.6.

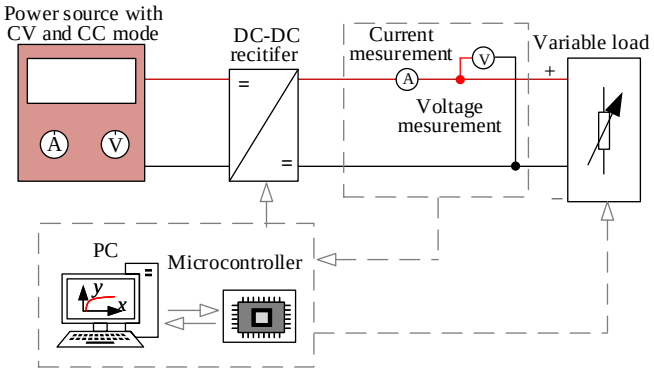

Figure 4.26: DC-DC experimental setup schematic

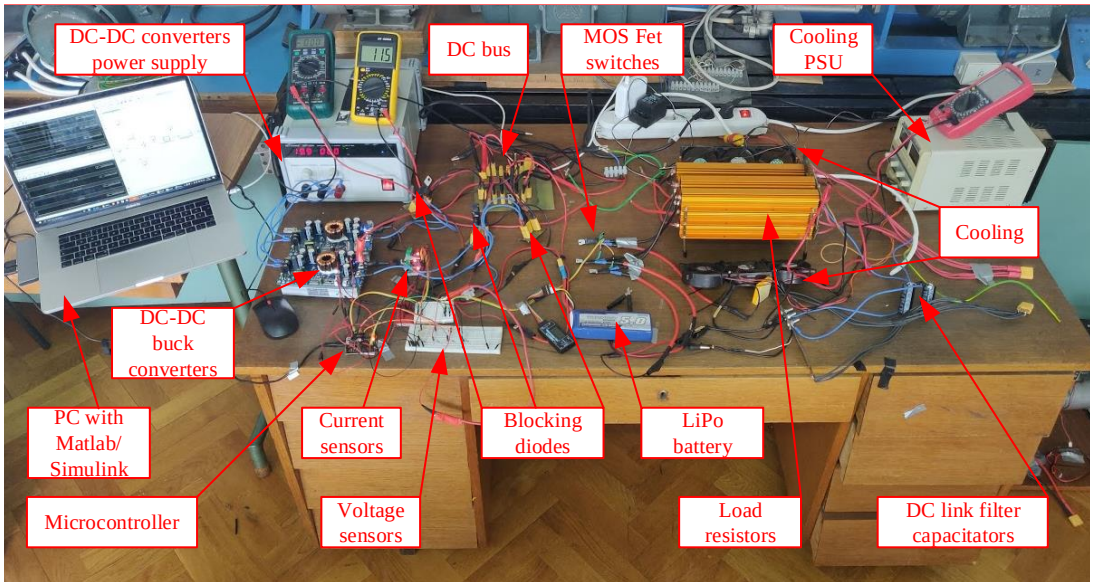

Figure 4.27: DC-DC experimental setup photograph

Table 4.6: Parameters experimental setup

Description	Value
DC–DC converters power supply	Laboratory grade high power switching supply, with current limiting and voltage regulation. 0–30 V, 0–50 A
DC bus	Positive and negative terminal for connection of loads and sources,(XT60 connectors)
Current sensor	ACS712 hall effect sensor, 20 A
Voltage sensor	Voltage divider with ratio = 11
Diode	High voltage Schottky rectifier diode, V_f = 0.37 V, I_{max} = 250 A
Load switches	Logic level n–channel MOSFET, IRLZ44, V_{dss} = 60 V, I_d = 27 A
Filter Capacitators	Total 1200 µF, electrolytic, 63 V
Battery	LiPo 5000 mAh, C
Load resistors	2 Ω, 500 W resistor network

4.4.2. Simulation model

The model of the buck converter circuit is obtained by applying Kirchhoff voltage and current laws which leads to sets of equation describing the buck converter circuit. The procedure of deriving the model equation and selecting the state variables was shown in Chapter 3. The model is configured with several parameters as shown in Figures 4.28 and 4.29. The parameters are the capacitance C, the inductance L and switching frequency. The power converter system model is highlighted in to three major segments: pulse–width modulator, buck converter system and the load. Because output voltage and current limiting control is embedded within the DC–DC power converter, the closed–loop power converter system will be treated as a black box model.

The buck converter dynamics with respect to output voltage reference is approximated by a first order lag term, with unit gain and average delay time obtained experimentally by recording the buck converter dynamic response to a stepwise reference change. Namely, it is assumed that the buck converter output voltage control system is characterized by quasi–aperiodic dynamics (no perceptible reference step response overshoot or transient oscillations), which can be approximated by the first–order aperiodic process model with unit gain and single time constant, given in the following compact transfer function form:

$$G_{cu}(s) = \frac{v_i(s)}{v_{Ri}(s)} = \frac{1}{T_{eu}s + 1} \tag{4.8}$$

where v_i is the buck converter output voltage, v_{Ri} is the voltage reference, and T_{eu} is the equivalent closed–loop time constant.

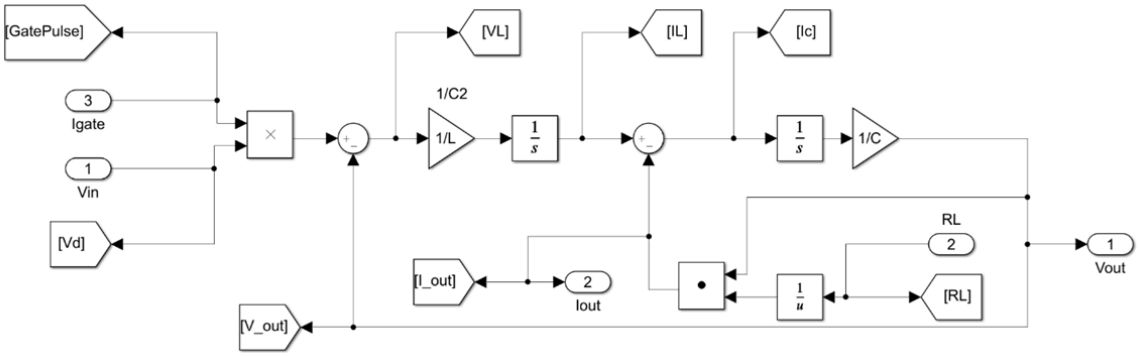

Figure 4.28: DC–DC converter smulation model of DC–DC buck converter in pure Matlab/Simulink

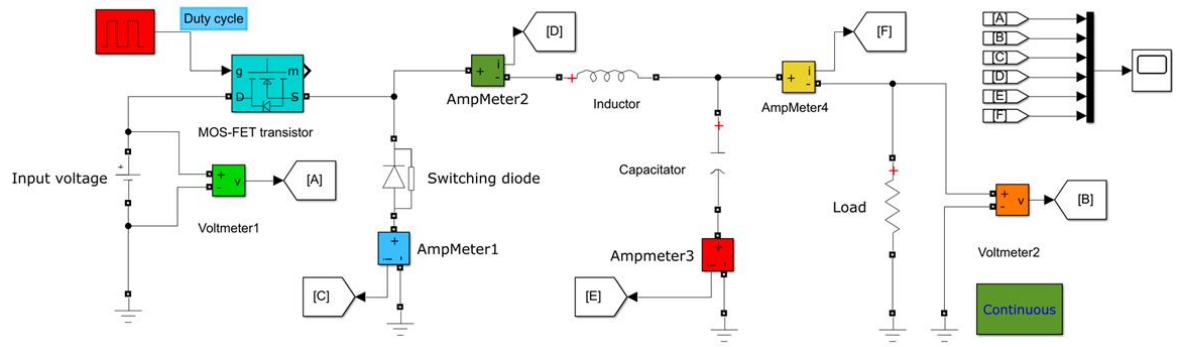

Figure 4.29: DC–DC converter simulation model realised by SimElectronics module of Matlab/Simulink

4.5. Propellers

To fully characterize a motor/propeller set, it is required to measure several parameters, such as motor voltage and current, PWM throttle input, mechanical load and motor torque, as well as motor speed [58]. In order to obtain a precise model of the propeller drive, it is required to run multiple tests with different input voltages and different loads. From measurements it is possible to obtain following relationships:

- Mechanical power (W) as function of motor torque (Nm) and motor speed (rad/s),
- Electrical power (W) as function of motor input voltage (V) and output current (A),
- Motor Efficiency as ratio of Mechanical power and Electrical power.

4.5.1. Experimental setup

The experimental setup for the identification of propulsion system physical parameters consists of the stand, DC power supply control unit and measurement equipment which enables data acquisition important for subsequent processing and analysis. The control unit facilitates rather straightforward programming and provides required control signals for the process model identification and other analysis.

In order to identify the propulsion physical parameters, two sensors are used. Aerodynamic forces where measured with load cell type sensor, while optical RPM meter is used to measure angular velocity. Voltmeter and amperemeter are used to measure the power consumption of the electrical motor as the product of the voltage across the DC link and the current drawn from the DC link. A commercially available test bench Series 1580/1585 produced by RC benchmarks [181, 182] was obtained in order to automate the

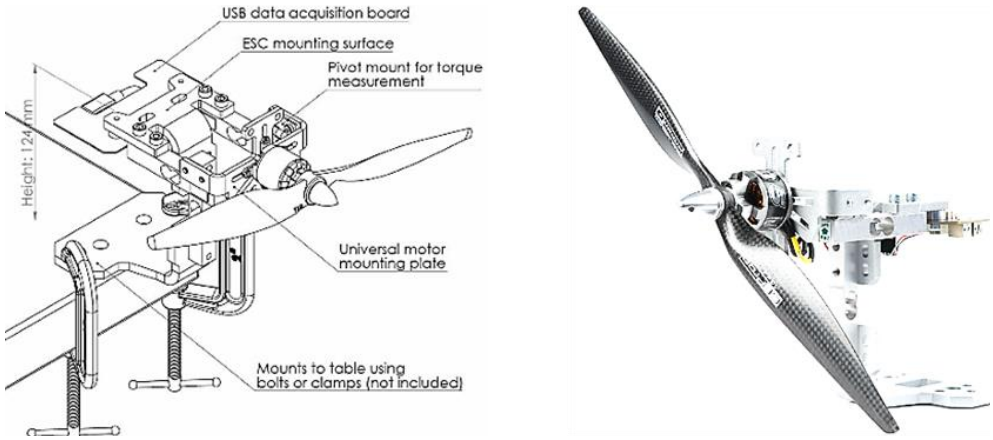

Figure 4.30: Thrust test bench schematic and photograph [181, 182]

measurement procedure. It is capable of measuring the propeller thrust, motor voltage, current draw and motor revolutions per minute (speed).

Based on these measurements it can derive the overall propulsor efficiency (kg/W) for the particular propeller drive configuration. Furthermore, it enables Electronic Speed Controller (ESC) manual and automatic control modes, and can execute custom user scripts and output data to CSV files. It also features a real–time sensor plots. The setup is shown in Figure 4.30, while its technical specifications are given in Table 4.7.

Table 4.7: Thrust stand specification [181, 182]

Description	Value
Model	Series 1580 Dynamometer
Thrust measurement	± 5 kgf 0.5% tolerance
Torque measurement	± 1.5 Nm 0.5% tolerance
Voltage measurement	0 – 35 V 0.5% tolerance
Current measurement	0.1 – 40 A 1% tolerance

4.5.2. Measurements

The identified parameters are presented as a function of the control signal from the control unit, with final parameter values obtained as the average of four successive measurements. In particular, for propeller dynamics simulation and control design it is necessary to estimate the respective thrust and drag coefficients. By using measurements of thrust, drag and RPM, it is possible to estimate the thrust coefficient in a straightforward manner. The same procedure applies to the drag coefficient estimation. Using

experimental setup and methods described by [58], the corresponding propeller–motor characteristics have been obtained. Propeller inertia can be obtained by pendulum experiments [47], CAD software or by direct calculation based on known propeller dimensions (arm length and thickness). Dynamic model of the propeller is shown in Figure 4.31.

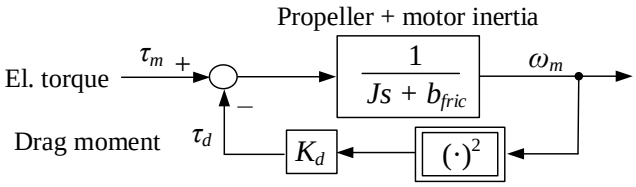

Figure 4.31: Propeller dynamics model

Tests have been conducted by propeller throttle variation from 0 to 100% in 15 steps. This procedure could also have been performed using the manufacturer's software custom scripting feature. Measurements were conducted on different sizes and here is displayed for 17–inch propellers and were conducted indoors, at approximate pressure 102.1 kPa, temperature 22 °C, humidity 30% and supply voltage from a DC regulated power supply. Propeller configuration was leading edge first spinning, air going towards the thrust stand. Determination of coefficients can be done by means of statistical methods, such as the least square approximation used in this work (Figure 4.32).

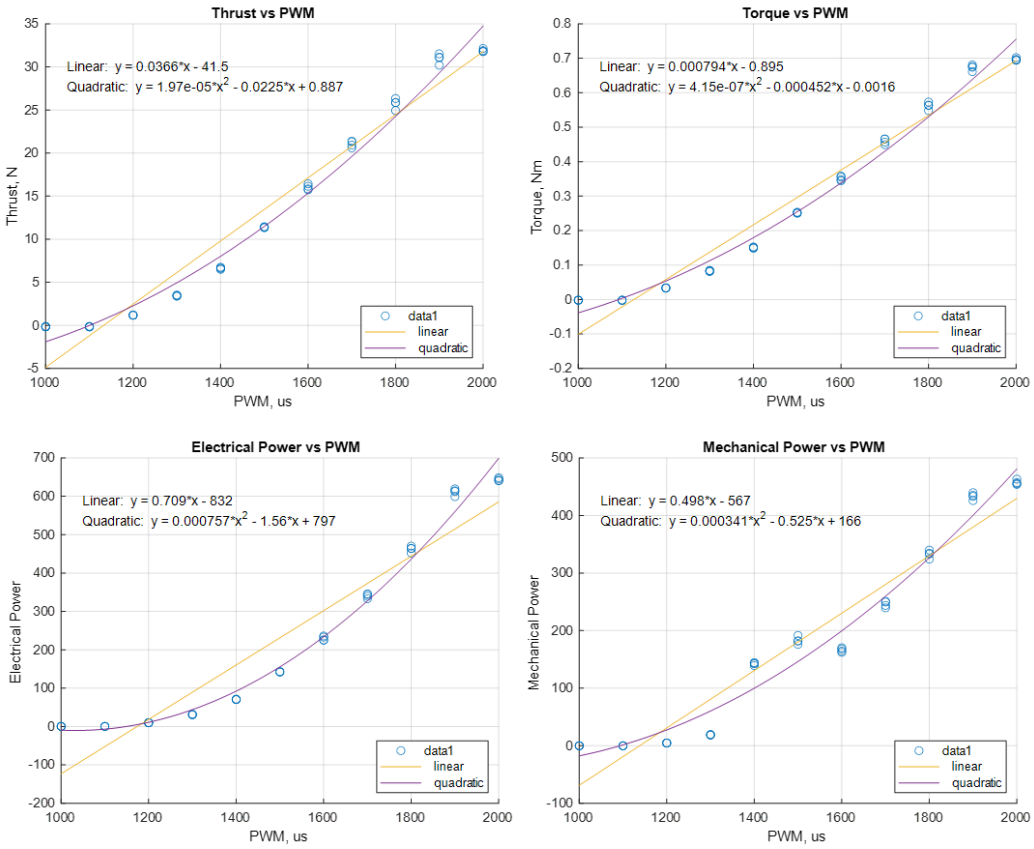

Figure 4.32: Obtained propeller data

5 Hybrid multirotor control systems

This chapter presents the design of hybrid power supply control system for multirotor UAV featuring ICE–based direct–current generator unit and optional DC power system. Also, it outlines the process models and attitude control system design for hybrid multirotor.

5.1. Considered topologies

This section briefly outlines the topologies of power supply system for a Hybrid Unmanned Aerial Vehicles (UAV), such as the Internal Combustion Engine (ICE) plus permanent magnet generator–based Direct Current (DC) power supply and the Direct Current to Direct Current (DC–DC) buck converter. The hybrid power supply system consists of an ICE, a electricity generator, a Lithium Polimer (LiPo) battery and an optional DC–DC power converter parallel network. Schematic representations of hybrid power systems suitable for UAV applications are shown in Figures 5.1 and 5.2, wherein Figure5.1 shows the hybrid power system topology with passive load sharing and Figure 5.2 shows the topology of semi–active load sharing system and the principal schematic of corresponding control system.

In the case of passive load sharing topology (Figure 5.1), the internal combustion engine supplies the mechanical power to the three–phase brushless DC generator with permanent magnet excitation at rotor side, which, in turn, supplies the common DC bus through a three–phase full–wave diode rectifier, thus forming the controlled DC power supply. A battery of suitable terminal voltage range and capacity is connected through a blocking diode to the common DC bus, wherein the diode is used to prevent uncontrolled battery charging from the DC bus. In this arrangement, battery is intended to cover for peak DC bus loads, which are manifested in lowering of the DC bus voltage, thus allowing the blocking diode to become forward biased, and in turn allowing the outgoing battery power flow towards the DC bus.

In the semi–active load sharing topology (Figure 5.2) based on DC power supply comprising the three–phase Brushless Permanent Magnet Syncronous (BPMS) generator

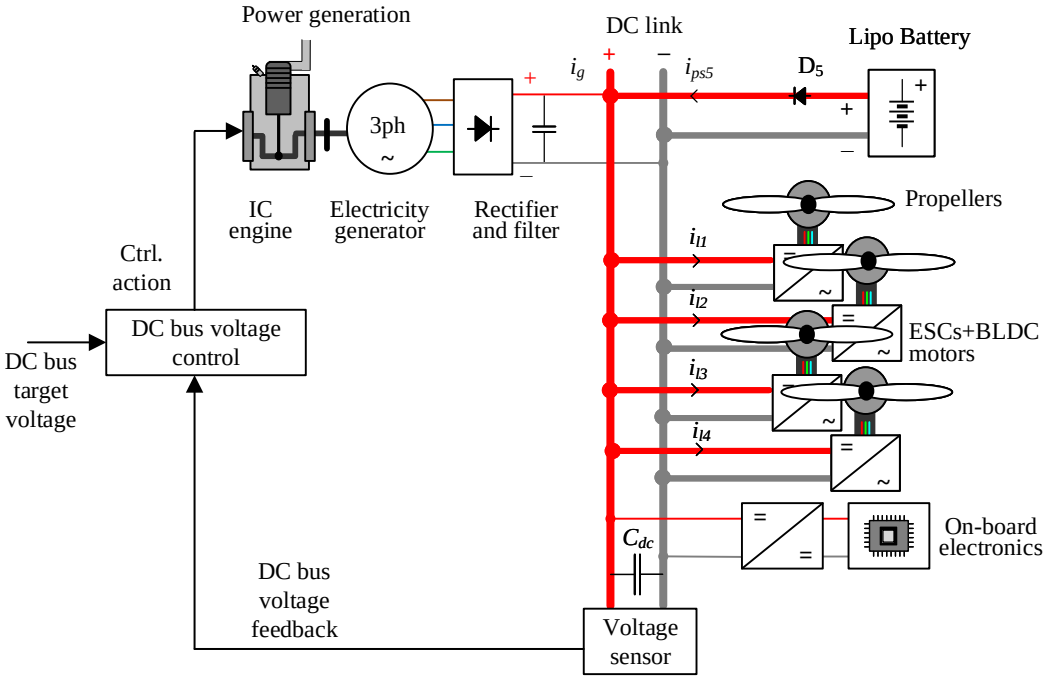

Figure 5.1: Passive load sharing hybrid propulsion topology

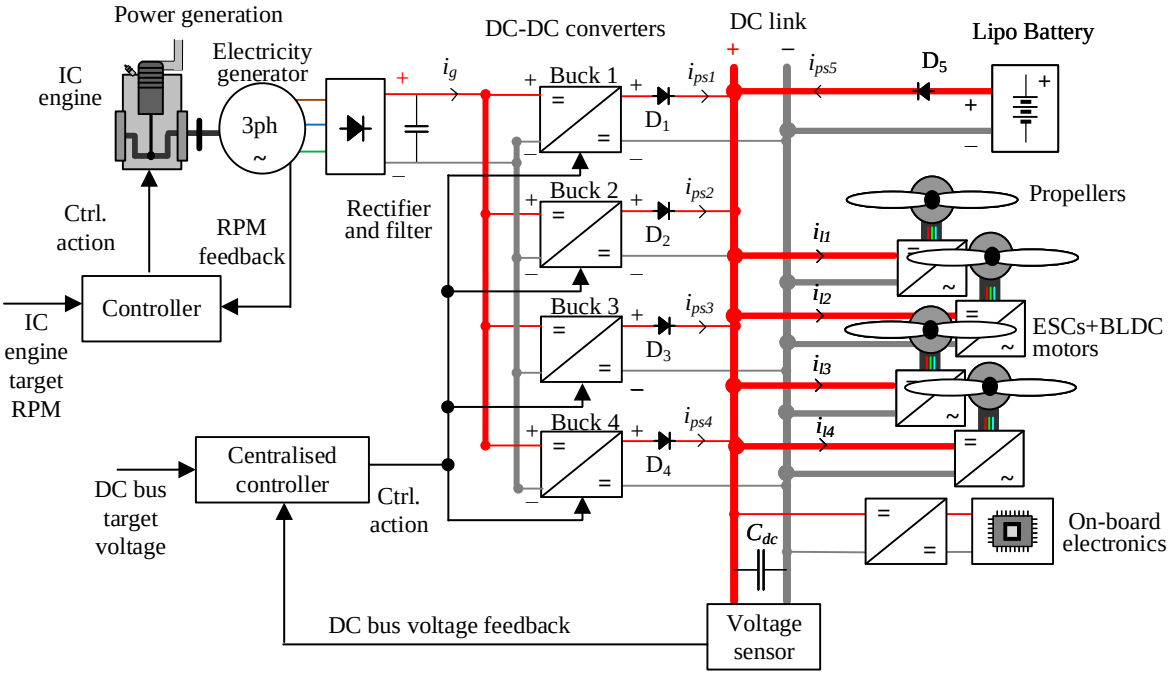

Figure 5.2: Semi–active load sharing hybrid propulsion topology

with permanent magnet excitation at rotor side supplies the DC voltage to the parallel–connected DC–DC buck converter network through the common rectifier unit with its output "smoothing" capacitor C_{in}. In this arrangement, the parallel–connected and output voltage–controlled buck converters are connected to the common DC bus (characterised by its "smoothing" capacitor capacitance C_{dc}) through series blocking diodes $D_{b1} \dots D_{b4}$, which prevent reverse current flow (current can only flow into the DC bus). A battery energy storage system (BESS), characterised by its battery electromotive force and internal battery resistance R_b, is also connected in parallel to the DC bus through its own series blocking diode D_{bb}, thus facilitating only discharging operation of the battery, and preventing unwanted high charging rates which would occur if DC bus voltage v_{dc} would exceed the battery electromotive force E_b. Under normal operating conditions, voltage–controlled buck converters can supply the DC bus up to their internal current limits I_{max}.

When the DC bus load exceeds the collective maximum current $max(i_{out}) = max(i_{out1} + i_{out2} + i_{out3} + i_{out4}) = \nu_{conv} I_m ax$, ($\nu_{conv} = 4$ is the number of parallel–connected buck converters herein), the DC bus voltage should exhibit a noticeable droop (sag) behaviour. Once the difference between the battery electromotive force E_b and the DC bus voltage exceeds the BESS blocking diode forward biasing voltage v_F (i.e. $E_b – v_{dc} > v_F$) BESS starts discharging, with the discharging current being effectively determined by the battery internal resistance R_b (i.e. $i_b = (E_b – v_{dc} – v_F)/R_b$). In that case, the DC bus voltage equilibrium state $v_{dc} = E_b – (i_L – \nu_{conv} I_{max}) R_b – v_F$ is achieved wherein the DC bus load is effectively covered by the sum of total limit current of the parallel–connected buck converters and the battery discharge current (i.e. $i_L = \nu_{conv} I_{max} + i_b$).

As shown in Chapter 4, for the Internal Combustion Engine, the dominant static and dynamic effects are typically modelled by using Mean–Value Engine Model (MVEM) modelling approach. In the case of a DC generator with permanent magnet excitation at rotor side, each stator phase winding is characterized by its respective internal resistance and inductance, and the induced electromotive force (EMF) dependent on the rotor speed. Battery is characterised by internal resistance and terminal voltage in form of static maps. Buck converter (used in the semi–active load sharing topology), comprises the active (switching) element (MOSFET Q) feeding the embedded inductor, with a parallel–connected freewheeling diode D used to suppress the inductor back–EMF during MOSFET switch turn–off (see Chapter 3, Figure 3–41). For the particular DC–DC power converter buck topology, the average value of voltage feeding the inductor can be calculated in the ideal case based on the commanded Pulse Widith Modulation (PWM) duty cycle D and input voltage v_{in} (DC bus voltage v_{dc}) [183].

Based on previously described topologies of power systems and models of individual

hybrid UAV power system components (elaborated in detail in Chapters 3 and 4), dedicated controllers of ICE throttle - DC bus voltage and buck converter output voltage are designed utilizing damping optimum criterion [184].

5.2. Damping optimum criterion

Damping optimum criterion [184] is a practical pole placement–like method of design of linear continuous–time closed–loop systems with a full or reduced–order controller, which results in straightforward analytical relations between the controller parameters, the parameters of the process model, and desired level of response damping via characteristic design–specific parameters. Damping optimum criterion has found application in those control systems where the closed loop damping needs to be tuned in a precise and straightforward manner. The tuning procedure starts with the transfer function of the closed–loop control system, preferably with no transfer function zeros:

$$G_c(s) = \frac{y(s)}{y_R(s)} = \frac{1}{A_c(s)} = \frac{1}{1 + a_{c1}s + a_{c2}s^2 + \ldots + a_{cn}s^n} \tag{5.1}$$

where $a_{c1} \ldots a_{cn}$ are the coefficients of the closed–loop system characteristic polynomial. The above closed–loop system characteristic polynomial $A_c(s)$ can be rewritten in terms of the damping optimum criterion in the following form:

$$A_c(s) = 1 + T_e s + D_2 T_e^2 s^2 + D_3 D_2^2 T_e^3 s^3 + \cdots + D_n D_{n-1}^2 \cdots D_2^{n-1} T_e^n s^n \tag{5.2}$$

where T_e is the so–called closed–loop equivalent time constant, and $D_2, D_3 \ldots D_n$ are the so–called damping optimum characteristic ratios of the n–th order system. When all characteristic ratios are set to the so–called "optimal" values $D_2, D_3 \ldots D_n = 0.5$ (e.g. by applying a full–order controller), the closed–loop system of any order l has a quasi–aperiodic step response characterized by an overshoot of approximately 6% (thus resembling a second–order system with damping ratio $\zeta = 0.707$) and the approximate settling time of $1.8 - 2.1\ Te$ (Figure 5.3a).

This particular closed–loop tuning may be regarded as optimal in those cases where small overshoot and related well–damped behaviour are critical, such as in controlled electrical drives and related servo drive control applications. By choosing larger T_e value, the control system robustness is improved, and the noise sensitivity is decreased (i.e. bandwidth $\Omega_{BW} \approx 1/T_e$), but, in turn, a slower response and less efficient disturbance rejection are obtained.

For a reduced–order controller with the number of free parameters equal to r, only the dominant characteristic ratios $D_2, \ldots, D_{r+1}$ should be set to desired values. In this case, however, the non–dominant characteristic ratios (corresponding to non–dominant

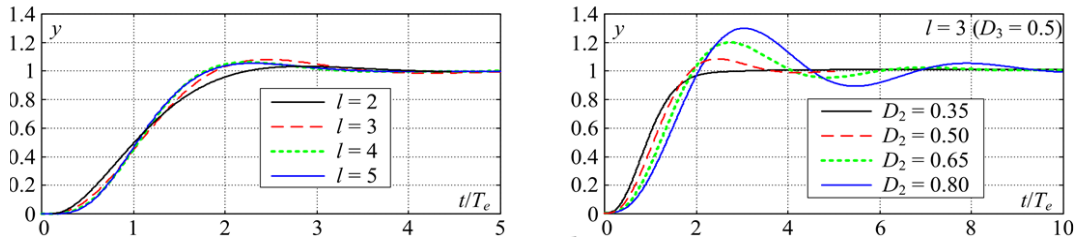

(a) (b)

Figure 5.3: Step response of prototype system tuned according to damping optimum (a) and illustration of closed–loop damping variation through dominant characteristic ratio D2 (b)

closed–loop poles) cannot be adjusted arbitrarily, so their effect to closed–loop damping should be analysed separately. In general, the response damping is adjusted through varying the characteristic ratios $D_2, D_3, \ldots D_n$, wherein the damping of dominant closed–loop dynamics (i.e. the dominant closed–loop poles damping ratio) is primarily influenced by the most dominant characteristic ratio D_2. By reducing the characteristic ratio D_2 to approximately 0.35 the fastest (boundary) aperiodic step response without overshoot is obtained. On the other hand, if D_2 is increased above 0.5 the closed–loop system response damping decreases (see Figure 5.3b).

5.3. DC bus voltage feedback control through ICE throttle command

As elaborated above, direct DC–bus voltage control can also be achieved by means of an ICE engine with DC bus voltage feedback used within a dedicated PID controller commanding the engine throttle angle command. The previously described linear engine model, simplified throttle dynamics model, and simple first–order lag voltage sensor model can be used for that purpose, thus forming the DC bus closed–loop model shown in Figure 5.4.

In the above model, the throttle unit delay and torque production dynamics can be lumped into a single time constant $T_{\Sigma ICE}$, which may also incorporate the sampling delay in the case of discrete–time (digital) controller [74].

$$T_{\Sigma ICE} = T_\theta + T_{IC} \tag{5.3}$$

$$T_{IC} = T_M + T_D + T_{AD} \tag{5.4}$$

which is integrated in the process model transfer function of model obtained by means of

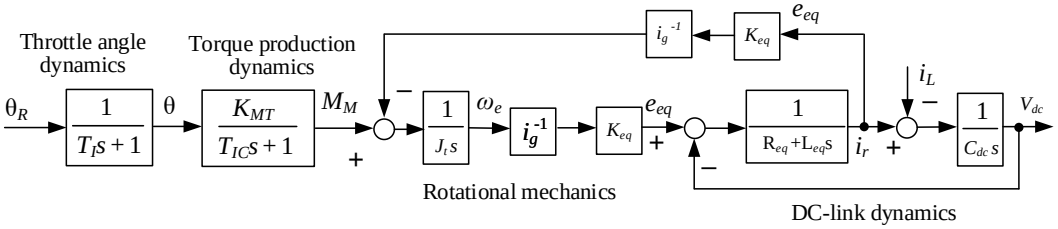

Figure 5.4: DC bus voltage control system process dynamics

transformations of the block–diagram in Figure 5.4:

$$G_p(s) = \frac{K_{MT}}{K_{PV}s(1 + T_{\Sigma ICE}s)(1 + T_{PV}s + T_{PV}T_{EQ}s^2)} \tag{5.5}$$

where

$$T_{PV} = \frac{JC_{DC}R_{EQ}}{K_{PV}K_{EQ*}} \tag{5.6}$$

$$T_{EQ} = \frac{L_{EQ}}{R_{EQ}} \tag{5.7}$$

$$K_{EQ*} = i_g^{-1}K_{EQ} \tag{5.8}$$

Thus obtained process model is of the fourth order, which might be a challenging task for the control system design based on proportional-integral-derivative (PID) controller. However, if its dynamics could be simplified to a third–order system, then it would be possible to derive explicit analytical expressions for the PID controller parameters, as in the case of PID control for the internal combustion engine, as shown in [185]. More precisely, if the second–order dynamic term

$$(1 + T_{PV}s + T_{PV}T_{EQ}s^2) = \Omega^{-2}s^2 + 2\zeta\Omega^{-1}s + 1 \tag{5.9}$$

would be characterised by $T_{PV} >> T_{EQ}$, then it might be approximated by the following first–order lag dynamic therm:

$$\frac{1}{(1 + T_{PV}s + T_{PV}T_{EQ}s^2)} \approx \frac{1}{(1 + T_{PV}s)} \tag{5.10}$$

Block diagram of the DC bus voltage feedback control system is shown in Figure 5.4, wherein a PID feedback controller is implemented. By equating the lower–order coefficients of the characteristic polynomial of the closed– loop system with the equivalent coefficients of the "prototype" damping optimum characteristic polynomial, the following expressions are obtained for the PID controller parameters:

$$T_E = T_I = \frac{1}{D_2D_3D_4}\frac{T_{PV}T_{\Sigma ICE}}{(T_{PV} + T_{\Sigma ICE})} \tag{5.11}$$

$$T_D = D_2 T_E \left(1 - \frac{D_2 D_3 T_E}{(T_{PV} + T_{\Sigma ICE})}\right) \tag{5.12}$$

$$K_R = \frac{K_{PV}}{K_{MT}} \frac{(T_{PV} + T_{\Sigma ICE})}{{D_2}^2 D_3 {T_E}^2} \tag{5.13}$$

$$K_{PV} = \frac{1}{i_g^{-1} K_{EG}} \left(J + i_g^{-2} {K_{EG}}^2 C_{DC}\right) \tag{5.14}$$

$$T_{PV} = \frac{J C_{DC} R_{EQ}}{K^*_{EQ} K_{PV}} = \frac{J C_{DC} R_{EQ}}{J + i_g^{-2} K^2_{EQ} C_{DC}} \tag{5.15}$$

Simulations are carried out based on the MVEM model of the internal combustion engine presented in Chapter 4 and used within the DC bus closed loop control system model. Figure 5.6 shows the DC–bus voltage control system responses with respect to rectifier (DC bus) load stepwise change from 0 A to 10 A and steady–state voltage reference of 48 Volts. The ICE responses show that the DC bus voltage control system featuring a PID feedback controller is characterized by a rather fast response: a speed drop after the disturbance is about 45 rpm and overall engine speed recovery lasts 0.4 s DC–bus voltage response is characterised by short transient of voltage drop (about 0.6 V) lasting about 0.25 seconds. Such favourable closed–loop system performance is mainly due to the fast action of the derivative term within the PID feedback controller.

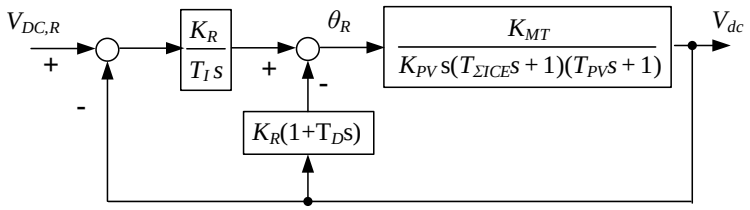

Figure 5.5: DC bus voltage control system

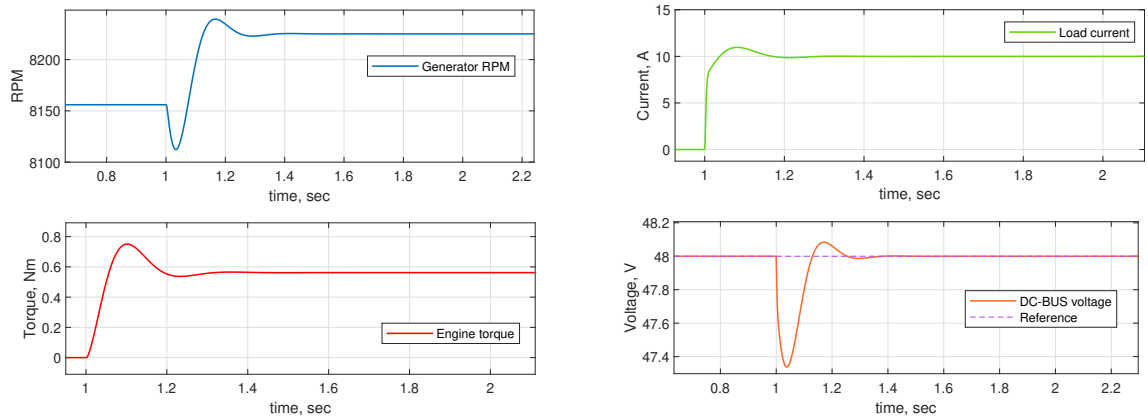

(a) (b)

Figure 5.6: Simulation results of ICE + BLDC generator DC–bus voltage control system with PID controller: ICE quantities (a), and BLDC generator quantities (b)

5.4. DC bus power sharing control system design

This section presents the primary and secondary level control of the common DC bus based on embedded voltage and current controllers within individual DC–DC power converters, and the superimposed load sharing control strategy, respectively. The design of individual controllers is based on the damping optimum criterion.

From the standpoint of designing of a superimposed controller, the inner closed–loop system tuned according to the damping optimum criterion may be approximated by the equivalent first–order lag transfer function model characterized by the closed–loop equivalent time constant T_e (under assumption of unit gain of the inner closed–loop system):

$$G_e(s) = \frac{1}{T_e s + 1} \tag{5.16}$$

This approximation is justified when the current and voltage controllers are tuned for well–damped response (with little or no step response overshoot), and if the power converter voltage control system operates in the linear mode, that is if the current load of the power converter is less that limit value. If current limit is reached, then the power converter output is saturated, and it behaves as the constant current source.

5.4.1. Primary–level voltage/current control

The primary level voltage/current control system is embedded within the DC–DC power converter unit, with the main functionality of output voltage control feasible up to the (externally adjustable) output current limit. This indicates that the primary–level control can be modelled by the transfer function model, valid in the case of output volt-

age control in the linear operating mode, and constant current source when output current–limit is reached.

This functionality is effectively obtained by the voltage/current cascade control system arrangement presented in Figure 5.7, illustrating the prospective DC–DC buck converter output voltage control system featuring proportional–integral (PI) voltage and current feedback controllers in the so–called cascade control system arrangement (see e.g. [160]). In this arrangement, the voltage PI controller commands the current reference to the inner current control loop.

This facilitates straightforward limiting of the buck converter current ic via the current limit I_{max} (either pre–set internally or provided externally). The buck converter voltage reference v_R is supplied from the superimposed secondary control level (see next subsection), wherein the voltage target is low–pass filtered in order to avoid unnecessary voltage reference step overshoots due to the PI controller zero ($S_z = -1/T_{cu}$)

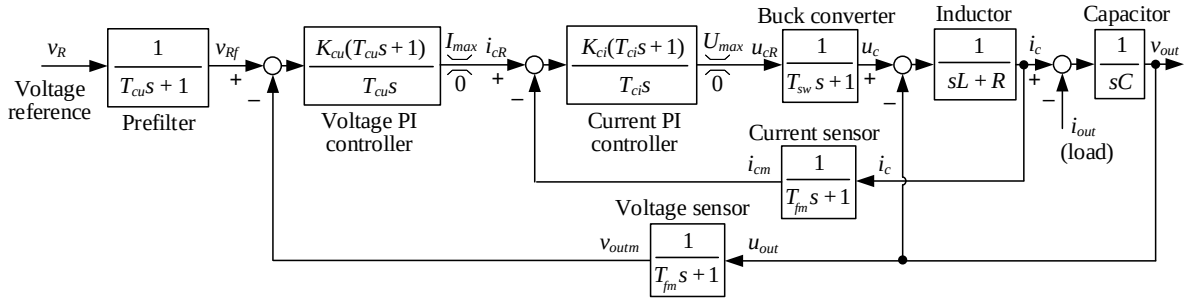

Figure 5.7: Buck converter cascade control system structure with voltage/current PI controllers

5.4.2. Secondary–level load sharing control

Figure 5.8 shows the block diagram representation of the load sharing control strategy, wherein a proportional–integral PI controller is used for DC bus voltage control based on DC bus voltage sensor feedback.

Again, the centralised PI feedback controller is designed according to the damping optimum criterion. For that purpose, the parallel–connected bank of voltage–controlled buck converters is assumed to have equal static and dynamic properties, i.e. to be characterised with equal voltage reference lags T_{eu}, as well as the blocking diode forward polarisation voltage v_F and dynamic resistance rd during diode conduction (forward biasing). In that case, the parallel–connected DC–DC power converter stack can be represented by the following equivalent model under forward biasing assumption for all blocking diodes:

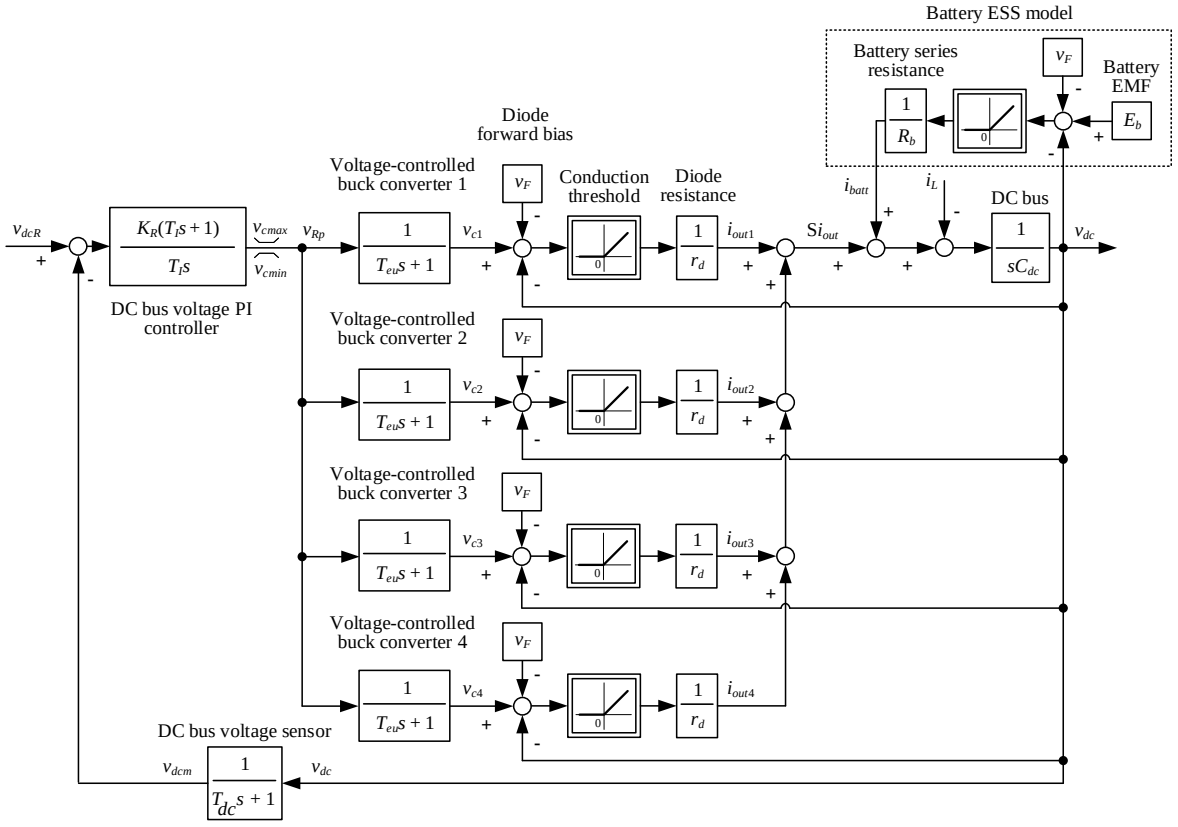

Figure 5.8: Block diagram of centralised load sharing strategy for DC bus voltage control

$$G_p(s) = \frac{\sum i_{out}(s)}{u_{rp}(s)} = \frac{1}{\frac{r_d C_{dc}}{n_{conv}} s + 1} \cdot \frac{1}{T_{eu} s + 1} \tag{5.17}$$

By lumping the DC bus voltage sensor time constant T_{dc} with the DC bus charging time constant $C_{dc} r_d / \nu_{conv}$, the resulting lag term with time constant $T_{\Sigma dc} = T_{dc} C_{dc} r_d / \nu_{conv}$(which may also include controller sampling effects in the case of digital controller) is used as a basis for PI controller damping optimum design. In the above case, the closed–loop transfer function characteristic polynomial reads as follows:

$$A_{cl}(s) = G_p(s) = \frac{T_{eu} T_{\Sigma dc} T_I}{K_R} s^3 + \frac{(T_{eu} + T_{\Sigma dc}) T_I}{K_R} s^2 + \frac{1 + K_R}{K_R} T_I s + 1 \tag{5.18}$$

By equating the above characteristic polynomial with the damping optimum characteristic polynomial, the following expressions for centralised PI controller parameters (closed–loop equivalent time constant T_{edc}, and controller proportional gain and integral time constant K_R and T_I) are obtained after some manipulation and rearranging:

$$T_{edc} = \frac{1}{D_{2dc} D_{2dc}} \cdot \frac{T_{eu} T_{\Sigma dc}}{T_{eu} + T_{\Sigma dc}} \tag{5.19}$$

$$K_R = \frac{T_{eu} + T_{\Sigma dc}}{D_{2dc} T_{edc}} - 1 \tag{5.20}$$

$$T_l = T_{edc}\left(1 - \frac{D_{2dc}T_{edc}}{T_{eu} + T_{\Sigma dc}}\right) \tag{5.21}$$

The proposed centralized controller–based load sharing strategy is verified by means of simulations in Matlab/Simulink. The load sharing strategy is also verified experimentally on the dedicated laboratory setup featuring off–the–shelf DC–DC buck converters [180] and lithium–polymer battery [179].

Figure 5.9 shows the responses of the buck converter cascade control system wherein the buck converter PWM voltage dynamics have been approximated by a linear first–order lag model in order to facilitate a more numerically efficient simulation of the power converter control system for subsequent analysis of the secondary–level control. Simulation analysis has been carried out for the case of load current step change from zero to 20 A. The buck converter output voltage v_{out} is characterized by a 0.9 V drop (3.75% drop from the target value $v_R = 24$ V), with output voltage recovery within 2.5 ms (top plot in Figure 5.10). Such favourable load suppression ability is obtained due to fast response of inner current control loop under voltage/current cascade control arrangement (middle and lower plot in Figure 5.10).

Figure 5.10 shows the simulation results of the centralised controller–based load sharing control strategy for two characteristic operating regimes: (i) the so–called small–signal regime (Figure 5.10a) characterized by a relatively small load change and operation of all buck converters well within voltage/current limit values, and (ii) the large signal regime (Figure 5.10b) characterized by large load change and buck converter operation at voltage/current limit values.

In the case of small signal operation, the centralised load sharing control system is characterised by a relatively small transient DC bus voltage drop after the DC bus load current change, particularly for a 20 A load current step, a 0.75 V DC bus voltage drop is observed (i.e. only 3.1% of the DC bus voltage target value of 24 V), characterised by 15 ms recovery time and settling within 50 ms of the load step instant (top plot in Figure 5.10a).

This control system performance is achieved primarily by means of DC–DC buck converter action, whose joint current supply to the DC bus i_{out}, commanded by the centralised PI controller via buck converter voltage reference change (bottom plot in Figure 5.10b) predominantly compensates for the transient DC bus voltage drop and stead–state load i_L in order to maintain the DC bus equilibrium state (middle plot in Figure 5.10a). The battery also compensates the DC bus load (albeit briefly) when the DC voltage drops below 23.3 V, because this effectively facilitates forward biasing of the BESS blocking diode. On the other hand, when the load sharing strategy operates in the large signal regime (characterised by 120 A load current step change), the DC bus voltage is characterised by a relatively small steady–state error of 1.1 V (4.6% of the DC bus

voltage target value), as shown in the top plot in Figure 5.10b This steady–state voltage drop is required so that the battery blocking diode forward bias voltage can be overcome, and as a result, the battery can supply the current excess with respect to the joint current limit of four buck converters connected in parallel ($\nu_{conv} I_{max} = 100$ A), as illustrated by the middle plot in Figure 5.10b.

Due to current limiting action of individual buck converters, the voltage command supplied by the superimposed PI controller cannot provide for the additional control authority, and is effectively limited to the maximum value of the buck converter output voltage (bottom plot in Figure 5.10b).

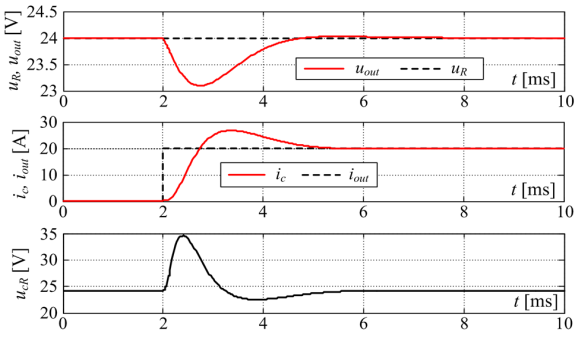

Figure 5.9: Simulation results of buck converter primary–level control system considered in secondary level power bus voltage control system validation

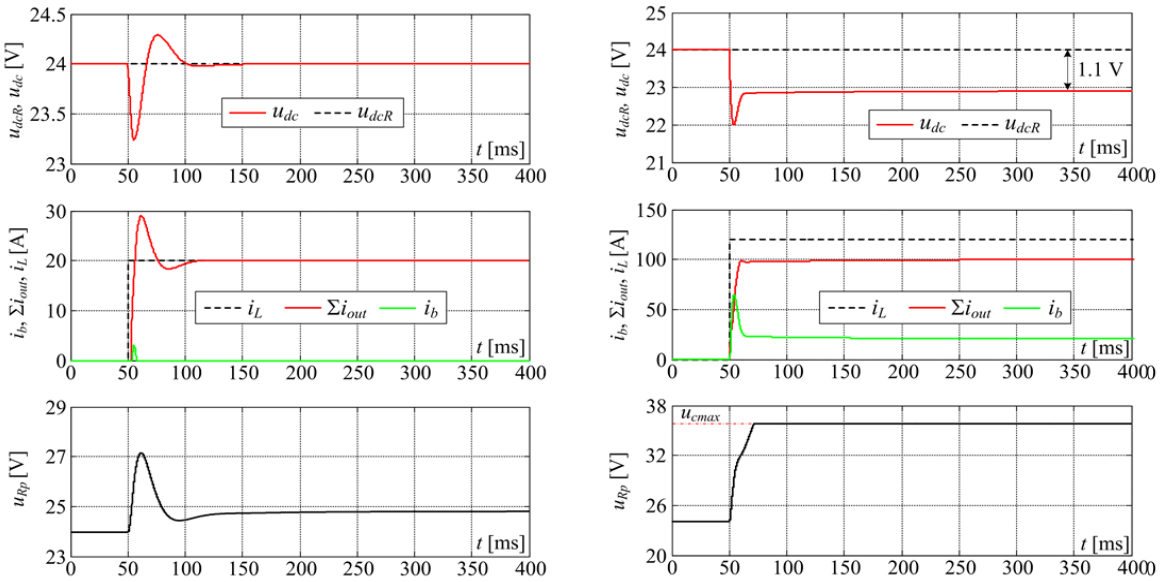

(a) (b)

Figure 5.10: Simulation results of centralised load sharing control strategy: small–signal regime (a) and large signal regime (b)

5.5. Hybrid multirotor control system design

Control system design is based on the developed multirotor mathematical model (see Chapter 2). In order to conduct the control system design, UAV model equations can be simplified based on following assumptions:

- Angular contributions to the accelerations depend on a multiple set of parameters, for near hover conditions a small angle approximation is used,
- Angular accelerations are dependent on change of angles with respect to f^E ,
- Transformation matrix $\mathbf{T}$ that defines the relation between the angular velocities with respect to f^E and the ones in f^B are close to the identity matrix, making the angular acceleration equations the same in f^E and f^B frames,
- Control algorithm provides control signals to propeller drives. With four controllable variables, it is not possible to regulate more than four DOF,
- Inner loop is controlling the altitude and attitude, while the outer loop is controlling quadcopter position by giving the attitude references to the inner loop.

The control of multirotor is achieved by means of two control loops:

- Rate Control, controls angular speeds ϕ, θ, ψ, by means of a 3–axis gyro
- Attitude Control, controls Euler angles ϕ, θ, ψ, by means of a 6–DOF or 9–DOF Inertial Measurement Unit (IMU)

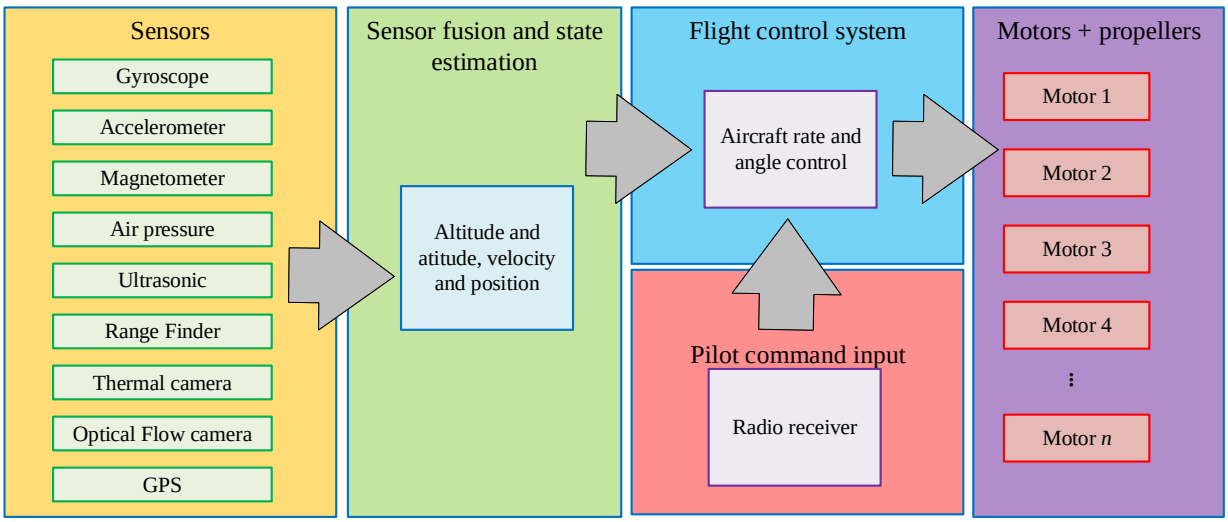

Figure 5.11: UAV signals and devices diagram

5.5.1. Rate Control (Inner Loop)

The Rate Control module performs PID control on angular rates ϕ, θ, and ψ, in order to achieve the steady–state match between the commanded references and sensor (feedback) signals. Input variables for these inner control loops can be divided in two parts, target or reference and sensor variables. Target variables are the desired altitude and yaw angle that are given by the task that multirotor needs to accomplish and desired roll and pitch angles, that are calculated in the outer control loop. Sensors give measured altitude, roll angle, pitch angle and yaw angle [92, 126, 43, 186]. When these reference rate targets are given by the RC command, the multirotor guidance mode is called acrobatic. Rate Controllers are usually given in the standard PI or PID form where the derivative part is often filtered by a Low Pass Filter (also known as Roll-Off Filter, see Figure 5.12). Outputs are saturated to a specific value (usually 100% of PWM duty cycle). Integrator anti–wind–up is also required in order to prevent controller error accumulation.

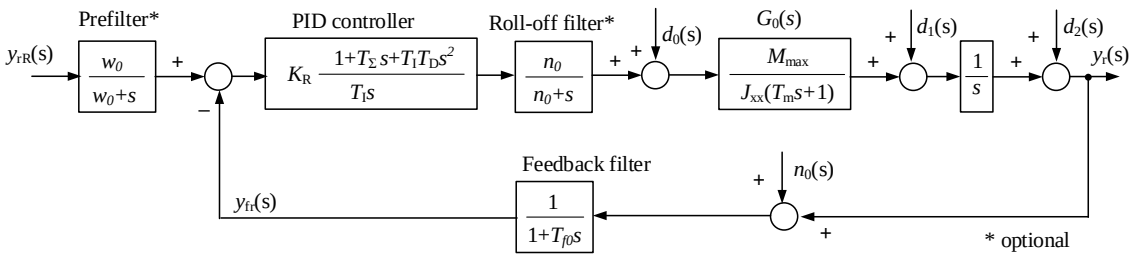

Figure 5.12: Inner loop – Standard angular velocity (rate) controller

The transfer function $G_0(s)$ corresponds to the transfer function from the normalized roll command (i.e. in range between –1 and 1) to the angular roll acceleration where $M_{\max}$ is the maximum torque, J_{xx} is the inertia in the particular axis of rotational motion, and the time constant T_m is related to the inherent lag between the acceleration and the torque. In order to prevent the reference overshoot due to the controller zero (or zeros in the more general case of parallel realization PID controller), a pre–filter can be included in the reference path.

In order to ensure system stability with zero steady state error, good disturbance rejection, high frequency noise attenuation and rapid system response, a PID rate controller (in form I+PD) is designed because for that case pre–filter can be omitted. The closed loop zeros can be optimised directly by adding a lead–lag term into the reference branch, i.e. feed forward control action can be used to independently condition the closed–loop system zeros. In order to simplify the control system design, time delays (lags) of the roll–off filter and feedback filter can be lumped together, thus resulting in the following

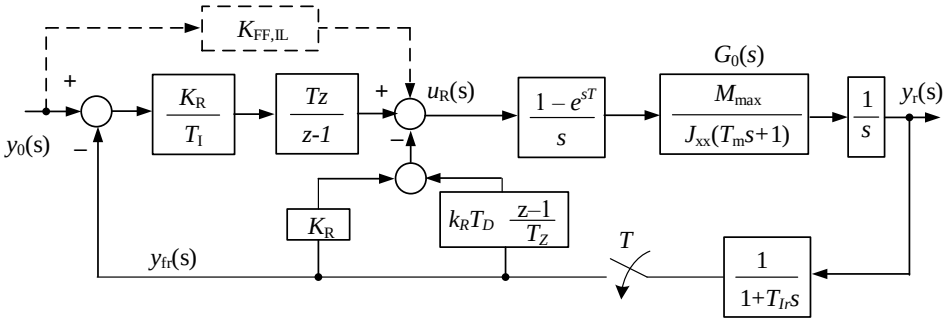

Figure 5.13: Inner loop – proposed modified angular velocity (rate) controller in the discrete–time (digital) form

fast "parasitic" lag term with equivalent time constant equal to the sum of filter lags:

$$G_{par}(s) = \frac{1}{1 + (T_{ro} + T_{fo})s} = \frac{1}{1 + T_{\Sigma o}s} \tag{5.22}$$

Based on above block diagram, the closed–loop system transfer function (feedback signal vs. the target value) is given in the following form:

$$G_{cr}(s) = \frac{y_R(s)}{y_0(s)} = \frac{1}{1 + T_I s + \left(T_D + \frac{1}{K_R K_P}\right) T_I s^2 + \frac{(T_{\Sigma 0} + T_p)}{K_R K_P} T_I s^3 + \frac{T_{\Sigma 0} T_P}{K_R K_P} T_{Ir} s^4} \tag{5.23}$$

By applying the damping optimum criterion–based control system design to the above closed–loop system model, the following expressions for controller proportional gain K_P, and integral and derivative time constants T_I and T_D q are obtained:

$$T_{er} = \frac{1}{D_{2r} D_{3r} D_{4r}} \cdot \frac{T_{\Sigma 0}}{1 + \frac{T_{\Sigma 0}}{T_P}} \tag{5.24}$$

$$T_I = T_e \tag{5.25}$$

$$K_R = \frac{1}{K_P} \cdot \frac{T_{\Sigma 0} + T_P}{D_2^2 D_3 T_e^2} \tag{5.26}$$

$$K_D = D_2 T_e \left(1 - \frac{D_2 D_3 T_e}{T_{\Sigma 0} + T_P}\right) \tag{5.27}$$

where D_{2r}, D_{3r} and D_{4r} are the damping optimum design characteristic ratios, while T_{er} is the control loop equivalent time constant (equivalent lag) which represents the dominant closed–loop dynamics for the upper–level (superimposed) control loop design. Feed forward control is realised by introducing a lead action to the reference signal. According to [185] optimal choice of $T_{FF,IL}$ is defined as $T_{FF,IL} = T_e\sqrt{1 - 2D_2}$. Feed-forward gain can be defined as:

$$K_{FF,IL} = \frac{K_R}{T_I} T_{FF,IL} \tag{5.28}$$

5.5.2. Attitude Control (Outer Loop)

Following the inner loop controller design, a similar method will be used for design of the outer loop control system, also called the attitude controller. Outer control loop is used because the multirotor is an under–actuated system and it is not possible to control all of the aircraft DOF directly. As mentioned before, the inner loop directly controls four DOF, those being three angles and altitude. To be able to indirectly control the aircraft position, an outer control loop is used. Outer control loop, as its outputs, provides desired commands of roll and pitch angles to inner control loops [92, 126, 43, 186].

The outer loop of the control system is known as the attitude controller. Attitude commands are interpreted from the input PWM radio signal and scaled to range in magnitude from –1 to 1. Attitude controllers are usually given in the standard PI or PID form (see Figure 5.14). Outputs are saturated to a specific value (usually 100% of PWM duty cycle). Integrator anti–wind–up is also required in order to prevent controller error accumulation. Saturation limits are also applied to the PID controller such that the output of the attitude controller is bounded from –1 to 1. The attitude controller acts as an outer loop to the rate controller by passing the output signals to the rate controller as command data.

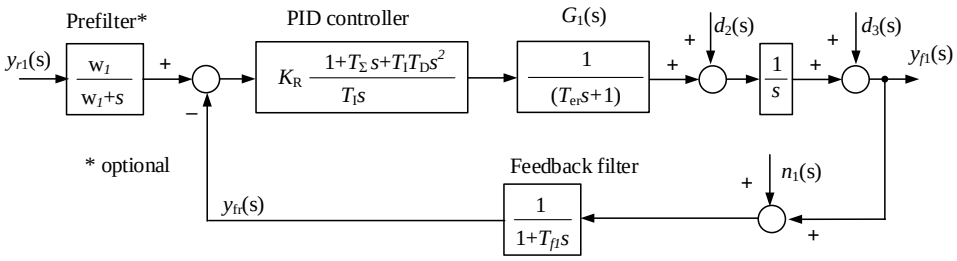

Figure 5.14: Outer loop – Standard angles (attitude) controller

As in the case of inner control loop, the most frequently used outer loop controllers are of PID–type, as shown in Figure 5.14, wherein the dynamics of the inner rate control loop $G_1(s)$ can be approximated by the first–order lag term

$$G_{cr}(s) \approx \frac{1}{1+T_{er}s} \tag{5.29}$$

which is valid if the closed–loop is tuned for well–damped behaviour by setting the closed–loop characteristic ratios to so–called optimal values $D_{2r} = D_{3r} = D_{4r} = 0.5$. Based on the block diagram in Figure 5–18, the following closed–loop model (feedback signal vs. reference value) is obtained:

$$G_{c1}(s) = \frac{y_{f1}(s)}{y_{R1}(s)} = \frac{1}{1+T_R s+\left(+\frac{T_R}{K_R}\right)s^2+\frac{(T_e+T_\Sigma)}{K_R}T_R s^3} \tag{5.30}$$

Discrete–time form of the control system, extended by a feed–forward proportional action (gain) in the reference path is shown in Figure 5.15.

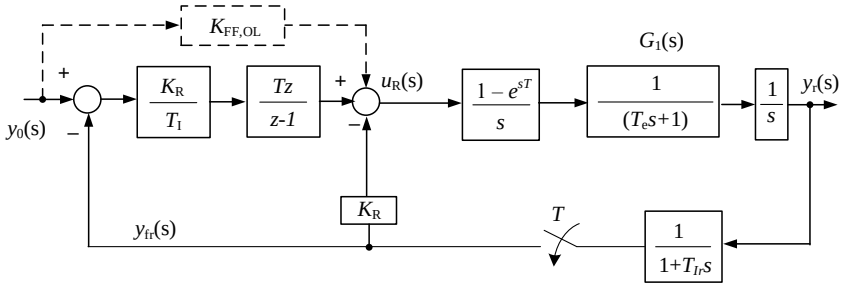

Figure 5.15: Outer loop – proposed modified angles (attitude) controller

By applying the damping optimum criterion–based control system design to above closed–loop system model the following expressions for controller gain K_R, and time constants T_{ea} and T_R are obtained:

$$T_R = T_{ea} = \frac{T_{er} + T_\Sigma}{D_2 D_3} \tag{5.31}$$

$$K_R = \frac{1}{D_2 T_e} \tag{5.32}$$

where D_2, and D_3 are the damping optimum design characteristic ratios, while T_{ea} is the attitude control loop equivalent time constant (equivalent lag). Feed forward control is realised by lead action to the reference signal, in a similar manner as for the rate controller. According to [185] optimal choice of T_{FF} is defined as $T_{FF} = T_{ea}\sqrt{1-2D_2}$. Feed-forward gain can be defined as:

$$K_{FF,OL} = \frac{K_R}{T_I} T_{FF,OL} \tag{5.33}$$

The behaviour of the controlled UAV system depends on the dynamic model of the multi rotor and the control algorithm. Generally speaking, PI(D) control with feed–forward action shows notable improvement in control system response speed and tracking of fast changing reference.

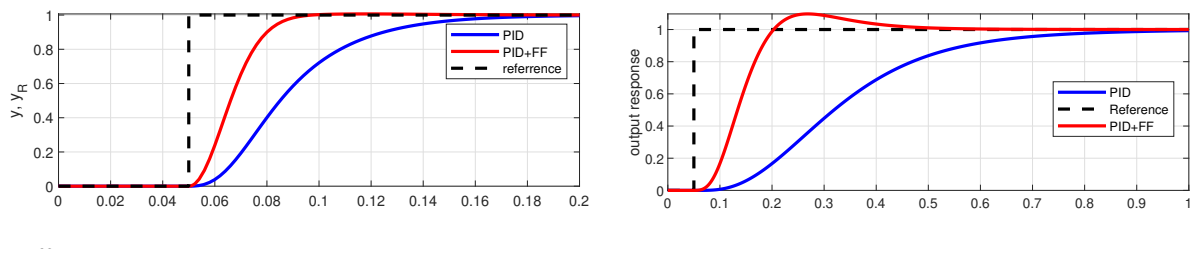

(a) (b)

Figure 5.16: Simulation results rates (a) and attitude (b) controllers

6 Experimental validation

This chapter describes the design and development of the proposed hybrid propulsion system for an unmanned aerial vehicle. In addition to the description of hardware implementation, the firmware (software) development is also presented utilising a rapid prototyping / fast development technique based on dedicated Matlab/Simulink toolboxes. Ultimately, the entire system was tested under realistic electrical load conditions in order to demonstrate its functionality.

6.1. Hybrid power unit

The proposed structure (topology) of the hybrid electrical power source (see Figure 6.1) is based on the controlled Internal Combustion Engine (ICE)–Direct Current (DC) generator set, wherein the increase of the load current (load demand at the common DC bus) requires an increase of both the speed and the developed torque of the ICE in order to deliver the required power to the common DC bus. A lithium–polymer battery with suitable number of cells (i.e. terminal voltage) is connected in parallel to the DC current generator (DC electricity generator equipped with a rectifier unit) on the common DC bus in order to achieve a synergistic effect where the battery would cover for peak energy requirements and respond quickly to pulsed load demands that the IC engine – generator set would be too slow to follow.

The experimental setup (photograph shown in Figure 6.2) consists of the frame that holds all components together. The setup comprises the engine–generator set connected to the common axle using a claw coupling and equipped with mechanical dampeners and springs, optional Direct Current to Direct Current (DC–DC) power converters, a Lithium Polimer (LiPo) battery, 0.5 litre graduated cylinder tank, and various electronic circuitry including the main processing unit (programmable microcontroller) and data acquisition processing unit (in the form of an additional programmable microcontroller), both programmed and monitored through a host portable computer running Matlab/Simulink software environment. Table 6.2 lists the key parameters of individual components used in the setup, along with brief descriptions of these components.

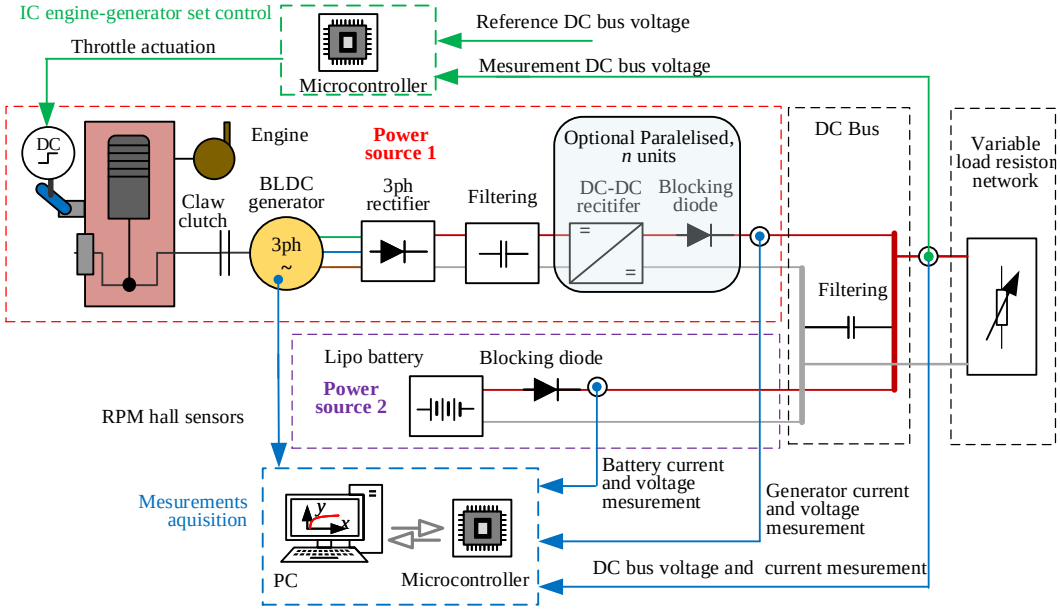

Figure 6.1: Schematic view of experimental setup

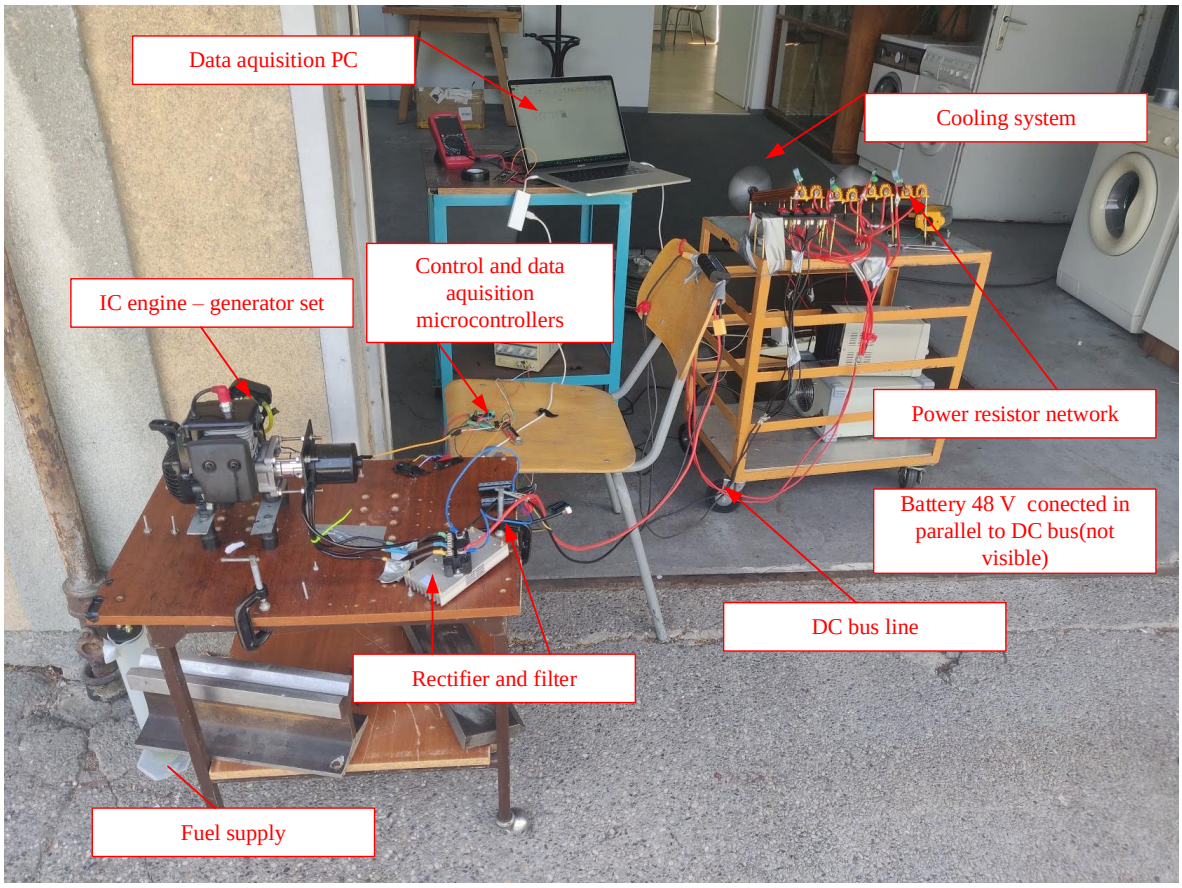

Figure 6.2: Photographs of laboratory experimental setup

Table 6.1: Parameters of experimental setup

Component	Description
Throttle actuator	Stepper motor, 5 V, high torque, separately powered
RPM sensor	Output of one hall, pull up logic, counting of impulses to determine speed
Current sensor	ACS758 hall effect sensor, 100 A, 3 qty
Voltage sensor	Voltage divider with ratio 22.3, 0.1% tolerance 0.5 W resistors
Diode	High voltage Schottky rectifier diode, $V_f = 0.37$ V, $I_{max} = 250$ A
Load switches	Logic level n–channel MOSFET, IRLZ44, $V_{dss} = 60$ V, $I_d = 27$ A
Filter Capacitators	1200 uF, electrolytic, 63 V
Battery	LiPo 10000 mAh, 25C, 12s
Computer and Microcontroller	Host computer: MacBook Pro 2018 with running Matlab/Simulink, Microcontroller: Arduino Mega, 2 qty.
Cooling fans	6–inch racing multirotors prop–motor set, 3 qty.

For the microcontroller used within the control and data acquisition system, the original idea was to implement a single microcontroller unit, using Matlab/Simulink Arduino support toolbox for code generation and data acquisition. However, this approach proved to be underpowered (in terms of code execution speed) for such requirements. To that end, separate microcontrollers needed to be used for the control and data acquisition/telemetry tasks (see Figure 6.3). The microcontroller used to execute the control algorithm is equipped with a DC–bus voltage sensor in order to provide DC voltage measurement needed for the proportional-integral-derivative (PID) feedback controller (see previous chapter). Moreover, this microcontroller also provides the actuation signal for the ICE throttle valve (by outputting suitable PWM signal) and running the control loops for generator rotational speed (output voltage) and the common DC bus power distribution strategy. In particular, by actuating the IC engine throttle, its rotational speed (and torque) are adjusted in turn, thus conditioning the overall power output of the hybrid system. To that end, the control system implemented on the target microcontroller manages the power flow from the battery and the generator in order to maintain the output power

availability all the times. This encompasses both the maintaining of steady–state balance between different power sources, as well as dynamic allocation of loads to individual power system sub–units during dynamic transients.

The second microcontroller is then used for data acquisition only. It is equipped with current sensors for the generator current, battery current, DC–bus total current, rpm hall sensor and DC bus voltage sensor. Data acquisition is performed within Matlab/Simulink software environment, using the so–called "external mode" execution of the simulation model, wherein the embedded microcontroller system are signal acquisition and processing, managing communication with the control PC and facilitating real–time telemetry.

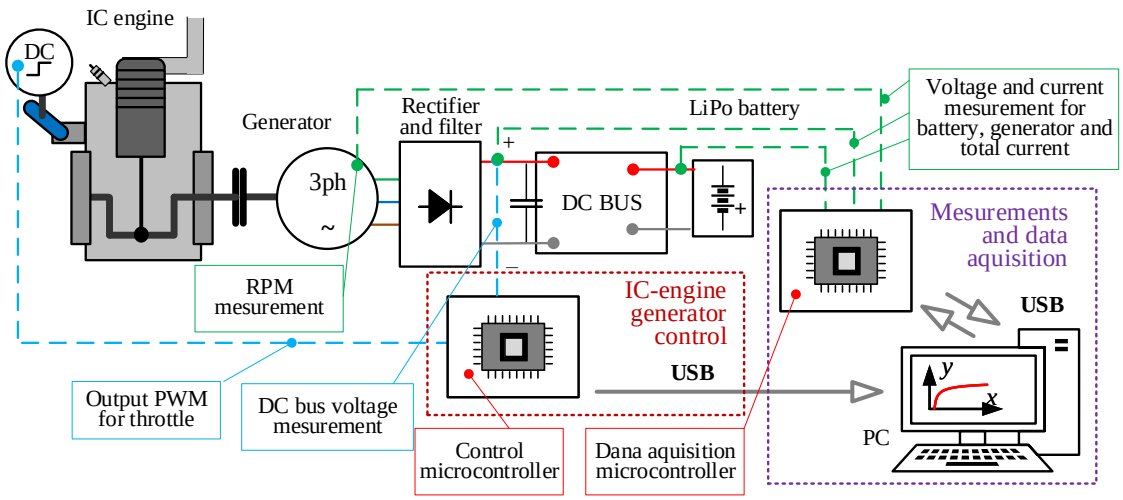

Figure 6.3: Principal schematic of connections of microcontrollers used for control and data acquisition

The processing core of the embedded microcontroller system is based on the ATmega2560 (16 MHz) microprocessor [187] (see Figure 6.4). This lightweight board has miniature size (38x52mm), and it is equipped with 16 MHz quartz–based clock generator. For USB connectivity, microcontroller uses onboard CH340G integrated circuit as the converter between UART and USB communication, which is capable of providing stable data exchange. For debugging and flashing the firmware a ST–LINK USB debugger/flashing tool is used [188] (see Figure 6.4). This tool allows real–time debugging and examination of processor memory locations, which is highly useful for programming and rapid software development. All of acquisition, control and telemetry algorithms are implemented in C++ for microcontrollers, which is the standard Arduino processor family programming environment by using Microsoft Visual Studio as IDE and GCC C/C++ compiler for executable code generation. For hardware in the loop testing, a microcontroller was interfaced with the PC and other systems, as shown on Figure 6.3. For fast development a Matlab/Simulink support package for Arduino was used, resulting in firmware

update being directly built from the Simulink environment. Also, it is possible to run the developed program in the so–called "external mode" that enables bidirectional communication between PC and microcontroller, and also live tuning of program parameters. Moreover, when used in the external mode, Simulink can visualize real–time data from sensor measurements.

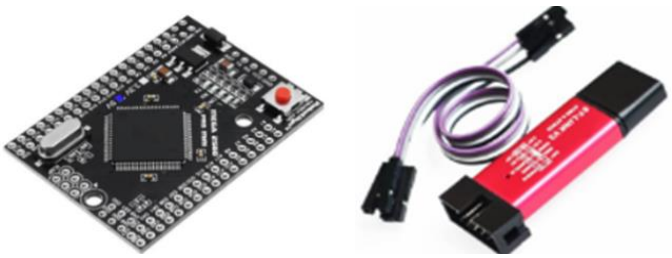

Figure 6.4: Microcontroller and debugging tools

Table 6.2: Microcontroller specifications [187]

Property	Description
Microcontroller	ATmega2560, 5 V Logic Level, 16 MHz Clock
Power IN	DC Jack 9–12 V
Power Consumption	5 V, 220 mA
Digital I/O, Analog I/O	54, 16
Memory Size	256 kb
Data RAM, Data ROM Type/Size	8 Kb, 4 Kb
Interface Type	ISP
Operating temperature	from −40 °C to 85 °C
Length Width	38×54mm

Data acquisition system was developed by using Matlab/Simulink software and Arduino support package. With Matlab/Support Package for Arduino it is possible to interactively communicate with an Arduino board (in this case ATMega pro mini). The package enables to acquire analog and digital sensor data, control other devices with digital and PWM outputs, drive DC, servo, and stepper motors, access peripheral devices and sensors connected over I2C or SPI, communicate with an Arduino board over a USB cable or wirelessly over Wi–Fi. It is also possible to build custom add–ons to interface

with additional hardware and software libraries. Figure 6.5 shows the Matlab/Simulink graphical user interface–based program for the microcontroller. The program includes several separate modules:

- DC bus voltage reading with signal filtering,
- DC bus total current reading with signal filtering,
- Generator current reading with signal filtering,
- Battery current reading with signal filtering,
- RPM reading from hall sensors with signal filtering,
- Communication by serial port and radio telemetry (optional),
- Other auxiliary functions such as on/off switches and similar (optional).

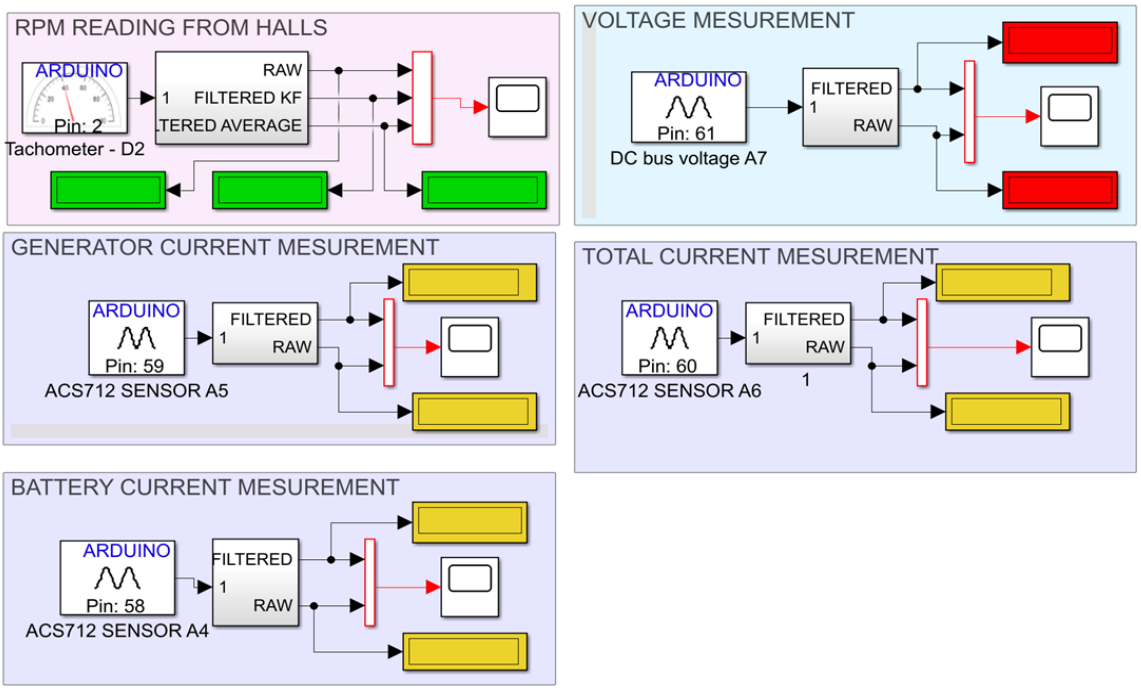

Figure 6.5: Software for microcontroller implemented in Simulink

As a current sensor, an ACS758 hall effect sensor rated for DC currents up to 100 A has been used. A simple function for current and voltage measurement is implemented utilising stock Simulink block, such as gain, and specified Arduino blocks such as “analog read”. As shown on Figure 6.6, the input signal is subtracted and then divided by a sensitivity factor. A moving average filter is used to smooth the final result.

DC bus and battery voltages are measured utilising simple voltage divider circuit s consisting of two resistors: resulting in the attenuation ratio 1/22.3 (see Figure 6.7). The

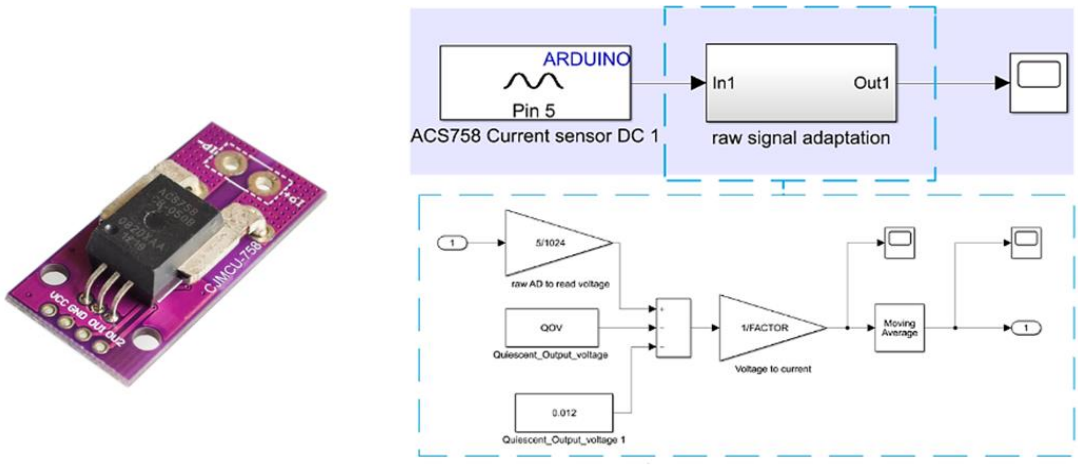

Figure 6.6: Current measurement sensor photograph [189, 190], application circuit and Simulink implementation

attenuated voltage divider signal is first fed to the Analog to Digital Conversion (ADC), then scaled to voltage and multiplied by the voltage divider inverse attenuation ratio.

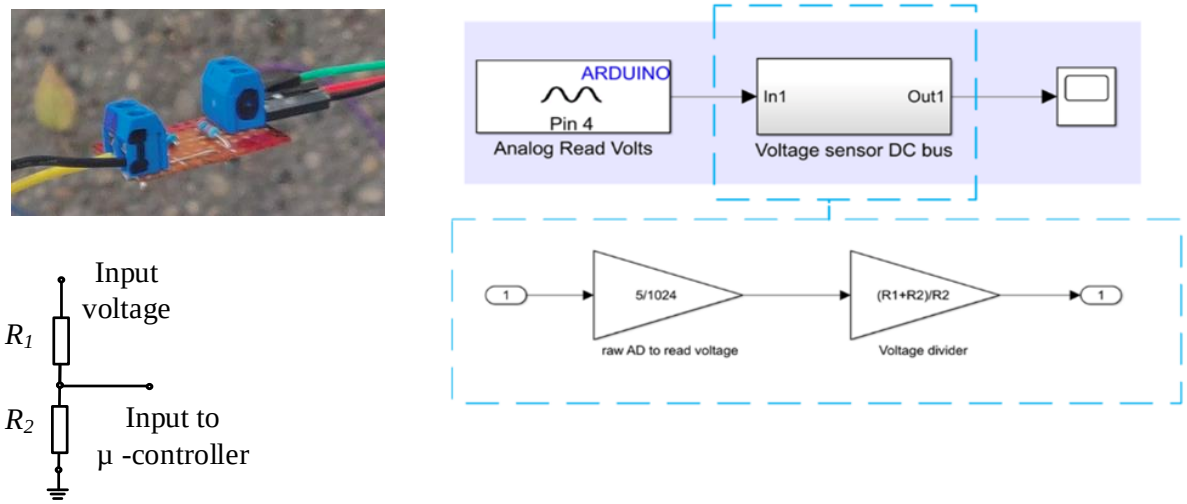

Figure 6.7: Voltage measurement sensor photograph, application circuit and Simulink implementation

The selected DC machine is equipped with three hall sensor signals in order to determine rotor position for electronical commutation when used as motor. For speed measurement, one hall signal is sufficient, and it is used for measuring the rotational speed or RPM of the engine (Figure 6.8). One full rotation corresponds to 7 pulses. Sensor output requires pull up resistor in order to produce proper square signal of active hall.

The throttle unit (throttle valve) of the combustion engine is controlled by a low–power servo motor (see Figure 6.9) powered by an isolated DC–DC converter (with 5V output) [191], while the servo motor driven axle [192] is directly linked to the lever which controls

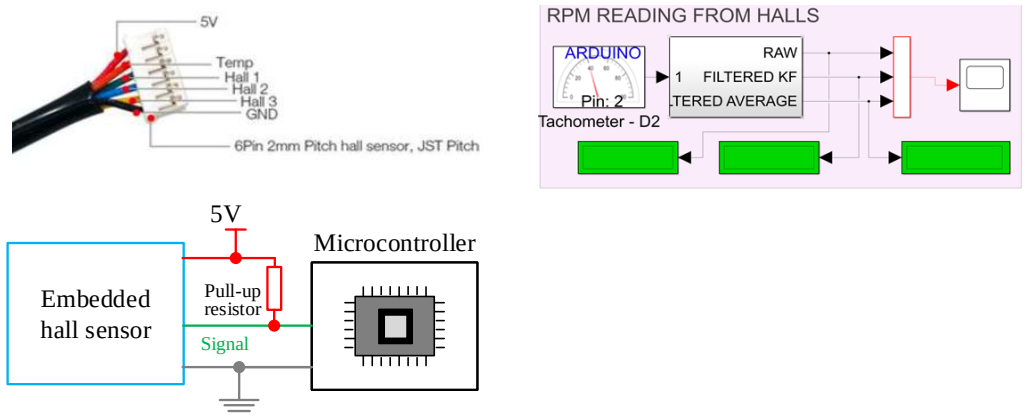

Figure 6.8: Revolutions per minute (RPM) measurement photograph [176], application circuit and Simulink implementation

the volume of the fuel–air mixture injected into the engine cylinder. The throttle servo drive reference position signal (target throttle valve opening) is defined by means of Pulse Widith Modulation (PWM), characterised by 50 Hz repetition rate, and pulse width between 1 ms and 2 ms. The aforementioned static and dynamic relationships between the PWM signal and throttle angle were recorded experimentally using the laboratory setup.

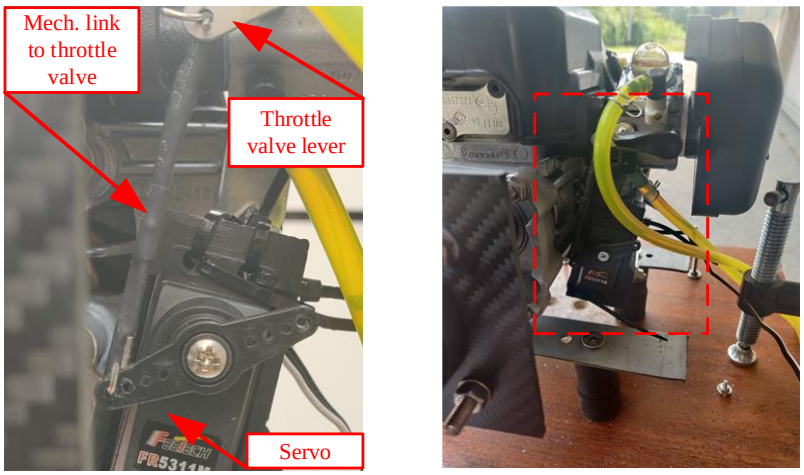

Figure 6.9: Throttle servo mechanical connection

One of most important parts of the test setup is the so–called “claw” coupling for the interconnection between the IC engine and the electricity generator. From many test and trials, it has been determined that coupling needed to be at least 40mm in diameter and rated for at least 15 Nm. All smaller, and, thus, weaker couplings have failed the full throttle/full load tests. In order to have a safe and reliable connection between the IC engine and generator, the coupling is mounted using an appropriate adapter with conical hole on the engine side in order to connect it to the engine shaft (Figure 6.10a). On the

generator side, coupling must be fixed using a screw characterised by sufficient strength in order to withstand the aforementioned load torques (locking pins, see Figure 6.10b).

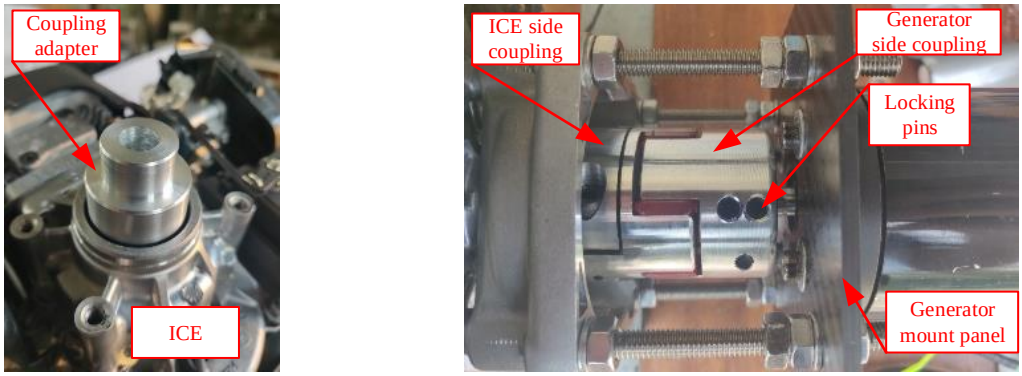

(a) (b)

Figure 6.10: Coupling of ICE and electrical genrator: (a) engine side adapter for claw coupling mount, (b) mounted claw coupling

Since the primary purpose of the battery in the hybrid–electric unit is to provide high–magnitude peak currents during load transients, it is necessary to have an appropriate battery management system. Battery cells monitoring has been implemented by way of measuring the terminal voltage for each cell and measuring battery pack temperature. The battery terminal voltage also defines the maximum speed of the engine–generator set if it is directly connected to the same common DC bus as the battery. Namely, when the generator generates its terminal voltage which would exceed the battery terminal voltage, the current would start to flow into the battery unless a blocking diode or a DC–DC converter is used at the DC bus interface to effectively decouple the battery from the DC bus and to restrict the battery charging current. Generally speaking, generator electrical load at the DC bus side results in a proportional load torque produced by the generator at the engine side, thus effectively restricting the engine rotational speed.

6.2. Experimental results

A total of two different tests were conducted to validate the effectiveness of the proposed control systems. The first test was performed for the purpose of characterizing the fuel consumption of the plant under load in order to be able to assess the applicability of the plant. The second test shows the effectiveness of the proposed DC bus voltage control system. In total, system was tested on 4 different loads: 4 Ω, 2 Ω, 1.33 Ω and 1 Ω, which corresponds to a power development of 600 – 2400 W at the operating voltage ranging between 46 and 50 Volts.

6.2.1. Engine fuel consumption measurement

For the purpose of measuring engine fuel consumption, the previously described test setup was used. Fuel consumption was measured at the engine idle regime first, and then at five characteristic points that designate the power range from 300 to 1700 W. Electrical power produced by the generator unit was dissipated by the power resistor network, while the developed electric power was measured by using a suitable DC wattmeter (see Figure 6.11).

Figure 6.11: Fuel consumption measurement

Each test was performed in steady–state stationary load conditions, where the engine was kept in the particular operating regime for a certain time (approximately 5 minutes). The initial and final volumes of fuel for each cycle were measured on the graduated cylinder tank. (see Figure 6.11). A total of five tests per regime were conducted. The obtained results are shown in the Figure 6.12, which indicate that fuel consumption characteristic is practically linear with the engine–generator unit electrical load.

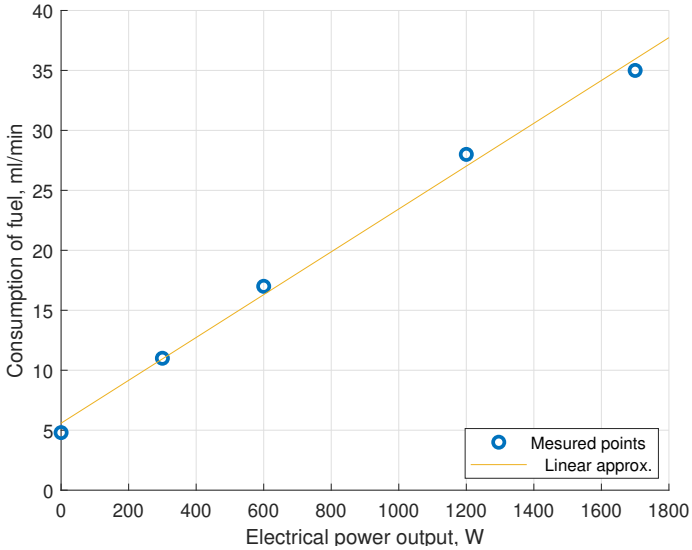

Figure 6.12: Fuel consumption measurement

6.2.2. DC bus electrical power measurements

To test the functionality of the proposed concept, hybrid power system was tested in no–load, low load, medium load and high load operating modes. The voltage reference is set to 50 V. The PID DC bus voltage controller was implemented in the C programming language complying to the proposed PID algorithm structures presented in Chapter 5. Based on the previous experience (and issues with mechanical failures of couplings), DC bus controller gains were set to slightly lower values than those obtained by the analytical design procedure presented in Chapter 5, thus resulting in slower responses and less abrupt throttle servo unit control efforts, ultimately assuring safe operation of the overall setup. Each test was repeated five times and consists of following ICE–generator set operating regimes:

- No load condition,
- 4 Ω load (low load),
- 2 Ω load (medium load),
- 1.33 Ω load (high load),
- 1 Ω load (peak load).

During tests, ICE is initially held in idle conditions for approximately 5 minutes in order to warm it up, and then its power was stepped up and down, holding it at constant values for several seconds for each load step.

Responses for the case of no–load conditions are given in Figure 6.13. The engine is kept at idle, corresponding to approx. 4000 rpm, with the throttle kept at minimum corresponding to PWM command of 130. In this case, the DC bus voltage is defined by the battery terminal voltage amounting to approximately 50V, with no noticeable current flowing through the DC bus. Small oscillations in engine–generator RPM are present at idle due to engine stroke–based operation. Offsets in current measurements are due to non–ideal sensor characteristics, notably emphasised while measuring low (near–zero) currents. In realistic implementations, these offsets would need to be removed by periodic re–calibration of current sensors, while during tests they could easily be subtracted from subsequent measurements under loaded engine–generator set conditions.

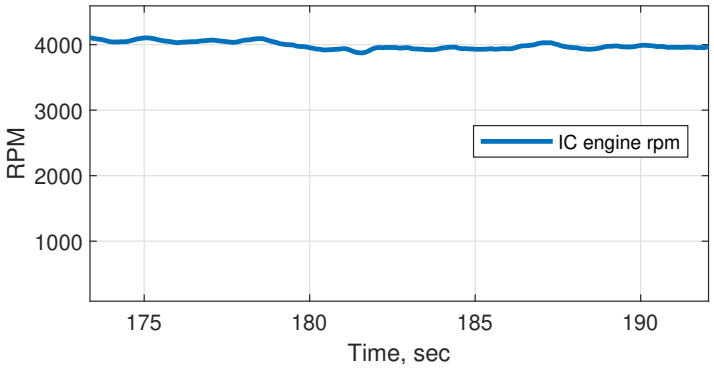

(a)

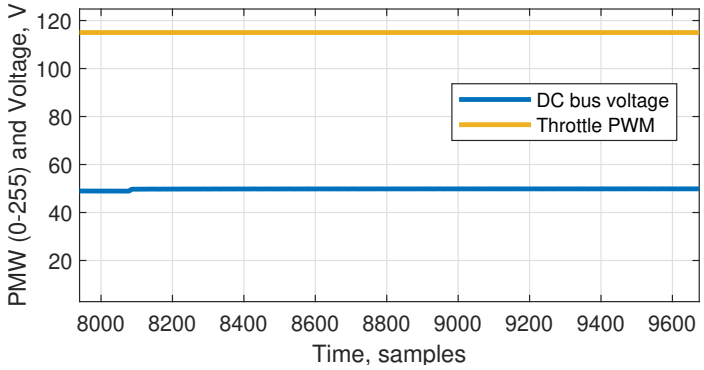

(b)

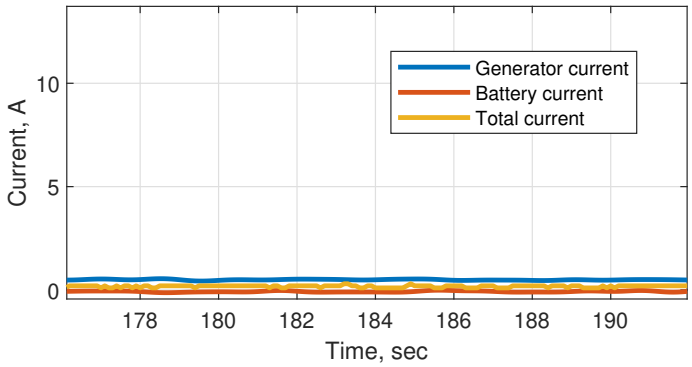

(c)

Figure 6.13: No load response

Low load responses are presented in Figure 6.14, with voltage reference set near 50V. Initially, the load consumes power from the battery (139 sec – 143 sec), but as the engine speed (rpm) increases from idle to around 10000 rpm, generator takes over the load and battery current drops to zero.

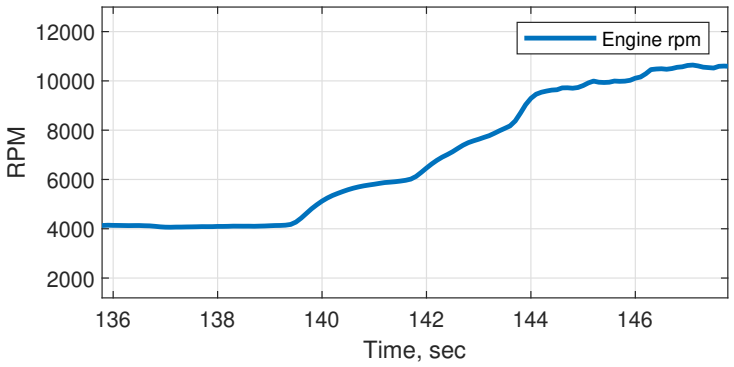

(a)

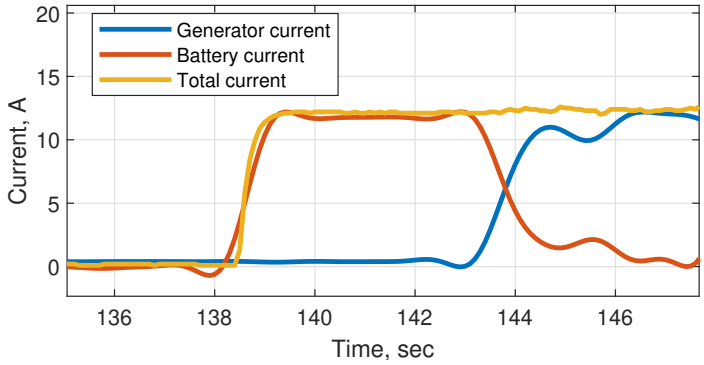

(b)

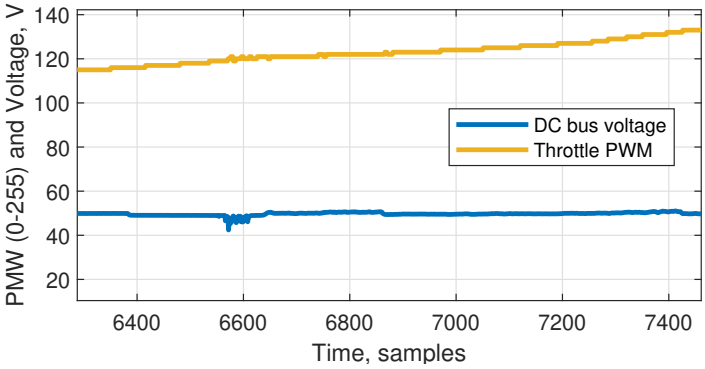

(c)

Figure 6.14: Small load (4 Ω) response

Results for medium high and high load regimes are shown in Figure 6.15. Engine ramps up its rpm to approximately between 13500 rpm and 14000 rpm. As in the case of low load, battery initially supplies the current to the load until the generator takes over. During testing, maximum current output of the generator itself (after the battery current drops to zero) is around 30 – 35 A, which corresponds to 1500 – 1750 W of power consumption at the load resistor network.

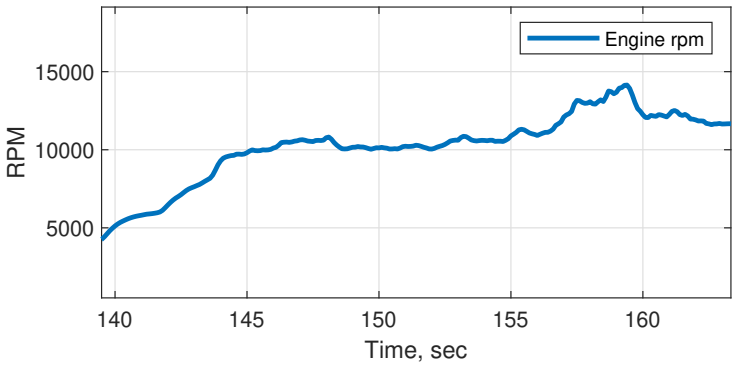

(a)

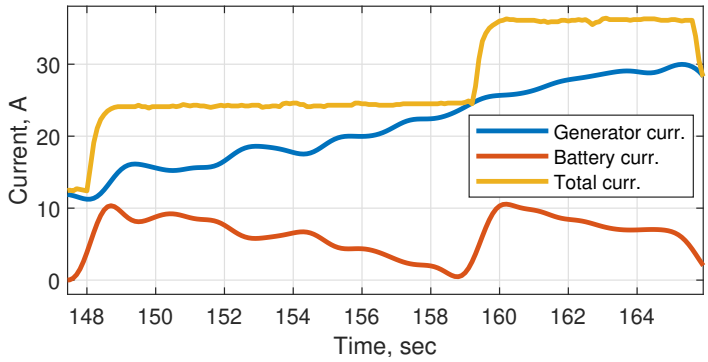

(b)

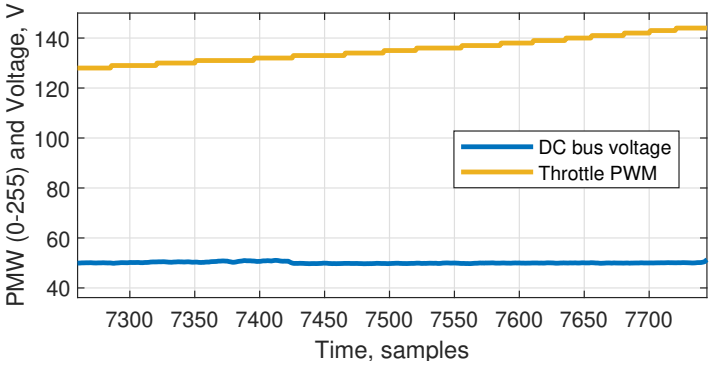

(c)

Figure 6.15: Medium load (2 Ω) and high load (1.33 Ω) response

Results for the case of peak load are shown in Figure 6.16. Due to limited engine–generator set power output, the battery feeds the additional current (approx. 16 A) to the load when the generator maximum current (30 A) is reached. In this case, the overall hybrid power system produces the maximum power, amounting to 2400 – 2500 W of total power output.

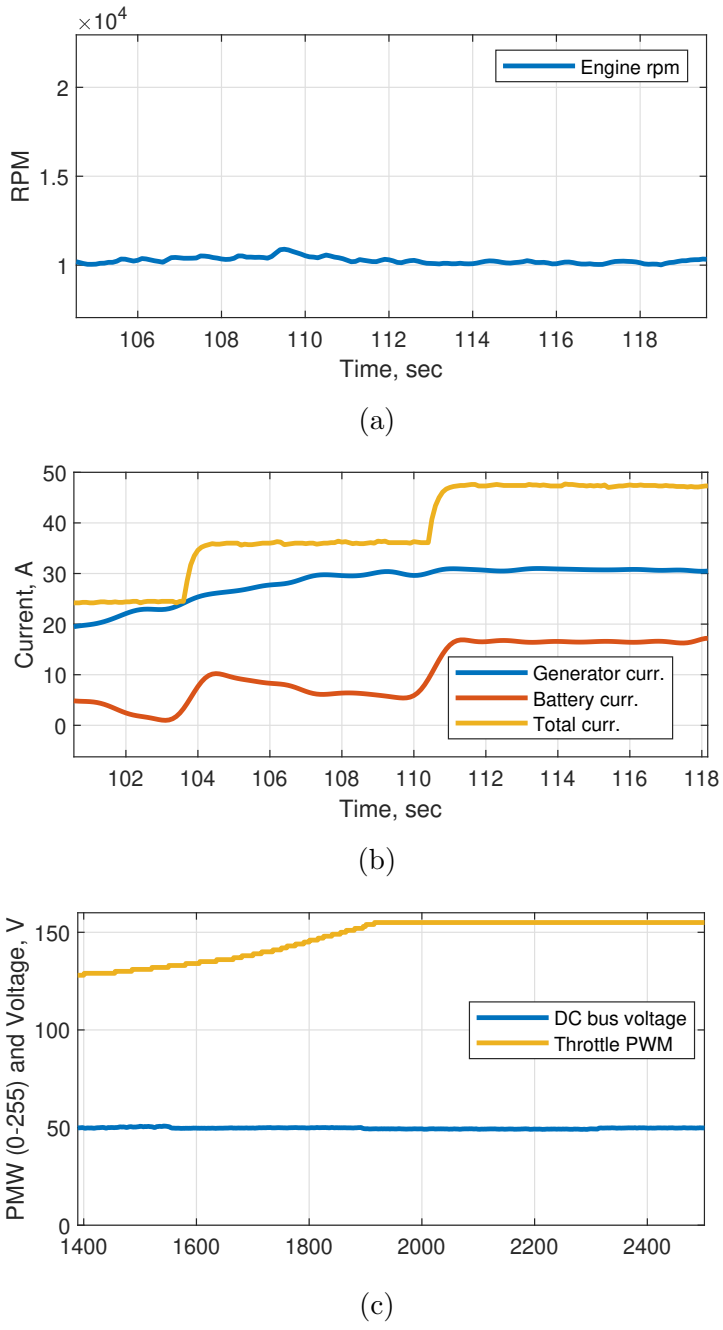

Figure 6.16: High load (1.33 Ω) and peak load (1 Ω) response

It can be concluded that the developed hybrid power system comprising an internal combustion engine–generator set and lithium polymer battery is functioning as expected. The DC voltage is relatively stable and is fully maintained by the power output of the ICE–generator set right up to 1700 W of electrical load. For larger loads, the battery pack supplies the additional energy to the DC bus, and a total of 2200 W (in best cases up to 2.5 kW) is obtained from the hybrid power system. The generator can continuously give up to 1200 W without significant heating or additional problems. At higher powers (> 1500 W) heating of the generator (up to 85 °C) was noticed, which should be further investigated.

Since the generator is completely closed, it is possible that there is no adequate cooling of the stator windings. It has also been observed that the PID control works relatively poorly in the engine idle state. This is the result of the non-linearity between the throttle and the realized torque (i.e. engine speed). The problem can potentially be solved with an adaptive controller. Mechanical vibrations of the setup are most emphasised in the engine idle mode, but even then, they are within safe limits that would guarantee no interference with the inertial measurement unit of a prospective hybrid propulsion–based UAV. This was tested using a Pixhawk flight controller, in particular the embedded vibration measurement implemented within the Ardupilot software [193]. No significant vibrations were observed at the anticipated engine operating point corresponding to approximately 10500 rpm. The overall efficiency of the presented hybrid power supply can be estimated as follows:

$$\eta_{ov} = \frac{P_{el}}{P_{mech}} \tag{6.1}$$

where P_{mech} is the mechanical power at the ICE output, and P_{el} is the electrical power dissipated at the load. According to the engine torque curve, the engine can produce 1.8 Nm of torque at 10500 rpm, which corresponds to 1980W of mechanical power. Electrical power obtained at that condition is 1500 W, so the overall efficiency of the generator + battery power system is estimated to be 0.75.

6.3. Analysis of hybrid vs conventional power unit

The analysis of the efficiency of a hybrid drive in relation to a conventional drive is based on the energy obtained within a certain reference interval. In order to be able to compare the amount of energy contained within the battery and that of the hybrid drive in a straightforward manner, the equivalent hybrid drive energy capacity in Wh was calculated based on the recorded data and compared with values of energy capacity of typical batteries for UAV applications.

According to the obtained fuel consumption measurement, engine consumes approximately 30 ml/min of fuel while producing 1500 W of power at medium to high loads. For one hour of operation, internal combustion engine consumes about 1.8 litres of fuel. Therefore, 1500 Wh are available in total with the overall mass of the hybrid power unit (engine, generator, rectifier, fuel) of 6 kg.

The UAV battery pack used in these tests can provide about 400 Wh of energy (as shown in Chapter 4, battery identification), whereas the total mass of the battery and the supporting equipment is about 3 kg. In order to meet the energy level of the hybrid power unit, a total of 4 battery packs are required (which would increase the battery system mass to 12 kg).

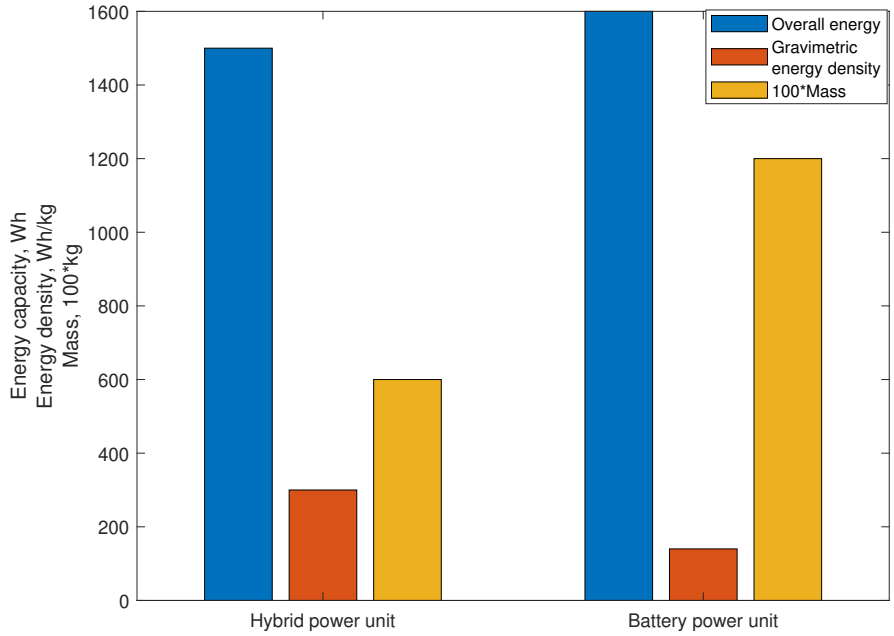

Figure 6.17: Analysis of hybrid and conventional power unit

Based on these data, the hybrid power unit using an engine–generator set is characterised by the gravimetric energy density of 300 Wh/kg, whereas the energy–equivalent battery pack is characterised by the energy density of about 140 Wh/kg. This clearly demonstrates that the autonomy of an aircraft equipped with a hybrid power unit is significantly improved compared to the "benchmark" case of purely electrical power supply solely based on batteries (see Figure 6.17).

7 Conclusion

The research presented in this thesis deals with the theoretical analysis and methodological approach to practical development and design of a hybrid–electric power unit system suitable for multirotor Unmanned Aerial Vehicles (UAV)s.

To that end, an introduction to the field of UAVs has been given in the first chapter of this thesis, along with the motivation for this work and its aims, hypothesis and expected scientific contributions. The advantages and disadvantages of different types of aircraft are considered, and the motivation for researching a multirotor UAV with a hybrid propulsion system was clearly defined. Furthermore, an in–depth literature review of research field has been conducted, which has pointed out that there is no significant quantity of hybrid power units for multirotors when compared to pure electric multirotors, or hybrid fixed–wing aircraft. In order to introduce basic tools to conduct research in this field, required preliminary theoretical background has been collected and processed in a systematic way, where important preliminaries include multirotor principles of operation, aircraft configurations, onboard avionics and components. Furthermore, mathematical tools necessary for aircraft modelling, such as dynamics modelling of a six degree of freedom body system applied to multirotors, are presented as a basis for later control system design. The most common types of power plants are presented, and their advantages and disadvantages are discussed.

Second chapter introduces a clear justification for hybrid multirotor utilisation, an analysis of suitable internal combustion engines and electric motors was performed. Based on the obtained market data for off–the–shelf–components and using already proven aircraft sizing methodology it has been shown that internal combustion engine used in radio–controlled car of 1:5 scale may represent a good candidate for hybrid–propulsion aircraft prime mover. As for electricity generators utilised within the hybrid power supply, it has been shown that lightweight brushless machines are an appropriate choice, with available power outputs up to several kilowatts.

Basic configurations of hybrid propulsion systems most commonly used in UAV aircraft with all their constituent components (subsystems) have been analysed in the third chapter. For each component, the operating principle is explained and dynamic models of the hybrid multirotor subsystem in question, which are appropriate for control system de-

sign were derived. Finally, development of a comprehensive dynamic model of the hybrid propulsion system was obtained by combining and properly interconnecting corresponding sub–models of individual UAV power–train components.

In order to validate the proposed approach and to identify physical constants for each component, a range of experimental setups were built within the Laboratory for Electrical Engineering, as illustrated fourth chapter:

- Laboratory setup for hybrid power unit testing as part of a hybrid unmanned aerial vehicle propulsion system based on an internal combustion engine and a DC electricity generator unit utilising a brushless Direct Current (DC) electrical machine and a full–wave rectifier,
- Laboratory setup for testing power flow management systems based on Direct Current to Direct Current (DC–DC) power converters and lithium–polymer batteries,
- Laboratory setup for testing propeller thrusters (propulsors) within the hybrid propulsion system.

Hybrid power supply control system design for a multirotor aircraft has been studied in detail and is presented in the fifth chapter. The crucial part of this work was to develop an embedded control system for Internal Combustion Engine (ICE)–electrical generator based power unit. To that end, two suitable hybrid propulsion topologies were described, and novel integrated control system of the ICE throttle and main DC bus voltage control have been developed in this work. DC–bus voltage control can be realised by means of an ICE engine with DC bus voltage feedback used within a dedicated proportional-integral-derivative (PID) controller commanding the engine throttle angle command. Such controller is based on the linearised engine model, simplified throttle dynamics model, PID controller and DC bus sensor. The responses of PID controller–based ICE control system shown load recovery performance and relatively small load–related speed drop. The proposed concept was tested experimentally in detail.

Main DC power bus controller can be also realised using a parallel DC–DC converters topology consisting of the primary and secondary level control of the common DC bus, in the form of a cascade control system. At the primary (inner) control level, voltage and current controllers embedded within DC–DC power converters are dealing with the individual DC–DC power converters current drain and maintaining the power converter output voltage, while at the secondary (superimposed) level the centralised controller deals with load sharing between individual power converters. Proposed approaches are original in a way of utilisation of inexpensive off–the–shelf components, which are connected in parallel configuration, and independently commanded within the hybrid power unit.

In order to investigate the validity of proposed control systems for hybrid multirotor application, sixth chapter presents the design and development procedures for the hybrid propulsion system, along with experimental validation results. In addition to the hardware implementation description, the firmware (software) development is also presented utilising a rapid prototyping / fast development technique based on Matlab/Simulink. Ultimately, the entire system was tested under realistic conditions in terms of electrical power demands, in order to demonstrate its functionality. Validity of scientific methods and approaches used in this research are satisfied because developed mathematical models have a sufficient degree of accuracy and faithfully reproduce the key stationary and dynamic behaviour of real components. Furthermore, results obtained from hardware experiments reproduce the key behaviour of the hybrid power system obtained through simulation analysis.

From the obtained simulation and experimental results, and also from the comparison of conventional battery power unit with the proposed hybrid power unit, multiple benefits are identified, which can be summarized as follows:

- A stable power source of higher gravimetric power has been obtained by means of conventional internal combustion engine generator set hybridisation (resulting in two-fold increase of gravimetric energy density compared to a purely battery-based power supply),

- Lower overall mass of hybrid power unit has been obtained with respect to the conventional system of similar energy capacity (in particular, the overall mass of the hybrid power system is two times smaller when compared to the battery-based system).

This confirms the hypothesis that utilising hybrid power units indeed improves autonomy of such aircraft.

As a conclusion of this research, it has been shown herein that the following aims have been realised:

- A comprehensive dynamic model of the hybrid propulsion system consisting of individual propulsion subsystem models of a multi–rotor unmanned aerial vehicle has been developed as shown in detail in the third and the fourth chapter),

- A systematic approach to flight control system design of multirotor aircraft with hybrid propulsion has been developed (as shown in detail in the fifth and the sixth chapter.)

A Attachments

A.1. Power consumption of motor–propeller set data

Model	Propeller size, inch	Pitch	Voltage constant, rpm/V	Throttle %	Thrust, g	Torque, Nm	Current, A	Voltage, V	Speed, rpm	Thrust per Watt, g/w
U7–V2.0	18	6.1	280	50	980	0.221	3.5	24	3313	11.67
U7–V2.0	18	6.1	280	75	2108	0.459	10.3	24	4538	8.53
U7–V2.0	18	6.1	280	100	3303	0.715	20.5	24	5680	6.71
MN505–S	18	6.1	380	50	1676	0.18	9	24	3961	7.78
MN505–S	18	6.1	380	75	3456	0.56	24.5	24	5595	5.89
MN505–S	18	6.1	380	100	5444	1.02	48.8	24	6975	4.68
MN5008	18	6.1	170	50	1343	0.29	2.74	48	3477	10.34
MN5008	18	6.1	170	75	2821	0.6	8.01	48	4945	7.47
MN5008	18	6.1	170	100	4100	0.87	14.63	48	5963	5.97
U7–V2.0	20	6	280	50	1267	0.309	4.8	24	2992	11
U7–V2.0	20	6	280	75	2717	0.639	14.24	24	4309	7.95
U7–V2.0	20	6	280	100	4078	0.973	27.4	24	5263	6.2
MN601S	20	6	170	50	1957	0.46	4.3	24	3851	9.5
MN601S	20	6	170	75	3572	0.8	10.1	24	5144	7.42
MN601S	20	6	170	100	5809	1.27	20.7	24	6482	5.93
MN505–S	20	6	320	50	1543	0.26	6.8	24	3286	9.42
MN505–S	20	6	320	75	3376	0.65	19.4	24	4973	7.25
MN505–S	20	6	320	100	5373	1.1	38.5	24	6276	5.83
MN601S	20	6	320	50	1492	0.35	6.4	24	3376	9.79
MN601S	20	6	320	75	3040	0.68	17	24	4748	7.63
MN601S	20	6	320	100	4904	1.07	34.2	24	5970	6.26
P60	20	6	170	50	2116		5.4	48	4152	8.16
P60	20	6	170	75	4002		13.2	48	5626	6.32
P60	20	6	170	100	6246		25.4	48	6992	5.12
U7–V2.0	22	6	280	50	1565	0.408	6.2	24	2856	10.52
U7–V2.0	22	6	280	75	3281	0.835	18.6	24	4052	7.35
U7–V2.0	22	6	280	100	4640	1.209	35.1	24	4809	6.2
U8 Lite	22	6.6	150	50	2376	0.6	5.2	48	3431	9.52
U8 Lite	22	6.6	150	75	4439	1.02	12.8	48	4686	7.22
U8 Lite	22	6.6	150	100	7243	1.62	26.5	48	5924	5.59
P60	22	6.6	170	50	2801		6.6	48	3703	8.84
P60	22	6.6	170	75	5372		17.1	48	5091	6.54
P60	22	6.6	170	100	8414		34	48	6374	5.16
MN505–S	22	6.6	320	50	2090	0.43	9.2	24	3197	9.46
MN505–S	22	6.6	320	75	4349	0.96	26.7	24	4623	6.8
MN505–S	22	6.6	320	100	6680	1.54	52.4	24	5625	5.35
MN701S	24	7.2	135	50	2692	0.85	5.5	48	2972	10.24
MN701S	24	7.2	135	75	5047	1.54	14.2	48	4024	7.49
MN701S	24	7.2	135	100	8011	2.31	28.6	48	4981	5.96
MN701S	24	7.2	280	50	2483	0.77	11.4	24	2880	9.22
MN701S	24	7.2	280	75	4963	1.49	27.1	24	4004	7.01
MN701S	24	7.2	280	100	7618	2.17	60.6	24	4935	5.69
U11 II	26	8.5	120	50	4590		10.1	48	2860	9.09
U11 II	26	8.5	120	75	8110		25	48	3900	6.49
U11 II	26	8.5	120	100	12420		47.4	48	4600	5.24
MN701S	26	8.5	135	50	3837	1.3	8.3	48	2812	9.7
MN701S	26	8.5	135	75	6613	2.21	20.1	48	3730	6.96
MN701S	26	8.5	135	100	9733	2.98	39.5	48	4468	5.28
P80 III	28	9.2	100	50	3220		6	48	2199	11.18
P80 III	28	9.2	100	75	6780		17.2	48	3175	8.21
P80 III	28	9.2	100	100	10800		34.7	48	4031	6.48
U11 II	28	9	120	50	5090		11.8	48	2760	8.63
U11 II	28	9	120	75	9140		30.4	48	3600	6.01
U11 II	28	9	120	100	12340		53	48	4300	4.66
U8II	28	9.2	85	50	2243	1.08	6	48	2268	11.22
U8II	28	9.2	85	75	5696	1.76	14.3	48	3002	8.3
U8II	28	9.2	85	100	8716	2.73	29.3	48	3709	6.2
U10 II	28	9.2	100	50	3119	0.97	5.8	48	2016	11.16
U10 II	28	9.2	100	75	5496	1.69	12.6	48	2735	9.01
U10 II	28	9.2	100	100	8629	2.62	24.2	48	3517	7.33
P80 III	30	10.5	100	50	4490		8.7	48	2164	10.75
P80 III	30	10.5	100	75	8960		23.2	48	3048	8.05
P80 III	30	10.5	100	100	14060		47.6	48	3984	6.15
MN805S	30	10	120	50	5037	1.62	11.25	48	2279	9.32
MN805S	30	10	120	75	9693	3.22	30.62	48	3210	6.6
MN805S	30	10	120	100	14300	5.22	64.69	48	4070	4.62
U10 II	30	10.5	100	50	4208	1.41	8	48	1918	10.84
U10 II	30	10.5	100	75	6982	2.35	17.2	48	2614	8.36
U10 II	30	10.5	100	100	10600	3.59	32.4	48	3240	6.74

A.2. IC engine data

Designation	Type	Power, HP	RPM min	RPM max	Volume, ccm	Bore, mm	Stroke, mm	Mass, g	Cost, $	Fuel cons. l/h
Desert Aircraft DA 150L	Twin cylinder boxer, two–stroke	16,40	1000	8000	150,00	49,00	40,00	3500,00	1800,00	5,09
Desert Aircraft DA 170	Twin cylinder boxer, two–stroke	18,00	1000	6500	171,80	52,00	40,50	3800,00	2200,00	5,59
Desert Aircraft DA 215	Twin cylinder boxer, two–stroke	20,00	1200	6000	215,00	56,00	44,00	5400,00	3200,00	6,21
Desert Aircraft DA 85	Single Cylinder, two–stroke	8,40	1200	7500	85,90	52,00	40,00	2200,00	1000,00	2,61
Desert Aircraft DA–100I	Twin cylinder inline, two–stroke	10,20	800	6700	100,00	42,00	35,00	2800,00	1350,00	3,16
Desert Aircraft DA–100L	Twin cylinder boxer, two–stroke	10,20	1000	6700	100,00	42,60	35,00	2800,00	1350,00	3,16
Desert Aircraft DA–120	Twin cylinder boxer, two–stroke	15,00	1000	6800	120,00	52,00	50,00	2500,00	1450,00	4,65
Desert Aircraft DA–200	Quad cylinder boxer, two–stroke	19,00	900	6700	200,00	42,60	35,00	5500,00	3800,00	5,90
Desert Aircraft DA–35	Single Cylinder, two–stroke	3,80	2000	8000	35,00	38,00	32,00	1050,00	500,00	1,18
Desert Aircraft DA–50R	Single Cylinder, two–stroke	5,00	1200	7500	50,00	42,60	35,00	1600,00	710,00	1,55
Desert Aircraft DA–60	Single Cylinder, two–stroke	6,00	1200	7200	60,50	44,00	40,00	1800,00	910,00	1,86
Desert Aircraft DA–70	Twin cylinder boxer, two–stroke	12,50	1000	6900	70,00	47,00	40,00	2000,00	1050,00	3,88
Desser Aircraft DA–200L	Four–stroke quad boxer	19,00	900	6700	200,00	42,60	35,00	5000,00	4150,00	5,90
DLA–116	Twin cylinder boxer, two–stroke	11,80	1500	8500	116,00	46,00	35,00	2800,00	624,00	3,66
DLA–116 I2	Twin cylinder inline, two–stroke	12,80	1500	8500	116,00	46,00	35,00	3800,00	900,00	3,97
DLA128	Quad cylinder boxer, two–stroke	13,00	1000	8000	128,00	37,00	30,00	3800,00	1500,00	4,03
DLA–180 B2	Twin cylinder boxer, two–stroke	18,50	1100	6800	180,00	53,00	41,00	4000,00	1200,00	5,74
DLA–64	Twin cylinder boxer, two–stroke	7,20	1500	8500	64,00	37,00	30,00	1900,00	600,00	2,23
DLE Engines DLE–20	Single Cylinder, two–stroke	2,50	1500	1000	20,00	32,00	25,00	820,00	300,00	0,78
DLE Engines DLE–222	Quad cylinder boxer, two–stroke	21,00	1000	7500	222.5	45,00	35,00	5700,00	1890,00	6,52
DLE Engines DLE–30	Single Cylinder, two–stroke	3,70	1600	8500	30,50	36,00	30,00	1300,00	300,00	1,15
DLE Engines DLE–35RA	Single Cylinder, two–stroke	4,10	1600	8500	34,50	38,50	30,00	1400,00	350,00	1,27
DLE Engines DLE–40	Twin cylinder boxer, two–stroke	4,80	1600	8500	40,00	32,00	25,00	1800,00	470,00	1,49
DLE Engines DLE–120	Twin cylinder boxer, two–stroke	12,00	1000	8000	120,00	47,00	35,00	2900,00	750,00	3,72
DLE Engines DLE–170	Twin cylinder boxer, two–stroke	17,50	1100	9000	170,00	52,00	40,00	4000,00	1050,00	5,43
DLE Engines DLE–60	Twin cylinder boxer, two–stroke	7,00	1000	8500	61,00	36,00	30,00	2000,00	550,00	2,17
DLE Engines DLE–85	Single Cylinder, two–stroke	8,50	1000	7500	84,88	52,00	40,00	2400,00	550,00	2,64
Evolution 10GX	Single Cylinder, two–stroke	1,68	2300	18000	9,83	24,00	21.5	650,00	200,00	0,52
Evolution 15GX	Single Cylinder, two–stroke	2,00	1600	13000	15,00	27,80	24,90	900,00	250,00	0,62
FF–320 Pegasus	Quad cylinder boxer, four–stroke	4,10	1800	8500	13,30	28,00	22,00	2200,00	2200,00	1,27
GP 61	Single Cylinder, four–stroke	6,50	1600	8900	61,00	46,50	40,00	1600,00	570,00	2,02
GP Boxer 123	Twin cylinder boxer, two–stroke	12,00	1600	8900	123,00	46,50	40,00	2600,00	985,00	3,72
GP Boxer 178	Twin cylinder boxer, two–stroke	21,00	1100	9000	178,00	53,00	45,00	4000,00	1800,00	6,52
GP Boxer 76	Twin cylinder boxer, two–stroke	8,00	1400	8000	76,00	38,00	35,00	2100,00	820,00	2,48
GP STD 88	Single Cylinder, two–stroke	9,00	1200	7700	88,00	53,00	42,00	2200,00	700,00	2,79
NGH GF30	Single Cylinder, four–stroke	2,70	1600	8500	29.91	36,00	29,40	1300,00	350,00	0,84
NGH GF38	Single Cylinder, four–stroke	3,50	1600	8000	37,97	39,00	31,80	1600,00	330,00	1,09
NGH GT17	Single Cylinder, two–stroke	1,80	1800	12000	16.91	29,00	25,60	850,00	200,00	0,56
NGH GT25	Single Cylinder, two–stroke	2,70	1600	11000	25,00	33.2	29,00	1100,00	210,00	0,84
NGH GT35	Single Cylinder, two–stroke	4,20	2000	9000	34.95	37.3	32,00	1400,00	250,00	1,30
O.S. Engine GT15	Single Cylinder, two–stroke	2,37	2000	15000	15,00	27,70	24,80	910,00	400,00	0,74
O.S. Engines FSA72 II	Single Cylinder, four–stroke	1,18	2400	12500	11,79	20,70	20,60	700,00	750,00	0,37
O.S. Engines GF30 II	Single Cylinder, four–stroke	2,76	1800	9000	29,94	38,00	26,60	1300,00	830,00	0,86
O.S. Engines GF40	Single Cylinder, four–stroke	3,75	1800	9000	40,00	40,00	31,80	1500,00	900,00	1,16
O.S. Engines GT120T	Twin cylinder boxer, two–stroke	9,86	1600	8000	59,90	44,00	39,40	2750,00	1700,00	3,06
O.S. Engines GT22	Single Cylinder, two–stroke	4,30	1800	9000	22,00	32,00	27,50	990,00	430,00	1,33
O.S. Engines GT33	Single Cylinder, two–stroke	3,85	1800	8000	32.98	36,00	32.4	1250,00	450,00	1,19
O.S. Engines GT–60	Single Cylinder, two–stroke	6,00	1600	8000	59.91	44,00	39.4	1700,00	700,00	1,86
Saito FA–170R3	Radial engine, 3–cylinder	5,30	2000	9500	27.82	24,80	19,00	1350,00	840,00	1,64
Saito FA–100	Single Cylinder, four–stroke	2,00	2000	11000	17,17	29,00	26,00	550,00	385,00	0,62
Saito FA–100T	Twin cylinder boxer, four–stroke	1,47	2500	10000	16.34	23,40	19,00	3500,00	520,00	0,46
Saito FA–100Ti	Twin cylinder inline, four–stroke	1,40	2000	10000	17.97	24,80	18,60	2500,00	520,00	0,43

Saito FA–120R3	Radial engine, 3–cylinder	3,75	1800	10000	19,15	22,40	16,20	1000,00	750,00	1,16
Saito FA–125a	Single Cylinder, four–stroke	2,17	2000	11000	20,52	31,70	26,00	700,00	380,00	0,67
Saito FA–150B	Single Cylinder, four–stroke	2,46	2000	10500	25,00	34,00	27,60	890,00	520,00	0,76
Saito FA–180B	Single Cylinder, four–stroke	2,80	2000	10000	29,00	36,00	28,60	888,00	570,00	0,87
Saito FA–182TD	Twin cylinder boxer, four–stroke	2,96	2000	10000	29.98	28,20	24,00	4500,00	750,00	0,92
Saito FA–200R3	Radial engine, 3–cylinder	6,36	1800	9500	33,00	27,00	19,20	1500,00	1100,00	1,97
Saito FA–200Ti	Twin cylinder inline, Four–stroke	5,00	1800	9500	32.98	28,20	26,40	5000,00	1330,00	1,55
Saito FA–300TL	Twin cylinder boxer, four–stroke	4,70	1800	8000	50.84	34,00	28,00	1900,00	890,00	1,46
Saito FA–325R5D	Radial engine, 5–cylinder	3,80	1700	7500	53.14	24,80	22.0	2400,00	1950,00	1,18
Saito FA–40a	Single Cylinder, four–stroke	0,90	2200	12000	6,50	22,00	17,40	300,00	200,00	0,28
Saito FA–450R3D	Radial engine, 3–cylinder	5,50	1200	8000	75.18	34,00	27,60	3000,00	1300,00	1,71
Saito FA–60T	Twin cylinder boxer, four–stroke	0,90	2000	10000	65,00	20,00	16,00	738,00	540,00	0,28
Saito FA–62b	Single Cylinder, four–stroke	0,90	2300	11000	10,16	26,20	19,00	470,00	240,00	0,28
Saito FA–82b	Single Cylinder, four–stroke	1,50	2300	11000	13,47	29,00	20,40	480,00	320,00	0,47
Saito FA–90R3	Radial engine, 3–cylinder	1,00	2000	10000	15,10	20,00	16,00	850,00	625,00	0,31
Saito FA–90TS	Twin cylinder boxer, four–stroke	1,20	2000	1000	14.98	22,40	19,00	723,00	630,00	0,37
Saito FG–100TS	Twin cylinder boxer, four–stroke	9,00	1000	6000	100.3	43.6	33.6	4380,00	1700,00	2,79
Saito FG–11	Single Cylinder, four–stroke	2,46	2000	9500	10,88	27,00	19,00	650,00	350,00	0,76
Saito FG–14C	Single Cylinder, four–stroke	3,50	1700	9500	13,80	29,00	20,40	720,00	575,00	1,09
Saito FG–17	Single Cylinder, four–stroke	2,95	2000	9500	17,00	29,00	26,00	900,00	590,00	0,92
Saito FG–19R3	Radial engine, 3–cylinder	1,38	1800	10000	19,18	22,40	16,20	1200,00	850,00	0,43
Saito FG–21	Single Cylinder, four–stroke	3,00	1800	9500	20,91	32,00	26,00	1100,00	450,00	0,93
Saito FG–30B	Single Cylinder, four–stroke	2,50	1800	9300	29,10	36,00	28,00	1460,00	700,00	0,78
Saito FG–33R3	Radial engine, 3–cylinder,four stroke	2,46	1700	9500	33,00	27,00	19,20	1800,00	1400,00	0,76
Saito FG–36B	Single Cylinder, four–stroke	3,50	1700	9000	36,30	35,00	32,00	1300,00	875,00	1,09
Saito FG–40	Single Cylinder, four–stroke	3,90	1700	8000	40.2	40,00	32,00	1700,00	700,00	1,21
Saito FG–57TS	Twin cylinder boxer, four–stroke	4,50	1500	7000	57,00	36,00	28,00	2100,00	1350,00	1,40
Saito FG–61TS	Twin cylinder boxer, four–stroke	4,60	1500	7400	60.9	37.2	28,00	2100,00	1300	1,43
Saito FG–73R5	Radial engine, 5–cylinder,four stroke	1,20	1200	7800	72.7	29,00	22,00	400,00	2000,00	0,37
Saito FG–84R3	Radial engine, 3–cylinder,four stroke	2,86	1200	7000	84.3	36,00	27,60	3500,00	1700,00	0,89
Titan ZG 20	Single Cylinder, two–stroke	1,75	1000	9000	20,00	32,00	25,00	1185,00	300,00	0,54
Titan ZG 26 SC	Single Cylinder, two–stroke	2,20	3000	13000	25,00	34,00	28,00	1660,00	330,00	0,68
Titan ZG 38S	Single Cylinder, two–stroke	2,60	1800	8000	38,00	38,00	33,00	1800,00	330,00	0,81
Titan ZG 45	Four–stroke single cylinder	3,50	2000	9000	45,00	43,00	31,00	2200,00	400,00	1,09
Titan ZG 62	Four–stroke single cylinder	4,30	2000	9000	62,00	47,50	62,00	2500,00	460,00	1,33
Titan ZG 80	Four–stroke twin boxer	5,40	2000	9000	80,00	40,50	31,00	3500,00	950,00	1,68
Turnigy 30cc Gas engine	Single Cylinder, two–stroke	2,70	1600	12000	30,00	34,00	28,00	1000,00	150,00	0,84
Turnigy TR–32	Single Cylinder, two–stroke	3,80	1800	8000	32.24	37,00	30,00	1100,00	196,00	1,18
Turnigy TR–55	Single Cylinder, two–stroke	5,60	1500	8000	55.6	45,00	35,00	1650,00	260,00	1,74
Valach Motors VM 120 B2–4T	Twin cylinder boxer, four–stroke	16,00	900	6200	120,00	47,00	35,00	4500,00	2500,00	4,96
Valach Motors VM 120I2–4T	Four–stroke twin cylinder inline	10,00	900	6200	120,00	47,00	35,00	4855,00	2550,00	3,10
Valach Motors VM 140 B2–FS	Four–stroke twin boxer	12,50	1000	6000	140,00	47,00	40,00	4300,00	4160,00	3,88
Valach Motors VM 170 B2–4T	Four–stroke twin boxer	13,00	900	6200	179,00	52,00	40,00	5600,00	2700,00	4,03
Valach Motors VM 210 B2–4T	Four–stroke twin boxer	16,00	800	5500	210,00	52,00	50,00	5900,00	2950,00	4,96
Valach Motors VM 280 B4–FS	Four–stroke quad boxer	18,00	800	6200	280,00	47,00	40,00	8000,00	4100,00	5,59
Valach Motors VM 70S1–4T	Single Cylinder, four–stroke	11,00	1000	6200	70,00	47,00	40,00	2500,00	1230,00	3,41
Valach Motors VM 85 B2–FS	Twin cylinder boxer, four–stroke	13,00	1000	6000	85,00	42,00	32,00	3200,00	1980,00	4,03
Valach Motors VM 60 S1–4T	Single Cylinder, four–stroke	10,00	1000	6200	60,00	47,00	35,00	2360,00	980,00	3,10

A.3. Electricity motor/generator data

Designation	KV parameter	Max continuous power, W	Max continuous current, A	Nominal Voltage, V	Internal resistance, mOhm	Mass, g	Cost, $
MAD8108	100	350,00	20	24	186,00	265,00	210,00
U8 Pro	135	490,00	15	24	179,00	257,00	300,00
U3	700,00	500,00	25,00	14,80	50,00	128,00	110,00
MAD M10	90	600,00	60	50			270,00
MAD8108	170	600,00	30	48	89,00	250,00	225,00
U8II	150	712,00	28	24	85,00	270,00	310,00
MAD8118	80	800,00	25	48	93,00	500,00	250,00
U7 2.0	280	800,00	35	24	71,00	318,00	150,00
MN5212	340	840,00	35	24	69,00	240,00	110,00
U5	400,00	850,00	30,00	24,00	116,00	195,00	126,00
U8 Lite	85	900,00	18	48	225,00	243,00	300,00
U8II	85	950,00	19	48	225,00	277,00	310,00
U7 2.0	420	1180,00	40	24	33,00	296,00	150,00
U10	80	1200,00	25	48	135,00	405,00	330,00
U8 Lite	150	1272,00	25	48	85,00	239,00	300,00
U7 2.0	490	1300,00	44	24	21,00	299,00	150,00
U8II	100	1400,00	25	48	170,00	272,00	310,00
MN5212	420	1440,00	60	24	69,00	249,00	110,00
MN1005	90	1500,00	32	48	168,00	255,00	250,00
MN701	280	1600,00	65	24	23,00	355,00	390,00
U10 II	100	1600,00	30	48	101,00	415,00	340,00
U10 Plus	100	1700,00	36	48	60,00	500,00	340,00
P60	170	1800,00	38	48	80,00	379,00	110,00
MN701	135	1900,00	42	48	94,00	350,00	390,00
MN705–S	260	2200,00	40	24	63,00	450,00	300,00
U12	90	2500,00	50	48	36,00	794,00	350,00
P80III	100	2700,00	60	48	45,00	650,00	200,00
MN705–S	140	2800,00	80	48	16,00	450,00	300,00
P80II	120	2800,00	60	48	45,00	650,00	200,00
P80	120	3000,00	70	48	37,00	650,00	200,00
U11	120	3000,00	60	48	99,00	815,00	350,00
U13	85	3120,00	65	48	23,00	370,00	370,00
P80III	120	3600,00	70	48	36,00	650,00	200,00
U13	100	3848,00	80	48	13,00	1300,00	370,00
U12II	120	4560,00	95	88	22,00	778,00	350,00
U13II	130	5600,00	118	48	18,00	990,00	380,00
MAD M30	100	7000,00	180	60		1450,00	630,00
U15II	80	8580,00	143	88	17,00	1740,00	690,00
U15II	100	9942,00	143	88	12,00	1740,00	690,00
MN805–S	120	3200,00	65,00	48,00	48,00	620,00	269,00
MN805–S	150	3600,00	75	48	32,00	625,00	269,00
MN805–S	170	4000,00	83	48	28,00	625,00	269,00
MN801–S	120	2200,00	45	48	80,00	470,00	250,00
MN801–S	150	2800,00	60	48	50,00	480,00	250,00
MAD M17	100	4200,00	90	50		820,00	326,00
X12090	120	8600,00	200	50		2048,00	250,00
MP 15470	55	15000,00	300	100		3500,00	620,00
MP 120100	80	22000,00	250	100		4000,00	520,00
MP 154120	55	40000,00	400	120		5900,00	1300,00
T8120	100	2260,00	48	48	215,00	556,00	300,00

A.4. Candidate CV

Matija Krznar, mag. ing. mech., (born in 1987) obtained the titles of university bachelor and master of engineering (field of mechanical engineering) in 2009 and 2010 at the Faculty of Mechanical Engineering and Naval Architecture, University of Zagreb. During his studies, he researched in the field of dynamics and control of electric motor drives with applications in mechatronic systems for oil and gas exploration. After completing his studies, he was employed first in the company Končar - energetski transformatori d.o.o. Zagreb (2011 - 2014) and then to Peti brod d.o.o. (2014-2018). In parallel with employment, in 2015 he enrolled in the postgraduate study of Mechatronics and Robotics at the Faculty of Mechanical Engineering and Naval Architecture, University of Zagreb. Since 2019, he has been employed at the Faculty of Mechanical Engineering and Naval Architecture, as an assistant at the Department of Robotics and Production System Automation at the Chair of Control Systems. He teaches Electrical Engineering, Marine Electrical Engineering, Electrical Engineering and Electrical Machines (Z), Electronics, Microprocessor Control, Power Electronics Systems, Development and Application of Microcontrollers, and Measuring Devices and Sensors. Current research interests include modelling the dynamics and synthesis of control systems for multirotor aircraft with an emphasis on hybrid propulsion systems, and the development of embedded microcontroller systems in multirotors. He is the author and co-author of 13 scientific papers published at national and international conferences, as well as in international journals.

A.5. Publications list

Journal articles

Scientific and review papers

Krznar, Matija; Kotarski, Denis; Pavković, Danijel; Piljek, Petar
Propeller speed estimation for unmanned aerial vehicles using Kalman filtering. // International Journal of Automation and Control, 14 (2020), 3; 284-303 (international peer review, article, scholarly)

Krznar, Matija; Kotarski, Denis; Piljek, Petar; Pavković, Danijel
On-line inertia measurement of unmanned aerial vehicles using on-board sensors and a bifilar pendulum. // Interdisciplinary description of complex systems, 16 (2018), 1; 149-161 doi:10.7906/indecs.16.1.12 (international peer review, article, scholarly)

Pavković, Danijel; **Krznar, Matija**; Komljenović, Ante; Hrgetić, Mario; Zorc, Davor
Dual EKF-based State and Parameter Estimator for a LiFePO4 Battery Cell. // Journal of Power Electronics, 17 (2017), 2; 398-410 doi:10.6113/JPE.2017.17.2.398 (international peer review, article, scholarly)

Kotarski, Denis; Benić, Zoran; **Krznar, Matija**
Control design for unmanned aerial vehicles with four rotors. // Interdisciplinary description of complex systems, 14 (2016), 2; 236-245 doi:10.7906/indecs.14.2.12 (information about peer review not available, article, scholarly)

Kotarski, Denis; Piljek, Petar; Krznar, Matija
Mathematical Modelling of Multirotor UAV. // International Journal of Theoretical and Applied Mechanics, 1 (2016), 233-238. (https://www.bib.irb.hr/886586) (peer review, article, scholarly)

Articles in press

Pavković, Danijel; Šprljan, Pavle; Cipek, Mihael; Krznar, Matija
Cross-Axis Control System Design for Borehole Drilling based on Damping Optimum Criterion and utilization of Proportional-Integral Controllers. // Optimization and engineering (2020) (international peer review, accepted)

Conference proceedings papers

Scientific conference proceedings papers

Pavković, Danijel; **Krznar, Matija**; Cipek, Mihael; Zorc, Davor; Trstenjak, Maja
Internal Combustion Engine Control System Design Suitable for Hybrid Propulsion Applications. // Proceedings of the ICUAS 2020 conference
Atena, Grčka, 2020. pp. 1614-1619 (lecture, international peer review, full paper, scholarly)

Krznar, Matija; Pavković, Danijel; Kozhushko, Yuliia; Cipek, Mihael; Zorc, Davor
Generator Set Control System Design for Unmanned Aerial Vehicle Hybrid Propulsion. // Digital proceedings of 4th South East Europe (SEE) Sustainable Development of Energy Water and Environment Systems (SDEWES) conference / Ban, Marko (ed.).
Sarajevo, Bosna i Hercegovina, 2020. pp. 1-18 (lecture, international peer review, full paper, scholarly)

Krznar, Matija; Pavković, Danijel; Cipek, Mihael; Crneković, Mladen; Zorc, Davor
Design of a low-cost DC/DC Converter Power Distribution System for a Hybrid Power Unit of the Multirotor Unamnned Aerial Vheicle. // Digital proceedings of 4th South East Europe (SEE) Sustainable Development of Energy Water and Environment Systems (SDEWES) conference / Ban, Marko (ed.).
Sarajevo, Bosna i Hercegovina, 2020. pp. 1-18 (lecture, international peer review, full paper, scholarly)

Krznar, Matija; Pavković, Danijel; Kozhushko, Yuliia; Cipek, Mihael; Zorc, Davor; Crneković, Mladen
Control System Design for Hybrid Power Supply of an Unmanned Aerial Vehicle Based on Linearized Averaged Process Models. // Proceedings of the ICUAS 2020 conference
Atena, 2020. pp. 582-587 (poster, international peer review, full paper, scholarly)

Krznar, Matija; Pavković, Danijel; Cipek, Mihael; Zorc, Davor; Kolar, Davor; Kotarski, Denis
Damping Optimum-based Design of State Controller and Observer for Drill-String Rotary Speed Control. // Proceedings of 18th IEEE International Conference on Smart Technologies EUROCON 2019 / Dumnić, Boris (ed.).
Novi Sad, Srbija: University, Faculty of Technical Sciences, 2019. 2323, 6 (lecture, international peer review, full paper, scholarly)

Kotarski, Denis; **Krznar, Matija**; Piljek, Petar; Šimunić, Nikola
Experimental Identification and Characterization of Multirotor UAV Propulsion. // Journal of Physics Conference Series, Volume 870
United Kingdom: Institute of Physics (Great Britain), IOP Publishing, 2017. pp. xx-xx (other, international peer review, full paper, scholarly)

Kotarski, Denis; Piljek, Petar; Benić, Zoran; **Krznar, Matija**
Fault tolerant control of a Coaxial Quadrotor UAV using PI-D Controller. // Proceedings of International Conference "Vallis Aurea", Vol.1, Vol.2. 2016 / Katalinić, Branko (ed.).
Požega: Polyteching School in Požega, DAAAM International Wienna, 2016. pp. xx-xx (other, international peer review, full paper, scholarly)

Pavković, Danijel; Komljenović, Ante; Hrgetić, Mario; **Krznar, Matija**
Experimental Characterization and Development of a SoC/SoH Estimator for a LiFePO4 Battery Cell. // Proceedings of IEEE EUROCON 2015 (16th International Conference on Computer as a Tool) / Haase, Jan ; Kakarountas, Athanasios ; Graña, Manuel ; Fraile-Ardanuy, Jesús ; Debono, Carl James ; Quintián, Héctor ; Corchado, Emilio (ed.).
Salamanca, Španjolska: IEEE Press, 2015. pp. 397-402 (lecture, international peer review, full paper, scholarly)

Bibliography

[1] Kimon P. Valavanis and George J. Vachtsevanos. *Handbook of unmanned aerial vehicles*. Springer Netherlands, Dordrecht, 2014.

[2] Reg Austin. *Unmanned aircraft systems : UAVs design, development and deployment*. Wiley, Chichester, 2010.

[3] Quan Quan. *Introduction to Multicopter Design and Control*. Springer-Verlag GmbH, 2017.

[4] Milan Erdelj and Enrico Natalizio. UAV-assisted disaster management: Applications and open issues. In *2016 International Conference on Computing, Networking and Communications (ICNC)*. IEEE, feb 2016.

[5] Iván Maza, Fernando Caballero, Jesús Capitán, J. R. Martínez de Dios, and Aníbal Ollero. Experimental results in multi-UAV coordination for disaster management and civil security applications. *Journal of Intelligent & Robotic Systems*, 61(1-4):563–585, dec 2010.

[6] Derek Kingston, Randal W. Beard, and Ryan S. Holt. Decentralized perimeter surveillance using a team of UAVs. *IEEE Transactions on Robotics*, 24(6):1394–1404, dec 2008.

[7] Stuart M. Adams, Marc L. Levitan, and Carol J. Friedland. High resolution imagery collection for post-disaster studies utilizing unmanned aircraft systems (UAS). *Photogrammetric Engineering & Remote Sensing*, 80(12):1161–1168, dec 2014.

[8] Xin Li and Lian Yang. Design and implementation of uav intelligent aerial photography system. In *2012 4th International Conference on Intelligent Human-Machine Systems and Cybernetics*, volume 2, pages 200–203. IEEE, 2012.

[9] Chung Deng, Shengwei Wang, Zhi Huang, Zhongfu Tan, and Junyong Liu. Unmanned aerial vehicles for power line inspection: A cooperative way in platforms and communications. *J. Commun*, 9(9):687–692, 2014.

[10] Yanbo Huang, Wesley C Hoffmann, Yubin Lan, Wenfu Wu, and Bradley K Fritz. Development of a spray system for an unmanned aerial vehicle platform. *Applied Engineering in Agriculture*, 25(6):803–809, 2009.

[11] *Harrier Jump Jet*, Accesed: July 2020. [Internet] https://en.wikipedia.org/wiki/Harrier_Jump_Jet.

[12] *Lockheed–Martin F–35 Lightning II*, Accesed: July 2020. [Internet] https://en.wikipedia.org/wiki/Lockheed_Martin_F-35_Lightning_II.

[13] *Bell–Boeing V–22 Osprey*, Accesed: July 2020. [Internet] http://www.bellhelicopter.com/military/bell-boeing-v-22#/?tab=features-tab.

[14] *Firefighter Drones – How Drones are being used for helping Fire Deparments*, Accesed: July 2020. [Internet] https://dronenodes.com/firefighter-drones/.

[15] *Pratt LCL. MQ-9 Reaper UAV*, Accesed: July 2020. [Internet] https://commons.wikimedia.org/wiki/File:MQ-9_Reaper_UAV.jpg.

[16] *UAV Flight Crew*, Accesed: July 2020. [Internet] https://en.wikipedia.org/wiki/General_Atomics_MQ-9_Reaper#/media/File:MQ-1_Predator_controls_2007-08-07.jpg.

[17] *Alta 8 Multirotor*, Accesed: July 2020. [Internet] https://store.freeflysystems.com/products/alta-8?variant=18143711559.

[18] *Multirotor Power Line Inspection*, Accesed: July 2020. [Internet] http://texasdroneprofessionals.com/wp-content/uploads/2015/04/Power-Line-Inspection.jpg.

[19] *Agricultural drone by Agridrones*, Accesed: July 2020. [Internet] https://en.wikipedia.org/wiki/Agricultural_drone#/media/File:4X-UHJ_Agridrones_d.jpg.

[20] *Microdrones md4-1000 DHL parcel service*, Accesed: July 2020. [Internet] https://en.wikipedia.org/wiki/Delivery_drone#/media/File:Package_copter_microdrones_dhl.jpg.

[21] Kristen McKinney, Jordan A Feight, Richard J Gaeta, and Jamey D Jacob. Implementation implications of hybrid-electric power systems on multi-rotor uas. In *2018 AIAA Information Systems-AIAA Infotech@ Aerospace*, page 0986. 2018.

[22] Mohamed Gadalla and Sayem Zafar. Analysis of a hydrogen fuel cell-pv power system for small uav. *International Journal of Hydrogen Energy*, 41(15):6422–6432, 2016.

[23] Sunghun Jung, Yonghyeon Jo, and Young-Joon Kim. Aerial surveillance with low-altitude long-endurance tethered multirotor uavs using photovoltaic power management system. *Energies*, 12(7):1323, 2019.

[24] Michael Fischer, Mathew Werber, and Peter V Schwartz. Batteries: Higher energy density than gasoline? *Energy policy*, 37(7):2639–2641, 2009.

[25] Asel Sartbaeva, VL Kuznetsov, SA Wells, and PP Edwards. Hydrogen nexus in a sustainable energy future. *Energy & Environmental Science*, 1(1):79–85, 2008.

[26] Mihael Cipek, Danijel Pavković, and Joško Petrić. A control-oriented simulation model of a power-split hybrid electric vehicle. *Applied energy*, 101:121–133, 2013.

[27] Mihael Cipek, Danijel Pavković, Zdenko Kljaić, and Tomislav Josip Mlinarić. Assessment of battery-hybrid diesel-electric locomotive fuel savings and emission reduction potentials based on a realistic mountainous rail route. *Energy*, 173:1154–1171, 2019.

[28] Ivan Lončar, Anja Babić, Barbara Arbanas, Goran Vasiljević, Tamara Petrović, Stjepan Bogdan, and Nikola Mišković. A heterogeneous robotic swarm for long-term monitoring of marine environments. *Applied Sciences*, 9(7):1388, 2019.

[29] Mitch Campion, Prakash Ranganathan, and Saleh Faruque. A review and future directions of uav swarm communication architectures. In *2018 IEEE International Conference on Electro/Information Technology (EIT)*, pages 0903–0908. IEEE, 2018.

[30] Anton Kohlbacher, Jens Eliasson, Kevin Acres, Hoam Chung, and Jan Carlo Barca. A low cost omnidirectional relative localization sensor for swarm applications. In *2018 IEEE 4th World Forum on Internet of Things (WF-IoT)*, pages 694–699. IEEE, 2018.

[31] Neel Dhanaraj, Nathan Hewitt, Casey Edmonds-Estes, Rachel Jarman, Jeongwoo Seo, Henry Gunner, Alexandra Hatfield, Tucker Johnson, Lunet Yifru, Julietta Maffeo, et al. Adaptable platform for interactive swarm robotics (apis): a human-swarm interaction research testbed. In *2019 19th International Conference on Advanced Robotics (ICAR)*, pages 720–726. IEEE, 2019.

[32] M Furci, G Casadei, R Naldi, RG Sanfelice, and L Marconi. An open-source architecture for control and coordination of a swarm of micro-quadrotors. In *2015 International Conference on Unmanned Aircraft Systems (ICUAS)*, pages 139–146. IEEE, 2015.

[33] Chao Liang and Chenxiao Cai. Modeling of a rotor/fixed-wing hybrid unmanned aerial vehicle. In *2017 36th Chinese Control Conference (CCC)*, pages 11431–11436. IEEE, 2017.

[34] Jian Zhang, Zhiming Guo, and Liaoni Wu. Research on control scheme of vertical take-off and landing fixed-wing uav. In *2017 2nd Asia-Pacific Conference on Intelligent Robot Systems (ACIRS)*, pages 200–204. IEEE, 2017.

[35] Mohammad Jafarinasab, Shahin Sirouspour, and Eric Dyer. Model-based motion control of a robotic manipulator with a flying multirotor base. *Computer Science IEEE/ASME Transactions on Mechatronics*, 24:2328–2340, 2019.

[36] Juntong Qi, Jinan Kang, and Xiang Lu. Design and research of uav autonomous grasping system. *IEEE International Conference on Unmanned Systems (ICUS)*, 2017.

[37] Yiannis Stergiopoulos, Efstathios Kontouras, Konstantinos Gkountas, Konstantinos Giannousakis, and Anthony Tzes. Modeling and control aspects of a uav with an attached manipulator. *4th Mediterranean Conference on Control and Automation (MED)*, 2016.

[38] Marius Beul, Nicola Krombach, Yongfeng Zhong, David Droeschel, Matthias Nieuwenhuisen, and Sven Behnke. A high-performance mav for autonomous navigation in complex 3d environment. *International Conference on Unmanned Aircraft Systems (ICUAS)*, 2015.

[39] Nischay Gupta, Jaspreet Singh Makkar, and Piyush Pandey. Obstacle detection and collision avoidance using ultrasonic sensors for rc multirotors. *International Conference on Signal Processing and Communication (ICSC)*, 2015.

[40] I. Kagan Erunsal, Alcherio Martinoli, and Rodrigo Ventura. Decentralized nonlinear model predictive control for 3d formation of multirotor micro aerial vehicles with relative sensing and estimation. *International Symposium on Multi-Robot and Multi-Agent Systems (MRS)*, 2019.

[41] Yuyi Liu, Jan Maximilian Montenbruck, Daniel Zelazo, Marcin Odelga, Sujit Rajappa, Heinrich H. Bulthoff, Frank Allgower, and Andreas Zell. A distributed control approach to formation balancing and maneuvering of multiple multirotor uavs. *IEEE Transactions on Robotics*, 34:870–882, 2018.

[42] Sergey Edward Lyshevski. Multi-agent distributed coordination and control for aerial systems. *International Conference on Unmanned Aircraft Systems (ICUAS)*, 2018.

[43] Denis Kotarski, Matija Piljek, Marina Tevčić, and Vedran Vyroubal. Mathematical modelling and dynamics analysis of flat multirotor configurations. *WSEAS transactions on systems*, 16:47–52, 2017.

[44] Denis Kotarski, Petar Piljek, Hrvoje Brezak, and Josip Kasać. Design of a fully actuated passively tilted multirotor uav with decoupling control system. *2017 8th International Conference on Mechanical and Aerospace Engineering (ICMAE)*, 2017.

[45] E. Cetinsoy, S. Dikyar, C. Hancer, K. T. Oner, E. Sirimoglu, M. Unel, and M. F. Aksit. Design and construction of a novel quad tilt-wing. *Mechatronics*, 22:723–745, 2012.

[46] Tomasz Goetzendorf-Grabowski and Mirosław Rodzewicz. Design of uav for photogrammetric mission in antarctic area. *Proceedings of the Institution of Mechanical Engineers Part G Journal of Aerospace Engineering*, 231:1660–1675, 2017.

[47] Matija Krznar, Denis Kotarski, Petar Piljek, and Danijel Pavković. On-line inertia measurement of unmanned aerial vehicles using on board sensors and bifilar pendulum. *Interdisciplinary Description of Complex Systems: INDECS*, 16(1):149–161, 2018.

[48] Robert Mahony, Vijay Kumar, and Peter Corke. Multirotor aerial vehicles: Modeling, estimation, and control of quadrotor. *Computer Science, Engineering IEEE Robotics and Automation Magazine*, 19:20–32, 2012.

[49] Bora Erginer and Erdinc Altug. Modeling and pd control of a quadrotor vtol vehicle. *IEEE Intelligent Vehicles Symposium*, 2007.

[50] Samir Bouabdallah and Roland Siegwart. Full control of a quadrotor. *2007 IEEE/RSJ International Conference on Intelligent Robots and Systems*, pages 153–158, 2007.

[51] G Bressan, D Invernizzi, S Panza, and M Lovera. Attitude control of multirotor uavs: cascade p/pid vs pi-like architecture. *5th CEAS Specialist Conference on Guidance, Navigation and Control-EuroGNC*, pages 1–20, 2019.

[52] Oualid Araar and Nabil Aouf. Full linear control of a quadrotor uav, lq vs hinf. *UKACC International Conference on Control (CONTROL)*, 2014.

[53] S. Bouabdallah and R. Siegwart. Backstepping and sliding-mode techniques applied to an indoor micro quadrotor. *Proceedings of the IEEE International Conference on Robotics and Automation*, 2005.

[54] K. Alexis, A. Tzes, and G. Nikolakopoulos. Model predictive quadrotor control: Attitude, altitude and position experimental studies. *IET Control Theory and Applications*, 6:1812–1827, 2012.

[55] Hadi Razmi and Sima Afshinfar. Neural network-based adaptive sliding mode control design for position and attitude control of a quadrotor uav. *Aerospace Science and Technology*, 91:12–27, 2019.

[56] Kasey A. Ackerman, Irene M. Gregory, and Naira Hovakimyan. Flight control methods for multirotor uas. *International Conference on Unmanned Aircraft Systems (ICUAS)*, 2019.

[57] Matko Orsag, Christopher Korpela, Paul Oh, and Stjepan Bogdan. *Aerial Manipulation*. Springer-Verlag GmbH, 2017.

[58] Denis Kotarski, Matija Krznar, Petar Piljek, and Nikola Šimunić. Experimental identification and characterization of multirotor uav propulsion. *Journal of Physics Conference Series*, 870:012003, 2017.

[59] Dmitry Bershadsky, Steve Haviland, and Eric N. Johnson. Electric multirotor propulsion system sizing for performance prediction and design optimization. *AIAA/ASCE/AHS/ASC Structures, Structural Dynamics, and Materials Conference*, 2016.

[60] B. Theys, G. Dimitriadis, P. Hendrick, and J. De Schutter. Influence of propeller configuration on propulsion system efficiency of multi-rotor unmanned aerial vehicles. *International Conference on Unmanned Aircraft Systems (ICUAS)*, 2016.

[61] James Robert Mevey. Sensorless field oriented control of brushless permanent magnet synchronous motors. *Kansas State University*, 2009.

[62] Ming-Fa Tsai, Tran Phu Quy, Bo-Feng Wu, and Chung-Shi Tseng. Model construction and verification of a bldc motor using matlab/simulink and fpga control. *6th IEEE Conference on Industrial Electronics and Applications*, 2011.

[63] Matija Krznar, Denis Kotarski, Danijel Pavković, and Petar Piljek. Propeller speed estimation for unmanned aerial vehicles using kalman filtering. *International Journal of Automation and Control*, 14:284, 2020.

[64] Darren Lance Gabriel, Johan Meyer, and Francois du Plessis. Brushless dc motor characterisation and selection for a fixed wing uav. *IEEE Africon '11*, 2011.

[65] Andrew Gong, Rens MacNeill, and Dries Verstraete. Performance testing and modeling of a brushless dc motor, electronic speed controller and propeller for a small uav application. *Joint Propulsion Conference*, 2018.

[66] Piotr Bogusz, Mariusz Korkosz, Adam Powrozek, Jan Prokop, and Piotr Wygonik. An analysis of properties of the bldc motor for unmanned aerial vehicle hybrid drive. *International Conference on Electrical Drives and Power Electronics (EDPE)*, 2015.

[67] Analiza Abdilla, Arthur Richards, and Stephen Burrow. Power and endurance modelling of battery-powered rotorcraft. *IEEE/RSJ International Conference on Intelligent Robots and Systems (IROS)*, 2015.

[68] Michal Podhradsky, Jarret Bone, Calvin Coopmans, and Austin Jensen. Battery state-of-charge based altitude controller for small, low cost multirotor unmanned aerial vehicles. *Journal of Intelligent and Robotic Systems*, 2013.

[69] Danijel Pavković, Matija Krznar, Ante Komljenović, Mario Hrgetić, and Davor Zorc. Dual ekf-based state and parameter estimator for a lifepo4 battery cell. *Journal of Power Electronics*, 17:398–410, 2017.

[70] Danijel Pavković, Ante Komljenović, Mario Hrgetić, and Matija Krznar. Experimental characterization and development of a soc/soh estimator for a lifepo4 battery cell. *Proceedings of IEEE EUROCON 2015 (16th International Conference on Computer as a Tool)*, 2015.

[71] I. Made Aswin Nahrendra, Widyawardana Adiprawita, Adrian Susanto, and Stefanus Kevin Hadinata. Engine control unit for 2 stroke internal combustion engine on medium altitude unmanned aerial vehicle. *International Symposium on Electronics and Smart Devices (ISESD)*, 2018.

[72] Mitchell D. Hageman and Thomas E. McLaughlin. Considerations for pairing the ic engine and electric motor in a hybrid power system for small uavs. *AIAA Aerospace Sciences Meeting*, 2018.

[73] Tomislav Haus, Marko Car, Matko Orsag, and Stjepan Bogdan. Identification results of an internal combustion engine as a quadrotor propulsion system. *25th Mediterranean Conference on Control and Automation (MED)*, jul 2017.

[74] Danijel Pavković, Joško Deur, and Ilya Kolmanovsky. Adaptive kalman filter-based load torque compensator for improved si engine idle speed control. *IEEE Transactions on Control Systems Technology*.

[75] Matija Krznar, Danijel Pavković, Yuliia Kozhushko, Mihael Cipek, Davor Zorc, and Mladen Crnekovic. Control system design for hybrid power supply of an unmanned aerial vehicle based on linearized averaged process models. *ICUAS 2020*.

[76] Danijel Pavković, Matija Krznar, Mihael Cipek, and Maja Trstenjak. Bldc generator speed estimation suitable for internal combustion engine control of hybrid propulsion multi-rotor uavs. *ICUAS 2020*.

[77] Wang Lu, Daibing Zhang, Jiyang Zhang, Tengxiang Li, and Tianjiang Hu. Design and implementation of a gasoline-electric hybrid propulsion system for a micro triple tilt-rotor vtol uav. *6th Data Driven Control and Learning Systems (DDCLS)*, 2017.

[78] J.Y. Hung and L.F. Gonzalez. On parallel hybrid-electric propulsion system for unmanned aerial vehicles. *Progress in Aerospace Sciences*, 51:1–17, may 2018.

[79] Alastair P. Thurlbeck and Yue Cao. Analysis and modeling of uav power system architectures. *IEEE Transportation Electrification Conference and Expo (ITEC)*, 2019.

[80] Matija Krznar, Danijel Pavković, Yuliia Kozhushko, Mihael Cipek, and Davor Zorc. Generator set control system design for unmanned aerial vehicle hybrid propulsion. *Sustainable Development of Energy Water and Environment Systems (SDEWES). 2020;.*

[81] Matija Krznar, Danijel Pavković, Mihael Cipek, Mladen Crneković, and Davor Zorc. Design of a low-cost dc / dc converter power distribution system for a hybrid power unit of the multirotor unmanned aerial vehicle. *Sustainable Development of Energy Water and Environment Systems (SDEWES). 2020;.*

[82] Binbin Lu, Qihui Yu, Xiangheng Fu, Yan Shi, and Maolin Cai. Parameter matching of hybrid coaxial rotors and multi-rotor uav's power system. *IEEE International Conference on Aircraft Utility Systems (AUS)*, 2016.

[83] Bohwa Lee, Poomin Park, Chuntaek Kim, Sooseok Yang, and Seokmin Ahn. Power managements of a hybrid electric propulsion system for uavs. *Journal of Mechanical Science and Technology*, 26:2291–2299, 2012.

[84] Christopher Depcik, Truman Cassady, Bradley Collicott, Sindhu Preetham Burugupally, Xianglin Li, Shah Saud Alam, Jose Rocha Arandia, and Jared Hobeck. Comparison of lithium ion batteries, hydrogen fueled combustion engines, and a hydrogen fuel cell in powering a small unmanned aerial vehicle. *Energy Conversion and Management*, 207:112514, 2020.

[85] Magdalena Dudek, Piotr Tomczyk, Piotr Wygonik, Mariusz Korkosz, Piotr Bogusz, and Bartłomiej Lis. Hybrid fuel cell–battery system as a main power unit for small unmanned aerial vehicles (uav). *Int. J. Electrochem. Sci*, 8(6):8442–8463, 2013.

[86] Tian Zhang, Xiaoping Zhu, Zhou Zhou, Rui Wang, and Ran Chen. Energy management of solar uav level flight. *IEEE International Conference on Prognostics and Health Management (ICPHM)*, 2018.

[87] Hyeon Bo Park, Joo Seok Lee, and Kee Ho Yu. Experiment and evaluation of solar powered uav by virtual flight system. *54th Annual Conference of the Society of Instrument and Control Engineers of Japan (SICE)*, 2015.

[88] P. Panagiotou, I. Tsavlidis, and K. Yakinthos. Conceptual design of a hybrid solar male uav. *Aerospace Science and Technology*, 53:207–219, 2016.

[89] *Quadrotor photograph*, Accesed: June 2020. [Internet] https://www.amazon.com/Hobbypower-Quadcopter-APM2-8-Controller-Brushless/dp/B01DLL6PIA.

[90] *Hexarotor photograph*, Accesed: June 2020. [Internet] https://www.amazon.com/Hobbypower-Hexacopter-Pixhawk-Flight-Controller/dp/B07KYM1ZPM.

[91] Denis Kotarski, Petar Piljek, Hrvoje Brezak, and Josip Kasać. Chattering-free tracking control of a fully actuated multirotor with passively tilted rotors. *Transactions of FAMENA*, 42:1–14, 2018.

[92] Denis Kotarski and Josip Kasać. Generalized control allocation scheme for multirotor type of uavs. *Drones - Applications / Dekoulis, George (ur.). London: IntechOpen.*

[93] *S500 frame photograph*, Accesed: June 2020. [Internet] https://www.unmannedtechshop.co.uk/product/s500-quadcopter-frame/.

[94] *S500 frame fuselage photograph*, Accesed: June 2020. [Internet] https://www.amazon.in/Quadcopter-Fuselage-Version-Carbon-Landing/dp/B01E50896C.

[95] *DC motor for Multirotors*, Accesed: June 2020. [Internet] https://www.aliexpress.com/i/32799676863.html.

[96] *BLDC Motor Emax MT2213 935KV*, Accesed: July 2020. [Internet] https://www.unmannedtechshop.co.uk/product/brushless-motor-emax-mt2213-935kv.

[97] *BLDC motor U8 KV100*, Accesed: July 2020. [Internet] https://store-en.tmotor.com/goods.php?id=322.

[98] José Carlos Gamazo-Real, Ernesto Vázquez-Sánchez, and Jaime Gómez-Gil. Position and speed control of brushless dc motors using sensorless techniques and application trends. *Sensors (Basel)*, 10:6901–6947.

[99] Lavanya Y, Bhavani N.P.G, Neena Ramesh, and Sujatha K. Sensorless vector control of bldc using extended kalman filter. *Signal and Image Processing International Journal*, 2015.

[100] Santanu Mondal, Abhirup Nandi, Indranil Mallick, Chirantan Ghosh, and Alapan Giri. Performance analysis of sensored and sensorless drive of bldc motor using different types of dc / dc converters in matlab / simulink platform. *Devices for Integrated Circuit (DevIC)*, 2017.

[101] *DYS BLHeli XM30A Mini ESC*, Accesed: July 2020. [Internet] https://www.getfpv.com/dys-blheli-xm-30a-mini-esc-oneshot-125.html.

[102] *Turnigy Multistar 30 Amp BLHeli Multi-rotor Brushless ESC*, Accesed: July 2020. [Internet] https://hobbyking.com/en_us/turnigy-multistar-30-amp-blheli-multi-rotor-brushless-esc-2-6s-v2-0.html.

[103] *Flame 180A ESC*, Accesed: July 2020. [Internet] http://store-en.tmotor.com/goods.php?id=733.

[104] *5045 propeller photograph*, Accesed: July 2020. [Internet] https://www.rc-planes.nl/en/category/propellers-/.

[105] *8045 propeller photograph*, Accesed: July 2020. [Internet] https://electronation.pk/product/8045-propeller/.

[106] *2266 propeller photograph*, Accesed: July 2020. [Internet] http://store-en.tmotor.com/goods.php?id=386.

[107] Emad Ebeid, Martin Skriver, and Jie Jin. A survey on open-source flight control platforms of unmanned aerial vehicle. *Euromicro Conference on Digital System Design (DSD)*, 2017.

[108] *F4 STM32 Flight Controller*, Accesed: July 2020. [Internet] https://www.getfpv.com/f4-advanced-flight-controller-mpu6000-stm32f405.html.

[109] *NAZA DJI flight controller*, Accesed: July 2020. [Internet] https://alexnld.com/product/dji-naza-m-lite-version-multi-rotor-flight-controller-gps-combo/.

[110] *Pixhawk 4 flight controller*, Accesed: July 2020. [Internet] https://docs.px4.io/v1.9.0/en/flight_controller/pixhawk4.html.

[111] *Lipo GensAce battery*, Accesed: July 2020. [Internet] https://www.gensace.de/uav-lipo.

[112] *TitanZG62PCI-HV*, Accesed: July 2020. [Internet] https://toni-clark-shop.com/ZG-62PCI-HV-with-Zenoah-Rubber-Plug-Cap-Microprocessor-Ignition.

[113] *Valach Motors VM 85 B2-FS*, Accesed: July 2020. [Internet] https://toni-clark-shop.com/Valach-Motors-VM-85-B2-FS_1.

[114] *Valach Motors VM-280 B4-FS*, Accesed: July 2020. [Internet] https://toni-clark-shop.com/Valach-Motors-VM-280-B4-FS-280ccm_1.

[115] *Valach VM R5-250 radial engine*, Accesed: July 2020. [Internet] https://toni-clark-shop.com/Valach-Motors-VM-R5-250-radial-engine.

[116] Guangtong Xu, Li Liu, and Xiaohui Zhang. Modeling and performance analysis for low altitude electric uavs. In *2016 International Conference on Civil, Transportation and Environment*. Atlantis Press, 2016.

[117] Danijel Pavković, Matija Hoić, Joško Deur, and Joško Petrić. Energy storage systems sizing study for a high-altitude wind energy application. *Energy*, 76:91–103, 2014.

[118] *Fuel Cell Module 800w photograph*, Accesed: July 2020. [Internet] https://www.unmannedsystemstechnology.com/wp-content/uploads/2017/03/800W-Drone-Fuel-Cell-Power-Module-e1555498237984-768x511.jpg.

[119] Guo, Zhou, Zhu, and Bai. Low-cost sensors state estimation algorithm for a small hand-launched solar-powered uav. *Sensors*, 19:4627.

[120] *HELIOS protoype flying wing NASA*, Accesed: July 2020. [Internet] https://en.wikipedia.org/wiki/File:Helios_Prototype_flying_wing.jpg.

[121] *Walkera Ql 1200*, Accesed: July 2020. [Internet] https://steemit.com/steemhunt/@tornad/walkera-ql-1200-petrol-electric-hybrib-drone-over-2h-flight-time.

[122] *H2 drone hybrid engine*, Accesed: July 2020. [Internet] https://richenpower.business.social/product/h2-drone-hybrid-engine.

[123] *GAIA 160 Hybird Multirotor*, Accesed: July 2020. [Internet] https://www.foxtechfpv.com/gaia-160-hybrid-hexacopter-arf-combo.html.

[124] P. G. Tait. On the rotation of a rigid body about a fixed point. *Cambridge University Press*, 6:430–434, 1869.

[125] G.H. Bryan. Stability in aviation: An introduction to dynamical stability as applied to the motion of aeroplanes. 88:406–407, 1912.

[126] Denis Kotarski, Petar Piljek, and Krznar Matija. Mathematical modelling of multirotor uav. *International Journal of Theoretical and Applied Mechanics*, 1:233, 2016.

[127] Joachim Schömann. Hybrid-electric propulsion systems for small unmanned aircraft. *Technische Universität München*, 2014.

[128] Nicu Bizon, Hossein Shayeghi, and Naser Mahdavi Tabatabaei. *Analysis, control and optimal operations in hybrid power systems: Advanced techniques and applications for linear and nonlinear systems*. Springer, 2013.

[129] John G Hayes and G Abas Goodarzi. *Electric powertrain: Energy systems, power electronics and drives for hybrid, electric and fuel cell vehicles*. John Wiley & Sons, 2018.

[130] Daniel Raymer. *Aircraft design: a conceptual approach*. American Institute of Aeronautics and Astronautics, Inc., 2012.

[131] V Ganesan. *Internal combustion engines*. McGraw Hill Education Ltd, 2012.

[132] Willard W. Pulkrabek. *Engineering fundamentals of the internal combustion engine*, volume 126. 2004.

[133] JB Heywood. *Internal Combustion Engine Fundamentals, Second Ed.* McGraw-Hill, New York.

[134] Kazimierz Lejda and Paweł Woś. *Internal Combustion Engines*. IntechOpen, 2012.

[135] Lino Guzzella and Christopher H. Onder. *Control of Engine Systems*. Springer Science & Business Media, 2010.

[136] Danijel Pavković, Almir Sedić, and Zvonimir Guzović. Oil drilling rig diesel powerplant fuel efficiencyimprovement potentials through rule-based generator scheduling and utilizationof battery energy storage system. *Energy conversion and management*, 121:194–211, 2016.

[137] Abeysekera M. Bastida H, Ugalde-Loo CE. Dynamic modelling and control of a reciprocating engine. *9th International Conference on Applied Energy, ICAE2017*, 142:1282–1287, 2017.

[138] Ivan Mahalec, Zoran Lulić, and Darko Kozarac. *Motori s unutarnjim izgaranjem*. 2010.

[139] Joško Deur, Vladimir Ivanović, Danijel Pavković, and Martin Jansz. Identification and speed control of si engine for idle operating mode. *SAE Technical Papers*.

[140] Danijel Pavković. *Procjena varijabli stanja automobilskog pogona s primjenama u regulaciji*. PhD thesis, Sveučilište u Zagrebu, Fakultet strojarstva i brodogradnje, 2007.

[141] Elbert Hendricks and Spencer C. Sorenson. Mean value modelling of spark ignition engines. *SAE Technical Papers*.

[142] Joško Deur, Davor Hrovat, Joško Petrić, and Željko Šitum. A control-oriented polytropic model of si engine intake manifold. *ASME 2003 International Mechanical Engineering Congress and Exposition*, 2003.

[143] Joško Deur and Željko Šitum. Modeling and experimental validation of si engine with emphasis on manifold thermal effects. In *Internal memorandum 10/21/02*. 2002.

[144] Joško Petrić, Joško Deur, Danijel Pavković, Ivan Mahalec, and Zvonko Herold. Experimental setup for si-engine modeling and control research. *Strojarstvo : časopis za teoriju i praksu u strojarstvu*, 46(1-3):39–50, 2004.

[145] Rajesh Rajamani. *Mean Value Modeling of SI and Diesel Engines*. Springer, 2012.

[146] Jacek F Gieras. *Electrical Machines: Fundamentals of Electromechanical Energy Conversion*. Crc Press, 2016.

[147] Juha Pyrhonen, Tapani Jokinen, and Valeria Hrabovcova. *Design of rotating electrical machines*. John Wiley & Sons, 2013.

[148] Theodore Wildi et al. *Electrical machines, drives, and power systems*. Pearson, 2014.

[149] Werner Leonhard. *Control of electrical drives*. Springer Science & Business Media, 2001.

[150] Rik De Doncker, Duco WJ Pulle, and André Veltman. *Advanced electrical drives: analysis, modeling, control*. Springer Science & Business Media, 2010.

[151] Nafaa Jeddi, Lilia El Amraoui, and Fernando Tadeo. Modelling and simulation of a bldc motorspeed control system for electric vehicles. *International Journal of Electric and Hybrid Vehicles*, 8:178, 2016.

[152] V. Aishwarya and B. Jayanand. Estimation and control of sensorless brushless dc motor drive using extended kalman filter. *International Conference on Circuit, Power and Computing Technologies (ICCPCT)*, 2016.

[153] Duane C Hanselman. *Brushless permanent magnet motor design*. The Writers' Collective, 2003.

[154] J. R. Hendershot and Timothy John Eastham Miller. *Design of brushless permanent-magnet motors*. Magna Physics, 1994.

[155] Muhammad H Rashid. *Power electronics handbook*. Butterworth-Heinemann, 2017.

[156] J. Muhlethaler, J. Biela, J. W. Kolar, and A. Ecklebe. Improved core-loss calculation formagnetic components employed in power electronic systems. *IEEE Transactions on Power Electronics*, 27:964–973, 2012.

[157] Jieli Li, T. Abdallah, and C. R. Sullivan. Improved calculation of core loss with nonsinusoidal waveforms. *IAS Annual Meeting (IEEE Industry Applications Society)*.

[158] TBR David Linden. *Handbook of Batteries*. McGraw Hill, 2002.

[159] Hongwen He, Rui Xiong, and Jinxin Fan. Evaluation of lithium-ion battery equivalent circuit models for state of charge estimation by an experimental approach. *Energies*, 4(4):582–598, 2011.

[160] Danijel Pavković, Mihael Lobrović, Mario Hrgetić, Ante Komljenović, and Viktor Smetko. Battery current and voltage control system design with charging application. *IEEE Conference on Control Applications (CCA)*, 2014.

[161] Andrzej M Trzynadlowski. *Introduction to modern power electronics*. John Wiley & Sons, 2015.

[162] Keng C Wu. *Power converters with digital filter feedback control*. Academic Press, 2016.

[163] Fang Lin Luo and Hong Ye. *Advanced DC/DC converters*. CRC Press, 2016.

[164] Pasquale M Sforza. *Theory of aerospace propulsion*. Butterworth-Heinemann, 2016.

[165] Milan Vrdoljak. *Osnove aerodinamike i mehanike leta helikoptera*. Fakultet strojarstva i brodogradnje, Zagreb, 2007.

[166] Wayne Johnson. *Rotorcraft aeromechanics*, volume 36. Cambridge University Press, 2013.

[167] Moses Bangura, Marco Melega, Roberto Naldi, and Robert Mahony. Aerodynamics of rotor blades for quadrotors. *arXiv preprint arXiv:1601.00733*, 2016.

[168] *Toni Clark Home page*, Accesed: July 2020. [Internet] http://www.toniclark.com/index_en.html.

[169] Toni Clark practical scale GmbH. *Titan ZG45PCI user manual*, 2020. http://www.practical-scale.com/ftp/ZG45PCI-HV_en.pdf.

[170] *Zenoah G320RC*, Accesed: July 2020. [Internet] https://www.zenoah.com/int/products/hobby-engines/g320rc/967289001/.

[171] *Zenoah G320RC Owner's manual*, 2020. http://www.davesmotors.com/site/zenoah-g320rc-owners-manual-ddm.pdf.

[172] *National Instruments CompactRIO Controller*, Accesed: July 2020. [Internet] https://www.ni.com/en-rs/shop/compactrio/what-are-compactrio-controllers.html.

[173] *Mitsubishi Electric Co. FX5 series*, Accesed: July 2020. [Internet] https://www.mitsubishielectric.com/fa/products/cnt/plcf/pmerir/option/index.html.

[174] Joško Petrić, Joško Deur, Željko Šitum, and Ivan Mahalec. Initial experiments on a setup for ic engine modeling and control research. *Proceedings IAT03*, pages 289–296, 2003.

[175] Mihael Cipek, Joško Petrić, and Danijel Pavković. A novel approach to hydraulic drive sizingmethodology and efficiency estimation based on willans line. *Journal of Sustainable Development of Energy, Water and Environment Systems*, 7:155–167.

[176] *Maytech MTO6374–170–HA–C brushless motor*, Accesed: July 2020. [Internet] https://maytech.cn/products/brushless-hall-sensor-motor-mto6374-170-ha-c.

[177] *HX711 load cell*, Accesed: July 2020. [Internet] https://electropeak.com/analog-digital-hx711.

[178] *GW Instek LCR 6000 Series*, Accesed: July 2020. [Internet] https://www.gwinstek.com/englobal/products/detail/LCR-6000.

[179] *Tattu 10000 mAh 22.2V 25C 6S1P Lipo Battery Pack*, Accesed: July 2020. [Internet] https://www.gensace.de/tattu-10000mah-22-2v-25c-6s1p-lipo-battery-pack.html.

[180] *800W high power DC step-down power supply output 30A constant voltage constant current adjustable input voltage DC 20V-70V module*, Accesed: July 2020. [Internet] https://www.aliexpress.com/i/4000353761772.html.

[181] RC Benchmark. *Thrust stand series 1580 User manual*, 2020. https://cdn-docs.rcbenchmark.com/manuals/series-15-enclosure/Series-15-Enclosure-User-Manual-V1.0.pdf.

[182] *RC Benchmark thrust stand series 1580*, Accesed: July 2020. [Internet] https://www.rcbenchmark.com/products/thrust-stand-series-1580?variant=16152808718438.

[183] Barry W Williams. *Power electronics: devices, drivers and applications*. Macmillan International Higher Education, 1987.

[184] Pierre Naslin. *Essentials of optimal control*. Iliffe, 1968.

[185] Danijel Pavković and Joško Deur. *Modeling and control of electronic throttle trive: a practical approach–from experimental characterization to adaptive control and application*. Lambert Academic Publishing, 2011.

[186] Adam Polak. Low-cost image-assisted inertial navigation system for a micro air vehicle. *Arizona State University*, 2014.

[187] *Mega 2560 Pro Mini Atmega2560*, Accesed: July 2020. [Internet] https://robotdyn.com/mega-2560-pro-embed-ch340g-atmega2560-16au.html.

[188] *STM debugging tool STlink V2*, Accesed: July 2020. [Internet] https://www.st.com/en/development-tools/st-link-v2.html.

[189] Allegro Microsystems. *ACS758 current sensor datasheet*, 2020. https://www.allegromicro.com/en/products/sense/current-sensor-ics/fifty-to-two-hundred-amp-integrated-conductor-sensor-ics/acs758.

[190] *ACS758 100A current sensor*, Accesed: July 2020. [Internet] https://www.makerfabs.com/acs758lcb-50a-current-sensor.html.

[191] *USB DC Step Down Module Isolated Power Supply Buck Converter Stabilizer1 2V 24V 36V 48V 72V to 5V 1A*, Accesed: July 2020. [Internet] www.icstation.com/step-down-module-isolated-power-supply-board-buckconverter-stabilizer-p-13388.html.

[192] *FEETECH Continuous Rotation Servo*, Accesed: July 2020. [Internet] https://www.pololu.com/product/3430.

[193] *Ardupilot. Pixhawk vibrations mesurement*, Accesed: July 2020. [Internet] https://ardupilot.org/copter/docs/common-measuring-vibration.html.